Determination of the Local Group Gravitational Acceleration using All-Sky Red-Shift Surveys.

Kenton J. D'Mellow

Doctor of Philosophy
The University of Edinburgh
2001

This thesis is my own composition except where indicated in the text.

March 21, 2002

Acknowledgements

I was surprised how many different ways people have contributed toward the life experience that has been my PhD. A PhD is more than just study. It's a way of life, and as such, almost all of the people in my life should be thanked for their help, in whatever way it was.

First and foremost, I'd like to thank those I've worked with directly. Will Saunders and Andy Taylor have both devoted a lot of their time and effort toward my education, and for that I thank them greatly. It has been a pleasure to work with them both, even though my confused face almost never left me throughout. Alan Heavens has too, been very supportive, and inspiring in the background, and has always been kind enough to provide an encouraging word in the final push. I also feel that John Peacock and Philip Best deserve a mention, so thankyou.

Secondly I would like to thank my friends at the ROE: Peter Watts, Rob Smith, Simon Glover, and Louisa Nolan. It's hard to know where to start with you. Going through a PhD together has been the most memorable experience of my life, and I couldn't have been luckier than having you to go with. You have been great to me, great to work with (especially Pete and Rob), great to play with (all of you), and great to watch dance (Simon). Rob especially has been a great man to live with. Thank you all for making my life in Edinburgh the experience it has been. Friends do not stop there of course. I have been lucky to be surrounded by the crowd that make the student population at the ROE. From oldies like Richard Knox, Simon Dye, Matthew Horrobin, Helen Valentine and Jo McAllister, to youngies like James Manners, Ali Higgins, Andy Digby and Michael Brown. Thanks. I'd like to make a special thankyou to Rachel Mason, who has been without exception a fantastic person to me in my final and often troubled year.

I'd also like to thank people who've inspired me along the way. These include

Victor Pruden, Chris Whitworth and Lewis Ryder for being excellent and enthusiastic tutors, and Jason Dale and Andrew Smith for being not only extremely good friends, but an almost constant intellectual stimulation. The enthusiasm of you all has made me the person I am today. As far as good friends go, I owe thanks to Richard Thacker who has been an excellent friend to me in this last year.

I owe a word or two to people at my new home in Glasgow, who have all helped me in the last stretch in one way or another. Thanks to Martin Hendry for being so very encouraging, Richard Barrett for inspiration, Hugh Potts, Helen Bryce, Gail Penny and Martin O'Dwyer for interest and support.

To my family who have supported me throughout in many ways. Mum, Dad, Dawn, Anita, Bob. Thankyou.

Finally I owe huge thanks to Hannah, to whom the thankyou is for so many reasons. You have been there for me more times than I could reasonably ask for, and I am certain I could not have pulled this off without your care and support throughout. From before the beginning to beyond the end, at work, at home, through laughter and sadness, you've been an absolute gem to me, and I cannot thank you enough. You're a star.

Abstract

A consolidation of the Local Group velocity as inferred from measurements of the Cosmic Microwave Background, and that inferred from gravitational arguments, is of major importance to modern cosmology. Agreement between the two lends strength to modern ideas of structure formation, and can in principle, be used to estimate the matter density parameter, Ω_m. Measurement of the change of the Local Group velocity with respect to increasingly distant objects can also be used as a probe of the mass of nearby structures.

Modern methods of velocity determination employ information about the local matter density to construct an estimate of the local gravitational field. The most effective current method of probing the local matter density is by using all-sky galaxy redshift surveys to map the 3-dimensional distribution of nearby galaxies, and then use these galaxies to infer the distribution of matter throughout the local Universe.

However, any practical determination of the Local Group velocity is fraught with errors. Among these are: distortion effects on the data introduced by using an galaxy's redshift as a measure of its distance; sampling effects caused by the approximate representation of a continuous mass distribution by a sample of discrete galaxies; intrinsic uncertainty caused by only sampling a nearby finite subset of the (effectively infinite) mass distribution; and the uncertainty in the determination of a correction for non-linear effects caused by nearby massive structures.

This thesis aims to give a definitive measure of the velocity of the Local Group from gravitational arguments while attempting to minimise errors in the calculation. Iterative techniques are used to converge on a self consistent solution to the Local Group velocity and surrounding spatial galaxy distribution. To minimise intrinsic survey error, a new dataset—the Behind The Plane (BTP) galaxy

redshift survey has been completed and analysed. The BTP is the low-latitude extension to the previously completed Point Source Catalogue redshift (PSCz) survey of galaxies. Near-infrared and radio techniques were used to identify and measure optically obscured galaxies that were excluded from the PSCz, increasing the overall sky coverage from 84% to 93%. This high degree of sky coverage makes the PSCz + BTP the best available dataset for dynamical studies of the local Universe. The reduction of the gap in sky coverage significantly reduces uncertainty in dynamical predictions, especially as the missing strip behind the Milky Way is known to include the Great Attractor.

The major result of this work is the possible discovery of an unexpectedly large mass concentration beyond the Great Attractor, at an approximate distance of $cz = 20,000 \mathrm{kms}^{-1}$ in the direction $l = 300, b = 0$. The misalignment between the inferred Local Group velocity vector and the CMB temperature dipole significantly increases, and β parameter estimates yield inconsistency with many other current and reliable estimates in the literature, if this structure is excluded. Upon the inclusion of this concentration, estimates for the Local Group velocity center upon $l = 245$, $b = 30$, and yield a value of $\beta_{IRAS} = 0.65 \pm 0.01$. Directional misalignment is consistent to within 2-σ, but is robust across significant variation in both the data and calculation method applied.

Contents

List of Figures

List of Tables

List of Abbreviations

AIPS	Astronomical Image Processing System
APM	Automated Plate Measuring (Machine)
ATNF	Australia Telescope National Facility
BTP	Behind The Plane (survey)
CCD	Charge-Coupled Device
CDM	Cold Dark Matter
CMB(R)	Cosmic Microwave Background (Radiation)
COBE	Cosmic Background Explorer
CTIO	Cerro Tololo Interamerican Observatory
DSS	Digitized Sky Survey
FITS	Flexible Image Transport System
FWHM	Full Width Half Maximum
GI	Gravitational Instability
HCON	Hours-Confirmation
HDM	Hot Dark Matter
IPAC	Infrared Processing and Analysis Center
IRAF	Image Reduction and Analysis Facility
IRAS	Infrared Astronomical Satellite
MACHO	Massive Compact Halo Object
NOAO	National Optical Astronomy Observatory
NRAO	National Radio Astronomy Observatory
NVSS	NRAO VLA Sky Survey
POSS	Palomar Optical Sky Survey
PSC	Point Source Catalogue
PSCz	Point Source Catalogue Redshift (survey)
SLAP	Spectral Line Analysis Package
VLA	Very Large Array

WIMPS	Weakly Interacting Massive Particles
ZOA	Zone of Avoidance

Chapter 1

Introduction

1.1 Big-Bang Cosmology

Big-Bang cosmology is arguably the most successful model of the Universe to date. It's beginnings lie in the early 20th century, when Einstein began work on his theories of Special and General Relativity. Prior to Einstein's theories, a widely regarded model of the Universe was one of steady state: the Universe was static and unchanging. A consequence of this is that the Universe was viewed to have always existed, and therefore be infinitely old—a popular viewpoint at the time. Einstein made two contributions that seriously challenged this paradigm. The first of his contributions was the formulation of the Cosmological Principle, which in turn has roots dating back to the Copernican Revolution in the early sixteenth century. Secondly, Einstein's theory of General Relativity leads to the prediction that the Universe is in general not static, but dynamic—either expanding or contracting.

1.1.1 The Cosmological Principle

The general framework of almost any modern cosmological model is that of the Cosmological Principle, and as such, it is of paramount importance in cosmology. The Principle states that on sufficiently large scales, the Universe is homogeneous and isotropic in space. This rather bold claim is less a scientifically testable statement of fact, but more a philosophical viewpoint based on the Copernican Principle. In the early 16th century, Nicolas Copernicus revolutionised our world view of astronomy from the previous Ptolemaic description, in which the Earth was at

the centre of the Universe, about which everything else revolves. Copernicus was unhappy with this view, and took the radical step of proposing that the Universe was actually centred upon the Sun, rendering Earth as nothing more than just another planet.

Ever since the Copernican revolution, the philosophical notion that we are not in any particularly special or privileged position in the Universe has become regarded as the most solid of tenets in cosmology, despite a strong disbelief and disapproval within the Catholic Church until the mid-nineteenth century. The principle is simply the humble viewpoint that we are not special, and this, quite depressingly, looks to be the case in light of all the available evidence.

If we accept the assumption that we are at a reasonably typical place in the Universe, then we must also suspect that the Universe at large, looks quite similar as viewed from any other typical position in the Universe. This suggests Universal homogeneity. However, it is simple to construct a universe which is homogeneous but anisotropic—one can imagine an infinite matrix of perfectly aligned magnetic dipoles, which is exactly homogeneous, but totally anisotropic. However, all observations to date point toward the Universe looking very similar in all directions, as viewed from our place within it. The crux of the issue is that if we see isotropy in the Universe, then so should all other observers. If all observers see isotropy, then both Universal isotropy and homogeneity are forced upon us.

1.1.2 The Dynamical Universe

The Framework

The dynamic nature of the Universe comes from simple solutions to Einstein's field equations that are consistent with homogeneity and isotropy. The line element in 4-dimensional space-time can be expressed as

$$ds^2 = g_{\mu\nu} dx^\mu dx^\nu \tag{1.1}$$

where ds is the infinitesimal length, $g_{\mu\nu}$ is the Riemannian metric, and x^μ, x^ν are the 4-vectors $(t, \mathbf{x})$, comprising time and space. The Cosmological Principle requires immediately that solutions take the form separable in space and time:

$$ds^2 = c^2 dt^2 - a^2(t) dl^2 \tag{1.2}$$

where $a(t)$ is the scale factor, usually chosen such that for the present time, $a(t_0) = 1$. From this we can immediately see that the proper distance and relative velocity between two points of comoving separation l, is simply

$$\begin{aligned} d &= a(t)l \\ v &= \dot{d} = \frac{\dot{a}}{a}d = Hd \end{aligned} \tag{1.3}$$

Here we can see that the relative velocity of two points is linearly related to their proper separation, and the first time derivative of the scale factor. This is Hubble's Law, named after the man who first discovered this through observation of Cepheid variables in so-called spiral nebulae. In doing so, he was able to show that the spiral nebulae are in fact stellar systems completely independent of our own galaxy, and he made a first estimate of the Hubble parameter, H.

We can also ask the question of how to measure recession velocity in an expanding Universe. Consider two points in space separated by proper distance Δl, which as a consequence, are receding from each other at a rate given by equation 1.3. A beam of light of initial wavelength λ_e is sent from one point to the other. The observed light will be Doppler shifted, to a longer wavelength, given by

$$\lambda_o = \lambda_e \left(1 + \frac{v}{c}\right) = \lambda_e \left(1 + \frac{\dot{a}}{a}\frac{\Delta l}{c}\right) \tag{1.4}$$

Then if we take the limit of $\Delta l \to 0$, then we get

$$\frac{\Delta\lambda}{\Delta t} \equiv \frac{\lambda_o - \lambda_e}{\Delta t} = \lambda_e \frac{\dot{a}}{ac}\frac{\Delta l}{\Delta t} \tag{1.5}$$

Given that $\frac{\Delta l}{\Delta t} = c$, we achieve the very simple result,

$$\frac{\dot{\lambda}}{\lambda} = \frac{\dot{a}}{a}, \quad \to \quad \lambda(t) \propto a(t). \tag{1.6}$$

Finally using this the redshift of a galaxy can be defined in terms of the expansion parameter:

$$z = \frac{\lambda_o - \lambda_e}{\lambda_e}, \quad \to \quad 1 + z = \frac{a_o}{a_e}. \tag{1.7}$$

Given that for us $a_o = 1$ by definition, this is a handy way of estimating the relative "size" of the Universe at a given redshift.

The Robertson-Walker Metric and Friedmann's Equations

Let us return to the metric of equation 1.2. Just as spatial homogeneity imposes the restriction that any metric must at a given time, have the same spatial curvature at all positions, spatial isotropy imposes spherical symmetry on any solution.

This brings us to another important result: the most general form of a metric satisfying both these constraints is the Robertson-Walker metric, merely extending equation 1.2 to spherical coordinates in a curved space (Weinberg 1972):

$$ds^2 = c^2dt^2 - a^2(t)\left[\frac{dx^2}{1-kx^2} + x^2\left(d\theta^2 + \sin^2\theta d\phi^2\right)\right] \tag{1.8}$$

where k is the curvature constant, obtained by integrating Einstein's equations. The solution $k = 0$ corresponds to a spatially flat Universe, whereas non-zero k implies either positive (hypersphere) or negative (hypersaddle) curvature.

The dynamical equations for the variation of the scale factor can be derived from the metric, together with Einstein's field equations and an ideal fluid treatment of energy in the Universe. Einstein's field equations make the radical connection between energy density, and curvature of spacetime:

$$R_{\mu\nu} - \frac{1}{2}g_{\mu\nu}R = \frac{8\pi G}{c^4}T_{\mu\nu} \tag{1.9}$$

where $R_{\mu\nu}$ and R are the Ricci tensor and curvature scalar, and $T_{\mu\nu}$ is the energy-momentum tensor. In a similar manner, the energy momentum can be represented as a perfect fluid, and solved to extract the Friedmann Equations (Weinberg 1972):

$$\frac{\ddot{a}}{a} = -\frac{4}{3}\pi G\left(\rho + \frac{3p}{c^2}\right) \tag{1.10}$$

$$\left(\frac{\dot{a}}{a}\right)^2 = \frac{8}{3}\pi G\rho - \frac{kc^2}{a^2}. \tag{1.11}$$

These equations are of paramount importance for steady state theories. In the modern, matter dominated Universe, the pressure term in equation 1.10 disappears, as the radiation energy density (due to relativistic species) drops as $a^{-4}(t)$. Immediately, we can see that the acceleration term $\ddot{a}$ is negative definite, which implies that the Universe is decelerating. We can see that equation 1.11 is equivalent to the square of the Hubble parameter. If k is negative or zero, then we know the right hand side of 1.11 will always remain positive definite, and so as the current value of $\dot{a}(t)$ has been measured positive, we know $a(t)$ will always increase. This is an ever expanding Universe (either open, or flat). Alternatively, if k is positive, then there will be a time in the future when the two terms on the right will balance, and as we know $\ddot{a}(t)$ is negative definite, $a(t)$ will begin to decrease, resulting in eventual Universal collapse. The critical line between the

open and closed Universe happens when $k = 0$, resulting in an expression for the critical energy density

$$\rho_{crit} = \frac{3H^2}{8\pi G} \tag{1.12}$$

It is standard to define the Cosmological Density Parameter Ω, as being unity in the critical case of a flat Universe. Hence

$$\Omega \equiv \frac{\rho}{\rho_{crit}} = \frac{8\pi G\rho}{3H^2}. \tag{1.13}$$

We see that if $\Omega > 1$, we have an overdense, and consequently positively curved, closed Universe which will eventually collapse in upon itself. If $\Omega \leq 1$, the Universe will continue to expand for ever. Given that this controls the eventual fate of the Universe, it comes as no surprise that the value of this parameter is felt to be of utmost importance in cosmology.

As an historical note, this result worried Einstein greatly, as it seemed impossible to obtain a stable steady state solution. To overcome this, Einstein introduced a so-called *Cosmological Constant* into the field equations, the effect of which was to provide a form of repulsive force, opposing natural gravitational collapse, and resulting in a set of static solutions. When the expansion of the Universe was verified observationally by Slipher (1917) and then later by Hubble, Einstein quickly dropped the term, discarding the event as a great mistake. Somewhat ironically, it seems that for reasons completely unrelated to Einstein's initial motivation, the Cosmological Constant has reappeared, and is now alive and well in the limelight of modern inflationary models.

1.1.3 Inflation

Einstein's prediction of a dynamic Universe together with observations of Universal expansion led to the conclusion that the Universe must have been smaller, and therefore hotter in the past. One can trace this back sufficiently in time to a point when the Universe was of classically zero size and infinite temperature. This birth scenario became known as the Hot Big Bang model of the Universe, and has been hugely successful in the prediction of many observational features associated with expansion from an extremely hot and dense epoch (*e.g.* the CMB, light element abundances etc.).

Despite the huge success of the Hot Big Bang model of the Universe, there have been a number of issues for which it has not been able to provide a satisfactory

answer. These problems have become renowned and until the introduction of inflationary theories in the early 1980's, caused significant concern to proponents of the Hot Big Bang. Here is a summary of a few of the more common problems:

• *The Horizon Problem:* Causally connected regions were of size $R \simeq 100$Mpc at the time of recombination, which subtends only about a degree on the sky today. If these regions are so small, how can the CMB be the same temperature in all directions?

• *The Flatness Problem:* We observe the modern Universe to have Ω of order 1. Yet any non critical Universe is necessarily driven away from critical density at a very fast pace. In order for us to still have $\Omega \simeq 1$, a very high degree of fine tuning must have occurred in the past.

• *The Magnetic Monopole Problem:* The standard Big Bang model predicts the creation of topological defects in the form of exotic particles such as magnetic monopoles. If this is the case, then surely we should see these relics of the Big Bang?

• *The Structure Problem:* Where did structure come from? The Big Bang model alone provides no mechanism for seeding structure in the Universe, and this seems a little unsatisfactory.

• *The Matter/Antimatter problem:* At early times, it is thought that photons, protons, and antiprotons were in equal abundances, and yet today, the Universe consists of predominantly matter $N_p/N_\gamma \simeq 10^{-9}$, with any antimatter being only transient in existence at most. Somewhere along the way, it would seem that we have violated baryon conservation. How did this initial asymmetry arise?

The key feature of all inflation models is an epoch of accelerated expansion of the Universe. This serves well to immediately solve the Horizon, Flatness, and Monopole problems. This is obtainable by enforcing the condition that $\rho + 3p^2/c^2 < 0$ in equation 1.10, therefore driving a period of exponential expansion. This generally involves a negative pressure, hence the term *vacuum energy.*

Details of inflationary models vary significantly, but they usually employ the slow rolling decay of a scalar field which drives the inflation, followed by rapid oscillation which serves to reheat the Universe via the creation of matter and radiation, to its original temperature prior to the inflationary epoch. Ending inflation was

a problem in early models. More recent theories often employ multiple fields that together, manage to do everything asked of inflation.

It is clear that inflation does not come without problems of its own. Often fields and potentials are created *ad Hoc*. Fundamental issues concern the nature of the driving fields. Exactly what are these fields/potentials? Can, or do scalar fields exist? We certainly have no other known examples of a scalar field in the Universe. If these fields do exist, are they testable? Will they fit nicely into a unified theory? There are many tens of models of inflation, all with specific features, and specific problems. A good review of inflation can be found in Kolb & Turner (1990).

1.1.4 Dark Matter

While the nature of dark matter remains an almost complete mystery, there is no shortage of evidence pointing toward its existence. The first evidence for dark matter was obtained by Zwicky in 1933 who inferred from measurements of orbital velocities of galaxies in the Coma Cluster, that the Cluster mass must be far greater than that attributable to the luminous matter alone. Not only that, but it is far greater than that which can be attributed to any baryonic matter in Coma.

Equally strong evidence is seen in galaxy rotation curves of large spiral galaxies, which point toward them being embedded in a halo of dark matter. Flat rotation curves are observed in many galaxies, and cannot be modelled with only disk and bulge masses, which produce a fall-off in velocity of $v \propto 1/r$. If a galaxy were embedded in a massive halo of radius significantly greater than that of the galaxy, then flatter rotation curves are expected, as observed (van Albada *et al.* 1985). 21cm observations have been used to measure far beyond the optically visible edge of galaxies with similar results (Schweizer, van Gorkom & Seitzer 1989)

We hit an immediate problem if we try to account for all the mass in the Universe. From nucleosynthesis arguments, baryonic mass accounts for perhaps only 1-2% of the total mass required to achieve critical density. Most modern estimates using a wide variety of techniques yield a total matter density of $\Omega_m \simeq 0.3$, leaving baryonic matter almost completely out of the gravitational picture.

The question of the nature of the dark matter is one of the major points of con-

troversy, with a significant divide between a population of brown dwarfs usually residing in the halo of a galaxy, and a more ubiquitous and generally non-baryonic form of dark matter. I shall concentrate upon the latter, as it is more likely to be able to account for a large portion of the missing mass. Non-baryonic dark matter falls into two broad classes—relativistic and non-relativistic, or Hot and Cold Dark Matter respectively. Cold dark matter is thought to consist of weakly interacting massive particles (WIMPS), particles thought to be left over from the Big Bang. These particles interact with normal matter only gravitationally, or if in any other manner, then with tiny cross-section. HDM would likely consist of neutrinos or other similar relativistic species. These both have their pros and cons: CDM would involve a massive low-velocity particle which is not yet accounted for in the Standard Model. However, N-body simulations using CDM are very successful and match observations closely. HDM on the other hand, would fit into our world view much more easily, as a good candidate for this is the τ-neutrino, with a still undetermined mass, but of upper limit a few eV (Fukuda & and Collaborators (1998), Beacom, Boyd & Mezzacappa (2000)). Unfortunately, HDM models are not as successful in numerical simulations, and this counts quite badly against them. Just recently there has been some attention to hybrid Warm Dark Matter models, under increasing pressure from simulation results.

One major concern when using galaxy redshift surveys is that the relationship between the distribution of dark matter and that of luminous galaxies is not obvious. To get over this, a simple model for the bias between these distributions is usually assumed. However, as this particular aspect is of more central importance to this work, I discuss bias in the next section.

1.1.5 The Cosmic Microwave Background

The Cosmic Microwave Background (CMB) radiation was a strong testable prediction of the Hot Big Bang theory. During most of the first 300,000 years in the life of our Universe, matter and radiation were strongly coupled by Thompson scattering of high energy photons by electrons. The energy imparted upon electrons in this scattering, would generally have been in excess of the ionisation energy of neutral gas, and so the electron-baryon soup remained in a permanent state of ionisation. The radiation field had a characteristic Blackbody spectrum as expected in a totally opaque soup of radiation and charged particles.

The temperature-redshift relation for the Universe is quite straightforward. From the Stephan-Boltzmann Law, the radiation energy density is proportional to T^4, but also decreases as the fourth power of the scale factor, *i.e.* a^{-4} due to the photon energy scaling as a^{-1}. We have

$$\rho_r \propto a^{-4} \propto T^4 \Rightarrow T \propto a^{-1}. \tag{1.14}$$

Combining this with the redshift dependence of the scale factor and normalizing to the current day gives

$$1 + z = \frac{a_0}{a} \propto T \tag{1.15}$$

$$\text{Therefore } T = 2.728(1 + z) \tag{1.16}$$

As the Universe cooled to below $\simeq$3,000K (at $z \simeq 1500$), the sea of radiation, although intense, no longer had enough energy to keep nuclei and free electrons from combining to form Neutral Hydrogen, Helium, and traces of other light elements. The totally ionised soup of charged particles combined for the first time to form neutral gas, and the radiation was free to stream effectively unobstructed in all directions. As the Universe continued to expand, the now free streaming radiation redshifted further, and today peaks in the microwave region of the electromagnetic spectrum, corresponding to a blackbody temperature of $\simeq$ 3K.

The original discovery of this ubiquitous radiation was made by Penzias & Wilson (1965) whilst working on a microwave receiver for a communications company. They detected what appeared to be an isotropic source of noise, which they were having problems removing. This first observation and those performed afterwards, confirmed a blackbody spectrum in all directions of the correct temperature. This discovery has been of utmost significance and importance to the Big Bang theory, and in turn, to modern cosmology as a whole.

In 1983, the Cosmic Background Explorer (COBE) satellite was launched, with the express aim to measure more carefully the temperature of the CMB, and any directional variation (Smoot *et al.* 1992). The mission can only be regarded as a great success despite a variety of technical difficulties, and is possibly one of the most important observational programs to have ever been conducted within the 20th century.

The resultant data covers the entire sky, and is presented in figure 1.1. The CMB temperature is a uniform 2.728K, to within one part in 10^3. A dipolar temperature anisotropy of this magnitude exists, and when removed, leaves all higher

order anisotropies at about one part in 10^5. These temperature anisotropies were first predicted by Sachs & Wolfe (1967) as a manifestation of perturbations in the energy density at the time of matter and radiation decoupling. Baryonic matter had little chance to cluster until after decoupling of matter and radiation, due to the battering it received from the interacting sea of radiation. However, dark matter does not couple with the radiation, so will begin to form deeper gravitational wells, while initially baryonic matter is held in place by the photons. After recombination, the now free streaming radiation finds itself in the partially evolved potentials created by clustering dark matter. The radiation will climb out of any potential well with an associated detriment to its energy, and corresponding temperature.

Of more significance to this work is the amplitude and direction of the temperature dipole, which can be directly attributed to our velocity through space relative to the surface of last scattering. In a uniform expansion model of the universe, the surface of last scattering as seen by an observer, is at a uniform distance in all directions. Therefore the degree of redshift of the CMB due to Universal expansion will also be uniform in direction. The frame in which the CMB would actually appear isotropic over large scales is the locally defined frame of the Hubble flow. Any velocity deviation from this frame will result in a dipolar temperature anisotropy from Doppler shifting the CMB's blackbody spectrum. In calculation of the gravitational acceleration acting upon the Local Group, the aim is in part to seek agreement between the gravitational acceleration vector and the CMB temperature dipole.

1.2 Large-Scale Structure and Peculiar Velocity

In the previous section, the general framework for a Universe expanding from a hot big bang or an inflationary phase has been set. After the relatively exciting birth of the Universe, there is a long period of time in which any perturbations in the matter density can mature. During this period, assumed initially stationary matter will begin to self gravitate according to the energy density fluctuations left over from inflation. Both density and velocity fields will evolve, and will be intimately related to each other.

1.2.1 Local Group Peculiar Velocity and the CMB Temperature Dipole

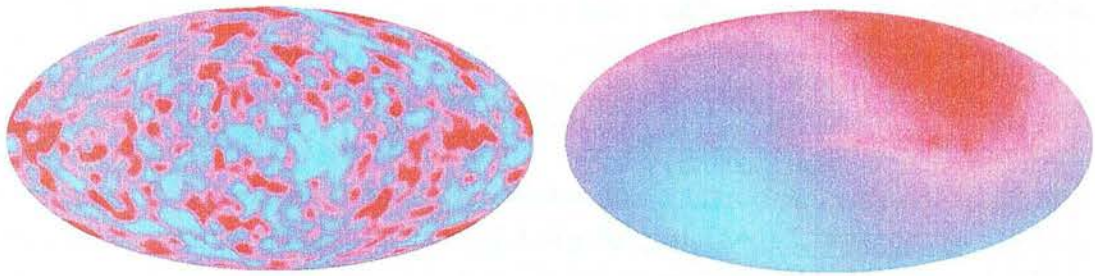

Figure 1.1: *The CMB radiation. Shown are the all sky maps decomposed into the small scale anisotropies (left), and the smooth dipolar component (right).*

Figure 1.1 shows all sky maps of the CMB decomposed into the smooth dipolar component of amplitude $\delta T/T \approx 10^{-3}$, and the remaining small scale anisotropies. The measured CMB dipole gives a motion of the heliocentric frame with respect to the Hubble flow. This corresponds to a motion of the centre of mass of the Local Group of $627 \pm 22 \mathrm{kms}^{-1}$ in the direction $[l, b] = [276 \pm 3°, +30 \pm 3°]$ (Galactic Coordinates), under the Local Group correction by Yahil, Tammann & Sandage (1977), which is given later.

The velocity dipole is calculated using a linear theory model, and so does not include any non-linear effects from the Local Group. The Local Group consists of the Milky Way, the Large and Small Magellanic Clouds (LMC and SMC) the Andromeda Galaxy M31, and a whole host of dwarf galaxies (see table 1.1), predominantly ellipticals and irregulars. The Local Group as a whole is a gravitationally bound system, with the galaxies orbiting each other around the system's centre of mass.

A linear gravitational acceleration vector calculation takes into account the action of the density field of the nearby universe ($r < 300 \mathrm{h}^{-1}\mathrm{Mpc}$) on the Local Group as a whole, and so relates to the peculiar velocity of the centre of mass of the Local Group. Thus we do not expect gravitational alignment with the measured CMB dipole, but with the *corrected* CMB dipole — *ie.* the dipole of the CMB as the centre of mass of the Local Group would see it. With this in mind, the gravitational attraction explanation to our peculiar velocity would be supported somewhat by the approximate agreement in direction with our gravitational acceleration vector.

Galaxy	RA	Dec	Type	m_v	dim	V_{rec}	Dist
WLM	00:02.0	-15:28	IB(s) IV-V	10.9	12 x 4	-42	4200
IC 10	00:20.4	+59:18	KBm	10.3	7.3 x 6.4	-83	4200
Cet dw	00:26.1	-11:02	dSph/E4				3000
NGC 147	00:33.2	+48:31	dE5 pec	9.5	15.0 x 9.4	+89	2400
And III	00:35.4	+36:31	dSph/E2	13.5			2900
NGC 185	00:39.0	+84:20	dE3 pec	9.2	14.5 x 12.5	+39	2500
M110	00:41.3	+41:41	E5 pec	8.5	19.5 x 12.5	-1	2900
And IV	00:42.5	+40:34	Irr				2900
M 32	00:42.7	+40:52	E2 (cE2)	8.1	11.0 x 7.3	+35	2900
M 31	00:42.7	+41:16	SA(s)b I-II	3.4	185.0 x 75.0	-59	2900
And I	00:45.7	+38:00	dSph/E3 pec	13.2			2900
SMC	00:51.7	-73:14	SB(s)m pec	2.3	280 x 160	-30	210
Scl dw	01:00.0	-33:42	dSph/E3 pec	10.5		+162	300
LGS 3	01:03.8	+21:53	Irr	15.4		+2	3000
IC 1613	01:05.1	+02:08	IAB(s)m V	9.2	20.0 x 18.5	-125	2900
And V	01:10.3	+47:38	dSph				2900
And II	01:16.4	+33:27	dSph/E0	13.0			2900
M 33	01:33.9	+30:39	SA(s)cd II-III	5.7	67.0 x 41.5	+3	3000
Phe dw	01:49.0	-44:42	Irr				1600
For dw	02:39.9	-34:32	dSph/E2	8.1	12.0 x 10.2		530
UGCA 86	03:59.9	+67:08	Irr/S0			+262	
UGCA 92	04:27.4	+63:30	Irr/S0			+66	3000
LMC	05:19.7	-68:57	SB(s)m	0.1	650 x 550	+13	179
Car dw	06:14.6	-50:58	dSph/E3	20.9			300
Leo A	09:59.4	+30:45	IBm V				7000
Sex B	10:00.0	+05:20	Ir+ IV-V				4000
NGC 3109	10:03.1	-26:09	Ir+ IV-V	10.0	16.0 x 2.9	+131	4100
Ant dw	10:04.1	-27:20	dSph/E3	14.8			4100
Leo I	10:05.5	+12:19	dE3	9.8			880
Sex A	10:11.1	-04:43	Ir+ V				4000
Sex dw	10:13.2	-01:37	dSph/E3				300
Leo II	11:13.5	+22:10	dSph/E0 pec				800
GR 8	12:58.7	+14:13	Im V	14.5	1.2 x 1.1	+165	5000
UMi dw	15:08.8	+67:12	dSph/E4	10.9	41.0 x 26.0		240
Dra dw	17:20.1	+57:55	dSph/E0 pec	9.9	51.0 x 31.0		280
Milky Way	17:45.6	-28:56	SAB(s)bc I-II			0	28
SagDEG	18:55.0	-30:30	dSph/E7				80
SagDIG	19:30.1	-17:42	IB(s)m V			15	2000
NGC 6822	19:44.9	-14:49	IB(s)m IV-V	9.0		+66	1700
Aqr dw	20:46.8	-12:51	Im V	13.9	2.3 x 1.2		2000
IC 5152	22:06.1	-51:17	IAB(s)m IV	10.6	4.9 x 3.0	+30	3000
Tuc dw	22:41.7	-64:25	dSph/E5				3000
And VII	23:27.8	+50:35	dSph				2900
Peg dw	23:28.6	+14:45	Im V				6000
And VI	23:51.7	+24:36	dSph				2900

Table 1.1: *A current census of Local Group Members, including morphological type, visual magnitude, angular subtention, recession velocity, and estimated distance.*

1.2.2 Linear Gravitational Instability Theory

All around us in the modern Universe, we see structure. Structure forms on a wide range of scales, from small planetary systems, star clusters and galaxies, up to the gigantic sheets and filaments consisting of many thousands of galaxies. The question of the origin of structure has been regarded as important ever since our knowledge of its existence. Within the big bang and inflation framework, quantum fluctuations in the energy density field at the time just prior to our last epoch of inflation were stretched out to much larger scales. These large but very slight perturbations from uniformity of the energy density can evolve under self gravity over the age of the Universe. This provides a mechanism for structure formation, which forms the basis of the most likely explanation of the structures we see today.

As described above, non-baryonic dark matter is free to move under the influence of gravity at all times. If we assume all matter starts with little or no bulk velocity, then baryonic matter will be attracted by the same potential wells as dark matter, and will flow in the same way. Not only does this lead to the overdensity field of baryonic matter being strongly coupled (but not identical) to that of dark matter, but it also leads to a general relationship between the velocity and matter density fields.

In practice however, we can only directly observe *luminous* matter. Using redshift surveys we can estimate the spatial distribution of a sample of galaxies. Although it is generally accepted that both baryonic and non baryonic matter will react in similar manners toward a gravitational potential, it is certainly not the case that the resulting distribution of luminous galaxies exactly matches that of dark matter. As such, it is important to establish a physically reasonable relationship between luminous galaxies and the surrounding dark matter. Strong evidence of the existence of dark matter, and its dominant gravitational influence is universally accepted now, so its exact connection with the distribution of observable galaxies is paramount.

It is by no means clear what the exact relationship between the number density of galaxies and the dark matter density is. It is standard to work with *overdensities* or *density contrasts* δ, rather than densities ρ, defined by

$$\rho_m(\mathbf{x}, t) = \rho_b(t)[1 + \delta_m(\mathbf{x})] \tag{1.17}$$

where ρ_b is the background or mean density, and ρ_m, δ_m are the local density and density contrast of matter. The most popular relationship that has been employed is the linear biassing scheme, whereby the density contrasts of galaxies, and matter are linearly related by the linear bias parameter

$$\delta_g = b\delta_m. \tag{1.18}$$

Here, galaxy formation is encouraged in higher density areas, and discouraged in lower density areas. This scheme has problems if $b > 1$. If this happens δ_g can fall below -1, giving a negative galaxy number density. Other forms of biassing, avoid this problem, and therefore may offer a more natural alternative. For example, power law biassing, and exponential biassing.

Other biassing scenarios are possible, but are generally regarded as being less likely. For example, galaxies could form in the regions of steeper gradient in the dark matter density field, where shocks created by differential inflow could compact matter into unusually dense structures. There are however, good arguments against this, most based upon the topology of the resultant spatial distribution. The subject of biassing schemes depends heavily on models of galaxy formation, and the environment in which this occurs. This subject is of immense complexity, is in itself, one of the largest issues addressed in modern cosmology, and far beyond the scope of this thesis.

Results from the equations for the dynamical evolution of the overdensity field lead to a very important and deceptively conceptual result, concerning the relation between the peculiar velocity of an object, and the surrounding matter density field. I shall summarize the salient points of the theory. I follow Peebles (Peebles 1993), and use the same notation. We start by writing down the equations for mass conservation, force, and gravitation.

$$\left(\frac{\partial \rho}{\partial t}\right)_{\mathbf{r}} + \nabla_{\mathbf{r}} \cdot (\rho \mathbf{u}) = 0 \tag{1.19}$$

$$\left(\frac{\partial \mathbf{u}}{\partial t}\right)_{\mathbf{r}} + (\mathbf{u} \cdot \nabla_{\mathbf{r}})\, \mathbf{u} = -\nabla_{\mathbf{r}} \Phi \tag{1.20}$$

$$\nabla^2_{\mathbf{r}} \Phi = 4\pi G\rho - \Lambda = 4\pi G\rho_b\,(1+\delta) - \Lambda \tag{1.21}$$

These are all expressed in proper spatial coordinates, $\mathbf{r}$ and time t, where $\mathbf{u}$ is the proper motion, Φ is the gravitational potential, G if the gravitational constant,

and ρ_b is the mean background density. Spatial coordinates comoving with the Hubble expansion can be defined for position and velocity:

$$\mathbf{x} = \frac{\mathbf{r}}{a(t)} \quad \nabla_{\mathbf{x}} = a(t)\nabla_{\mathbf{r}} \quad \mathbf{u} = \frac{d\mathbf{r}}{dt} = \frac{d}{dt}(a\mathbf{x}) = \dot{a}\mathbf{x} + a\dot{\mathbf{x}} \tag{1.22}$$

where $a(t)$ is the expansion parameter. Here, the last term in the velocity expression, $a\dot{\mathbf{x}}$ is just the peculiar velocity relative to the local comoving coordinate frame, and thus we can let $a\dot{\mathbf{x}} = \mathbf{v}(\mathbf{x}, t)$. The partial time derivative of a comoving function $f(\mathbf{x} = \mathbf{r}/a, t)$ in proper coordinates is:

$$\left(\frac{\partial f}{\partial t}\right)_{\mathbf{r}} = \left(\frac{\partial f}{\partial t}\right)_{\mathbf{x}} - \frac{\dot{a}}{a}\mathbf{x} \cdot \nabla f \tag{1.23}$$

We can use equations (1.22) and (1.23) to convert equations (1.19), (1.20), and (1.21) to a neater comoving form expressed in the density contrast of equation (1.17). We get

$$\frac{\partial \delta}{\partial t} + \frac{1}{a}\nabla \cdot [(1+\delta)\,\mathbf{v}] = 0 \tag{1.24}$$

$$\frac{\partial \mathbf{v}}{\partial t} + \frac{\dot{a}}{a}\mathbf{v} + \frac{1}{a}(\mathbf{v} \cdot \nabla)\,\mathbf{v} = -\frac{1}{a}\nabla\phi \tag{1.25}$$

$$\nabla^2\phi = 4\pi G\rho_b\delta \tag{1.26}$$

In the Newtonian limit of small overdensities and velocities, we can ignore all second order terms in equations (1.24) and (1.25) - *ie* all terms in v^2, and δv. Then we can combine these, by taking the time derivative of (1.24), and the spatial derivative of (1.25). We get

$$\frac{\partial}{\partial t}(1.24) \Longrightarrow \quad \frac{\partial^2\delta}{\partial t^2} + \frac{1}{a}\nabla \cdot \dot{\mathbf{v}} + \nabla \cdot \mathbf{v}\frac{\partial}{\partial t}\left(\frac{1}{a}\right) = 0 \tag{1.27}$$

$$\nabla \cdot (1.25) \Longrightarrow \quad \nabla \cdot \dot{\mathbf{v}} + \frac{\dot{a}}{a}\nabla \cdot \mathbf{v} = -\frac{1}{a}\nabla^2\phi \tag{1.28}$$

Now, substituting $\frac{\partial}{\partial t}\left(\frac{1}{a}\right) = -\frac{\dot{a}}{a^2}$ into (1.27), and combining with (1.28), we obtain (with 1.26)

$$\frac{\partial^2\delta}{\partial t^2} + 2\frac{\dot{a}}{a}\frac{\partial\delta}{\partial t} = 4\pi G\rho_b\delta \tag{1.29}$$

Which has a solution of the form

$$\delta = A(\mathbf{x})\,D_1(t) + B(\mathbf{x})\,D_2(t)\,. \tag{1.30}$$

$D_1(t)$ and $D_2(t)$ are the growing and decaying modes, for which there may or may not be an analytic solution. Now, if we wait until late times, the only important

term is the growing mode. We can then then express the linear mass conservation equation (derived from 1.24) as

$$\nabla \cdot \mathbf{v} = -a\frac{\partial \delta}{\partial t} = -a\delta\frac{\dot{D}}{D} \tag{1.31}$$

which can then be inverted to give an expression for the velocity field.

$$\mathbf{v} = \frac{H_0 f}{4\pi}\int_{Volume}\frac{\delta(\mathbf{r})\,\hat{\mathbf{r}}}{|\mathbf{r}^2|}\,d\mathbf{r}, \tag{1.32}$$

where f is defined in the appendix as being

$$f(\Omega_0, \Lambda) \equiv \frac{1}{H_0 D_1}\frac{dD_1}{dt} = \frac{1}{H_0 D_1}\frac{dD_1}{da}\frac{da}{dt} = \frac{d\ln D_1}{d\ln a}. \tag{1.33}$$

A good approximation for f in the general case, is

$$f \approx \Omega^{0.6} + \frac{\Omega_\Lambda}{70}\left(1 + \frac{1}{2}\Omega_0\right) \tag{1.34}$$

given by Lahav (1991). The small dependence of f on Λ allows us to rewrite (1.34) as $f \approx \Omega^{0.6}$. We can use the result given in (1.32) when determining our peculiar velocity relative to the Hubble flow, by relating the galaxy density to the matter density, using a linear bias parameter b. By doing so, (1.32) forms the basis of a calculation of the peculiar velocity of the Local Group:

$$\mathbf{v} = \frac{H_0\beta}{4\pi}\sum_{galaxies}\frac{\hat{\mathbf{r}}}{\psi\,|\mathbf{r}^2|}, \quad \beta = \frac{f}{b} \tag{1.35}$$

In measuring this quantity, the matter density Ω, and bias parameter b are degenerate. We therefore make direct measurements of β instead of Ω, with the caveat that β is specific to galaxy type, *i.e.* $\beta = \beta_{IRAS}$ in this work.

As mentioned above, equations 1.32, 1.35 seem like an extremely simple and intuitive result: the velocity of an object is proportional to the inverse square weighted mass distribution around it. This is simply Newton's law of gravity, combined with Newton's second law of motion, $F = ma$. The acceleration obtained from combining these laws is transformed into a velocity by simply integrating in time over the age of the Universe (or at least, since the decoupling of matter and radiation), which in the linear regime, is separable and manifests itself in the form of the pre-constants to the integral. The linear approximations made ensure that the gravitational potential felt by an object does not change significantly over

the course of evolution. This is the case when the distance travelled by an object is very small in comparison to the size of the surrounding potential well. When this is not the case, the object will feel a changing acceleration and consequently its resultant velocity will not in general be aligned with its current acceleration. For our purposes we will see that the linear approximation is in almost all cases sufficient for a velocity calculation on the Local Group. This will be discussed further in chapter 3.

1.2.3 Ergodicity

A regularly encountered concept in statistical cosmology is that of Ergodicity. In an attempt to measure the statistical properties of a distribution, one often appeals to the expectation value of a measure. However, the expectation of a measure is technically its ensemble average, and not its spatial one. For example, in a matter distribution, we would perhaps like to know the expected overdensity $\langle \delta(r) \rangle$. The correct way of calculating this is to measure and average the densities at position r in many Universes. Of course, we cannot do that as we only have one Universe to measure. We can however, measure and average the densities at many different positions r_i in one Universe. It is important to realise that cosmological fields are usually homogeneous and isotropic and therefore, the expectation should also be homogeneous in space. If and only if this is the case, then we can approximate the ensemble average by the spatial average. We can only do this if we sample a suitably large region, so we can assume that subsets of that region can be treated as being independent of each other. These independent regions can be treated as members of the ensemble.

The Ergodic Hypothesis states exactly this. If we average over a sufficiently large volume, then we can approximate the ensemble average with the spatial one – *i.e.* volume and ensemble averages become equivalent. This is a very useful concept, but is often taken for granted. It is not always easy to prove this (Adler 1981), but can be used with care throughout much of statistical cosmology.

1.3 Overview

This chapter has introduced the topic of Local Group motion and its consolidation with the motion inferred by the CMB temperature dipole. In order to test

this a practical determination of the matter density in the local Universe is necessary, and arguably the most effective way to map this is by conducting a galaxy redshift survey over as much of the sky as possible. However, the determination of the Local Group velocity from galaxy redshift catalogues is fraught with errors. Among these are redshift-space distortions, shot noise (finite sampling), cosmic variance (finite depth), and determination of the Local Group velocity correction from non-linear effects. This thesis addresses the problem of how to extract the most accurate velocity dipole from an all-sky galaxy redshift survey. The relevant methods, effects, and errors are discussed in relation to dipole measurements calculated using the PSCz and BTP galaxy redshift surveys, but are applicable in general.

1.3.1 Breakdown of Thesis

In chapter 2, I describe the PSCz and BTP datasets, and their suitability to the task of velocity dipole calculation. The observational techniques used in the completion of both PSCz and BTP surveys are presented. These include the initial candidate selection criteria and identification methods, and the follow up data acquisition and reduction techniques using both near-infrared, and 21cm radio spectra. Examples of the data are presented for illustrative purposes, although the entire dataset is not presented due to its size.

I concentrate on dipole calculation methods in chapter 3, and the errors and effects that need to be considered in such a calculation. More specifically, I discuss redshift-space and pseudo real-space velocity dipole calculations, using both iterative and non-iterative techniques, and compare with velocities inferred using PIZA reconstructions of (Valentine 2000). Velocity dipole results are presented for these calculation methods.

Finally, in chapter 4 I discuss the results and their implications. A large concentration is found in the data which cannot at present be shown to be an artifact of the data itself. Furthermore, inconsistencies appear when this anomaly is ignored. The results and some ideas for the continuation of this work are discussed.

Chapter 2

The PSCz + BTP Surveys: Data Acquisition and Reduction

2.1 PSCz + BTP as an Ideal Dataset

The PSCz is a survey designed with definite aims in mind. Firstly, measurement of the topography of the local Universe (making a map of nearby clusters, voids, and general structure), secondly, measuring the local gravity field, and thirdly, to use a well defined, highly uniform and complete dataset for statistical studies of the IRAS galaxy population and its distribution. Much more cosmology can, and has been done with the survey, but these basic intentions shaped the survey. For both of the main goals, sky coverage is paramount: proper reconstruction of the local gravity field requires knowledge of the local mass field in all directions. Like its predecessors - the IRAS 1.2Jy and QDOT 1 in 6 redshift surveys - the PSCz aims to achieve all-sky coverage, and has not only been the most successful in this goal, but is also much deeper and fainter, and thus more richly sampled than previous data. However, within the selection criteria, the PSCz lacks a total of 16% of the sky. To improve upon this, a low-b extension to the PSCz, the Behind The Plane (BTP) survey (Saunders *et al.* 2000a), was created. BTP collaborators are Will Saunders and Kenton D'Mellow (Edinburgh), Brent Tully (Hawaii), Bahram Mobasher (University of London), Steve Maddox (Cambridge), Will Sutherland (Oxford/Edinburgh), Esperanza Carrasco (INAOE, Puebla), George Hau (Santiago), Dave Clements (Cardiff), and Lister Staveley-Smith (CSIRO). The BTP was intended as a supplement to the existing PSCz data, pushing to lower galactic latitudes, increasing the sky coverage to 93%. These two datasets combined

are unparalleled in the field of all-sky redshift surveys, and look to remain so for quite a long time. Possible improvements over this work lie in the work on the redshift survey based on the 2 Micron All Sky Survey (2MASS – Skrutskie *et al.* (1995)). The 2MASS Redshift Survey (2MRS – Huchra *et al.* (1998), Huchra (2000)) which plans to obtain initially $\tilde{2}50{,}000$ galaxy redshifts over the whole sky to a limiting K_s magnitude of 12.2 and then up to a million galaxies with $K_s < 13.5$. Incompleteness is predicted to be less than 1% at $|b| > 30°$ and as little as possible at lower latitudes. The 2MASS team also plan to measure 21cm line widths and optical rotation curves to obtain Tully-Fisher distances to $> 10,000$ galaxies within the sample, putting excellent constraints on the local velocity field.

2.2 Overview of Survey Parameters

2.2.1 The IRAS PSCz and BTP Redshift Surveys

The PSCz is a near all-sky catalogue of infrared sources, drawn from the Infrared Astronomical Satellite (IRAS) Point Source Catalogue (PSC) (see the Explanatory Supplement of the Joint IRAS Science Working Group (1988)). The IRAS satellite flew in 1983, and mapped the entire sky at 12, 25, 60, and 100μm. The IRAS program generated a lot of data, and from these, the Point Source Catalogue was created. The PSCz covers approximately 84% of the sky: excluded were areas of high galactic extinction close to the galactic plane (often inaccurately quoted as $|b| < 10°$), and also two thin strips in ecliptic longitude, which did not receive enough coverage by the IRAS satellite – 2HCONS ("Hours Confirmation". Each HCON consists of repeated observations separated by more than 100 minutes, but less than 38 hours – see the Explanatory Supplement). Some 1HCON sources that had optical counterparts in the Faint Source Survey were also added to the survey. The PSCz is flux limited at 60μm > 0.6Jy, and sources are colour selected by the ratios of 25μm, 60μm and 100μm fluxes: $f_{60} > 0.5 f_{25}$ to exclude stars (too hot), and $f_{100} < 4 f_{60}$ to exclude galactic cirrus (too cold). In total the PSCz consists of 16422 sources, 15411 are galaxies with determined redshift. The data was officially released in late 2000 (Saunders *et al.* 2000c), and full details of the survey parameters are published in that work. The data are also available on-line at the main PSCz website *http://www.astro.physics.ox.ac.uk/~wjs/pscz.html.*

The BTP extension to the PSCz is now practically complete, and the data will be released alongside the PSCz in the near future. Some examples of the data can be seen here, but this by no means represents the entire dataset. While also nominally complete to 0.6Jy at 60μm, the higher extinction and galactic source density present in the galactic plane hampers the BTP slightly, and consequently it suffers an estimated incompleteness of 10 - 20%. Figure 2.1 shows the sky coverage of the PSCz redshift survey (white background), and of the BTP extension (yellow). The red mask is the remaining area uncovered by either survey, and is predominantly composed of the galactic plane (4%), and the two IRAS coverage gaps of constant ecliptic longitude (3%). The survey has a nominal depth of

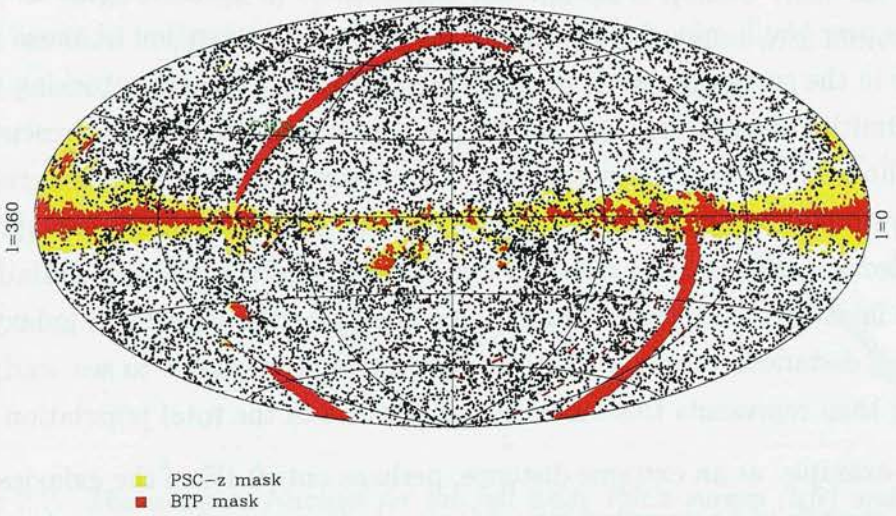

Figure 2.1: *A view of the PSCz and BTP masks in galactic coordinates. The galactic plane is clearly seen; the galactic centre is at the extremes* 0/360°. *The two strips of ecliptic longitude can also be seen clearly, and other patches of high noise have been masked.*

approximately 300h^{-1}Mpc, although there are some concerns of its completeness beyond ~200 h^{-1}Mpc. These concerns will be further addressed in chapter 3. The main catalogue excludes the Local Group galaxies, and thus all sources can be used in a linear theory Local Group velocity calculation.

2.2.2 The Selection Function

The selection function is essentially a measure of the expected number density of sources that satisfy the catalogue selection criteria, as a function of either

recession velocity or distance.

The concept of the selection function $\psi(r)$, has its basis in the luminosity function $\Phi(L)$ of the population of galaxies to be considered, and is usually defined as the proportion of the galaxy population visible at a distance, given a flux or magnitude limit. For the PSCz survey, the selection functions defined are normalized versions of the traditional definition, and so represent the actual number density of visible galaxies in the entire population, as a function of distance:

$$\psi\left(r\right) = \bar{n}\frac{\int_{4\pi r^2 f_{min}}^{\infty} \Phi\left(L\right) dL}{\int_{L_s}^{\infty} \Phi\left(L\right) dL} \tag{2.1}$$

where $\bar{n}$ is the true mean number density of IRAS galaxies, and the ratio of integrals over the luminosity function $\Phi(L)$ gives the proportion of those galaxies visible in the survey. As such, the lower limits are $4\pi r^2 f_{min}$ (*i.e.* picking brighter than limiting magnitude f_{min}), and L_s, a sensibly chosen value representing the lower limit of the luminosity function. The reason why we need a selection function is simple: in a redshift survey, every galaxy that is luminous enough to pass the selection criteria must also represent a portion of the galaxy population that is too faint to see at that distance. As you place the detectable galaxy at increasing distances, more of the population becomes too faint to see, and so that galaxy then represents this increasing proportion of the total population.

As an example, at an extreme distance, perhaps only 0.1% of the galaxies will be bright enough to be accepted into the survey. However, the matter density field will be related to the total number density of galaxies, irrespective of whether we can see them or not, and so the selection function is in a way, a compensatory measure. While the value of the selection function is related to the proportion of galaxies that are bright enough to enter the survey, we should apply a weight inversely proportional to this function, to every visible galaxy, and this will compensate properly for those that are too faint to be seen at that distance. For this extreme example, we would have a value of ψ^{-1}=1000$\bar{n}$.

Two parametric selection functions have been calculated for the PSCz, at different flux cuts: 0.595Jy calculated by Saunders *et al.* (2000c) and 0.745Jy calculated by Tadros *et al.* (1999). The form of the parametric selection function is given by

$$\psi(r) = \psi_* \left(\frac{r}{r_*}\right)^{1-\alpha} \left[1 + \left(\frac{r}{r_*}\right)^{\gamma}\right]^{-\left(\frac{\beta}{\gamma}\right)} \tag{2.2}$$

Parameter	Description	0.6Jy Value	0.75Jy Value
α	small scale slope	1.88654	1.88784
β	large scale slope	4.38595	4.58371
γ	shape parameter	1.54554	1.54983
r^*	turnover scale	89.3572	84.2616
ψ^*	normalisation	0.0067941	0.0064301

Table 2.1: *Parameter values for the two selection functions used at 0.6Jy and 0.75Jy, as described by equation 2.2*

Figure 2.2 shows the distribution of PSCz and BTP data, with the fitted parametric selection functions. For both flux cuts, the selection function falls off rather steeply at large radii (as r^{-3}). Because this fall off is quicker than the inverse square law used in calculating the dipole, the *action* associated with more distant galaxies actually increases, and they are assigned large masses.

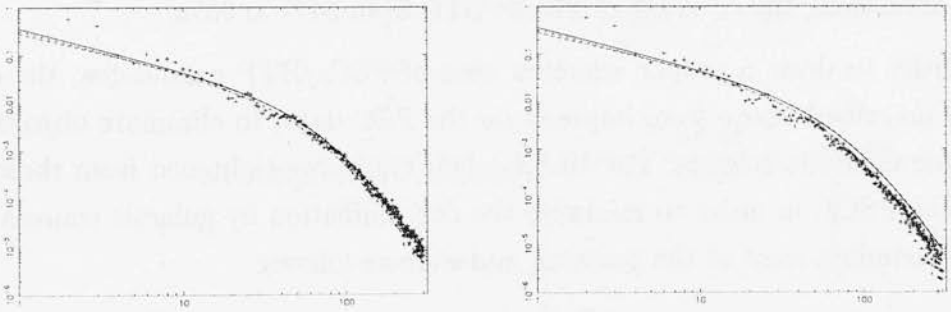

Figure 2.2: *The selection function for the full 0.6Jy PSCz survey (left) and for the 0.75Jy flux limited subset (right). Both selection functions appear in both panels (0.6Jy solid line, 0.75Jy broken line), with the number counts of the data cropped at these flux limits overlaid. Notice how the tail end falls of as r^{-3}, leading to distant galaxies being associated with large masses.*

2.3 Survey Objects

The IRAS PSC is a database of fluxes, and positions of unresolved (point) sources. Consequently, the classes of object expected to be detected cover literally any unresolved object that emits in some or all of the four chosen wavebands. As mentioned before, stars and galactic cirrus both feature in the catalogue, but so does a whole zoo of other objects - moons and planets, comets and asteroids (which have been removed already, and do not form part of the official PSC, but

are available separately), HII regions, supernova remnants, quasars and AGN, large ellipticals, etc., to name just a few. To sort out which objects were to be considered as realistic candidates, a rigorous method of identification was required, as is detailed in this section.

2.3.1 BTP Sky Coverage and Selection Criteria

The BTP mask is shown in red in figure 2.1 and consists of four main components. Firstly, the IRAS coverage gaps (3%). Secondly, areas flagged as high source density at 60μm made up approximately another 3%, where the PSC processing was changed to ensure reliability at the expense of completeness. Thirdly, areas flagged as high source density at 12 or 25μm on the basis that identifications would be impossible. Lastly, areas with $I_{100} > 100\mathrm{MJy\,ster}^{-1}$ because of excessive contamination by galactic sources. The final sky coverage of the BTP is about 9%, increasing the coverage of PSCz+BTP from 84% to 93%.

In order to draw a proper selection base of PSCz/BTP candidates, the colour cuts described above were imposed on the PSC data, to eliminate objects with uncharacteristic colours. The IRAS colour cuts were tightened from those used for the PSCz, in order to minimise the contamination by galactic sources while still including most of the galaxies, and were as follows:

$$\begin{aligned} f_{60}/f_{25} &> 2 \\ f_{60}/f_{12} &> 4 \\ f_{100}/f_{60} &> 1 \\ f_{100}/f_{60} &< 5 \end{aligned}$$

The total amount of IRAS PSC sources with $f_{60} > 0.6$Jy within the area described is 3,517. Of these, only 1,353 point sources pass these criteria—approximately one third. These sources pass on to the subsequent stages in the selection procedure. This procedure is described below and is also shown in figure 2.3.

2.3.2 Identifications

Those objects satisfying the colour criteria are still not all galaxies, so proper identification is required. Of the PSC sources remaining, 140 were found to have previously known redshifts in the literature. Of those that did not, many are immediately identifiable as galaxies from visual inspection of sky survey plates.

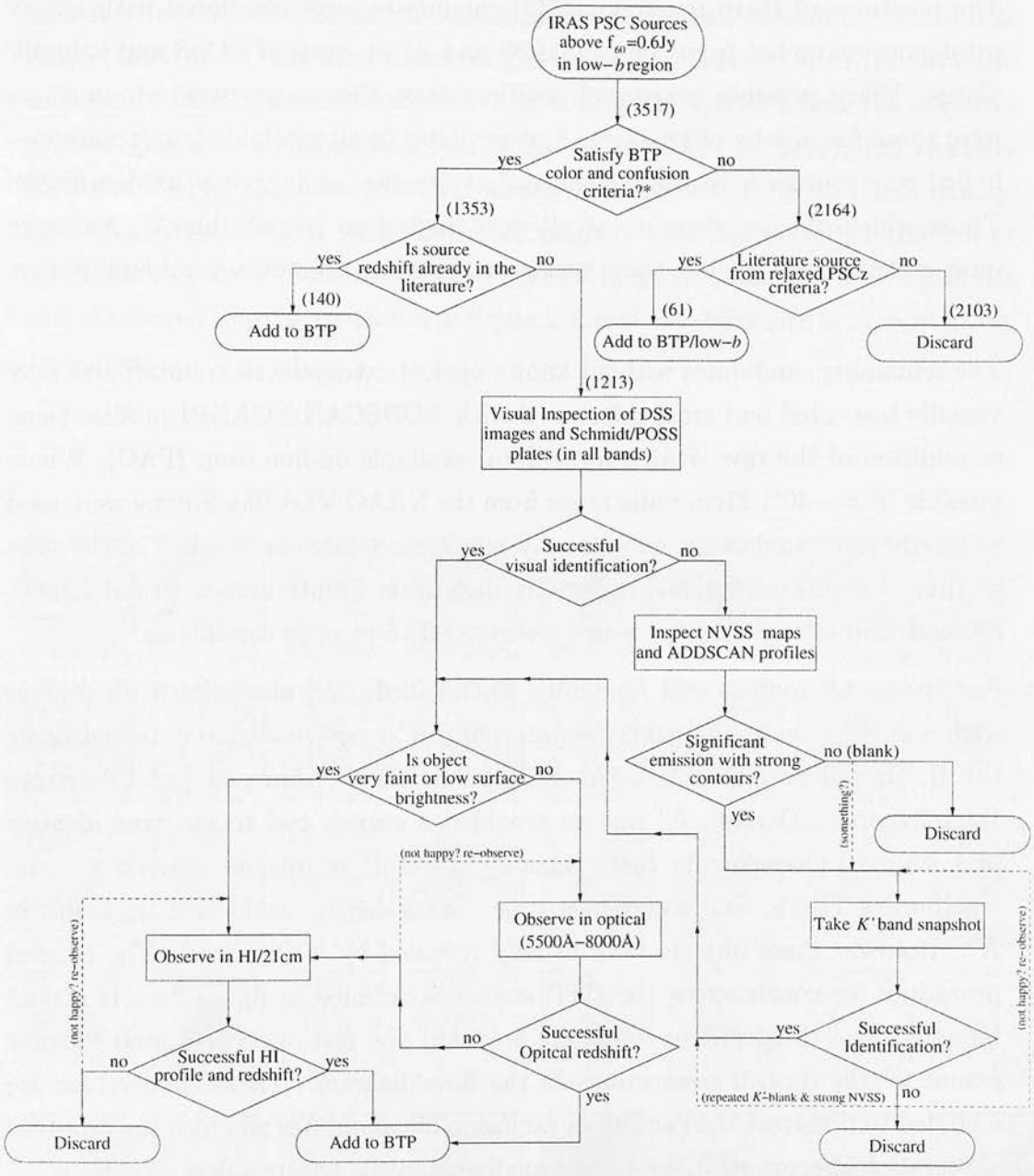

Figure 2.3: *The process by which the BTP galaxy redshift survey was constructed. There are two major sections to this flow diagram, lying above and below the bottleneck: Above, PSC selection criteria and existing data define the dataset to be observed with associated source numbers in parentheses at each step; Below is the process by which candidates are identified and included into the final survey. Dashed connections represent decisions made to ensure completeness by repetition or caution. Source numbers are not given here due to the circulatory nature of this section.*
(see selection criteria described in section 2.3.1)*

The positions of these remaining BTP candidates were correlated with galaxy catalogues extracted from the COSMOS and APM scans of POSS and Schmidt plates. When possible, arcsecond positions from these scans were obtained, as were those for nearby offset stars. Survey plates in all available bands were eyeballed, and sources were either confirmed as galaxies, or flagged as unidentifiable. Those which did not show up at all were flagged as visually blank. Although most galaxies are visible to some extent on sky survey plates, several hundred are not.

The remaining candidates without known optical extragalactic counterparts were visually inspected and cross referenced with ADDSCAN/SCANPI profiles (scan co-addition of the raw IRAS survey data, available on-line from IPAC). Where possible ($\delta > -40°$) 21cm radio maps from the NRAO VLA Sky Survey were used to clarify those undecided and visually blank candidates as detailed in the next section. In addition to this, millimetre data from Wouterloot & Brand (1989), Simbad, and other literature sources were used to identify candidates.

For almost all sources still remaining unclassified, and also almost all sources with a faint ($r > 18.5^m$) galaxy counterpart, K' snapshots were obtained using the U. Hawaii 88″, UNAM 2.1m, ESO 2.2m, CTIO 1.5m and Las Campanas 1m telescopes. Overall, K' images provided a crunch test to the true identity of a source. Occasionally there remained possible confusion between galaxies and buried YSO's, and sometimes very faint galaxies would still be blank in K'. However these objects were usually revealed by NVSS data. The general procedure for constructing the BTP survey is detailed in figure 2.3. It should be noted that the decisions made are not hard and fast, as is indicated to some extent by the dashed connections in the flow diagram. These connections are included to illustrate the caution in exclusion of candidates and also the repeated observations necessary to ensure completeness in the construction process.

2.3.3 NVSS Radio Maps

The NRAO VLA Sky Survey (NVSS - Condon *et al.* (1998)) covers the entire sky north of J2000 $\delta = -40°$, at 20cm (1.4GHz). It consists of about 200,000 sources brighter than 2.5mJy, and has positional accuracy (for unresolved point sources) ranging from $\leq 1''$ for strong sources, up to $7''$ at the survey limit. This is particularly useful, as IRAS galaxies are predominantly large spirals, with

high star formation rates and a large quantity of HI gas. Condon, Anderson & Helou (1991) show that there exists a tight correlation between the FIR and radio emission of IRAS galaxies, and the NVSS is deep enough to detect the majority of IRAS galaxies with $60\mu m$ flux $f_{60} \leq 0.28$Jy (Condon *et al.* 1998), and virtually all above 0.6Jy. Therefore if a PSC source is suspected to be an IRAS galaxy, then cross referencing it with the NVSS maps can do well to either confirm or reject the suspicion. Some examples of NVSS maps of confirmed PSCz galaxies and of rejected sources are shown in figure 2.4, and the difference is in most cases, quite clear.

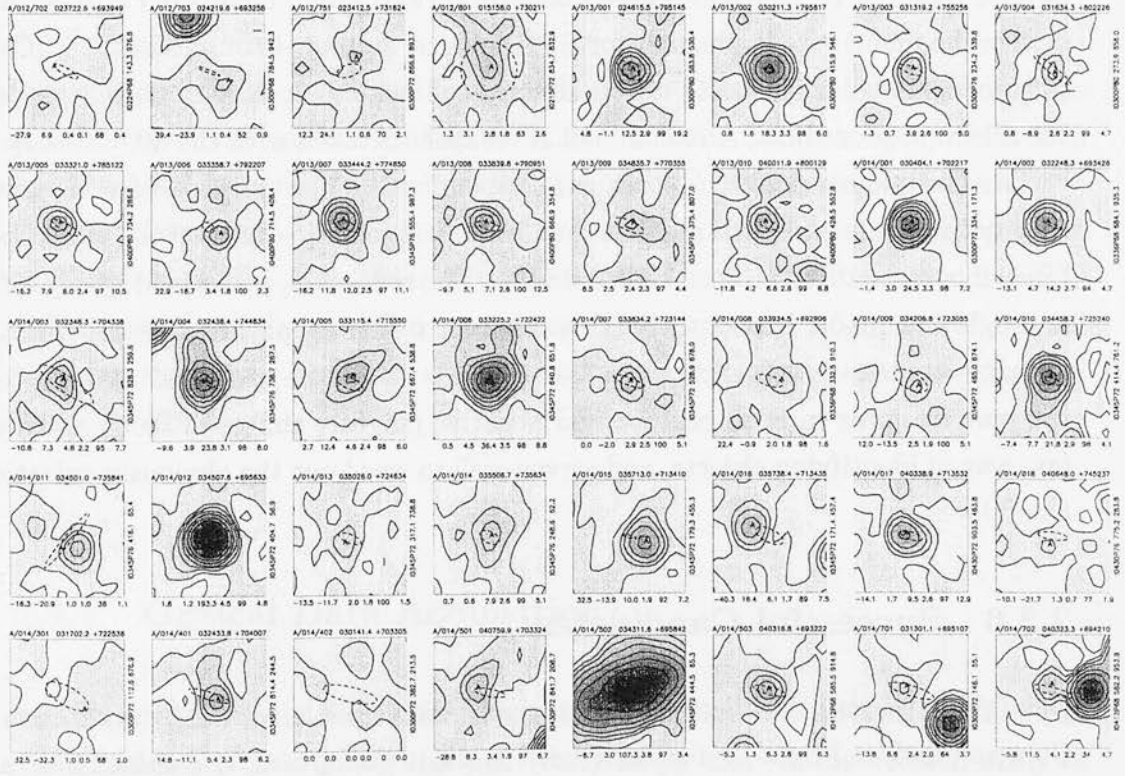

Figure 2.4: *20cm NVSS radio maps of a portion of the PSCz designated as "A-band" sources. These contain predominantly confirmed galaxies with determined redshift, but also contain some discarded candidates. Discarded are the following: A/012/702, A/012/703, A/012/751, A/013/009, A/014/008, A/014/013, A/014/014, A/014/301, A/014/402, A/014/501. Overlaid are the PSC error ellipses for the candidate positions.*

2.3.4 Visual Inspection

Digitized Sky Survey Images (Djorgovski *et al.* 1992) were often useful in visual identification, and examples of the DSS images used to identify sources for observation at CTIO's 60" telescope are given in Appendix E. In some cases DSS scans were either too poor quality, or not high enough resolution to be able to properly identify candidates, and so a visual inspection of POSS or Schmidt plates proved necessary. If necessary, the remaining borderline low-b PSCz and BTP candidates were then imaged at K' for final identification.

2.3.5 NIR Snapshots

Several hundred K' snapshots were taken by various group members (Will Saunders in the main), predominantly for BTP sources, and low-b sources in the PSCz, to provide visual identification of undetermined sources as final confirmation in the selection procedure. A selection of K' snapshots taken with the 40" telescope at Las Campanas in 1996 is shown in Appendix D. The purpose of these low quality images is purely to confirm the identity of galactic candidates, for acceptance into either the PSCz or BTP datasets. The reduction, performed by myself, is rough and ready, but as there is no need for a more sophisticated treatment, a simple successive subtraction method is used. It can be seen that features in the image appear in both positive and negative (slightly shifted). This is a very fast way of identifying objects, and served well to weed out the obviously galactic candidates.

2.3.6 Successful Candidates

Candidates passing the selection criteria were observed either optically or at 21cm. Compact and/or bright sources were tried in the in the optical, and those failures, together with low surface brightness candidates, and candidates with many magnitudes of extinction were observed in HI. Between 1997 and 1999 we used the 67m AAO Radiotelescope at Parkes, the CTIO 36" (snapshots only), 60", and 4m telescopes, and also Jodrell Bank's Lovell Telescope. We also received data from a service time proposal with the AAT. During this time, other collaborators also collected data from Kitt Peak, Parkes, Las Campanas, CTIO, and other instruments. As a result of these observations, the PSCz catalogue reached com-

pleteness, and the BTP extension is also now virtually complete. Current BTP redshifts number 789 included in the catalogue with another 300+ identified and awaiting inclusion, bringing the total to around 1100. Sections 2.4 and 2.5 detail the observation and reduction methods used for both the 21cm observations at Parkes and Jodrell Bank, and optical observations at CTIO and Cananea. The entire dataset is quite substantial, and so is not presented in this thesis, but samples are presented in the appendices and data may be obtained upon request to PSCz/BTP group members.

2.4 Optical Spectral Observations

The optical data are presented here in two parts. First, I detail more closely the spectroscopic observations made at the CTIO 60" and 4m telescopes, which Will Saunders and I are responsible for. In the second section, I discuss the reduction of these data, and also of spectroscopic data obtained from an observing run at Cananea (1996). The reduction of these data are described alongside CTIO reductions, although any differences are specified explicitly. I do not overly detail observation method practised at Cananea, as these data were observed by Will Saunders alone.

2.4.1 Optical Data Acquisition

At CTIO, 85% of our targets for this run were satisfactorily observed. The run was scheduled a little late in the year (early May), and for this reason, many of our targets were already 3-5 hours west even at the start of the night. In general both telescopes performed excellently. However, on two occasions, technical problems consumed 1+ hours at the beginning of the night, and these combined with occasional poor weather were the primary reasons for failing to observe the remaining 15% of targets. 237 positive identifications and well determined redshifts were measured on the 60", and another 61 on the 4m. The instrument setup and observation techniques are described in this section.

CTIO Instrument Specification and Setup

We used two spectroscopic instruments at CTIO: the 1.5m Ritchey-Chretien (Cassegrain) spectrograph combined with the Loral 1K CCD, and the 4m RC spectrograph with the Loral 3K CCD. On both systems, the spectrographs are very efficient and offer high dispersion, and the Loral CCDs are markedly more red sensitive than previous detectors.

The 1.5m Cassegrain spectrograph is an ultraviolet transmitting grating spectrograph which is used at the f/7.5 focus where the scale is 18.1 arcseconds/mm. The Loral 1K CCD fringes at wavelengths longer than 7500Å. However the lack of significant flexure in the 1.5-meter Cassegrain spectrograph and camera means it is possible to remove most of the fringing using dome flats, and virtually all using sky flats, as demonstrated below.

On the 4m, we used the Blue Air Schmidt (BAS) and Loral 3K CCD (L3K). The Air Schmidt camera is a field-flattened Schmidt camera of 229 mm focal length and 229 mm clear aperture (f/1). The Local 3K is a thinned 3Kx1K CCD with 15μm pixels. The CCD has a two layer Ar coating and is UV flooded to maximize its quantum efficiency over a wide range of wavelengths.

On both instruments we operated at a central wavelength of approximately 7000Å, placing rest-frame Hα (6563Å) centrally, Na absorption (5395Å) at the blue end, and just under $\simeq$7500Å at far red, allowing maximum redshift detection of $z \simeq 0.2$.

Target Identification and Acquisition

Target acquisition on both telescopes was provided via image intensifier TV's, with a field of view of about 20 arcseconds. This system constantly integrates, to provide a real time image of the target. In principle, and also in practice, this system can perform well, but is far better suited to observations of a small number of targets. The time overhead is quite significant, and for shorter integrations of the type we required, acquisition can take up to 50% of the time. One major design problem with the finders at CTIO is that they are oriented incorrectly: the finders cannot be orientated N up and E left. On the 1.5m we resorted to physically rotating the TV, but the 4m finder is bolted to the console so could not be rotated. Another major problem with the CTIO setup is that the TV

display has different scales on the N-S and E-W axes. These two effects combined can completely destroy human pattern recognition capabilities, and significant amounts of time were lost due to this. There is no scale overlay facility on the screen so measurement of offsets is more guesswork than quantitative. If this were provided, it would allow for much faster acquisition of faint targets - they could be placed straight down the slit in a single small offset from the initial position as seen on the finder.

On the basis of advice as to the power of the 4m acquisition TV, we did not systematically prepare arcsecond positions or offset stars. From our experience, arcsecond coordinates and offsets for targets fainter than B_j=19^m should be mandatory, as they are at AAT. This will drastically reduce the time spent in target identification. Because of this, we wasted 20 or 30 seconds per target, and sometimes several minutes, until we managed to prepare positions for the remaining observations. This could and should be avoided, especially when performing short integrations on many targets.

CCD Binning Methods

Before observing we were not able to get adequate information on the efficiency and throughput of the 1.5m gratings and spectrograph. As a consequence we observed our first night unnecessarily close to the read-noise dominated regime. This was in part due to the fact that many of our sources were low surface brightness, and/or suffer from heavy extinction. In both of these cases, the signal to noise on any particular pixel is low, either because the object is intrinsically faint, or distributed across many pixels. Spatial resolution on the Loral 1K chip is excellent (0.27Å/pix), as is wavelength resolution. To overcome this read-noise domination, we adopted a 2x2 binning scheme, bringing the read-noise down by a factor of four. Spatial binning imposes no real degradation of spectrum quality, as the spectra typically measure more than two pixels wide. Wavelength binning does compromise resolution, but given the extended nature of the sources, was less of an issue. Having a wide slit allows more light onto the chip, so while the projected slit width is greater than the spatial resolution, binning does not further impair the wavelength resolution. 2x2 binning reduced the number of raw image pixels to 672 along the dispersion axis. It was completely unnecessary to use the entire width of the chip (spatially), so to minimize readout time the useful

chip section was limited to 300 pixels (150 binned elements). Further to this, the illuminated part of the chip covered only 595 pixel rows, the end sections being clipped off during the reduction.

2.4.2 Optical Data Reduction Techniques

There are three general stages to the reduction of spectra. These are: 1. the preprocessing of the image frames, to compensate for instrument distortions and biases, and to also wavelength calibrate the images; 2. the extraction of one-dimensional spectra from the dispersed light fallen on the two-dimensional CCD; and 3. the analysis (usually line fitting) of the resulting spectra, to extract the desired information (in our case, redshift). There are many well established techniques which can be applied to each of the stages, and our reduction follows these standard procedures in many places, and in general follows those set out in Massey (1997), and Massey, Valdes & Barnes (1992). However, we occasionally deviate from these standards if we can apply a more optimal procedure. The reduction details are given in this section.

Flatfielding

Flatfielding is a process which extracts the response function of the instrument from the image frames taken. When an observer takes an image with an instrument, the resultant CCD readout has been tainted with features characteristic of the instrument. These predominantly come in the form of additive features (*e.g.* bias current, sky background) and multiplicative effects (*e.g.* illumination variation across the chip from optical characteristics, and individual pixel responses). These effects add up to make to total response function of the instrument, and can, at worst, vary on an observation by observation basis. When the flatfield is extracted, the data can be treated with it, to yield an image that would be seen by an instrument free of imperfections and biases. Almost all of the image processing and data reduction presented in this thesis was performed with NOAO's IRAF data reduction package (Tody (1986), Tody (1993)). Those interested in using IRAF should consult Barnes (1993).

The method of flatfielding varied as the data changed, but generally followed the prescription described below. The frames used for flatfielding are in general, bias

(zero exposure) frames, and sky frames (short exposures of the twilight sky). Bias frames measure the pre-illuminated bias level and structure of the CCD, and can be a few hundred ADUs. This bias structure is purely additive, and should be removed before further processing. Twilight sky frames are taken because the evening sky provides a very even illumination of the CCD, and so is good to use as a diagnostic for CCD and optical response. Sometimes, it is necessary to use "dark" frames: those with long integration time with the shutter closed. On top of the bias structure of the chip, these measure the accumulation of charge on the chip over a period of time. This is only necessary for chips with high dark currents, and/or with very long CCD exposure times. The chips we used were all of very low dark current, and our exposures were quite short ($\leq$ 500s, and typically 100s), so it was not necessary to compensate for this effect.

Ideally, many bias frames and sky frames are taken, and statistically combined, to remove any individual image fluctuations which are uncharacteristic of the true bias and sky. In general, it is good to use at least 10 frames of each type, to produce the final bias and sky frames. In the case of bias frames, each frame was scaled relative to its mean average, and then median combined with the others. The result was scaled as the mean of the means. In practice, this requires virtually no rescaling, as bias frames are very similar on the large scale. The purpose of this process is therefore to average over frame to frame variations in each pixel. At this stage, all other frames have the bias frame subtracted from them, and are bias free to first order. Sky frames are treated similarly. About 10 frames of the twilight sky (preferably cloudless), are scaled according to their mean averages. Sky frames will vary significantly in brightness, as the evening sky dims. Exposures need not be the same length, as dark current is minimal and exposure times are very short (a few seconds), but it is good to expose the chip such that a good strong signal is obtained (at least two thirds or three quarters of the saturation level). The mean scaled frames are median combined (this completely removes cosmic rays).

The next step in extracting the pixel to pixel response of the CCD, is to consider the variation in illumination along the length of the slit (spatial direction), and also in the wavelength (dispersion) direction. The sky frame can be median filtered along the wavelength direction with a small but statistically robust filter size, to yield a smooth sky frame without pixel to pixel variations. Dividing the sky frame by its median filtered counterpart, leaves only the pixel to pixel

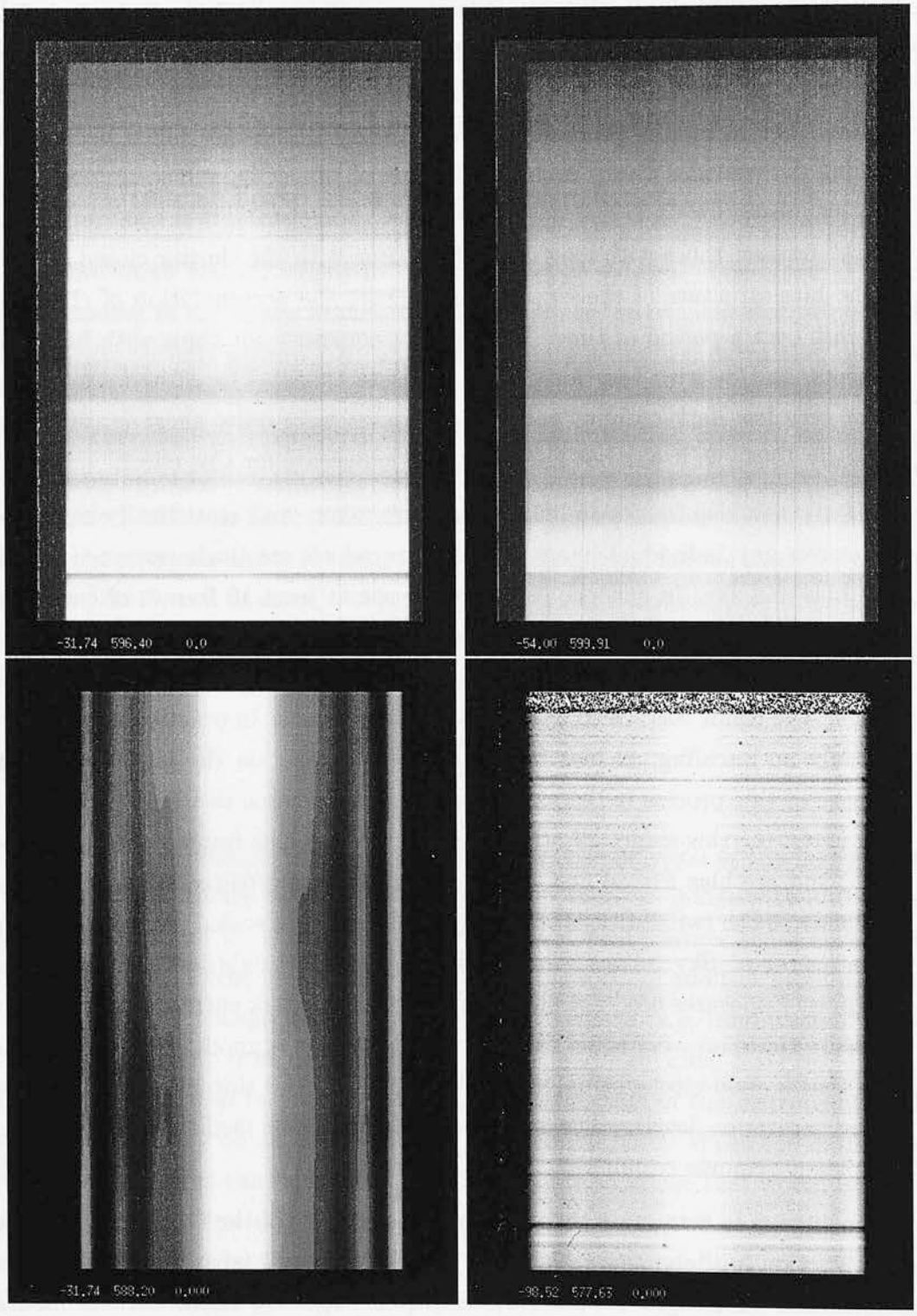

Figure 2.5: *Stages in the flatfielding process. From top left to bottom right: The twilight sky frame S_{sky}, the median filtered twilight sky frame S_{med}, the illumination function frame I, and the final flatfield obtained by $F = S_{sky}I/S_{med}$.*

variations due to the CCD itself. This now has to be multiplied only by the illumination function of the slit, to yield the total response of the instrument to an evenly illuminated sky. The illumination function of the slit can be calculated by fitting functions of some variety (polynomial or spline) in the spatial direction, at various points along the dispersion direction. Each polynomial/spline is normalised with respect to the maximum illumination at that point, so as to ignore the effects of varying illumination in the dispersion direction (an effect that is due to the nature of the source light, and not something to be compensated for). For the Cananea data, the creation of the illumination function was performed by the *illum* function in the longslit IRAF package. Various stages in the flatfielding process are shown for night one of the Cananea 1996 observing run in figure 2.5.

For the CTIO data, the illumination function was created from first principles, using the twilight sky frame described above, to get

$$F = \frac{S_{sky} M_{box}(S_{med})}{S_{med}} \tag{2.3}$$

where S_{sky} is the twilight sky frame, S_{med} is the spatially median filtered twilight sky frame, and $M_{box}(S_{med})$ is a boxcar smoothing of S_{med} along the entire dispersion length of the chip. Although this method is insensitive to illumination variation with wavelength, it does overcome inaccurate function fitting in the spatial direction. This was found to be more suitable for the 60" data because of a steep gradient in the slit illumination function at one edge of the chip (over about 20 rows).

Another problem that was encountered, is that this causes the spatial median to be overestimated at the edge (41 pixel spatial median, reflecting at the boundary). If this happens, the skyflat F is underestimated, and flatfielded object frames are overestimated. This can effectively be ignored, as it's not an important part of the chip: object spectra are spatially centred on the chip, and completely unaltered by this upturn. We explored using the *boundary=nearest* flag in the IRAF *median* task, which extrapolates off the chip by assuming the boundary value, but this has the opposite effect, so underestimates S_{med}. To get an idea of the magnitude of this effect, a median was calculated each way and the ratio taken (reflect/nearest). The upturn can be seen at the edge, but was small. As expected, the rest of the chip was completely unaffected, so the matter was pursued no further.

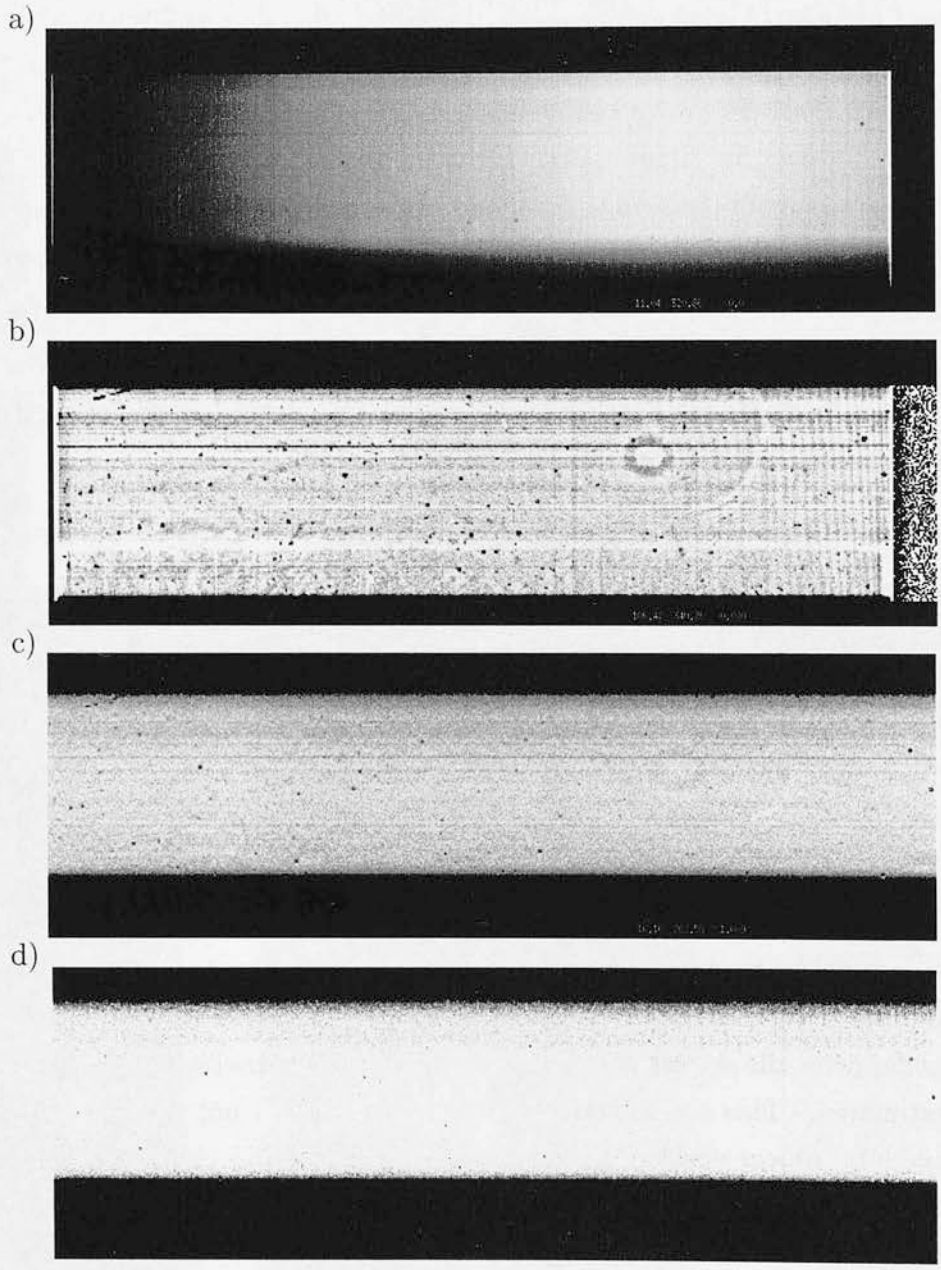

Figure 2.6: *Domeflats versus skyflats. From top to bottom: imcombined domeflat, pixel-to-pixel variation of the domeflat (created by dividing through by a median filtered domeflat), skyflat, and twilight sky frame.*

All flatfielding frames were initially bias subtracted. On the first night using the CTIO 60", only three skyflats were taken, and these were at the end of the night. However, there were 10 Dome flats, and these could be used in the flatfielding. Dome flats have a problem with a different illumination of the slit: because the telescope is focused on infinity, and the dome is only metres away, then any specks or irregularities in the optics would cause features to be blurry and different from object frames. A test was performed, and the results are shown in 2.6.

A domeflat was created (a), and then in order to find the pixel to pixel variation, it was divided by its median filtered counterpart (a 41 pixel median filter in both position and dispersion) to produce (b). This was compared with a skyflat (c) calculated from only three sky frames. Both look similar, except for fringing apparent in the domeflat. As a test, the skyflat was divided by the domeflat to see if they were significantly different. The fringing effect remains (not present in the skyflat), but the frame shows no other structural differences bar the underestimated strip due to the median filtering of the skyflat discussed above. The pixel to pixel deviations are of order a fraction of a percent. From this it can be seen that the skyflat is an excellent flatfield, and the benefit from similar illumination of the slit to the object frames far outweighs the small increase in noise.

Optical Flatfielding Scripts

In the spirit of the above flatfielding method, two script files were written to automate flatfielding. These are shown in appendix B, with their associated parameter (*.par*) files. Upon executing the first of these, a normalization of the flatfield is returned. It is necessary to manually normalize the flatfield, by editing the parameter file of the second script. The scripts intake standard ascii frame lists as depicted by @objlist, @sflist, and @zlist. It's necessarily in two parts, as it requires the image median, given by the *imstat* package's output labeled MIDPT, to be returned into the script as a variable. However, this small complication aside, it consistently produces beautiful flatfields, as can be seen in figure 2.6.

Dispersion Correction

Dispersion correction, also known a wavelength calibration, is simply a correction for the non-linear wavelength scale as seen by the chip. Modern spectrographs attempt to disperse the source light as linearly as possible, but they are not

perfect. Consequently, proper quantification of measured wavelength versus pixel column (or row) number is necessary in order to extract the correct spectrum. The method of doing this is normally quite simple, and involves comparisons of features in the object frames, with features in test frames containing known emission lines.

It was chosen to apply the dispersion correction to the two dimensional image frames and then extract one dimensional spectra from those, rather than just apply the dispersion correction to the extracted spectra. There are a two good reasons to do this. Firstly, the CCD chip is not guaranteed to be seated squarely along the dispersion axis of the spectrograph. This means that the wavelength of a pixel column can change across the chip. If the object spectra are not all placed on the same CCD rows, then a customized extraction of the relevant arc lamp frame would have to be performed for each object. Further to that, flexure in the spectrograph (discussed in more detail below) causes a bulk shift of the CCD with respect to the telescope's optical axis, which is entirely dependent upon the telescope's orientation and is therefore different for each object. This shift is compensated for by matching atmospheric absorption lines which are already removed from one dimensional spectra. It should be noted that in the case of negligible flexure and exact and consistent placing of objects on the chip, then a one dimensional wavelength calibration is acceptable.

There are two effects that need to be compensated for. Firstly, the non-linear dispersion of light along the CCD, and secondly, a bulk shifting of the spectrum up or down the CCD. This bulk shift is unique for each image taken, and caused predominantly by flexure in the spectrograph casing. This effect can be of order a couple of pixels, so must be compensated for carefully. A series of test images were taken while illuminating the CCD with an halogen arc lamp. Several types are available, and should be chosen on the basis of relevant spectral features in the wavelength region to be measured. We used a Neon arc lamp, initially taken at the position of a well known standard star, Feige 56. The same positioning of the telescope for both frames ensures very similar spectrograph flexure, and so the features of these images can be compared immediately. On most nights however, Neon arc lamp illumination frames were taken at the zenith, as were the sky frames. The features to compare are the emission lines of the Neon arc lamp, versus the well known absorption features in the Earth's atmosphere. The calibration for non-linear dispersion can be performed using just the arc lamp, and

was performed with the *autoidentify, reidentify* and *fitcoords* packages in IRAF. Object frames were initially bulk shifted with respect to the zenith sky flat frames, so as to align their atmospheric absorption features. This was performed using the *specshift* package, using image strips each side of the object spectrum, and compensates for the flexure of the spectrograph casing. Then frames were dispersion corrected according to the template calculated in the arc lamp spectrum by *fitcoords*. The resulting frames are properly wavelength calibrated, and are ready for spectral extraction.

Spectral Extraction and Analysis

After the raw image data are preprocessed to flatfield and wavelength calibrate it, one dimensional spectra can be extracted. To illustrate this process, figure 2.7 highlights the important parts of the chip that are used in the extraction. The *apall* task was used to extract spectra from the 2d images, and its usage is fully detailed in (Massey, Valdes & Barnes 1992). The apall task is extremely versatile, and allows extractions ranging from fully automatic, to fully interactive. In a best case scenario (bright stellar spectra), simply supplying *apall* with a list of images is sufficient to perform good extractions. However, our observations of extremely faint or low surface brightness extended sources demand a wider slit, and so images quite often contain other spectra of nearby stars. In cases like this, *apall*'s automatic aperture finding algorithms will find the brighter and more defined sources, so interactive extraction is not only preferable, but absolutely necessary.

The steps involved in extracting a spectrum are straight forward. First, a range of spatial pixel rows, or *aperture*, needs to be defined, which contains the spectrum. In practice, approximate values can be provided interactively, and then *apall* can refine these values according to a profile fit. In figure 2.7, this region on the chip is highlighted in red, although the spectrum profile will dictate a much narrower aperture (*e.g.* a 2σ cut on the profile would be reasonable, but this depends upon noise – see later). The background regions can be pre-defined in the algorithms parameters, to begin and end at a chosen number of rows each side of the spectrum aperture. In practice, it is good to have wide background apertures to minimise statistical noise in the background subtraction.

Once the apertures are defined, *apall* then traces the spectrum along the chip.

This is necessary, as it is completely expected that the true dispersion axis will not be exactly perpendicular to the spatial axis, or aligned with the CCD rows. This misalignment can be for many reasons, among which are distortions in the camera optics, misalignment of the diffraction grating/grism, and the differential refraction of light caused by the atmosphere when pointing the telescope anywhere other than the zenith. For these, and possibly other reasons, the dispersion axis will in general, trace out a slightly curved path across the chip, and it is important that the aperture is continually adjusted to envelope the entire width of the spectrum.

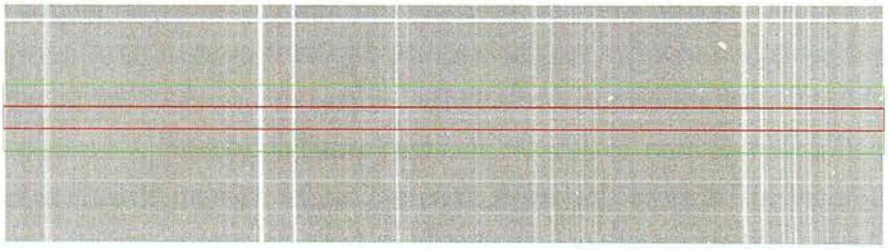

Figure 2.7: *Processed image frame of object K/098/504, a Q1 spectrum with Hα at 7028Å, placing this galaxy at* $cz = 21,204 Kms^{-1}$. *The object spectrum runs from left to right. Highlighted are the spectrum (red), and adjacent background strips (green) that are used in the extraction.*

Once the object and background apertures have been defined, *apall* then calculates the one dimensional spectrum, as a sum over pixels. The user is left free to choose which summation method to use: either an unweighted, or an inverse variance weighted sum, as described in Horne (1986) and Marsh (1989):

$$\begin{aligned} \text{unweighted}: S_i &= \Sigma_j I_{ij} - B_i \\ \text{variance}: S_i &= \frac{\Sigma \frac{P_{ij}^2}{V} \frac{I_{ij}-B_i}{P_{ij}}}{\Sigma \frac{P_{ij}^2}{V}}, \end{aligned} \tag{2.4}$$

where S_i is the one dimensional spectrum flux at a particular wavelength (λ_i), I_{ij} is the pixel value, B_i is the estimated background at that pixel, V_{ij} is the estimated pixel variance, and P_{ij} is the estimated normalized profile value for that pixel. Inverse variance weighting is often referred to as an optimal extraction

since it is a minimum variance estimator of the total flux integrated under the two dimensional profile. This was the extraction method of choice.

The noise model used in the inverse variance weighting and profile fitting consists of a constant Gaussian noise representative of the estimated read-noise in the image, and a photon count dependent Poisson noise estimate. The photon count is estimated using the gain parameter (the number of photons per ADU), and the Poisson noise is approximated as Gaussian with sigma given by the root of the number of photons. A more detailed description of this model is given in the help pages of the *apvariance* task in IRAF, as well as in Horne (1986) and Marsh (1989). This is all calculated within the *apall* task, and allows the user to be confident of using the correct statistic, without having to worry about its proper implementation. An example of the extracted spectra is given in figure 2.8.

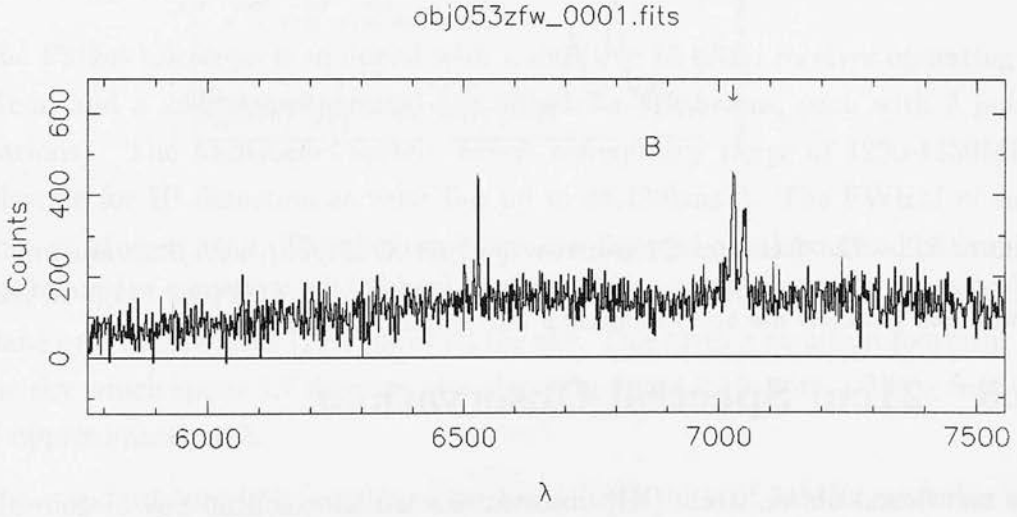

Figure 2.8: *The extracted Q1 spectrum of object K/098/504 (also appearing in figure 2.7, and figure 2.9). Hα can clearly be seen at 7028Å, between the NII pair. SII can be just seen at 7192/7207Å.*

Finally, this spectrum can be fitted using a line deblending procedure, to estimate the object redshift. I used a minimization code developed by Will Saunders to calculate the best fit redshift, FWHM, and equivalent widths in the Hα, NII, and SII lines of the continuum subtracted spectrum. The code is robust, and user friendly. An example of the resultant output is given in figure 2.9, and further examples are shown in appendix G.

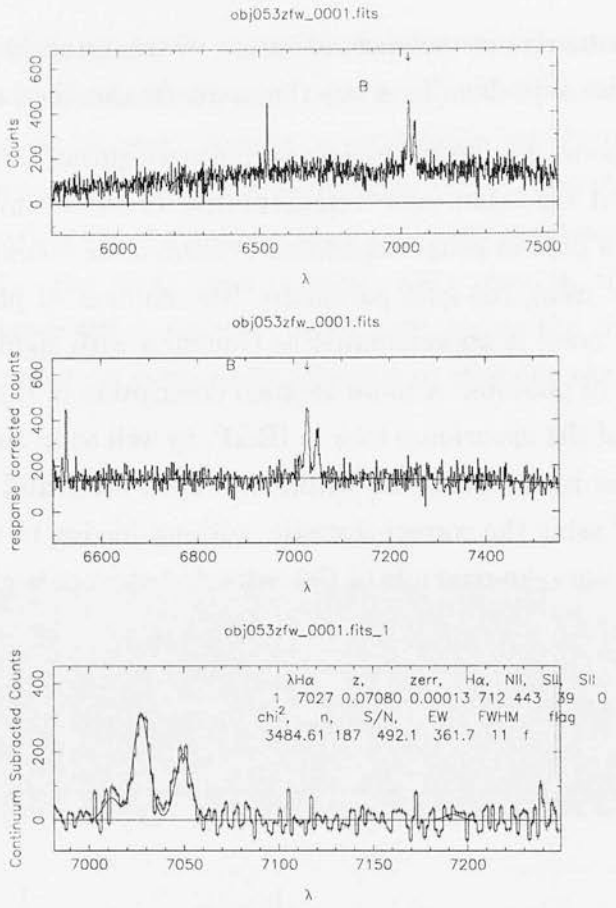

Figure 2.9: *The deblended Q1 spectrum of object K/098/504, with fitted line profiles. The three figures are (top) the entire spectrum, (middle) the continuum subtracted spectrum, and (bottom) the best fit emission line profiles, and fit parameters.*

2.5 21cm Spectral Observations

As mentioned above, 21cm (HI) observations are an excellent way of determining galactic redshifts. IRAS galaxies are typically bright spirals with much star formation. As such, they have a lot of neutral hydrogen, and are easily detected. Furthermore, HI suffers very little from dust, allowing observation of galaxies with 30+ magnitudes of optical extinction. This type of observation allows an all-sky redshift survey such as the PSCz/BTP to push right through the galactic plane, maximizing sky coverage. It is also excellent for low optical surface brightness candidates, for which it is difficult to obtain adequate signal to noise in optical spectra.

Given that the galactic plane reaches well into both the Northern and Southern hemispheres, a complete HI complement to the BTP must involve both Northern

and Southern observatories. For the BTP data observed throughout this project, we were fortunate enough to secure some time on the ATNF's 64 metre radiotelescope at Parkes, and also on the 76 metre Lovell radiotelescope at Jodrell Bank. Both of these telescopes have been fitted with near identical multibeam instruments, which are detailed below. The Multibeam instrument (Staveley-Smith *et al.* 1996) and its software were primarily designed as an instrument for efficiently mapping large areas of sky, by scanned observations – either drift scans or driven scans, commonly used in blind HI searches (Staveley-Smith 2000). As such, we were the first ever observers to make pointed observations with a multibeam instrument, and much of the discussion in this section will detail the principles behind such observations, and the techniques applied on both the 13 beam receiver at Parkes, and its 4 beam cousin at Jodrell Bank.

2.5.1 Pointed Observations Technique 1: Parkes

The Parkes telescope is equipped with a sensitive 13 beam receiver operating at 21cm, and a 26 channel spectral line correlator (13 beams, each with 2 polarizations). The Multibeam system covers a frequency range of 1230-1530MHz, allowing for HI detection at velocities up to 46,300kms^{-1}. The FWHM of each horn at 21cm is 14'.4. The thirteen horns are disposed in a hexagonal pattern as seen in figure 2.10 (Staveley-Smith *et al.* 1996), separated by 25cm in the image plane or 2 beamwidths (29arcmin) on the sky. This gives a resultant footprint on the sky which spans 1.7 degrees, also shown in figure 2.10, with a filling fraction of approximately 0.3.

The standard correlator configuration has a bandwidth of 64MHz, and this can be placed anywhere within the 1230-1530MHz range. We used 64MHz bandwidth centred at 1394.5MHz, allowing a detection range from -737kms^{-1} to 12,422kms^{-1}. We used 2048 channels (the maximum) which subdivide the frequency range, giving a velocity resolution of 6.4kms^{-1}.

The 64 metre dish at Parkes has three legs supporting the focus cabin. These can support strong standing waves in the instrument, especially at certain angles from the sun. Observations during the day do suffer from these standing waves, and the manifestation of this effect is in a baseline ripple in the radio spectrum. This baseline ripple can be removed in the subsequent analysis of the spectra, but there was no facility for pipeline removal. As a result of this, it was sometimes difficult

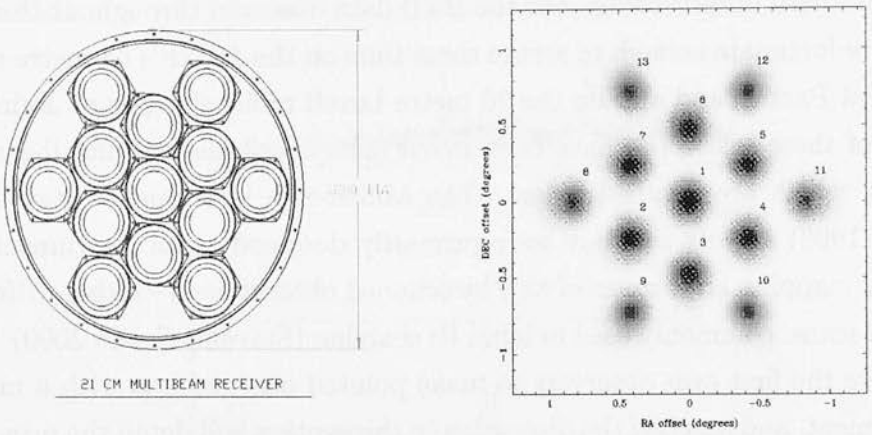

Figure 2.10: *Left: Layout of the 13 feed horns of the 21cm Multibeam receiver (Taken from Stavely-Smith* et al. *1996). Right: The theoretical sensitivity footprint at 1370MHz (Taken directly from Stavely-Smith 1997).*

to make positive identifications in real-time, as any extragalactic signal could easily be lost in strong baseline ripples. The consequences of this are considerable for a dynamic observing schedule, which requires constant feedback about the success of an observation. The susceptibility of the instrument to baseline ripples of this type is a complicated and reasonably ill-determined function of the altitude and azimuth of the telescope, and the relative position of the sun (although L. Stavely-Smith has investigated this to some degree). It is therefore important that the off-target observations used to remove baseline ripple, are as close to the on target observations as possible, both in time (because the sun moves continually), and alt/az position.

13/7 Beam Pointing strategy

For pointed observations, only one beam can be centred on the source at any time, and it makes sense to use the other beams as a measure of the background. There are a number of problems associated with doing this, primarily that the 13 beams act and respond independently of each other. The detector responses, temperatures, amplifiers, correlators and filtering electronics are all completely separate for each beam, and in practice these cannot be treated as identical instruments.

The controlling software is clever enough to allow the specified target position

to be placed down any of the beams, and given the minor differences between beam responses, it made good sense to observe the target in all the employed beams, so as to average the signals. Movement of the telescope not only imposes a significant time overhead (15-20 seconds), but also puts strain on the driving mechanism (There was a general concern that many small stop/start movements would increase the wear on the gears and bearings). It was decided to employ only the central beam, and the six beams on the inner ring. Integrating on each of the seven employed beams not only retained some sense of symmetry in background determination, but also provided a more time efficient observing strategy, and reduced the strain on the telescope itself. Integrating enough to obtain <6mJy noise per channel takes about 15 minutes, and so by restricting the observations to only 7 pointings, rather than 13, cuts down significantly on the re-positioning time, from 21% to just 12% of the total observation time. The beams are numbered, and are as follows: beam 1 is the central beam, beams 2-7 are the inner ring, and beams 8-13 are the outer ring. Our pointing strategy was therefore quite straight forward, integrate on beams 1,2,3,4,5,6,7 in that order. The telescope begins centrally positioned, then moves out to beam 2, and round in a circle through beams 3-7. Baseline subtraction and bandpass calibration of the spectra was done using all six of the off-target pointings that each beam integrated. This is described in section 2.5.3.

The multibeam instrument reads out what are called *cycles*, which are the resultant signal accumulated at the detector after a 5 second integration. We chose to use 24 cycles per pointing, or *scan*. 7 scans (per beam) make one complete observation. Our integration time was therefore 5x24x7/60=14 minutes, and total observation time about 16 minutes. This allowed us to observe a little over three sources per hour, for the entire period of useful observation time. The telescope and instrument were controlled by scripts called *sched* files (for schedule), and the sched template constructed for the 7 beam pointed observation is as follows:

```
$ unit 1
freq = 1394.5
config = mb7_64_2048_swap
bandwidth = 64
fcc_p_trk = disabled
source = AAAAAAAA
fitsname = BBBBBBBB
```

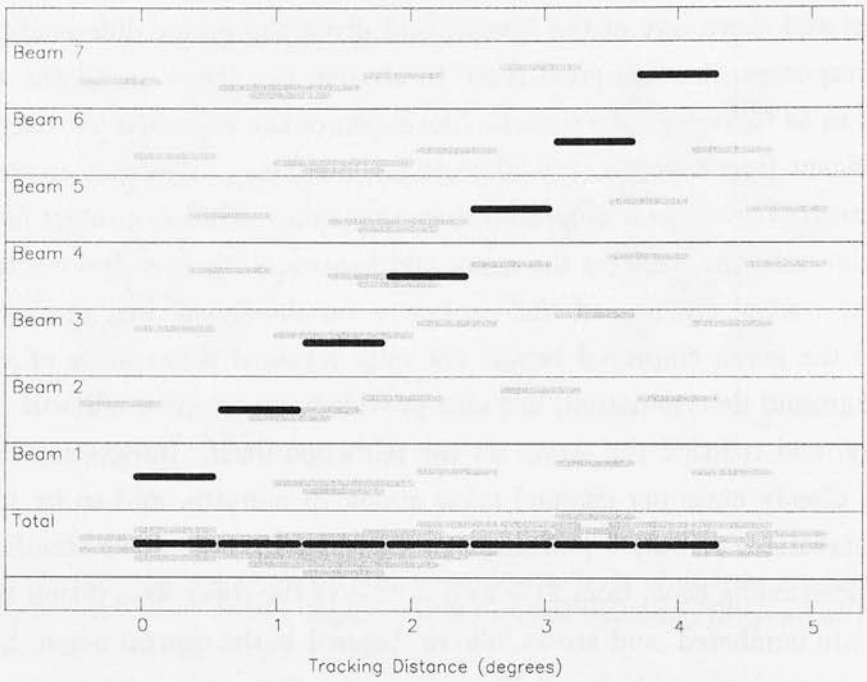

Figure 2.11: *The coverage of the seven beams on any one given observation. Grey scans are off-target, and black are on. Each beam is represented separately, and the total coverage given at the bottom.*

```
cycles = 24
raj = RRRRRRRR
decj = DDDDDDDD
fcc_rot = 0.0
mx
closef
```

The process is simple, `$ unit` describes the observation number, and `fcc_p_trk` and `fcc_rot` are parameters controlling the orientation of the instrument focal plane. The important parameters were `config` which gives the name of the 7 beam pointing scheme described above, the `mx` command which begins the integration, and `closef`, which ends integration and closes the file. This template file used and the object names and J2000 coordinates were batch substituted to create a unique sched file for each target.

2.5.2 Pointed Observations Technique 2: Jodrell Bank

Jodrell Bank has been equipped with a 4-beam instrument, each beam being identical to those of its larger cousin at Parkes. These four beams are 12' FWHP,

20' separation, and are arranged in a rhombus shape, as is dictated by hexagonal packing. The normal setup is 64MHz bandwidth centred as before on 1394.5MHz, only 1024 channels (the maximum available at Jodrell Bank), and 2 polarisations on each of the 4 beams. With this setup, we obtained a 6mJy noise per channel in 30 minutes of integration.

At Jodrell Bank, there is strong broad-band interference between 1397-1391MHz (5000-6100km/s), and it was not possible to get any usable data in this region. There is also narrow-band interference at 9800km/s and 11100-12000km/s. Our data had good baselines at night, even at low elevation (10-20°), but our baselines were much worse (10MHz ripple, up to 100mJy amplitude) in the daytime even when pointing away from the sun. This made observations very difficult.

4 Beam Pointing strategy

The immediately obvious choice would be to put the source in each of the four beams in turn for some fixed number of cycles per beam, and perhaps repeat this circuit a number of times in order that a beam's off-target observations are not too distant from its on-target ones. However, the telescope takes about 30 seconds to move between beams, so the best solution is a compromise between the time overhead (and again, the strain it puts on the telescope), and getting reference beams close enough in time to get good baselines.

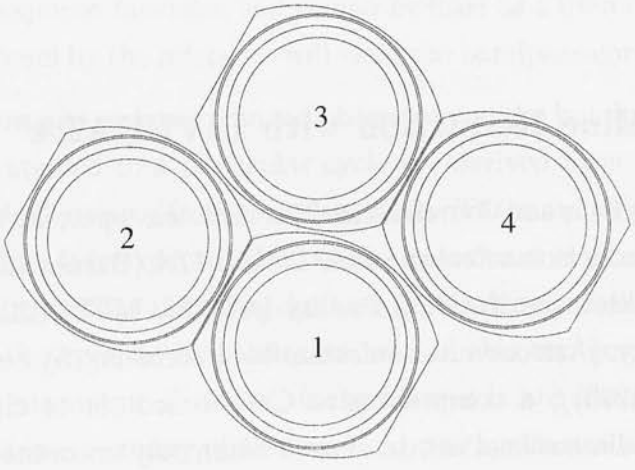

Figure 2.12: *The relative positions of the 4 beams in Jodrell Bank's multibeam receiver.*

We tried two strategies. The first strategy was to point with beams 214412 in that order. This is 2 circuits of 60 cycles on each of 3 beams, and takes ≃35 minutes for 30 minutes integration. It was decided that beam 3 would be dropped on advice from the control staff that beam 3 was noisier than the others. The second strategy adopted was beams 1234123412341234. This is 4 circuits of 24 cycles per beam on all 4 beams, and takes ≃45 minutes for 32 minutes integration. We did not find any great improvement in baselines when we reduced the dwell-time in each beam. The sky coverage for each of the pointing strategies is given in figure 2.13. Of importance is the relative position of the off-target observations of a given beam, with its associated on-target observations.

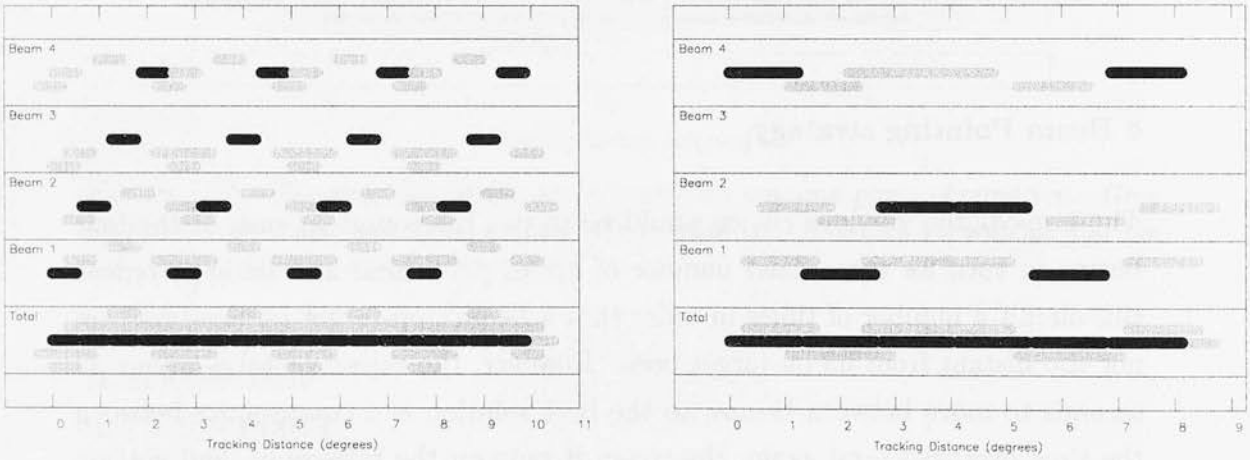

Figure 2.13: *The coverage of the four beams on any one given observation, given by (left) the 4x1234, and (right) the 412214 strategies. Grey scans are off-target, and black are on. Each beam is represented separately, and the total coverage given at the bottom.*

2.5.3 Pipeline Reduction with LIVEDATA

Both the Parkes 64m and Jodrell Bank 76m radiotelecopes, are equipped with the same pipeline reduction software suite, *LIVEDATA* (Barnes 1998), developed by the Australia Telescope National Facility (ATNF). LIVEDATA is based on the AIPS++ library (Astronomical Information Processing System, Croes (1993), Glendenning (1996)), a comprehensive C++ based set of classes for processing large multi-dimensional arrays of data commonly encountered in astronomy. Initially designed to operate in scanned mode observations, LIVEDATA can be persuaded (with some difficulty) to pipeline reduce pointed (or dwell mode) obser-

vations. A wealth of information on LIVEDATA can be obtained from any of the ATNF multibeam group members, and those interested in the practicalities of using LIVEDATA in pointed mode, a rough users guide is available online at the Jodrell Bank website, *http://www.jb.man.ac.uk/~multi/multibeam_pointed_notes.html*.

The Pipeline reduction process is split into a few stages. One cycle of raw spectral data is received every 5 seconds, containing either 1024 or 2048 channels, for each of two polarisations per beam. On-target observations need to be bandpassed, to correct for the frequency filtering and dependent response function the detector and its associated electronics imposes on the signal. After that any baseline ripple discussed above needs to be subtracted. It is quite common for the physical signal to be completely obscured until the baseline is subtracted. Scanned observations are a relatively new technique, and the traditional methods of bandpassing have been modified somewhat to account for the new nature of the received data. I shall discuss the methods used by the LIVEDATA software, and describe how we used these to treat our pointed observations.

Bandpassing

One well-established method of bandpassing is *signal-reference subtraction*, whereby the observer integrates on the target (signal), and then shifts to a (hopefully) empty piece of sky adjacent to the target (reference). This is a similar technique to optical spectroscopy, where adjacent sky regions are used to measure the response of the instrument. An integration on blank sky will still suffer from the instrument response function, and so can be used as a direct measure of this. Division of the signal by the reference will yield the bandpass-corrected spectrum.

As LIVEDATA usually reduces scanned observations, the bandpassing and baseline subtraction applied to a particular cycle are derived from the set of cycles taken before, and afterwards from the same beam. These are referred to as precycles and postcycles. It is expected that as the instrument is moving with respect to the celestial sphere that the precycles and postcycles are independent of both each other, and the cycle to be calibrated, and in this manner, represent a reference spectrum estimator. However, independence is not always the case with pointed observations, as many of the pre- and postcycles are also on-target. It is therefore important to ensure the number of pre- and postcycles used in calibration is sufficiently large that the median filtering applied in bandpassing is

not affected by the non-independence of some of the pre- and postcycles. By estimating the reference spectrum using median statistics, we ensure the cycle is treated in a very similar manner to traditional signal-reference subtraction. As follows from this, we set the pre- and postcycles to a large number, and the median estimator option in LIVEDATA.

Multibeam Gridder - Gridzilla

The Multibeam writes files in a modified FITS format (.mbf or .hpf), and the LIVEDATA output format is also non-standard (.mscal files), in which each cycle has with it an associated position and time stamp. These data can be "Gridded" in position to make data cubes in right ascension, declination, and frequency/velocity, and in practice, was performed by a utility known as *Gridzilla.* This is not only perfect for, but also essential to any large HI blind survey. As we already knew the exact positions of our targets, and pointed precisely at them rather than scanning across, this gridding procedure was in part, rendered somewhat redundant. It was at the same time an incredibly useful tool to combine the spectra of all the beams, and combine repeated observations of the same target. Our only major requirement was that Gridzilla should not attempt to spatially resolve our objects, but this was a simple matter of choosing the positional resolution to be larger than a single beam, but small enough to exclude adjacent beams — using unweighted gridding into 4' pixels with a 6' search radius seems fine for this purpose.

Key LIVEDATA and Gridzilla Parameters

A more detailed guide to pointed observations can be found online, but the rough parameter set required to persuade LIVEDATA to reduce pointed observations is as follows. For details of the less relevant parameters, see the online documentation available at the Parkes or Jodrell Bank Observer Resources sections.

In the LIVEDATA window:	In the Gridzilla window:
Auto-queue OFF	Parameter set GENERAL
Bandpass calibration ON	Autosize ON
Monitor output OFF (doesn't work)	Image size 4' x 4'
Write data ON	Channels 1-1024
Statistics OFF	Projection SIN
Integrations 1	Av type *
Log Interval 200	Smoothing radius 6'
Observation mode DWELL	Clip fraction *
Prescale mode OFF *	Weighting 0
Bandpass mode MEDIAN	Polarisation 0
Velocity frame BARY	Processor 50% ≠
Fit order 0	Truncated 16-bit OFF
Tukey 25Bandpass Interval 10 *	
Number of precycles 80 †	
Number of postcycles 80 †	
Check field name OFF	
Check central beam only OFF	
Check time OFF	
Check position ON (Min 10, Max 300, Jump 300)	
Gridder ON	

∗ Bandpass interval determines how often (in cycles) the bandpass is recalculated. We found that 10 was sufficient.

† This was the largest we could get LIVEDATA to accept. As it is not possible to look forward/back by more than 80 cycles for reference beams. This suggests 40-60 cycles as a good dwell time in each beam.

‡ Jump is the maximum allowed difference in positions before data gets discarded

⋆ When the baseline is good, medianing is fine, mean with say 5-10% clipping gains you maybe 20% S/N. When the baseline is bad, all this is irrelevant compared with getting as smooth a ripple as possible, on top of which you might hope to see your galaxy. So we turned off the prescaling and used a mean with no clipping, all in the hope of a smooth baseline.

≠ less if running more than one Gridzilla process

Extraction of Spectra for analysis

The output from Gridzilla is also a little non-standard, employing two types of fits file: Firstly, a two dimensional positional array of the number of scans obtained in each positional bin (so called *.scancounts.fits* files), and secondly, a three dimensional data cube containing the spectral information at each position on the sky. We found it necessary to re-order the fits file dimensions. To extract a one dimensional spectrum, we created the following script using the *miriad* package.

```
fits in=$1 op=xyin out=tmp1
imsub in=tmp1 out=tmp2 region=box'('$3,$4,$3,$4')'
reorder in=tmp2 out=tmp3 mode=312
puthd in=tmp3/object value=$2 type=ascii
fits in=tmp3 out=tmp4 op=xyout
echo $1 — sed 's/.fits/s.fits/' — sed 's/.*p291_//' > tmp5
cat tmp5 — awk '{print "mv tmp4",$0}' > tmp6
echo 'rm -rf tmp*' ≫ tmp6
chmod 744 tmp6
./tmp6
```

execution syntax: miriad.script fitsname objectname xpix ypix

The script takes command line arguments xpix and ypix are the pixel number from the .scancounts.fits files, which start with pixel zero.

2.5.4 Spectral Line Analysis Package (SLAP)

The extracted and re-ordered spectra were analysed using the *Spectral Line Analysis Package* (SLAP, Staveley-Smith (1985)). SLAP is a simple but powerful command line driven package, allowing interactive manipulation and measurement of spectra.

SLAP was used to remove any residual continuum contribution, by fitting a Chebychev polynomial to the spectra, and then subtracting it to yield a flat baseline. From this, the HI profile was fitted and integrated to give the mean velocity, total flux (in Janskys), and profile widths and velocities. We fit half Gaussians to the profile edges in order to derive velocity widths at the half, quarter and fifth

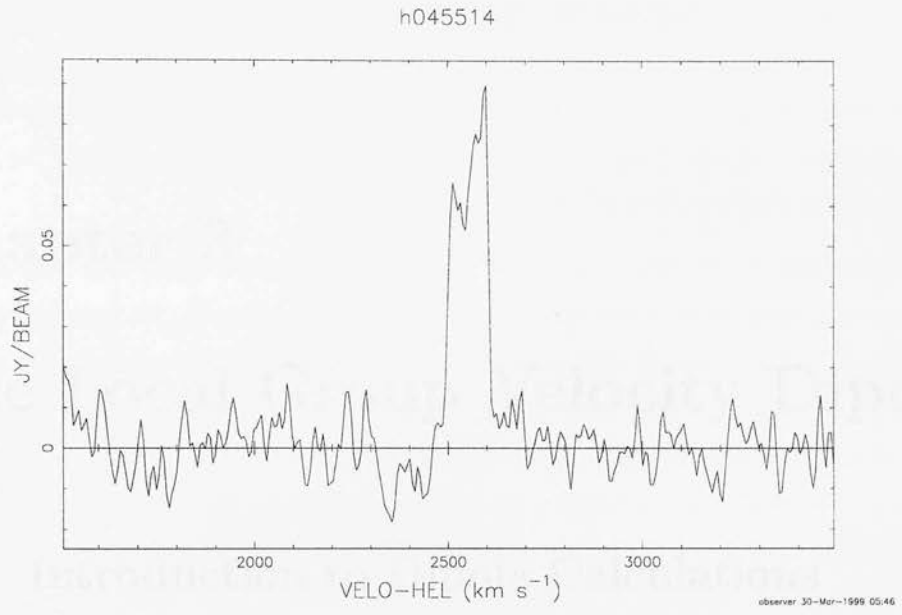

Figure 2.14: *The baseline subtracted HI spectrum of H/045/514 showing a clear double horned profile typical of edge-on spiral galaxies.*

power points on each side of the profile. An example of the output spectrum from SLAP is given in figure 2.14, and a more varied selection of reduced HI spectra is given in appendix H.

Chapter 3

The Local Group Velocity Dipole

3.1 Introduction to Dipole Calculations

The motivation behind determining the gravitational acceleration of the Local Group is many-fold. Firstly, it is aesthetically pleasing to achieve agreement with the CMB temperature dipole. If the temperature dipole is interpreted as a Doppler shift due to the bulk motion of the Local Group, then we should be able to reconstruct this motion using physically motivated arguments and appropriate measurements. Our argument is that of Gravitational Instability (GI), which ties the current Local Group velocity to the mass distribution throughout the surrounding local Universe. The possibility of angular agreement with the CMB by applying the measurement of the local matter density field to these arguments provides a major test of GI theory. The second main motivation is that GI theory leaves unconstrained the mean density of the Universe, Ω_0, and constraints on this can be made by normalization of the inferred velocity with respect to the magnitude of the CMB temperature dipole. Also, by observing what proportion of the Local Group acceleration is generated at different distances, it is possible to glean information not only about the power spectrum of density fluctuations, but also about how far we can push the assumptions in linear GI theory. Another consideration is that of *bias*. It is in no way clear that the number density of galaxies is simply related to the underlying mass density, and so probing the true matter density is a difficult task. 2D and 3D galaxy surveys are a tool we can use as a starting point, but it is important to attempt to infer a sensible relation between the mass and the galaxy population we use as tracers of the mass. Addressing this issue properly is a vastly complicated task, and much

current research is being done to achieve this goal. Biassing is discussed at greater length later on in this chapter. Dipole calculations by nature, are not the best tool to analyse the exact biassing relation. Under the simple assumption of a linear biassing scheme, constraints on the bias parameter can be only be inferred upon making assumptions about Ω.

In this chapter, I will describe a brief history of dipole calculation methods and the datasets they have been applied to. I will then describe in detail the errors, effects and other considerations that need to be taken into account in order to produce a definitive and quantitative analysis of the dipole. I will give details of the various methods available for a calculation of this type, and their respective merits and features. I introduce a new iterative scheme for calculating the dipole, and apply this and other chosen methods of to the PSCz and BTP survey data, and present the results. I compare my results with the recent dipole results obtained from PIZA reconstructions of the PSCz (Taylor & Valentine (1999), Valentine, Saunders & Taylor (2000a)), and discuss anomalies. Several features in the results imply the possible existence of a very large mass concentration at and around 20,000kms^{-1}, and the implications of this for current cosmological models are discussed.

3.1.1 A History of dipole calculations

The first attempts to determine the gravitational acceleration on the Local Group began before all-sky redshift surveys existed. It's not completely necessary to have three dimensional data, in order to approximate the local velocity. It can be seen quite easily that because both force and light comply with the inverse square law, then 1.32 can be approximated by replacing the $1/r^2$ term with the luminosity. The peculiar velocity becomes directly proportional to the normalized dipole of the light distribution. The assumptions used are that of a constant mass-to-light ratio for galaxies, and neglecting extinction. For individual objects, this assumption is not good, but for a large enough survey the sheer number of objects significantly reduces the statistical error introduced by this, and the assumption holds reasonably well. This however still suffers from the problem of the bias between the galaxy and matter distributions, and also from extinction bias, which increases monotonically with distance.

Author	Sample	Lon.	Lat.	Misalignment	Comments
Meiksin & Davis (1986)	6730 galaxies uniformly selected using the IRAS PSC	$l = 235$	$b = 45$	30	$\beta = 0.5$
Yahil, Walker & Rowan-Robinson (1986)	IRAS 60μm selected sample	$l = 248(9)$	$b = 40(8)$	26(10)	$\beta = 0.86$
Villumsen & Strauss (1987)	8387 IRAS selected galaxies, $\|b\| > 10°$	$l = 239$	$b = 36$	30	$\beta = 1.2(0.36)$
Lahav (1987)	15,000 optical galaxies, based on the UGC, ESO, and MCG catalogues	$l = 227(23)$	$b = 42(8)$	37	$\beta = 0.3$
Harmon, Lahav & Meurs (1987)	10,554 galaxies from the IRAS Point Source Catalog. Estimated average misalignment of 8 deg between the IRAS galaxy dipole and the CMB	$l = 272.6$	$b = 30.6$	5.4	Flux weighted
		$l = 228.1$	$b = 22.3$	36.4	Flux weighted + bright gals
		$l = 270.0$	$b = 32.6$	5.8	Equally weighted
		$l = 274.6$	$b = 31.3$	7.2	Equally weighted + bright gals
Lahav, Lynden-Bell & Rowan-Robinson (1988)	IRAS and optical samples	$l = 250$	$b = 38.0$	20.6	
Kaiser & Lahav (1989)	IRAS and optical samples	$l = 259$	$b = 34$	12.5	IRAS
		$l = 261$	$b = 27$	11.0	Optical

Table 3.1: *Flux-Based Local Group Velocity Dipoles*

Many people have applied this method up to and including Meiksin & Davis (1986), who applied this method to the IRAS PSC using 6730 sources, and found a dipole anisotropy in the galaxy distribution that points in the direction $l = 235°$, $b = 45°$. Table 3.1 shows an approximate history of flux-based dipole calculations.

With the advent of redshift surveys, the dipole was able to be measured much more accurately. Davis & Huchra (1982) first applied this to the CfA and Revised Shapley-Ames surveys (Sandage, Tammann & van den Bergh 1981), followed by Pellegrini & da Costa (1990), using redshifts from many different surveys. Only recently however were more uniform all-sky redshift surveys created, all of which have been based on the Infrared Astronomical Satellite (Beichmann 1985) which flew in 1983. The dipole has been calculated on all of these surveys: QDOT (Rowan-Robinson *et al.* 1990), the IRAS 1.2Jy survey (Strauss *et al.* 1992), the PSCz survey (Rowan-Robinson *et al.* (2000), Saunders *et al.* (2000d)), and now with the addition of the Behind the Plane survey (Saunders *et al.* 2000b) designed to supplement the PSCz.

Table 3.2 shows in more detail the history of redshift based dipole calculations. Both of these tables indicate the quite large range of directions obtained from the respective calculations, and are often in disagreement with one another and currently assumed values, given the quoted errors. Also, note the range of predicted values of the β parameter (where $\beta \simeq \Omega^{0.6}/b$), which are in general disagreement. The values obtained are heavily dependent upon the data and analysis used, and it is sometimes unclear which analysis can be relied upon. Almost all previous authors in this area indicate that sky coverage is probably their biggest source of error.

The most interesting feature of these results, is the systematic disagreement in dipole direction. As with the results found in this thesis, the scatter of dipolar directions is not centred on the CMB temperature dipole direction of $l = 273°, b = 30°$, but rather more toward lower l. This is perhaps confirmatory of the suspicions of the above authors, that sky coverage is crucial. This point will be revisited in later sections.

Author	Sample	Lon.	Lat.	Misalignment	Comments
Davis & Huchra (1982)	2400 CfA and Revised Shapley-Ames survey galaxies covering the Northern and Southern polar caps.	$l = 218$	$b = 67$	50	$0.36 < \beta < 0.74$
Pellegrini & da Costa (1990)	4577 optically selected galaxies from CfA and SSR(S) surveys	$l = 305$	$b = 29$	33	$0.24 < \beta < 0.56$
Rowan-Robinson *et al.* (1990)	QDOT 1 in 6 all-sky redshift survey (2387 galaxies)	$l = 240(24)$	$b = 36(27)$	28	$\beta = 0.94$
Strauss *et al.* (1992)	IRAS 1.2 Jy all-sky redshift survey (5288 galaxies)	$l = 251$	$b = 35$	19	Iterative technique involving the adiabatic introduction of β
Schmoldt *et al.* (1999)	11,206 galaxies from the IRAS based PSCz all-sky redshift survey	$l = 259.2$	$b = 33.8$	14.7	$\beta = 0.7^{+0.35}_{-0.2}$
Valentine, Saunders & Taylor (2000a)	15,000 galaxies from the IRAS based PSCz all-sky redshift survey	$l = 264.4$	$b = 41.7$	15.0	$\beta = 0.51 \pm 0.14$
Rowan-Robinson *et al.* (2000)	15,000 galaxies from the IRAS based PSCz all-sky redshift survey	$l = 253.0$	$b = 26.3$	18.0	Found convergence only beyond 10,000 kms^{-}1 with $\beta = 0.82(0.15)$

Table 3.2: *Redshift-Based Local Group Velocity Dipoles*

3.1.2 2-dimensional Dipoles

To illustrate the benefits of the dipole obtained from the PSCz + BTP data, I will briefly discuss an equivalent calculation on the 2D dataset (where the redshift information is discarded) and analysis of the errors involved in using 2D data. The most immediate downfall of a 2D calculation is of course the lack of a reliable distance indicator, and so it is wise to determine the magnitude of the error caused by this before an in depth analysis of 2D data is undertaken.

However this is not the only point for consideration. Obtaining reliable redshifts for the BTP involved the verification of many candidate galaxies that were previously confused with cirrus, and therefore the PSC and PSCz+BTP dipole calculations would not necessarily be based on the same sources. It was noted by (Meiksin & Davis 1986) that the dipolar anisotropy of IRAS sources could be dominated by the dipolar anisotropy of Galactic cirrus, and so restriction to higher galactic latitudes would be necessary ($b > 10°$). The BTP has allowed us to probe the lower galactic latitude regions with more confidence, because the requirement of an extragalactic redshift eliminates the problem of contamination by galactic cirrus. Consequently, the low-b regions should not really be used in a purely 2D calculation.

The Importance of Distance

Almost all of the galaxies in the PSCz and BTP surveys have spectroscopic redshifts, and the dipolar calculations presented in this thesis use only these candidates. The intrinsic error in a spectroscopic redshift is negligible in comparison to the errors arising from redshift space distortions (with which this is degenerate). In a similar manner, redshift space distortions cause errors in the velocity dipole which are negligible with respect to those caused by sparse sampling. While it is therefore safe to ignore small random intrinsic spectroscopic errors, these errors can become large if the uncertainty in their true distance is large enough. Considering equation 1.32 again:

$$\mathbf{v} = \frac{H_0 \beta}{4\pi} \sum_{galaxies} \frac{\hat{\mathbf{r}}}{\psi \, |\mathbf{r}^2|} \tag{3.1}$$

If we assume our measured distances have significant errors associated with them, then the expected error on the dipole becomes (for one source)

$$\langle \Delta v_i^2 \rangle = \left(\frac{H_0 \beta}{4\pi} \right)^2 \left(\frac{2}{\psi r_i^3} \right)^2 \langle \Delta r_i^2 \rangle \tag{3.2}$$

If the measurement errors are random (*i.e.* statistically independent), then this has a small effect, as the errors add in quadrature. Equation 3.2 was calculated using the PSCz + BTP data assuming $\Delta r_i = 1h^{-1}$Mpc, and yielded an expected 1-σ error of only 24βkms^{-1}. This equates to an angular misalignment of approximately one degree – negligible to that caused by shot noise. However, if systematic errors are correlated across the sky, then this can be of huge influence. When using spectroscopic redshifts, it is relatively easy to avoid systematics like this, but this is not the case with other distance indicators, like those used in dynamical work before redshift surveys. Two dimensional dipole calculations inevitably related magnitude or angular diameter, to an estimate of distance, and systematics in the measurement of these quantities can creep in with ease, as will be demonstrated in the next section.

Systematic Errors in Magnitude Estimation

It appears to be a little tricky to find a good distance estimator that isn't redshift, and to highlight this several plots are shown in figure 3.1. The two panels on the left show the relationship between the velocity of recession from the Local Group and angular diameter of the major axis, for the sources in the Southern hemisphere. The angular diameters are (top) measured by the COSMOS plate Measuring Machine, and (bottom) the RC3/UGC/MCG/ESO diameter. It can be clearly seen that although there is a well defined upper limit to the size of an object with distance, it is nevertheless difficult to assume any definite distance given the object's apparent size. The same is true on the right hand side: these two panels are for the same sources, plotting (top) the COSMOS measured magnitude against recession velocity, and (bottom) the COSMOS magnitude versus COSMOS diameter. Again, in the top of these panels, a well defined lower limit exists to the magnitude of an object with distance, but only a lower limit. The bottom panel illustrates the more interesting and better defined relationship between size and magnitude, but this is somewhat irrespective of distance – small close galaxies are degenerate with large distant ones. As discussed above, from a

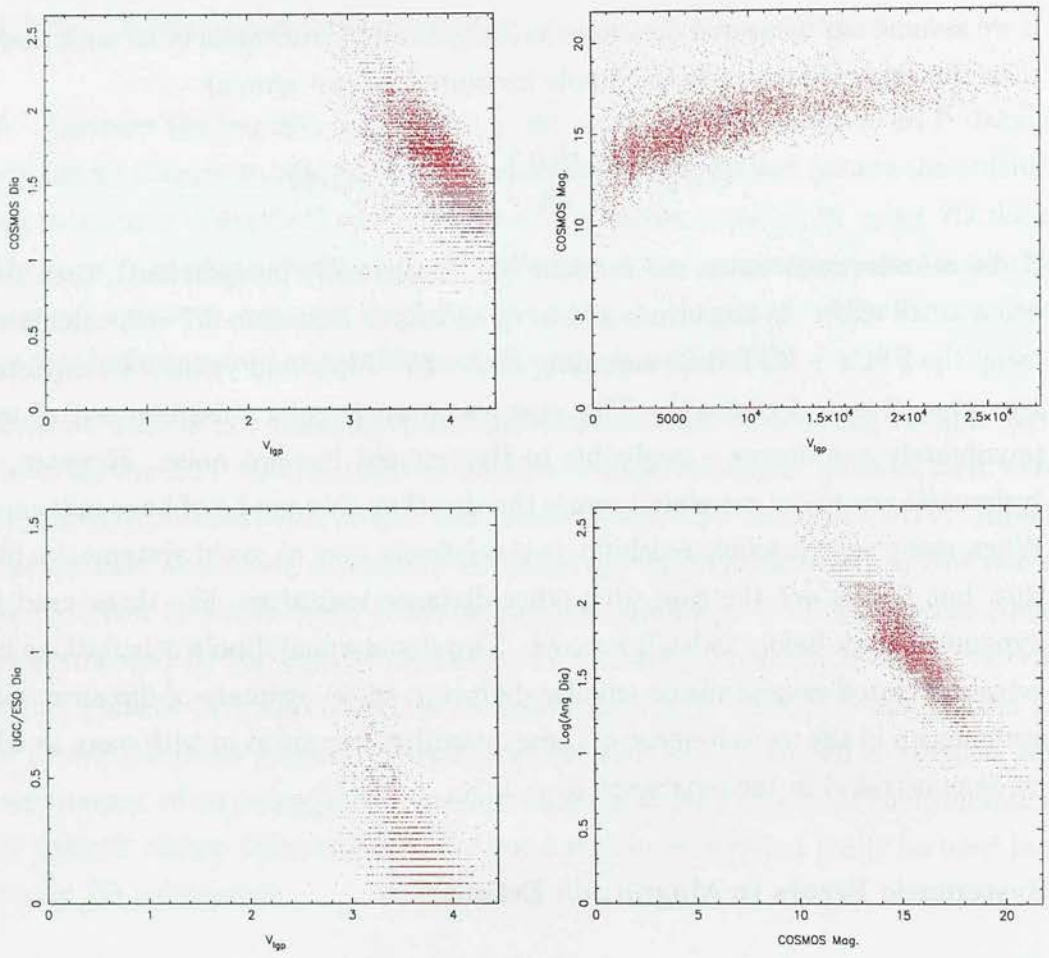

Figure 3.1: *PSCz Southern galaxy correlations: Top left: Angular Diameter 1 vs. V_{lgp}. Top right: COSMOS magnitude vs. V_{lgp}. Bottom left: UGC/ESO Diameter vs. V_{lgp} Bottom right: COSMOS magnitude vs. COSMOS Angular Diameter.*

dipole calculation point of view, the possibility of systematics means the problem does not stop there. The Northern hemisphere was necessarily treated with different instruments to the South. In the North, Palomar Optical Sky Survey (POSS) plates were scanned with the APM plate measuring machine in Cambridge, while in the South, Schmidt plates (UK Schmidt) were scanned using the COSMOS machine in Edinburgh. Systematic differences between the two projects, predominantly in the scanning and magnitude estimation procedures causes problems when attempting a uniform treatment of the whole sky. The same four plots are shown in figure 3.2 for the Northern hemisphere, and it can be seen that the scatter is far greater. Most noticeably, the bottom right hand plot is no longer a power law, but rather it turns over at the bright end. The APM machine treated all objects with a stellar profile in estimation of the magnitude, in order

to compensate for saturation of the photographic plate. Magnitudes are then estimated by integration under the profile, and this leads to wildly overestimating the magnitudes of large close galaxies. At the faint end, the scatter conforms to

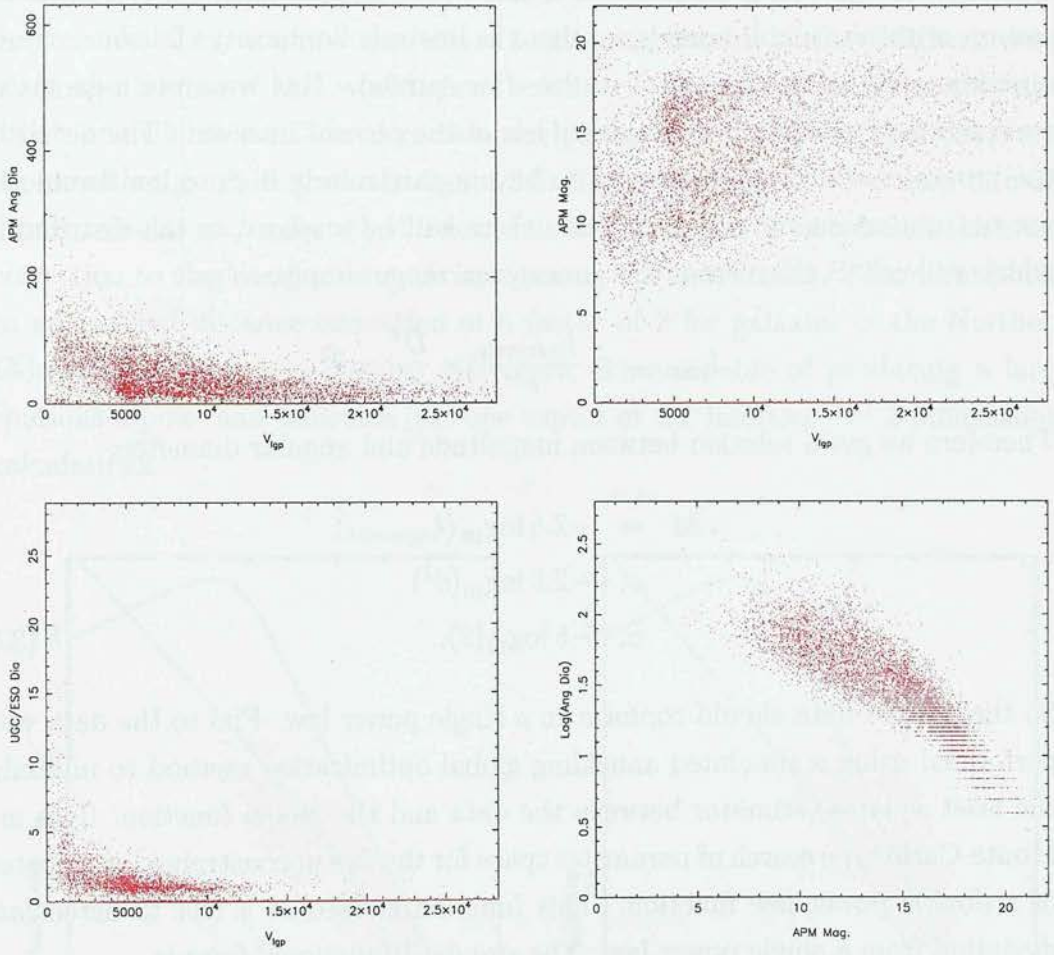

Figure 3.2: *PSCz Northern galaxy correlations. Top left: Angular Diameter 1 vs. V_{lgp}. Top right: APM magnitude vs. V_{lgp}. Bottom left: RC3/UGC/MCG/ESO Bottom right: APM magnitude vs. APM Angular Diameter.*

the expected power law relationship, but is systematically offset. This systematic faint end offset and bright end turnover can be corrected for in a simple manner by association with the Southern dataset. For our intents and purposes, a detailed correction of each individual source is not essential. It is rather more important to equate the average properties of the Northern and Southern halves of the sky, in order to avoid spurious and nonphysical dipolar contributions. Let us first consider the form of the relationship, before attempting a correction of the data. As mentioned before, the apparent luminosity of a source goes as the

inverse square of its distance, and the angular size of a source goes as the inverse of its distance:

$$l_{apparent} \propto \frac{l_{intrinsic}}{r^2}, \qquad \theta \propto \frac{D}{r} \tag{3.3}$$

where D is the source's true diameter, and θ is its angular diameter. We can also assume with reasonable confidence that the intrinsic luminosity of a source scales approximately as the square of its size (for spirals). This is purely a geometric consideration, and in no way an analysis of the physics involved. The details of the processes which cause galaxies to have a particularly high or low luminosity are not important for our purposes – there will be a spread in the distribution which will reflect this. From this we can rearrange simply, to get

$$l_{apparent} \propto \frac{l_{intrinsic}}{r^2} \propto \frac{D^2}{r^2} \propto \theta^2. \tag{3.4}$$

Therefore we get a relation between magnitude and angular diameter:

$$\begin{aligned} M &= -2.5 \log_{10} (l_{apparent}) \\ &\propto -2.5 \log_{10}(\theta^2) \\ &\propto -5 \log_{10}(\theta). \end{aligned} \tag{3.5}$$

So the plotted data should conform to a single power law. Fits to the data were performed using a simulated annealing global optimization method to minimize the least squares estimator between the data and the model function. This is a Monte-Carlo type search of parameter space for the five unconstrained parameters of a double power law function. This function is used as a test to detect any deviation from a single power law. The standard functional form is

$$\theta = \frac{Al^a}{(1 + (l/l_0)^c)^{\frac{a-b}{c}}} \tag{3.6}$$

where A is the function amplitude, l_0 is the turnover point, c is the shape parameter, and the slopes are determined by a and b. The minimization was performed using least squares on the data, and also least squares on the log of the data. Both yield essentially the same results, giving rise to slopes of -0.357 (faint end), and -0.108 (bright end) on the graphs shown.

The Southern magnitude-angular diameter relation looks to conform more closely with a single power law, but as a consistency test, these data were also fitted to the over-constrained double power law function and yielded an artificial turnover

at one end of the data, indicating agreement with a single power law relation as suspected.

So now we are equipped with a quantified measure of the statistical differences between the Northern and Southern halves of the data, and given the Southern's proven reliability, a simple correction to the magnitudes of the Northern data, to fit the Southern half would seem sensible if we wish to avoid nonphysical dipole contributions. This correction was performed on the Northern data, and the resulting graph is shown in figure 3.3. These data can now be used in a 2D dipole calculation, as described below, but first it should be noted that the mean correction to the Northern data is in excess of 1.5 magnitudes. This corresponds to an implied distance correction of a factor of 2 for galaxies in the Northern Hemisphere. This is a massive systematic error capable of producing a large spurious dipole, and indicates just one aspect of the inferiority of 2-dimensional calculations.

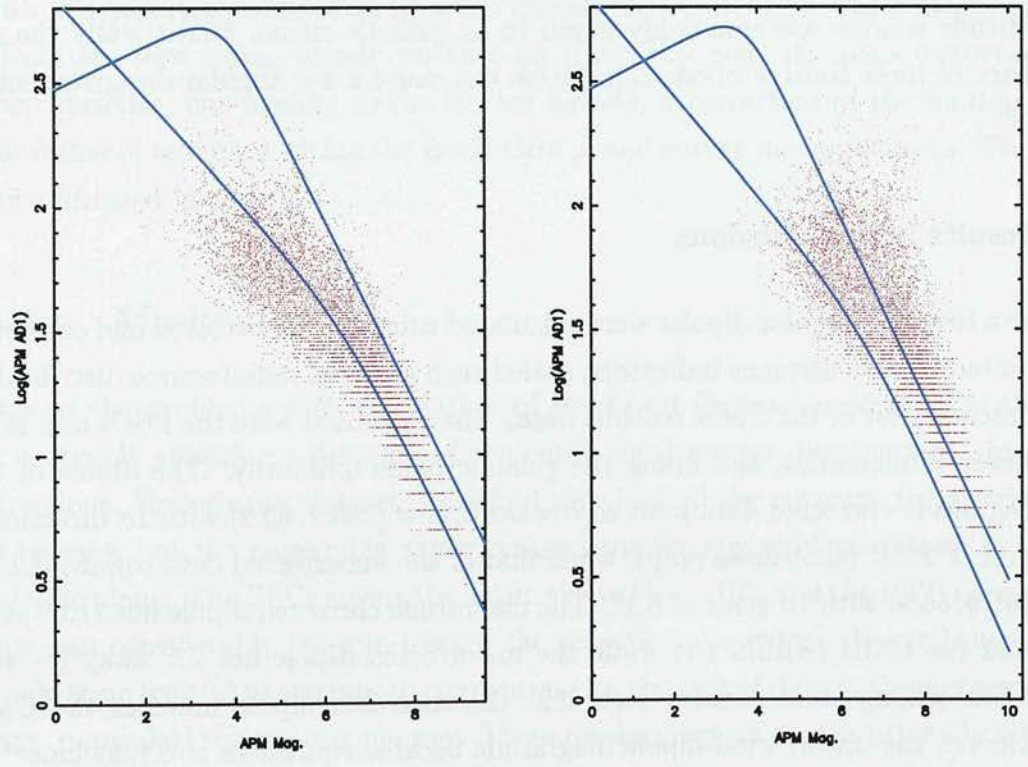

Figure 3.3: *PSCz Northern galaxy distribution of the corrected APM magnitude vs. Log(APM angular diameter). This correction serves to provide consistent statistics between Northern and Southern halves of the sky, according to the power-law fitting described in equation 3.6. Left: The uncorrected magnitudes display a break in power. Right: The corrected magnitudes are consistent with a single power-law.*

Source selection – PSCz versus PSC

The predominant issue here, is that the data used by a 2D calculation (in the absence of spectroscopic verification of sources as galaxies), would inevitably be a superset of the actual redshift survey, because the process of obtaining redshifts for all objects will reveal some candidates not to be galaxies. It would then be prudent to consider quantification of this in an unbiased comparison of 2D versus 3D dipole calculation. A simple measure of the error this would introduce can be deduced from the difference between the number of galaxies in the PSC and PSCz datasets, using Poisson statistics to evaluate the expected disagreement. From my selection criteria, the PSCz + BTP comprises a total number of 13,862 sources, taken from an expected number of 16,884 serious extra-galactic candidates. This yields a difference of 3,022 sources, approximately uniformly distributed throughout the dataset, but with a concentration at lower galactic latitudes. These sources have been excluded because spectroscopic observations of these sources have shown them to be galactic for one reason or another - low latitude sources are commonly found to be galactic cirrus. Statistically the absence of these sources in one calculation can cause a 1-σ angular disagreement of 25°.

Results in 2 dimensions

As a test, the angular dipoles were calculated using the uncorrected and corrected luminosities as distance indicators, scaled such that the radial source distribution matched that of the PSCz redshift data. The data used were the PSCz and BTP survey luminosities, and filling the galactic plane uniformly. The dipole of the magnitude corrected data pointed toward $[l, b] = [280.7, 39.2]$ with 1σ directional error of 22.9° (shot-noise only), while that of the uncorrected data toward $[l, b] = [281.9, 56.9]$ with 1σ error of 6.1°. The magnitude corrected dipole lies 11.6° away from the CMB (within 1σ) while the uncorrected dipole lies 27° away ($> 4\sigma$). When scaling these dipoles such that the corrected dipole matches the CMB velocity, the uncorrected dipole magnitude became equivalent to 14,660kms^{-1}, a huge result which is reflected in the relative smallness of the 1σ angular error. As these errors are shot-noise based, it can be seen that the main source of error lies elsewhere. This is an example of the large spurious result alluded to above. Alternatively, scaling this result to the CMB would produce an estimated value

of $\beta = 0.042 \pm 0.004$, which is equally unrealistic.

Although the magnitude correction has performed well, the dipole is extremely sensitive to the exact correction applied. This is expected when applying such a large scale systematic correction to the data in half of the sky. This example does well to illustrate the unreliability of the method. In the past, equivalent results have been achieved this way, using smaller datasets, but the goodness of a result lies in its robustness. It is clear from this that 2D data is stricken with systematic errors far greater than those of redshift data.

3.2 Effects to be Considered

This section concerns the errors and effects that influence a dipole calculation, not only from the dataset, but also considerations of the limitations imposed by assumptions used in development of the theory, and by problems associated with the practical calculation of a self consistent result. The major errors and effects are shot noise, cosmic variance on a cut sky, redshift space distortions (two varieties, one leading to the Rocket Effect), a correction of the motion of our frame of reference within the Local Group, and survey incompleteness. These are addressed in turn.

3.2.1 Masks

One of the problems with calculation of the Local Group acceleration is that it is strictly speaking a function of the entire local matter distribution – in all directions. Historically, datasets have had very limited sky coverage for a variety of reasons, but the underlying sky coverage issue for any modern dataset is the galactic plane. The PSCz covers the entire sky to $|b| \simeq 10°$, and the BTP narrows that gap considerably (no gap toward the galactic anti-centre). Nevertheless, it would seem fruitful to attempt to compensate for the lack of data in these coverage gaps, or masked regions in some way. These masked regions are traditionally filled with fake sources, generated in a variety of ways. Two methods of introducing artificial data are used here – there is also a third popular method, and I shall discuss it below.

The first and easiest method is to fill masks with sources which have uniformly

random angular positions, and are radially distributed according to the selection function. These uniform masks can be oversampled to reduce Poisson noise, and then given a reduced weighting in compensation. This is perhaps the safest method, as nowhere is there the chance that structure can be introduced into the masked regions without good reason. However, it may be good to attempt to introduce structure in such a way that the expectation of the misalignment decreases.

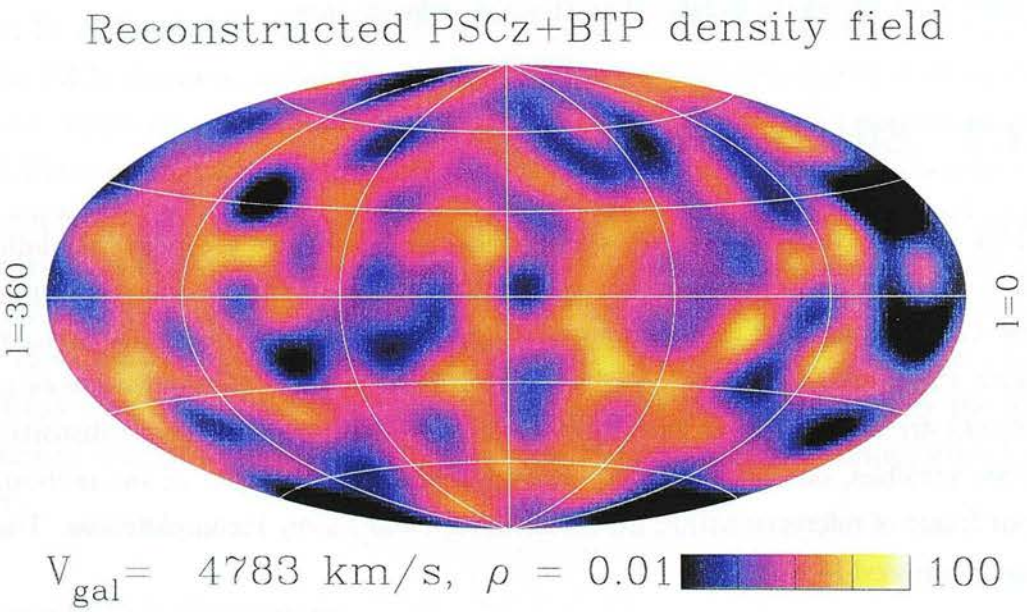

Figure 3.4: *The PSCz + BTP data decomposed into spherical harmonics. This 'onion skin' is at 4783kms^{-1}*

The second method attempts to do this, and is rather more sophisticated than uniform filling. The local density field can be decomposed into spherical harmonics and Bessel functions generated from the existing data, and the masked regions interpolated across. This method seems to work well when the interpolation regions are of order the resolution scale of the harmonic decomposition. The addition of the BTP survey to the original dataset narrows the mask in the galactic plane significantly, and so makes this a suitable method of reconstructing the density field behind the plane. Discrete data is obtained by sampling the interpolated harmonic decomposition. Using this method, Will Saunders produced sets of artificial sources for easy addition to the catalogue. Figure 3.4 shows one radial shell of an harmonic reconstruction across the plane, from which mask sources are picked. In the dipole calculations that follow, I use artificial data generated

by this method, to supplement the PSCz and BTP catalogues.

The third method for generating data within the masked regions is mirroring of the true data above and below the galactic plane. This was a method commonly used in previous attempts to calculate the dipole, again in an attempt at a more sophisticated treatment than just uniform filling. However, I do not use this method in this treatment for many reasons.

For statistical analyses, mirroring of data is a viable method of obtaining all sky coverage, and Lynden-Bell, Lahav & Burstein (1989) claim that the statistical properties of the sample remain unchanged. This could be all well and good for correlation functions, power spectra etc, but not so much for the dipole. Before we consider why, it is worth mentioning that the statistical properties of the sample do not necessarily remain unchanged.

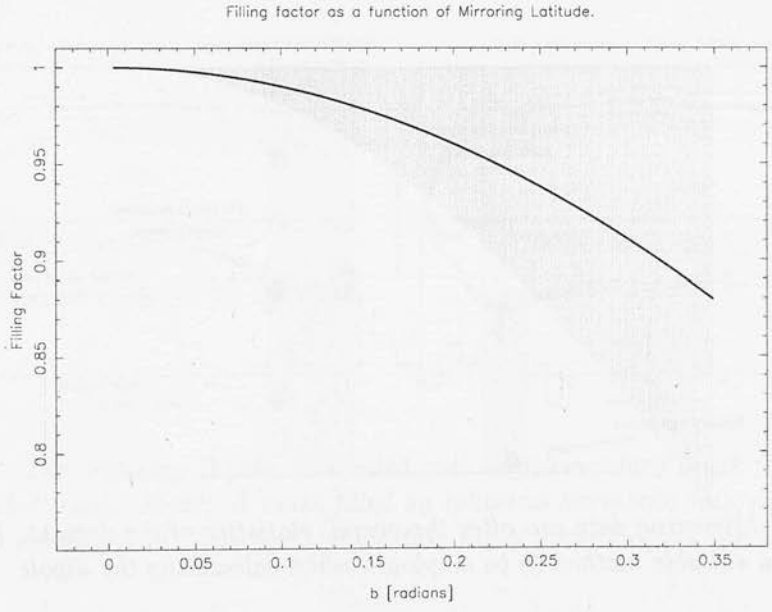

Figure 3.5: *Mirrored data is deficient as smaller solid angles are mapped onto larger ones at lower latitudes. Filling factor is the ratio of solid angle pairs around the mirroring line, and is unity when there is no deficiency (at the mirror). The shaded region represents the range of deficiencies produced, and the solid line the overall deficiency when mirroring about a certain latitude.*

Imagine a strip from $5° < b < 10°$, being mirrored onto the masked region $0° < b < 5°$. The solid angle subtended in the region defined by a strip is $\Omega_{b_1,b_2} = [2\pi \sin b]_{b_1}^{b_2}$, and so strips at different latitudes subtend different solid angles. This means that when a higher latitude strip is mapped onto a lower

latitude strip, the mean sampling density of the strip is not preserved (it becomes in this example $\Omega_{5,10}/\Omega_{0,5} = .992$ times the density of the higher strip). The lower latitude strip will always be deficient, but even more importantly, the deficiency will not be uniform across the strip: the deficiency is greatest as the highest latitudes are mapped onto the lowest ones. See figure 3.5.

The complications do not end there. The PSCz + BTP dataset do not have a uniform lower limit in galactic latitude: the boundary shape is complicated, so local mirroring of the data immediately above the masked region boundary can dissemble structures that were previously there. Not only that, but adjacent areas of the masked region would be filled to different densities depending upon the latitudes of the mask boundary at the respective longitudes. This is illustrated on the left in figure 3.6, where you can see a mirrored structure split in two, across a change in boundary latitude.

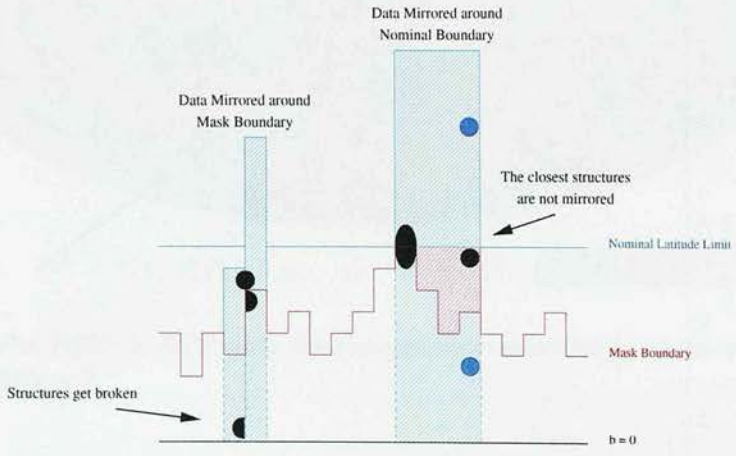

Figure 3.6: *Mirroring data can alter the overall statistics of the dataset. It is not clear that this is a suitable method to be employed when calculating the dipole*

Alternatively, one could choose to mirror about a nominal lower latitude boundary, overcoming this problem (see the right hand side of figure 3.6). But when doing that, there are areas (shaded in pink) that do not get represented in the mask, in preference for areas further away. The entire ethos behind mirroring is that nearby structures are correlated, and so this can be a good approximation. With this scheme however, the mirroring is of more distant structures, and could yield completely different results. This invalidates the method somewhat, and can introduce signal into the end calculation that has little scientific basis. It is better to avoid this situation.

With either of these mirroring schemes, an irregular transformation is performed on the data, and it would be unlikely that the statistics remain unchanged. The validity of generating structures on this basis is not clear either. More importantly for our purposes, introducing structures *ad Hoc* like this will create contributions to the dipole that are almost entirely unjustified, and should be avoided.

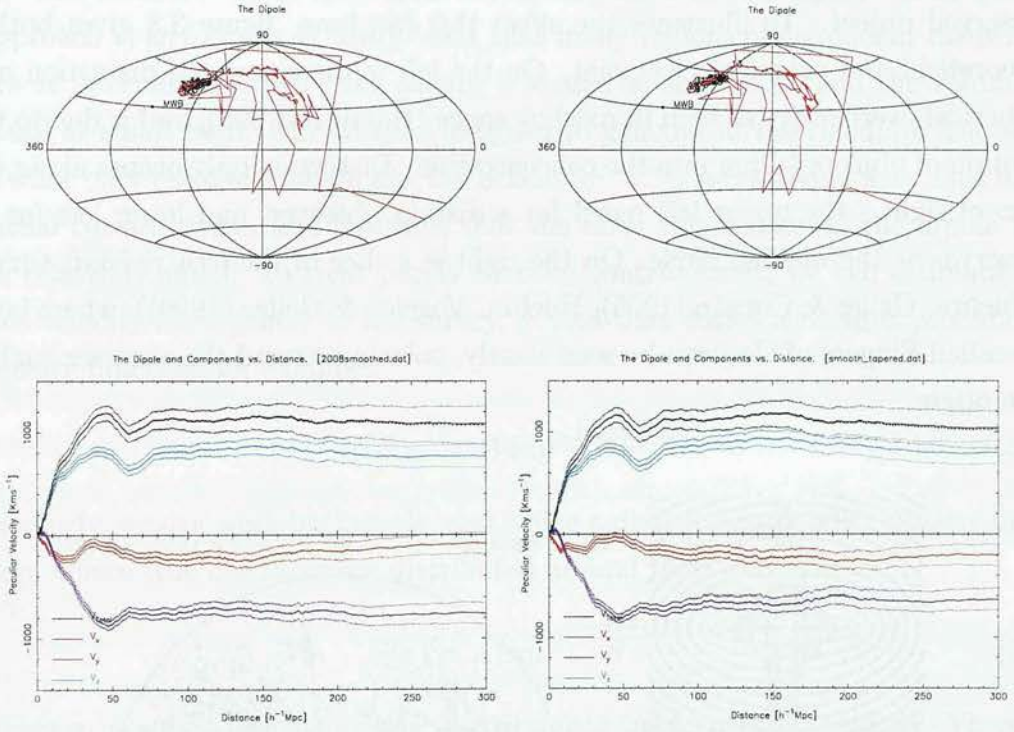

Figure 3.7: *The Velocity Dipole, computed with supplementary mask files. Left: A randomly filled mask. Right: A mask filled by spherical harmonic interpolation of the surrounding density field. Disappointingly this mask doesn't affect the dipole significantly.*

3.2.2 Redshift Space Distortions

Redshift is an ambiguous measure of distance, due to the degeneracy between the radial component of a source's peculiar motion, $\hat{\mathbf{r}}\,(\hat{\mathbf{r}} \cdot \mathbf{v})$, and its comoving distance, $H_0 d$. Plots in redshift space show distinct features, distortions that are the result of peculiar motion, superposed onto universal expansion. Here, I shall consider two types of distortion, generated by motion of the source galaxies, and by our motion with respect to the frame of the Microwave Background. It

will become clear that the latter of these two motions causes significant problems when calculating the dipole.

Peculiar motions of sources.

One major type of redshift-space distortion is that caused by the motion of the observed object. To illustrate the effect this can have, figure 3.8 gives both a theoretical and practical viewpoint. On the left is the computed distortion of a spherical overdensity as seen in redshift space (Hamilton 1998), and is due to the motion of objects falling into the concentration. Distortion only occurs along the line of sight - the upper left panel for a distant observer, and lower left for an observer at the marked circle. On the right is a slice of the CfA redshift survey (Huchra, Geller & Corwin (1995), Huchra, Vogeley & Geller (1999)), where large so-called Fingers of God can be seen clearly, pointing toward the observer (us) at the origin.

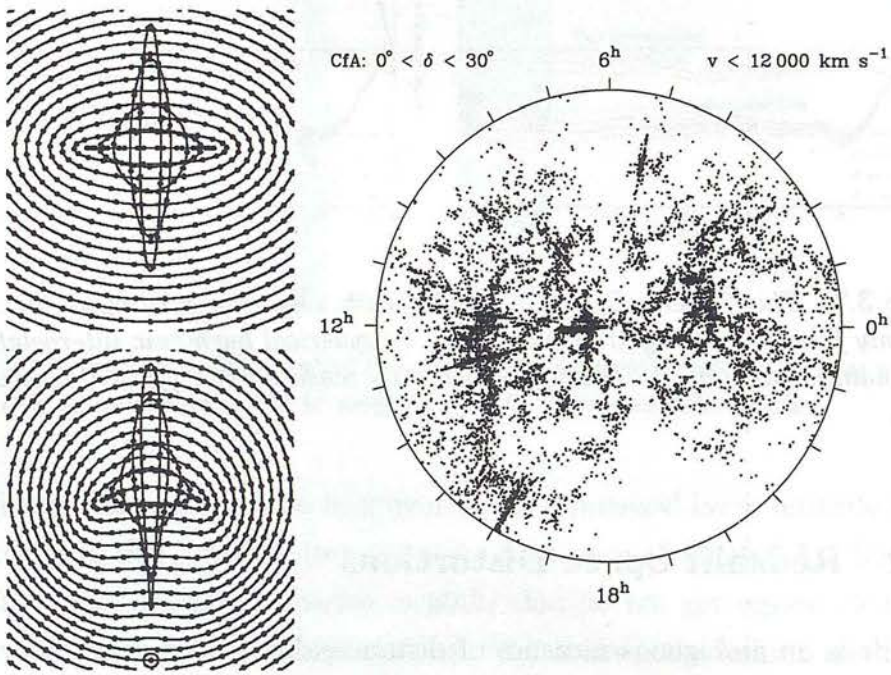

Figure 3.8: *Redshift Distortions. Left: The distortion of a spherical overdensity in redshift space, due to motion in the cluster. The top and bottom cases are at large and small distances respectively. Right: A slice of the CfA redshift survey. Fingers of God are clearly seen, where the magnitude of virialised motion in the clusters is significantly larger than the clusters spatial dimension (as measured in velocity units).*

In the past, Fingers of God have been collapsed to a common redshift before the dipole is computed. This is undoubtedly a good idea, but it does lack consistency. Lesser collapsed structures may not appear as fingers, but as slightly flattened ovals etc., and would be missed out of this kind of correction procedure. A completely self consistent method of converting redshift space to real space for all overdensity sizes has not yet been developed. However, it is important to consider first, the effect that these distortions have on the dipole. A simplistic approach is as follows: It is apparent that many regions of significant distortion are at intermediate radii—the sample is sparse at large radii, and the volume is small at small radii. The weights assigned to galaxies at intermediate distances are not only relatively small, but the action $(\psi^{-1}r^{-2})$ is relatively flat. This is an initial consideration, and indicates that the error this causes on the dipole will be relatively small. To treat purely thermal contributions, we can estimate the rms velocity for a galaxy in the survey, σ, and then define a redshift probability density function, for example:

$$P(Z_{obs}) = A \exp^{-\frac{(Z_{obs}-H_0 r)^2}{\sigma^2}} \tag{3.7}$$

Similarly, we can work backwards, and define a distance probability density function, where true distances are distributed around their redshifts:

$$P(r) = A \exp^{-\frac{(r-cz/H_0)^2}{\sigma_r^2}} \tag{3.8}$$

where σ_r is now the rms apparent displacement due to peculiar velocity. Then we can assign a weight to every galaxy, obtained from integrating over its distance probability density function.

$$K = \int_{-\infty}^{\infty} \frac{P(r)}{r^2\psi(r)} \mathrm{d}r \tag{3.9}$$

Instead of doing this for every galaxy, we can instead use this to convert the redshift space selection function, to a real space selection function, as is shown below in figure 3.9. However, it can be seen that this is only a second order effect: Integrating a linear function over a symmetric probability distribution will yield only the mean value of the distribution, and will not change the selection function. Indeed, the figure shows that the real space corrected selection function is very similar to its redshift counterpart. This shows that a treatment of redshift space distortions of this kind is not crucial to the result of a dipole calculation. The effect it has on the dipole is minimal, especially in view of the much larger errors

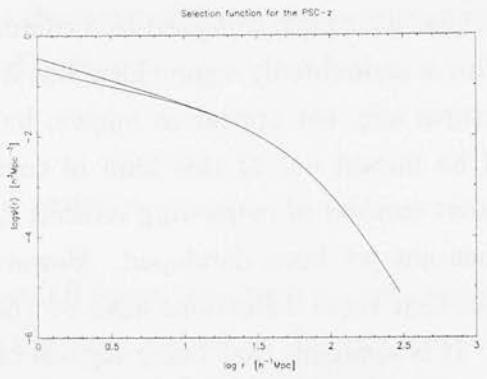

Figure 3.9: *The Selection Function in Real Space (red) calculated from the Redshift Space function (blue) with* $\sigma_r = 5\mathrm{h}^{-1}Mpc$. *It can be seen that there is no significant difference at all but small radii, where the integral has been prematurely truncated.*

due to shot noise, and cosmic variance. It should be noted that this does not directly treat coherent infall in the linear regime, but this is acceptable when you consider that objects undergoing infall into a concentration do so from behind along the line of sight (thus generating a blueshift component), and from in front (adding to the redshift). Given that the action over much of the survey is relatively flat, this is only a second order effect, of the same order of magnitude as the error obtained by the purely thermal treatment.

The Rocket Effect

Now lets turn to distortions due to *our* motion. Consider a set of stationary galaxies in expanding space, of which we are one. We see redshifts of the other galaxies, related exactly to their distances from us by the Hubble law, $v = H_0 d$. If we now board a rocket, and move through space relative to our locally defined Hubble frame, we see a distorted picture of the Universe, given by the revised equation

$$H_0 \mathbf{d}_{apparent} = \left[H_0 - \mathbf{v} \cdot \hat{\mathbf{d}} \right] \mathbf{d} \tag{3.10}$$

The galaxies ahead appear closer than they are, and those behind appear farther away (see fig 3.10). This is the *Rocket Effect*, or *Kaiser Effect* (Kaiser 1987), and it has some disastrous consequences for the dipole. If we calculate the dipole and infer a velocity $\mathbf{v}$, we then have to realise that the distances associated with our measured redshifts were initially wrong. We have to put galaxies ahead of us farther away than they were previously, in order for them to maintain the same redshifts as those measured. Similarly, galaxies behind us are really closer

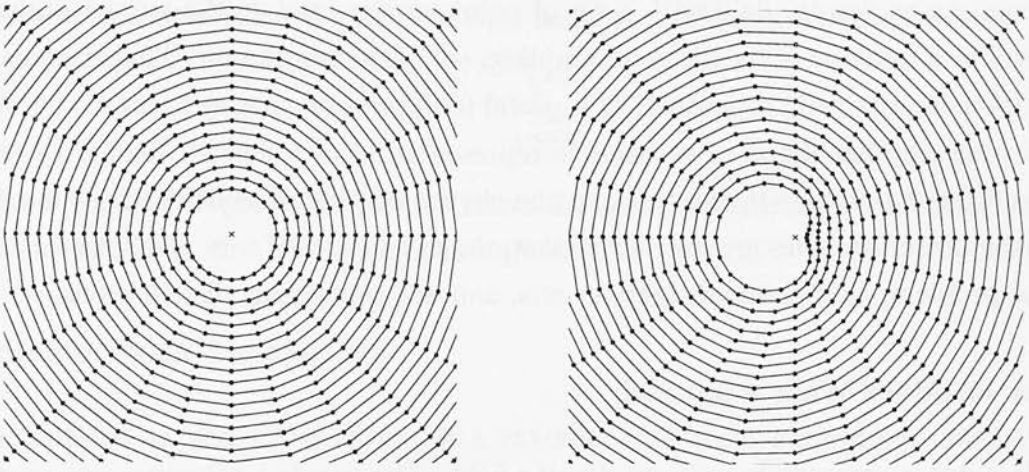

Figure 3.10: *The Rocket Effect. Shown are two maps in real (left) and redshift (right) space. The distortion caused by us moving to the right takes on the shape of increasingly accentuated cardioids. Notice how the lines of sight are preserved (as required), and how even galaxies almost perpendicular to the direction of motion can be affected.*

than our original estimation. So we need to repeat the calculation with our new revised set of radial distances. Because the selection function falls off as r^{-3}, we assign the farthest galaxies with the greatest weights ($\propto \frac{r^{-2}}{r^{-3}} = r$). Those galaxies are ahead of us, and so we then get a new dipole result indicating a stronger pull in the same direction. We then have to infer a greater velocity, put the farthest galaxies even further away, infer an even greater pull, etc., etc. This nonsensical situation is unavoidable when the selection function falls off quicker than r^{-2}, and is the reason behind the divergence problem of iterative calculations of the dipole. Volume limited samples would not be affected by this divergence, but would nevertheless yield a biassed result as a consequence of this behaviour. There are a couple of ways of combating this divergence. Weighting the data according to a scheme whereby sparse sampling errors are minimized, helps prevent excessive weight being given to these distant noisy sources. There is also motivation for changing the frame of reference of the Local Group gradually while calculating the dipole, and this also seems to curb divergent behaviour. These methods will be discussed in more detail in sections 3.3.2 and 3.3.3.

3.2.3 Shot Noise

Shot noise is the uncertainty in the result caused by the discrete sampling of the underlying continuous density field. It is impossible to exactly represent a

continuous density field with a set of point sources, and so the answer obtained will be a function of the discrete sampling, not of the continuum. This discrepancy can be statistically estimated. It is useful to appreciate that as a sample becomes sparse, the likelihood of reasonable representation of a density field with fewer and fewer points is decreased, and the chance of a significantly erroneous result (the *noise*) becomes greater. Poisson statistics lends itself very nicely to this type of problem, as it treats discrete events, and not continuous distributions.

A Random Walk Approach

Imagine a completely uniform density field. The peculiar velocity generated by this field would be zero. However, the galaxies we see in the field are a randomly sampled selection of points, so the sum of their gravitational acceleration vectors would most probably give a non-zero velocity. We would in this case, infer a false velocity. Consider one galaxy, labelled i. Its direction is random, its distance $\mathbf{r}_i$, and thus its contribution to our velocity is $\mathbf{v}_i$. We can define its realization-average effect on us:

$$\langle V \rangle = v_i \left[\langle \cos\theta_i \cos\phi_i \rangle \hat{\mathbf{i}} + \langle \cos\theta_i \sin\phi_i \rangle \hat{\mathbf{j}} + \langle \sin\theta_i \rangle \hat{\mathbf{k}} \right] = 0, \quad \langle V^2 \rangle = v_i^2 \quad (3.11)$$

where $v_i = |\mathbf{v}_i|$. This can be seen by vector addition of a randomly oriented vector on to another. The expected length of the sum will simply be

$$\langle V \rangle = 0, \quad \langle V^2 \rangle = v_i^2 + v_j^2 - 2v_i v_j \langle \cos(\theta_i - \theta_j) \rangle = v_i^2 + v_j^2 \quad (3.12)$$

where θ_i, θ_j represents the angle between the vectors. The generalisation of this becomes trivial, and we get

$$\langle V \rangle = 0 \ , \ \langle V^2 \rangle = \sum_i^N v_i^2 \quad (3.13)$$

with the familiar result in the case of equal $|v_i|$ resulting in:

$$\sqrt{< V^2 >} = v\sqrt{N} \quad (3.14)$$

For a real survey, we can consider integrating over radial spherical shells r_i, each with number of sources $n_i = 4\pi\psi r_i^2 \delta r$, each of weight $\propto 1/\psi r_i^2$. The expected noise from this shell is then

$$< v_i^2 >= \left(\frac{H_0\beta}{4\pi}\right)^2 \sum_{j=1}^{n_i} \left(\frac{1}{\psi r_i^2}\right)_j^2 = \left(\frac{H_0\beta}{4\pi}\right)^2 \frac{4\pi\psi r_i^2 \delta r}{(\psi r_i^2)^2} \quad (3.15)$$

Then we can determine the effect of shot noise as a function of survey depth:

$$\langle V_{sn}(R)^2 \rangle = \sum_{i, r_i \leq R} < v_i^2 > \tag{3.16}$$

where $\langle V_{sn}(R)^2 \rangle$ represents the cumulative shot noise contribution from all galaxies out to radius R. This is shown in Figure 3.11.

Random Walk Simulations

Simulations to verify the effects of a random walk were performed. Initially random walks were performed on 2D square grids, and 3D cubic lattices, with equal step lengths. Then random walks were performed in spherical polars, and then finally, weighting the step length according to equation (3.15). Upon running the simulations, typically a thousand walks of each length between 2 and 300 steps were taken (100 for the grid simulations). The averages were then plotted as a function of distance, and are below.

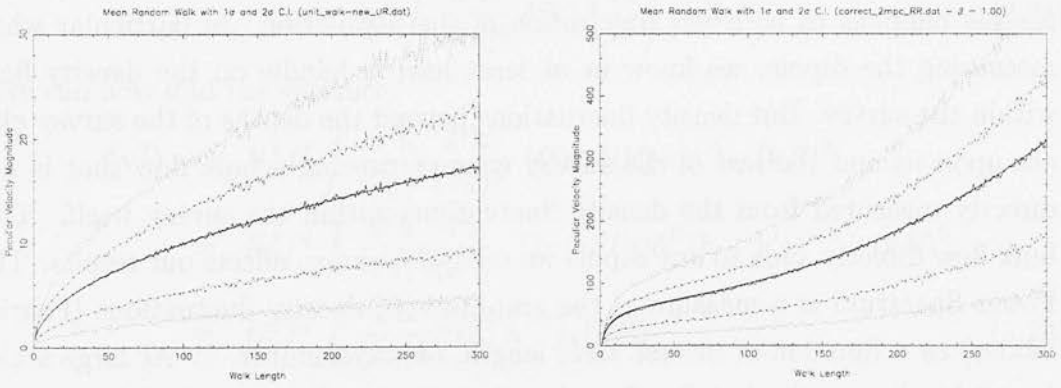

Figure 3.11: *Plots showing the expected displacement from the origin as a function of step number. The Random walk simulations (jagged lines at the mean, and 1- and 2-σ boundaries) reproduce the results expected from theory (smooth). The left panel shows a uniform step walk. Right: walk with step lengths of equation 3.15*

The two boxes in Figure 3.11 are spherical polar random walks, with uniform step and weighted step lengths. These are plotted together with the theoretical mean value of Equation 3.14 (solid line), and the simulation's 1σ and 2σ limits. This simulates the effect that the Poisson sampling of the density field has on a dipole calculation as a function of depth. The completely uniform angular distribution over which the step directions are taken simulates the false velocity one may infer

from a calculation of this sort, if we were in a uniform density field with zero peculiar velocity. To convert from our simplified uniform density assumption, we can just superpose this onto our true (but unknown) density field. This would give us the probability distribution of expected results from a dipole calculation in a particular realization. More usefully, we superpose the uniform density random walk onto the calculated value of our velocity vector, as is shown in the dipole plots above.

3.2.4 Cosmic Variance

Cosmic variance is an uncertainty in our results due to finite survey size. As detailed earlier, the Ergodic hypothesis allows us to exchange spatial and ensemble averages, and so in our calculations we approximate ensemble average quantities by using a sample (the volume of the survey) from the whole accessible population (the entire universe). Whenever inferring statistics about a population on the basis of a smaller sample, an uncertainty arises from being unsure if the sample happens to be a fair description of the population. In particular when measuring the dipole, we know or at least have a handle on the density field within the survey. But density fluctuations beyond the depths of the survey also act upon us and the rest of the survey volume, causing a bulk flow that is not directly measured from the density fluctuations within the survey itself. This bulk flow directly adds to any dipole we measure, and so affects our results. The Power Spectrum is a measure of the amplitude of density fluctuations (Fourier modes) as a function of inverse scale length, or wavenumber, k. At large scales (small k), the amplitude tails off, and so there is an approximate 'maximum scale length' defined in the loosest sense. Fluctuations much larger than this length have small amplitude, and so as we look deeper we can be more certain that unusually significant structures are not present. Mathematically we can explore the effect cosmic variance will have on the dipole. The velocity produced from a density field is given by (1.32) given again here.

$$\mathbf{v} = \frac{H_0 f}{4\pi} \int_V \frac{\delta(\mathbf{x})\ \mathbf{x}}{x^3}\ d^3x \tag{3.17}$$

We can express this in Fourier space, to give (Taylor & Valentine (1999), hereafter TV99)

$$\mathbf{v} = \frac{H_0 f}{4\pi} \int \frac{d^3\mathbf{k}}{(2\pi)^3}\, \delta(\mathbf{k}) \left(\frac{\partial}{\partial i\mathbf{k}}\right) \int_V d^3\mathbf{x} \frac{e^{i\mathbf{k}\cdot\mathbf{x}}}{x^3} \tag{3.18}$$

where $\delta(\mathbf{k})$ is the Fourier decomposition of the overdensity field. Now, the integral over volume on the far right can be transformed through spherical symmetry, to a radial integral. It should be noted that we require the cosmic variance from the volume beyond our survey. The result is quoted here (TV99):

$$\int_V d^3\mathbf{x}\, \frac{e^{i\mathbf{k}\cdot\mathbf{x}}}{x^3} = 4\pi \int_R^\infty \frac{j_0(\mathbf{k}r)}{r}\, dr \tag{3.19}$$

where j_n is the n^{th} spherical Bessel function and R is the nominal survey depth. Then we can use the fact that

$$\begin{aligned} \left(-i\frac{\partial}{\partial\mathbf{k}}\right) 4\pi\frac{\mathbf{k}}{k} \int_R^\infty \frac{j_0(\mathbf{k}r)}{r}\, dr &= -4\pi i \frac{\mathbf{k}}{k} \int_R^\infty dr\; j_1(\mathbf{k}r) \\ &= 4\pi \frac{i\mathbf{k}}{k^2} j_0(\mathbf{k}R) \end{aligned} \tag{3.20}$$

to express (3.18) as

$$\mathbf{v} = H_0 f \int \frac{d^3\mathbf{k}}{(2\pi)^3}\, \delta(\mathbf{k}) \left(\frac{i\mathbf{k}}{k^2}\right) j_0(\mathbf{k}R)\,. \tag{3.21}$$

We can now find the variance:

$$\begin{aligned} \langle \mathbf{v}^2 \rangle &= H_0^2 f^2 \int \frac{d^3\mathbf{k}}{(2\pi)^3} \frac{d^3\mathbf{k}'}{(2\pi)^3}\, \langle \delta(\mathbf{k})\, \delta(\mathbf{k}') \rangle\, k^{-2} j_0(\mathbf{k}R)^2 \\ &= H_0^2 f^2 \int \frac{d^3\mathbf{k}}{(2\pi)^3} \frac{d^3\mathbf{k}'}{(2\pi)^3}\, (2\pi)^3 P(\mathbf{k}) \delta^D(\mathbf{k}-\mathbf{k}') k^{-2} j_0(\mathbf{k}R)^2 \\ &= H_0^2 f^2 \int \frac{d^3\mathbf{k}}{(2\pi)^3} P(\mathbf{k})\; k^{-2} j_0(\mathbf{k}R)^2 \end{aligned} \tag{3.22}$$

where δ^D is the Dirac delta function and $P(\mathbf{k})$ is the power spectrum of density fluctuations. This end result is dependent upon the power spectrum assumed, but it can be seen that as the survey volume tends to infinity, the j_0 term goes to zero, thus giving zero cosmic variance, as required. Figure 3.12 shows the cosmic variance calculated for the PSCz, using the PSCz power spectrum with turnover at $k_c = 0.03$. Also shown is the shot-noise contribution to the errors, and the total error obtained by adding these two in quadrature. As can be seen, cosmic variance is the dominant source of error at small scales, but by the nominal survey depth, contributes very little to the total error. The PSCz and BTP surveys are unique, because for the first time in an all-sky survey, the relative error caused by cosmic variance is effectively negligible.

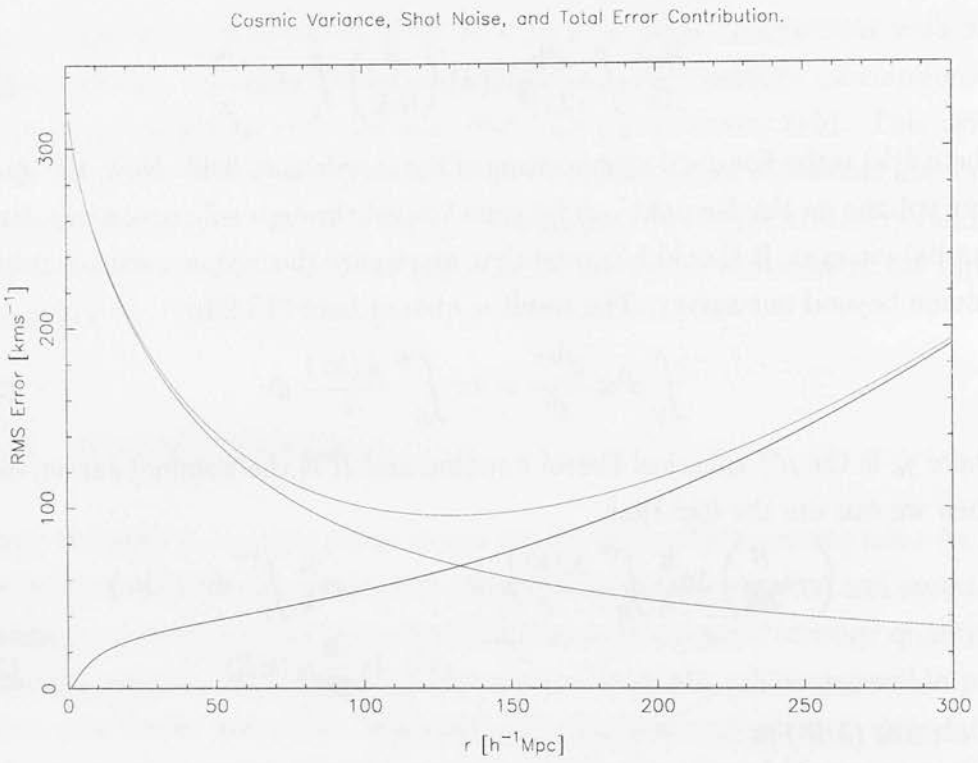

Figure 3.12: *The relative contributions of the two dominant sources of error in calculating the velocity dipole. Cosmic variance dominates on small scales, but gives way to the increasing effect of shot noise on larger scales.*

3.2.5 Supplementary Mask Files

The mask is described in terms of 41167 IRAS *lune bins*, each of approximately 1 sq. degree (Saunders *et al.* (2000c), Lawrence *et al.* (1999)). These mask the areas not covered by the survey. Complete coverage would be ideal in the case of dipole computation, and so we try to fill in the gaps, by creating supplementary mask files—files of artificial sources, distributed in various believable ways as described above. All these files have been generated by Will Saunders for general use to supplement the PSCz and BTP datasets. The two types of mask used have been randomly filled masks, and masks filled by spherical harmonic interpolation from the surrounding density field as described by the PSCz. Because the survey is not complete, calculations of errors like shot noise are not completely correct. In the case of shot noise, the only real error comes from areas of the sky included in the survey. We can calculate the directional components of the shot noise in the survey by considering the exact coverage of the survey. For example, the x

quadrupolar coefficient

$$w_x = \frac{1}{4\pi} \int_{survey} (\hat{\mathbf{r}} \cdot \hat{\mathbf{i}})^2 \, \mathrm{d}\Omega \tag{3.23}$$

These weights were evaluated by taking each component of every lune bin not in the mask. The results are $w_x = 0.261$, $w_y = 0.265$, $w_z = 0.314$. The results from this short calculation were used when computing the shot noise on each component. When a mask is included, shot noise from it is also a factor. However, shot noise can be reduced by increasing the source density in the mask files, and reducing their weights correspondingly. For example, the mask file could contain a tenfold source density, with each source having one tenth the gravitational effect. This in itself can reduce shot noise errors generated within the mask. An advantage of the spherical harmonic interpolation of the density field is that it seems to predict some rather dense regions in areas that appear appropriate, *e.g.* the Great Attractor. The dipole is consistently about 15° away from the measured CMB dipole, in the direction exactly opposite to that of the suspected Great Attractor. A back of the envelope calculation will show that if the Great Attractor were solely responsible for the remaining alignment of the dipole, it would be about two orders of magnitude greater in mass than the Virgo Cluster. Nevertheless, spherical harmonic mask files fail to make that much difference to the dipole, as seen above, in Figure 3.7. Perhaps this is due to an inadequacy in our relation of galaxy number density to the matter field. It is known that IRAS galaxies (predominantly large star-forming spirals) tend not to be at the centre of large clusters, because all the gaseous star forming regions are torn out of the galaxies by a relatively high galaxy merger/collision rate, and this in itself may explain why effects of the Great Attractor may not show up too strongly in dipole calculations.

3.2.6 Local Group Correction

It is standard that astronomical observations are interpreted in the heliocentric frame of reference. The COBE/DMR data are translated to this frame, as are the spectral observations that go to make the PSCz redshift catalogue. However, linear theory can only predict motion on larger scales, and this is commonly interpreted as approximately the scale of the Local Group. Under this assumption, the bulk motion of the Local Group can be treated under linear theory, whilst

motions inside the group must be dealt with differently. Our main consideration is motion of the heliocentric frame with respect to the Local Group barycentre, and is composed roughly of two main parts. Firstly, the orbital motion of our galaxy around the group's barycentre, and secondly, the orbital motion of our Sun around the galaxy. The definitive study of this motion was done by Yahil, Tammann & Sandage (1977), and they report the total correction to be

$$|\mathbf{v}| \approx 300\text{kms}^{-1} \text{ towards } l = 107^\circ,\ b = -8^\circ. \tag{3.24}$$

Before proceeding, it is important to note that this particular choice of non-linear scale is not hard and fast. The scale of the Local Group is certainly a lower limit of the scale of non-linearity, but there is the possibility of non-linear contributions to the bulk motion of the Local Group from some of the larger nearby external structures, *e.g.* Virgo. That said, it is well known that the local flow is very cold (something simulations have struggled to mimic), and all evidence points towards being able to neglect non-linear contributions to our velocity from outside the Local Group (van de Weygaert & Hoffman 1999).

It is interesting to consider the effect of an erroneous Local Group correction on the alignment of CMB and gravitational vectors. The Local Group correction features in two places. Firstly, it is required to adjust the measured CMB dipole vector to the direction as seen by the Local Group barycentre. This is the direction of bulk velocity of the Local Group, and therefore, of its acceleration vector in linear theory. Error in this is first order, any error in the local group correction corresponds to a direct misalignment.

Secondly, the Local Group correction is used in the initial conversion from redshifts to distances. We measure the redshifts in the heliocentric frame, and these incorporate the Local Group peculiar velocity, the heliocentric to Local Group correction, source peculiar velocity, all of which are superposed onto universal expansion. In this case, error in the Local Group correction translates to a misplacement of sources in real space, along their radial directions. This is reputedly a relatively small effect, and for this reason has historically been approximated by the correction

$$\mathbf{v}_{hel} = \mathbf{v}_{lg} + 300 \sin l \cos b \tag{3.25}$$

where $\mathbf{v}_{hel}$ and $\mathbf{v}_{lg}$ are the recession velocities in the heliocentric and Local Group barycentric frames respectively. This approximation assumes the correction to

be 300kms^{-1} in the direction $l = 90°, b = 0°$. However, the error in the approximation is only small for sources along the line of the erroneous correction vector. Perpendicular sources suffer considerably more. In this case, the vectors $(l, b) = (90, 0)$ and $(107, -8)$ subtend an angle of 18.74° on the sky. From this the largest error is consequently $300 \sin(18.74) \simeq 96\text{kms}^{-1}$. In practice, this means that initial estimates of source distances are up to 96kms^{-1} closer on one half of the survey, and further on the other half. In this context, the result appears more startling and its implications on the velocity dipole seem serious. Indeed, in a quick comparison of corrections, the velocity dipole changed in direction by over two degrees, and its amplitude changed by $40b/\Omega^{0.6}$ kms^{-1}.

However, it is now good to know that any further error on the Local Group correction only affects individual sources by $\simeq 4\text{kms}^{-1}$ per degree error ($627 \cos(1°) \simeq 4$). In comparison this will have a relatively small further effect on the dipole, and so to all intents and purposes can be overlooked unless a significant revision of the Local Group correction is made.

3.3 Calculation Methods

3.3.1 Direct Dipole Methods

A calculation of our peculiar velocity can be quite useful. We can use the magnitude of the dipole in CMB – which represents the the magnitude of our peculiar velocity – to normalize the gravitational velocity calculation, which depends upon, and thus yields an estimate of Ω_0/b. As seen above, a major result of gravitational instability is the prediction that the velocity dipole vector can in principle, be determined by integrating the gravitational force from either the density field, or the overdensity field over the entire volume of the universe:

$$\mathbf{v} = \frac{H_0 f}{4\pi} \int_{Volume} \frac{\delta(\mathbf{r})\ \hat{\mathbf{r}}}{|\mathbf{r}^2|}\ d^3\mathbf{r}\ , \quad f \approx \Omega^{0.6} \tag{3.26}$$

where $\delta(\mathbf{r}) = (\rho(\mathbf{r}) - \bar{\rho})/\bar{\rho}$ is the usual measure of overdensity. In practice, we directly measure the number density of galaxies of a particular type, and relate this to the matter density field. So, using the assumption that luminous matter is a linearly biased representative tracer of the underlying dark matter density

field [1] we can write $\delta_{luminous} = b\delta_{matter}$, where b is the linear bias parameter. The above equation reduces to a summation:

$$\mathbf{v} = \frac{H_0\beta}{4\pi} \sum_{galaxies} \frac{\hat{\mathbf{r}}}{\psi\,|\mathbf{r}^2|} \quad , \qquad \beta \approx \frac{\Omega^{0.6}}{b} \tag{3.27}$$

For a basic attempt at calculating the dipole, we can perform the summation of equation (3.27) over all galaxies in the survey. A simple way of doing this is to convert all the redshifts directly to distances (measured in velocity units) using the Hubble relation, and performing a component-wise summation of the weighted Cartesian vectors. The contribution from each galaxy is assigned the simple weight of $1/\psi r^2$ to compensate for sparse sampling. However, this calculation is performed (by definition) in the rest frame of the Local Group, and as such, only nearby galaxies are given approximately the correct distance.

Typically we get a vector magnitude of $\sim 1000\beta\mathrm{kms}^{-1}$ and when normalized by the CMB velocity magnitude, yields a value of $\beta \sim 0.6$. The calculation is performed cumulatively with radius, giving information on how the velocity dipole vector grows as a function of depth. This gives a good picture of exactly where most of the dipole is being generated. Although this simple Local Group frame calculation ignores the rocket effect, redshift space distortions, shot noise, and cosmic variance, it still provides us with a reasonably robust and consistent result. The results are given in figure 3.13. The conversion of the redshifts to distances is not too detailed, but requires more than the above explanation. We need to correct the redshifts for our motion around the barycentre of the Local Group, as mentioned above. This then gives redshifts that are distorted only by the peculiar velocities of the sample galaxies, and the Bulk motion of the Local Group which we intend to measure. The problem of redshift distortions from both of these effects is non-trivial as seen before, and the application of a solution to this shall be predominantly addressed in the next section.

As seen in the left of Figure 3.13, the dipole components seem to start at non-zero values. This is due to a few close sources, that have been assigned far too much weight. Because the volume at small radii is very small, the density field in this nearby influential region is not represented well by the few nearby sources in the catalogue, and this causes a large Poisson error. At small distances, sources are

[1] This assumption can be flawed, as will be discussed later

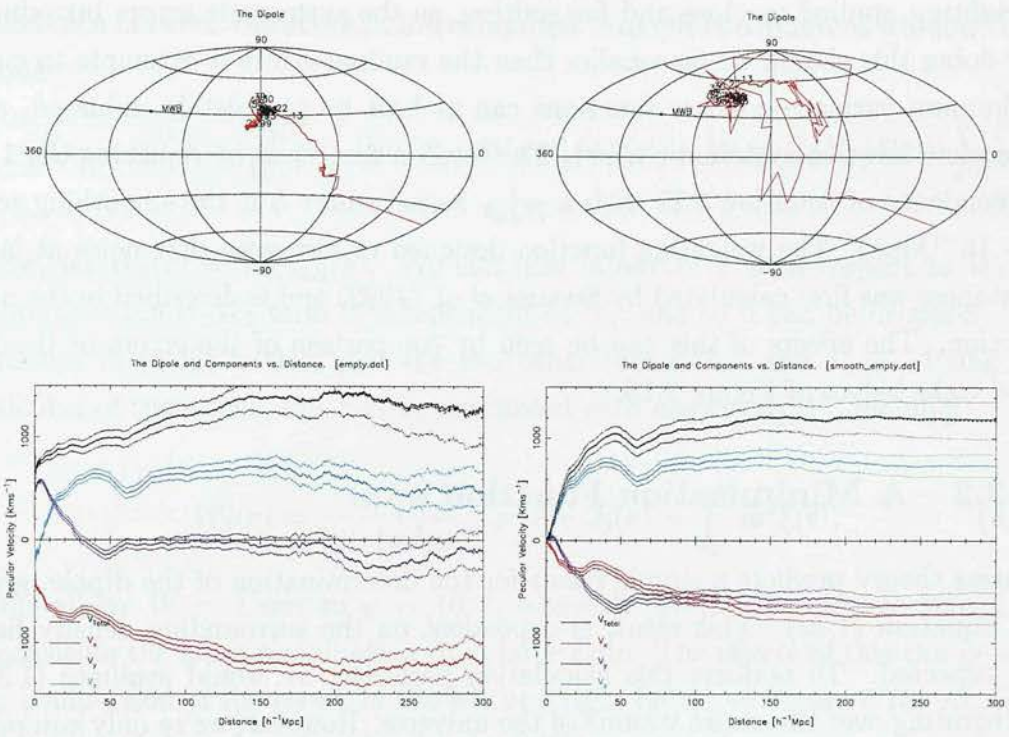

Figure 3.13: *The velocity dipole. Top Left: The projection of its direction as a function of distance. Bottom Left: The dipole components as a function of distance. Notice how the dipole seems to be non zero at the beginning. This is due to a few close sources that are being assigned far too much weight. This is, in effect, shot noise from very close by. Top Right: As top left, but using a force smoothing kernel and weighting function. Notice how the direction is more aligned with the MWB. Bottom Right: Here, we can see that the application of a force smoothing kernel and reduced weighting at large distances gives better results, and smaller shot noise errors.*

very influential because gravity scales as $1/r^2$. At large distances too, sources are very influential because of the large weight they are assigned by the steep selection function. We can compensate for this by applying a force smoothing kernel at small distances and employing a weighting function that minimizes error at large distances (right of Figure 3.13). The selection function is by definition the correct weighting to assign to sources in the survey, but it is susceptible to the effects of shot noise. This is apparent from the plot of cumulative shot noise against distance (Figure 3.11). This plot rises steeply at both small and large distances, where the shot noise contributions are greatest. Firstly at small distances, the surveyed volume is small, and so very local and influential matter is represented by only a few point sources, leading to large Poisson errors. Secondly, at large distances, the survey becomes increasingly sparse, and shot noise rises

accordingly. It is good to minimise the effects of this noise by reducing the weighting applied to close and far sources, as the systematic errors introduced by doing this should be far smaller than the random errors it attempts to curb. Minimum variance window functions can at best be completely unbiased, and therefore have no systematic effect. The force is smoothed by replacing the $1/r^2$ dependence of equation 3.27 with a $\frac{1}{r^2+\alpha^2}$ kernel where α is the smoothing scale ($\sim 1\mathrm{h}^{-1}\mathrm{Mpc}$). The weighting function designed to minimise shot noise at large distances was first calculated by Strauss *et al.* (1992) and is described in the next section. The effects of this can be seen by comparison of the errors in the left and right halves of Figure 3.13.

3.3.2 A Minimisation Function

Linear theory predicts a simple result for the determination of the dipole, given in Equation (1.32). This result is dependent on the surrounding density field, as expected. To perform this calculation perfectly, we would evaluate (1.32), integrating over the entire volume of the universe. However, we're only equipped with a redshift survey, and this suffers predominantly from shot noise and finite survey size (cosmic variance), among other things. It should be asked what is the best way to extract a best guess dipolar acceleration vector from a sample suffering from these effects. We should use a window function that suppresses noise, and yet leaves the result as unaffected as possible. To rephrase, we need a window function that is expected to give us the closest result to the true value: a minimum variance result. Let us rewrite (1.32) with the inclusion of a window function, $W_i(\mathbf{r})$

$$\mathbf{v} = \frac{H_0\beta}{4\pi}\int_{Volume} W_i(\mathbf{r})\delta(\mathbf{r})\frac{\hat{\mathbf{r}}}{|\mathbf{r}^2|}\ d^3\mathbf{r}, \tag{3.28}$$

Here, in our perfect world scenario (and the true CMB dipolar result), we would have the window function:

$$W_{CMB}(\mathbf{r}) = 1, \quad \text{for all } r \tag{3.29}$$

However, the errors present in our sample indicate that a more sensible window function would tend to zero at very large distances. The complete derivation of this optimized window function can be found in (Strauss *et al.* 1992), and so here,

I will only describe the salient features. We can write down the mean squared difference between the acceleration computed through two different window functions.

$$I = \left\langle (v_1 - v_2)^2 \right\rangle = \frac{H_0^2 \beta^2}{16\pi^2} \int \left[W_1(\mathbf{r}) - W_2(\mathbf{r})\right] \left[W_1(\mathbf{r}') - W_2(\mathbf{r}')\right] \left\langle \delta(\mathbf{r})\delta(\mathbf{r}') \right\rangle \frac{\hat{\mathbf{r}} \cdot \hat{\mathbf{r}}'}{r^2 r'^2} d\mathbf{r} d\mathbf{r}' \tag{3.30}$$

Now, let $W_2(\mathbf{r}) = W_{CMB}(\mathbf{r})$. We can now minimize I with respect to $W_1(\mathbf{r})$. Note that the $W_2 W_2$ term is independent of W_1, and so it can be dropped. The product in (3.30) is then just the two other terms, I_W, and I_{WW}. Using the calculus of variations, this can be minimised with respect to W_1, yielding

$$W_1(r) = \frac{4\pi J_3 \psi}{1 + 4\pi J_3 \psi}, \quad \text{where } J_3(r) = \int_0^r dr' \xi(r') \tag{3.31}$$

This allows $W = 1$ out to $\psi \sim 10^{-4}$, where W drops smoothly to zero, thus decreasing the noise contribution from large radii. The effects of this can be seen by comparison of the errors in the left and right halves of Figure 3.13. An early estimator of the value of $4\pi J_3 \psi$ for the PSCz was $\approx 10^4$.

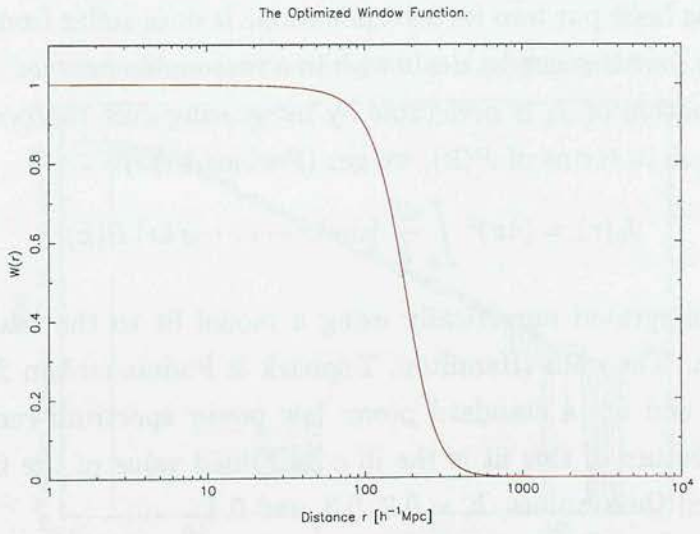

Figure 3.14: *The Optimized Window Function. The function tails off smoothly with increasing distance, to minimise the effects of shot noise from the deepest parts of the survey.*

As stated before, J_3 had previously only been estimated for the PSCz catalogues, at $J_3 \simeq 10^4$. However, to obtain the most physically motivated dipole possible,

this could become a reasonably critical matter. The precise form of J_3 dictates the depth of the smooth cutoff in the generation of the Local Group acceleration. From the spherical harmonic maps (shown in Appendix C), there are large structures at the cutoff scale ($\simeq 200\mathrm{h}^{-1}$Mpc when $J_3 = 10^4$), although there are other matters arising with these structures. A proper computation of J_3 would help to settle the matter of the importance of the cutoff scale.

This is a relatively hard thing to compute with reasonable confidence, because it relies strongly upon the power at the large scale end of the power spectrum. To clarify this, let's look at how to constrain J_3 with a real dataset. There are two main approaches one can choose to try. The first is a direct evaluation of the equation 3.31 by measurement of the galaxy autocorrelation function, and the second is by re-expressing J_3 as an integral over the real space power spectrum. Both methods have their relative merits, and are able to constrain J_3 to within reasonable limits. The autocorrelation function is most well known on intermediate scales; on small scales, Poisson noise yields large errors, and on large scales, we can not choose many large regions within our survey volume that are statistically independent, in order for us to obtain a tight constraint. The advantage of dealing with the power spectrum directly is that its form is well known, and much effort has been put into its determination. It does suffer from ill-constraint on large scales, but this can be dealt with in a reasonable manner. For these reasons, determination of J_3 is preferable by integrating over the power spectrum. Re-expressing J_3 in terms of $P(\mathbf{k})$, we get (Peebles 1993)

$$J_3(r) = (4\pi)^2 \int_k \frac{dk}{k} \left[\sin kr - kr \cos kr\right] P(k). \tag{3.32}$$

This can be integrated numerically using a model fit to the real space power spectrum data. The data (Hamilton, Tegmark & Padmanabhan 2000) is shown in figure 3.16 and fits a standard power law power spectrum remarkably well. The poorest feature of this fit is the ill constrained value of the turnover scale, k_c. I have fitted three values, $k_c = 0.2$, 0.3, and 0.4.

Figure 3.15 shows $J_3(r)$ calculated for these values of k_c, alongside the assumed constant, 10^4. For the majority of the dipoles calculated, I have defaulted to using $k_c = 0.3$, as this is by far the most reasonable estimate given the data. I have however, explored the effects of variation of this value to check for sensitivity. The results show very little response to changes in the parameter k_c, and the implications of this are discussed later.

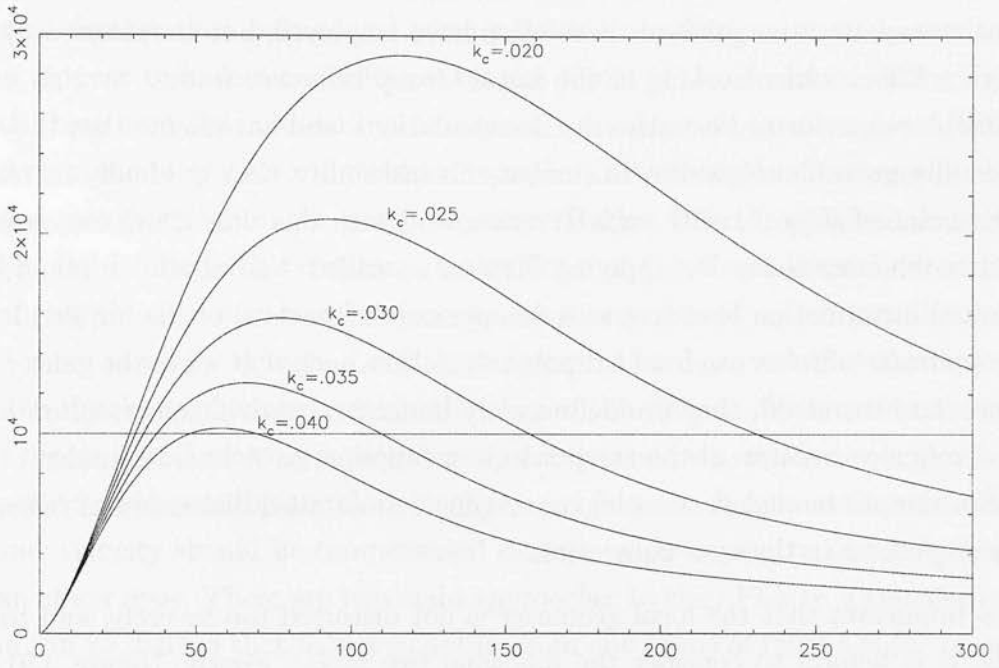

Figure 3.15: *The functional form of $J_3(r)$, calculated for parameter k_c =0.2, 0.25, 0.3, 0.35 and 0.4. Plotted as comparison is the previously assumed constant of* 10^4.

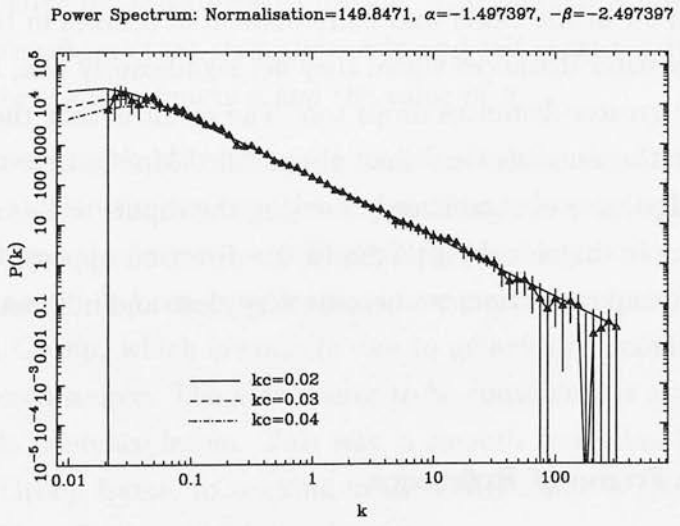

Figure 3.16: *The Real-Space PSCz Power Spectrum. The model fit is a standard power law fit with the parameter values shown at the top.*

3.3.3 Iterative Dipole Methods

The problem with non-iterative dipole calculations, as described above, is that they make incorrect assumptions upon the geometry of the survey, and are there-

fore, fundamentally inconsistent and unphysical. In an attempt to attain self-consistency, iterative methods have often been employed, but are plagued by the Rocket Effect when working in the Local Group reference frame. Strauss *et al.* (1992) have performed iterative dipole calculations, and have found that they are generally unstable. However, to combat this instability, they gradually increased their value of β by 0.1 with each iteration, and with this they claim convergence within ten iterations. By applying Strauss' so-called " adiabatic" method, the gradual introduction of β acts as a damper on the reaction of the implied Local Group frame of reference from a dipole calculation, such that when the galaxy distances are corrected, they are deliberately undercorrected. Overcorrection leads to divergence because of the steep selection function, so deliberate undercorrection attempts to ensure eventual convergence. A detailed discussion of reference frames follows in the next subsection.

It is important that the local geometry is not distorted too severely, and to see this, it is helpful to consider the following two facts. Firstly, (figure 3.9) the selection function at small distances is flat, so the action of $1/r^2\psi(r)$ at small distances drops faster than at intermediate ones. Secondly, the volume in a shell of radius r goes as r^2, and so does the corresponding number of sources at this distance. So at worst case, by applying a strong correction to local galaxies, we not only move a lot of the closer and more influential sources in the direction of our motion, to greater distances where they act significantly less, but the source density at these greater distances drops too. The result is that the galaxies that represent the matter on scales less than about $50h^{-1}$Mpc (where the bulk of the dipole is generated) moves significantly, causing the dipole to become erroneous. Equally worrying is that nearby galaxies in the direction opposite to that of the inferred Local Group correction can become very close and influential, drastically affecting the outcome.

Changing the Frame of Reference

One important thing to remember is that the result of a dipole calculation inevitably tells us that the distances to the galaxies we have used are not quite what they seem. We assume galaxy distances, from that we infer a velocity in some direction. The projections caused by our inferred velocity causes the distance estimates to be incorrect, so we should recalculate all the source distances. When

we do this, we find that those sources in the direction of our inferred motion appear further than before, and when weighted according to the selection function, appear to have more influence on the dipole. A recalculation of the dipole with these new distances will yield a greater acceleration in the same direction, and continued iteration will yield an asymptotically divergent dipole result. This is one manifestation of the nasty runaway "Rocket Effect" explained in section 3.2.2, and is due to this constant recalculation of distances. We should consider changing the distances to all objects in our survey (based on our peculiar velocity) more carefully though. Looking at figure 3.13 we can see that the majority of the dipole is generated within the closest $50h^{-1}$Mpc. Within this distance, our dipole is still growing rapidly, so any acceleration we experience is also being experienced in part, by our closest galactic neighbours. It follows that the effects of our velocity should be compensated more so with respect to distant galaxies, than closer ones. There are two main approaches to this: Firstly, a transfer function can be defined that passes smoothly from one frame of reference to the next. However, there is little physical motivation behind any *a priori* assumption of the form of this function, or for the characteristic transfer scale at which it acts (*e.g.* Rowan-Robinson *et al.* (2000) employs a crude sharp switch between frames at 3000kms^{-1}). The other, and more holistic approach is to allow the data to self-consistently define its own transfer function. This method is presented as part of a new iterative scheme that simultaneously and self-consistently determines the reference frame transfer function and the value of β.

We can self-consistently determine the transfer function by first considering the gravitational acceleration we experience due to our closest neighbours, and then altering the frame of reference accordingly before looking at more distant sources. After each source has been considered, a new peculiar velocity can be inferred for the Local Group, which is entirely due to galaxies from the volume interior to the considered source. The next source to be considered is now corrected with respect to this reference frame. This way, a smooth transition between working in the Local Group frame, to working in the CMB frame is achieved during the calculation. The effective calculation becomes

$$\mathbf{v} = \frac{H_0\beta}{4\pi}\sum_{i=1}^{N}\frac{\hat{\mathcal{R}}_i w\left(\mathcal{R}_i, k_c\right)}{\psi\left|\mathcal{R}_i^2\right|} \tag{3.33}$$

where the corrected source distance is given by

$$\mathcal{R}_i = \mathbf{r}_i + \hat{\mathbf{r}}_i \cdot \frac{\beta_{old}}{4\pi} \sum_{j=1}^{i-1} \frac{\mathcal{A}_j \hat{\mathcal{R}}_j w\left(\mathcal{R}_j, k_c\right)}{\psi \left|\mathcal{R}_j^2\right|}. \tag{3.34}$$

The prefactor $\mathcal{A}_j$ is j/N for adiabatically introduced β, and unity otherwise. It can be seen from this pair of equations, that the corrected distances can only be calculated once the previous Local Group velocity has been inferred. This method of making a smooth transition between frames has its own problems associated with the Rocket Effect: compensating for the velocity of the Local Group requires *a priori* knowledge of β, to which the magnitude of the incremental changes in reference frame are proportional. However, a self-consistent estimate of β can be carefully made by normalization of the dipole magnitude to the CMB. Re-iteration of the entire calculation using the previously yielded value of β serves to ensure that the reference frame the calculation ends in is indeed the CMB frame. Adiabatic introduction of β in the manner described above was employed but using this iteration scheme, it was found to be not entirely necessary. Given that the majority of the dipole is generated within the first $50\mathrm{h}^{-1}$Mpc, adiabatic introduction predominantly hinders the change in reference frame from this major contribution to the dipole. The convergence of the iteration does not suffer from this, but the angular agreement is impaired somewhat.

The way in which this scheme skirts around the Rocket Effect is by beginning each iteration in the Local Group frame of reference. The result of the previous iteration does not significantly distort the geometry of the local volume, as indeed it shouldn't if one wants to preserve small scale coherence in the velocity field. This means that the wild divergence caused by moving a lot of distant sources closer, is avoided.

The results of applying this scheme are shown in figure 3.17.

3.4 Dipole Calculations

3.4.1 Redshift Space Dipoles

True redshift-space dipoles are calculated directly upon the catalogue, allowing only for the heliocentric to Local Group correction, and are therefore performed entirely in the Local Group frame of reference. This is a valid approximation at

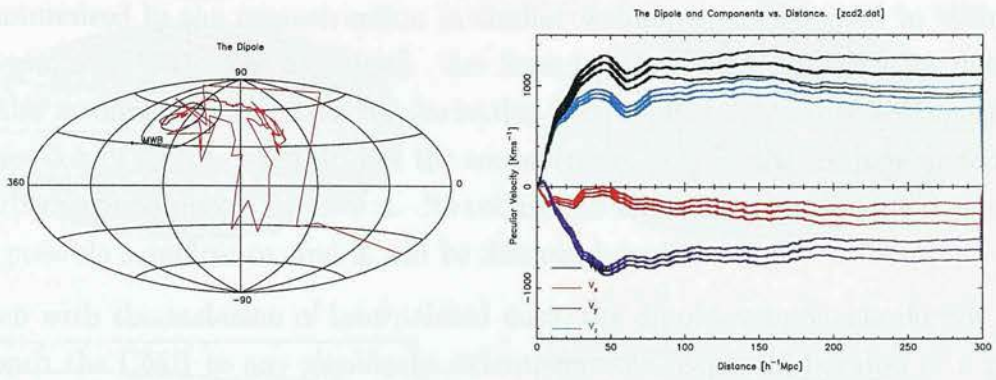

Figure 3.17: *The Velocity Dipole, computed by correcting for the motion of the Local Group as increasingly distant sources are considered. In the Aitoff projection, 1σ and 2σ shot noise error contours have been calculated. Notice how the CMB lies outside these contours, indicating a much more significant alignment problem.*

first, as discussed above, as nearby members are likely travelling alongside us in the local bulk flow. Dipoles are presented throughout this section in figures 3.18 through 3.22. Figure 3.18 shows the dipole calculated on the PSCz only (with and without J_3 weighting). These have not been filled throughout the galactic plane.

Immediately it can be seen from the dipole components that the minimum variance calculation (right) has cut off the influence of regions beyond approximately 20,000kms^{-1}. At about 5,000kms^{-1}, the dipole seems to have reached its closest approach to the CMB, but steadily works its way to higher latitudes as it encounters more structure. At 20,000kms^{-1}, the weighting scheme curbs further influence. It is interesting that without the scheme, the dipole actually returns to lower latitudes again. This is due to what would appear to be a large change in the dipolar components between 20,000kms^{-1} and 30,000kms^{-1}. The absolute differential velocity is a good indicator of influential structures, because it measures the change of acceleration of the Local Group as the dipole is calculated at increasing depth. As can be seen in the bottom panel of 3.18, there exists a corresponding peak in the differential velocity at around 20,000kms^{-1}. Overlaid is the 1σ expectation of differential velocity from Poisson sampling alone. The peak is apparent at the 4σ level in the unweighted dipole.

The next obvious step is to fill the galactic plane with a distribution of artificial sources (figure 3.19). This has been done and dipoles are calculated on this with and without the minimum variance weighting scheme. The interpolation

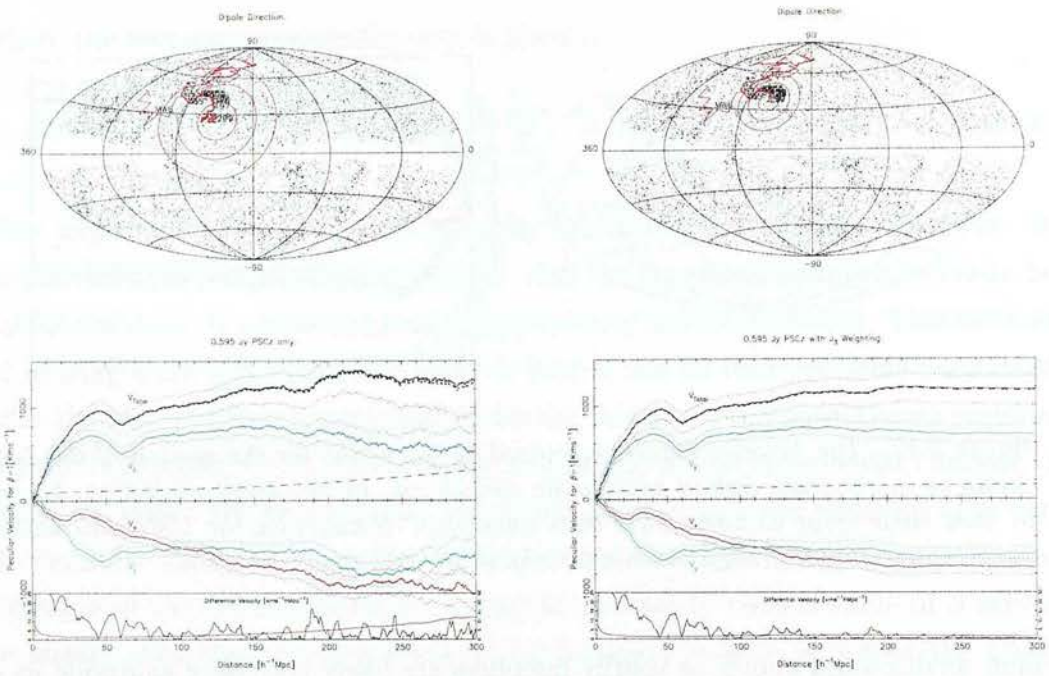

Figure 3.18: *Aitoff projection of the dipole direction, and (below) the dipole velocity components as functions of distance for two dipoles produced using the PSCz data only (without and with J_3 weighting). This non-iterative calculation was performed in redshift-space, in the Local Group reference frame. The Aitoff projection includes 1-3σ error contours, centred on the direction given at the calculation limiting depth. The total velocity and components are shown with 1σ shot-noise limits. As in figures 3.19 – 3.22, 3.24, 3.26 and 3.27, an additional panel measuring the absolute differential velocity is shown. This differential velocity component measures the rate of growth of the dipole, so peaks in this profile correspond to gravitationally influential structures within the data. Shown in red is the 1σ expected contribution from Poisson noise at that depth. Notice the peak centred on $180h^{-1}Mpc$.*

across the galactic plane by Saunders & Ballinger (2000) (Appendix C) has been generated by expanding the survey volume in spherical harmonics and spherical Bessel functions, and extending these into the galactic plane. The predominant area which is filled by this is the galactic centre, shown here at the extremes of the Aitoff projection. One would naturally expect the direction of the dipole to move to lower latitude and increasing longitude, as this is where the largest gap in coverage is located. Not only this, but in the creation of the supplementary interpolated data, Saunders & Ballinger (2000) found it difficult to prevent a large concentration from forming in the galactic plane at $b \simeq 300°$. To avoid unstable reconstructions in regions of missing data, regularization was applied in the form of a dampening "penalty" term being added to the likelihood function which

is minimised in the reconstruction (a similar technique to that used in Weiner-filtering *e.g.* Lahav *et al.* (1994). See Saunders & Ballinger (2000) for details of the reconstruction). This regularization was applied to remove the spurious formation of objects like this, but the concentration was robust to these measures deliberately employed to curb it. Its robustness is interpreted as a good sign of its possible significance, and it will be discussed again later.

Even with the inclusion of interpolated data, the dipole components do not approach the CMB to any significant extent, but this is purely because of a projection effect. The total sky coverage in these calculations have put as much emphasis on the cartesian dipolar components in the galactic plane, as on the polar component, with the consequence that the components in the plane have been shortened, and thus the angular projection climbs to higher latitudes. Notice that the turnaround at 20,000kms^{-1} has sharpened in the unweighted calculation, and again been cut short in the minimum variance calculation. The Aitoff projections have 1-, 2-, and 3-σ errors on them calculated purely from shot noise. Quite importantly, it can be seen that the unweighted dipoles are consistent with the CMB to within approximately 1-σ, and yet the minimum variance dipoles are not anywhere close to this level of agreement.

The same is true of dipoles using both the PSCz and BTP datasets. The BTP has proved to be very successful in mapping the low latitude regions of the survey, despite the expected and inevitable greater incompleteness than the PSCz dataset. The dipole recalculated with the inclusion of the BTP shows remarkable agreement with the predictions from the PSCz + interpolation calculations, as can be seen in figure 3.20. The galaxy distribution had been overlaid in these plots, to indicate the relative source densities in the lower latitude regions. There are reasonably clear strips above and below the galactic plane which are undersampled compared to the rest of the survey, and the central part of the galactic plane itself. This incompleteness is not fully understood at present, but it is well quantified and has been taken into account properly in these calculations. The incompleteness has been measured locally in the BTP region and the BTP data contain incompleteness compensation weightings associated with the locale of each source. Again, the directional agreement suffers considerably in the hands of the minimum variance weighting scheme, due to the cut off imposed at 20,000kms^{-1}, and the results no longer agree at the 3-σ level. This disagreement imposed by the minimum variance scheme, in combination with other findings, raises ques-

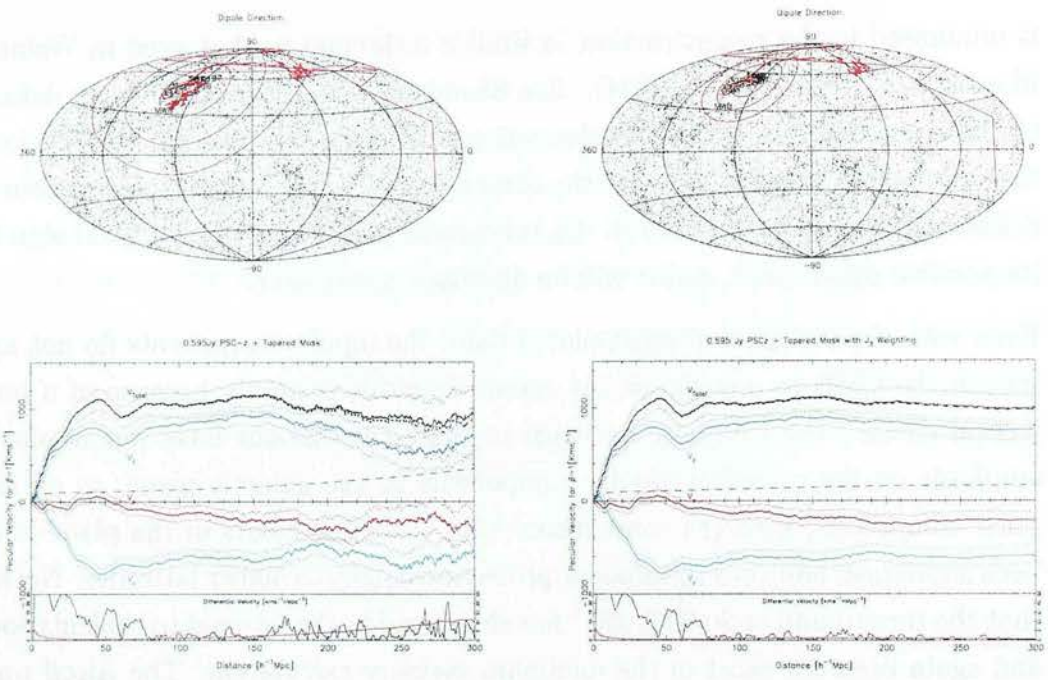

Figure 3.19: *Non-iterative dipoles calculated in redshift-space in the same manner as figure 3.18, on the PSCz data, but with the inclusion of spherical harmonic mask data. These were calculated without (left) and with (right) J_3 weighting.*

tions to its validity. This will be explored in greater detail in the next section. The amplitude of the dipole across all variations of dataset and supplementary artificial data, remains remarkably consistent, yielding values (as can be read directly from the graphs) of $|\mathbf{v}| \simeq (1000 \pm 100)\beta \mathrm{kms}^{-1}$. This, when normalised to the magnitude of our Local Group velocity inferred from the CMB temperature dipole, immediately gives a β for IRAS galaxies of $0.627^{+0.07}_{-0.06}$ at the 1-σ level. This promisingly robust result is consistent with current results calculated by a variety of other methods in the literature (*e.g.* Nusser *et al.* (2001) obtain $\beta = 0.5 \pm 0.1$ from comparing ENEAR and PSCz velocity fields, Valentine, Saunders & Taylor (2000b) obtain $\beta \simeq 0.6$ using PIZA reconstruction of the PSCz, Hamilton, Tegmark & Padmanabhan (2000) measure $\beta = 0.41^{+0.13}_{-0.12}$ in their linear redshift distortion analysis, Tadros *et al.* (1999) obtain $\beta = 0.47 \pm 0.16$ in a spherical harmonic analysis of the PSCz galaxy density field). This dipole shows consistently that the majority of the "power" is generated within the closest $\simeq 50\mathrm{h}^{-1}\mathrm{Mpc}$, but there are significant contributions ($\sim 20\%$) from between 50 and $200\mathrm{h}^{-1}\mathrm{Mpc}$, and the possibly significant indication of non-negligible power at greater depths, up to and including the largest scales probed by the survey.

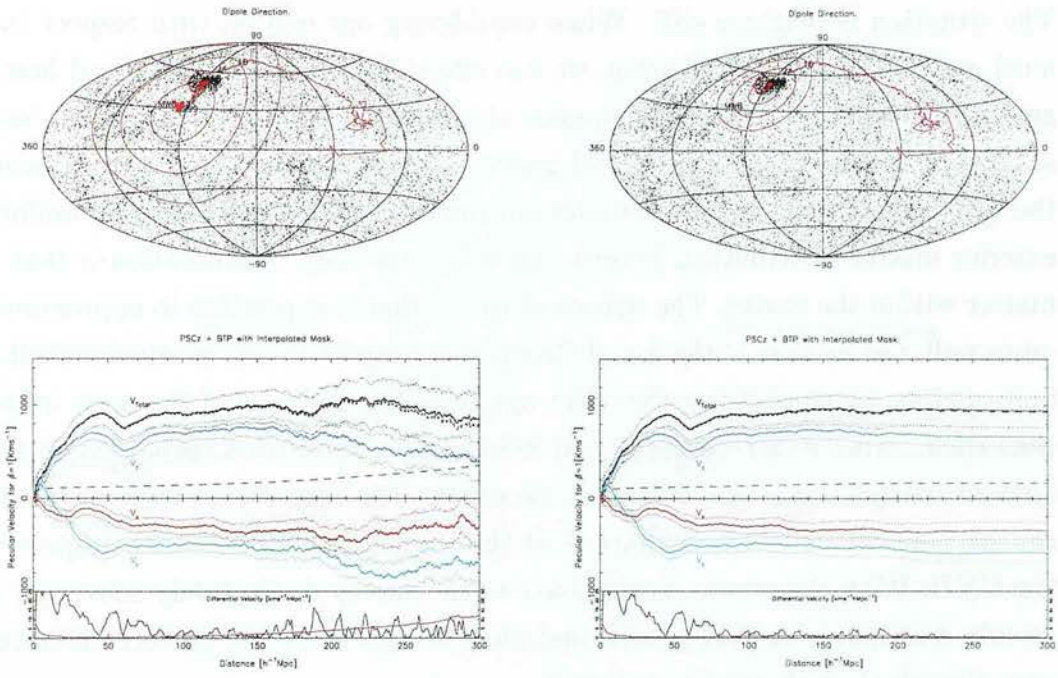

Figure 3.20: *Non-iterative dipoles for PSCz + BTP data with the plane filled with a spherical harmonic mask. Calculated without (left) and with (right) J_3 weighting. The peak at around $180h^{-1}$Mpc remains the most significant feature in the outer regions of the survey (4σ). In the J_3 weighted dipole, the feature can still be seen at the 3σ level, but is heavily suppressed by the weighting scheme. Weighting also leaves the dipole stranded at high latitude.*

3.4.2 Variable Reference Frame Dipoles

As discussed above, there are many good reasons to change the frame of reference as a dipole calculation proceeds. In section 3.2.2, I highlighted the two major separable components to redshift-space distortions; that due to our own motion, and that due to the peculiar motions of the survey galaxies. I detailed the difference between these in terms of their influence in a dipole calculation, and the outcome is that the former type carries much more importance. The motions of the sources themselves are only a second order effect, as can be seen by the redshift-space selection function shown in figure 3.9. This is because there is weak correlation between the radial peculiar velocity components of sources as a function of position. In contrast to this, the distortion due to our own motion is highly correlated across the sky. Any error in this affects the entire survey in a systematic manner. Luckily, this major source of error can be tackled by adjusting just one quantity - our Local Group motion.

The situation is brighter still. When considering our motion with respect to a local and finite mass distribution, we can effectively ignore the (assumed homogeneous) distribution of matter outside this considered volume. This is a basic statement of electrostatics: the field inside a hollow sphere is zero. Analogously, the gravitational field inside a cavity surrounded by an approximately uniform exterior matter distribution, is zero. Therefore the only consideration is that of matter within the cavity. The upshot of this is that it is possible to approximate quite well, the motion of the Local Group with respect to any particular shell of finite radius, by considering the effect upon the Local Group of the mass within that shell. This is particularly good news, as a good initial correction to this form of redshift-space distortion can be made. The amplitude of the distortion can be normalised to the amplitude of the local group motion with respect to the CMB. With the correct normalisation, the survey is effectively converted to pseudo real-space, in that groups and clusters appear at the correct distances, even though their shapes are incorrect.

Figure 3.21 shows the dipole calculated using this technique. As in the redshift-space dipoles, there are two obvious differences between the minimum variance calculation and the unweighted calculation: firstly, the cut off at high latitude, when the unweighted data would like to return to lower latitudes at 20,000kms^{-1}, and secondly, the even more noticeable sudden change in dipole components at this distance, and corresponding 4σ peak in the differential velocity component. The minimum variance function was calculated as in section 3.3.2, using $k_c = 0.03$hMpc^{-1}. As this value is critical to the normalisation of J_3 (see figure 3.15), it is possible that our assumed value of the ill-constrained turnover may cut dipolar contributions too soon, ignoring otherwise influential structure. As a test, a value of $k_c = 0.02$ was used in calculating the minimum variance weighting. The lower k_c causes J_3 to increase, and therefore contributions from greater depths are weighted more significantly. However, even for $k_c = 0.02$, contributions beyond 20,000kms^{-1}, are heavily suppressed as can be seen in figure 3.22. The left hand side of 3.22 shows the dipole still being cut short by far, and the influence of any structure at 20,000kms^{-1} is reduced, although still visible. Iteration of this technique yields a self-consistent value of β, through normalisation with the CMB dipole magnitude, and the resultant dipoles of all the iterative dipole calculations are given in table 3.3. A scatter plot of the dipole directions quoted in the table is also given in figure 3.25.

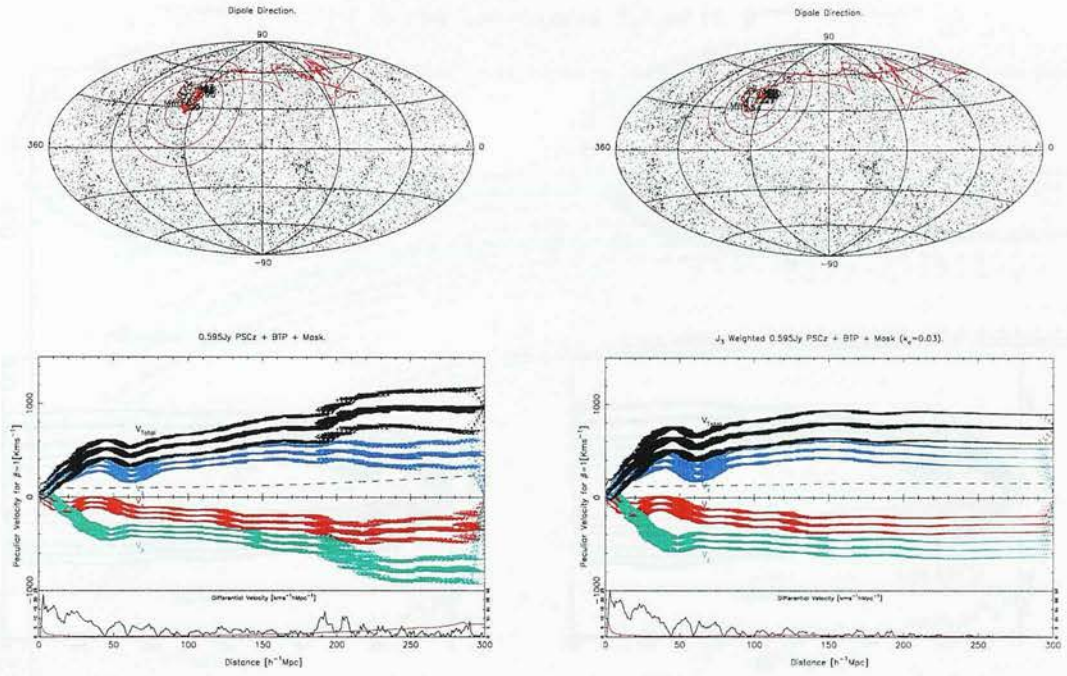

Figure 3.21: *Iteratively calculated dipoles for the* $0.595Jy$ *PSCz + BTP with a spherical harmonic mask interpolating across the coverage gap. Calculated without (left) and with (right)* J_3 *weighting for* $k_c = 0.03$. *The Local Group frame of reference was changed repeatedly according to the iterative procedure described in the text. This produces a horizontal smearing effect on the velocity components, where the magnitude of the smear is given by the influence of objects as that distance.* β *is introduced immediately in each iteration, and dipolar convergence was obtained within 15 iterations. The differential velocity profile shows two influential* (4σ) *peaks around* $200h^{-1}Mpc$ *in the unweighted dipole.*

The 4σ change in dipole components at 20,000kms^{-1} is so striking, that serious doubts of the validity of the minimum variance weighting technique have been raised. Section 3.3.2 outlines the calculation of J_3, and specifically makes certain assumptions about the properties of the matter distribution - namely, that it is Gaussian random, and that we're in a typical region of the universe – *i.e.* nothing in our locality is unusually large. The nature of J_3 is such that assuming there is nothing too unusual in the vicinity, it will cut off contribution at a certain depth, purely because the signal generated beyond this depth is predominantly noise, and should therefore be discarded. It fails in this case because there is something particularly influential just at the edge of this critical depth. This is by design, the depth at which we can no longer be very sure of the survey's reliability, and at which we also do not expect to see a genuine feature inconsistent with shot noise. This feature appears throughout all the iterated calculations not involving

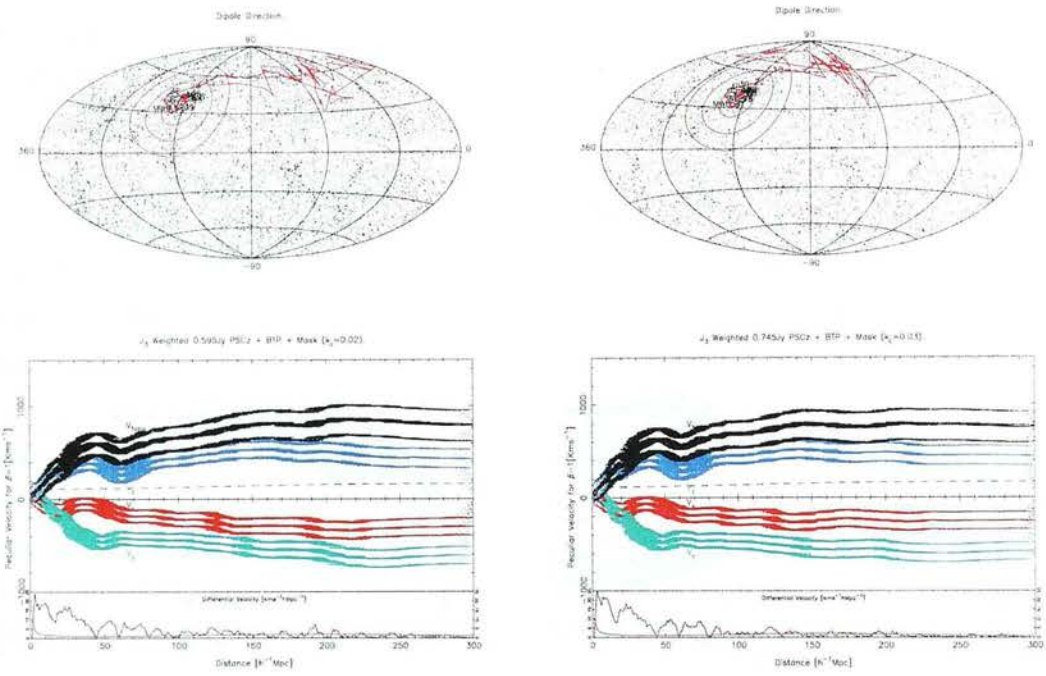

Figure 3.22: *Iterative dipoles calculated for the PSCz + BTP + data with spherical harmonic mask. Left: J_3 weighting was calculated according to equation 3.32 using turnover scale of $k_c = 0.020$. Using this lower value the concentration at $200h^{-1}$Mpc begins to show. This highlights the critical dependence of the dipole on k_c. Right: The flux limit was increased to 0.745Jy with the effect that the dipole direction increased to higher latitude. This is expected given that close to the survey depth, the direction approaches from above and moves to lower latitude with increasing distance.*

J_3, and in doing so, converges reliably to $\beta \simeq 0.65$ (see figure 3.23). When using the minimum variance scheme, convergence to $0.75 < \beta < 0.85$ is consistently achieved. This is not consistent with the other current methods in the literature (see references above and those contained therein). This higher value is a natural consequence of dampening a significant genuine contribution. If the dipole is cut short, the integral in equation 1.32 is underestimated, and so to maintain self-consistency, β is overestimated.

To test for obvious defects in the catalogue, the calculations were performed using a higher flux cut of 0.745Jy at 60μm. Above this flux limit, the catalogue is undoubtedly much more complete. (Tadros *et al.* 1999) give a selection function for the 0.745Jy subset of the PSCz, which was used in replacement of the 0.595Jy function. The right hand side of figure 3.22 shows the dipole calculated for this higher flux limit, but again, the same behaviour is observed, giving first

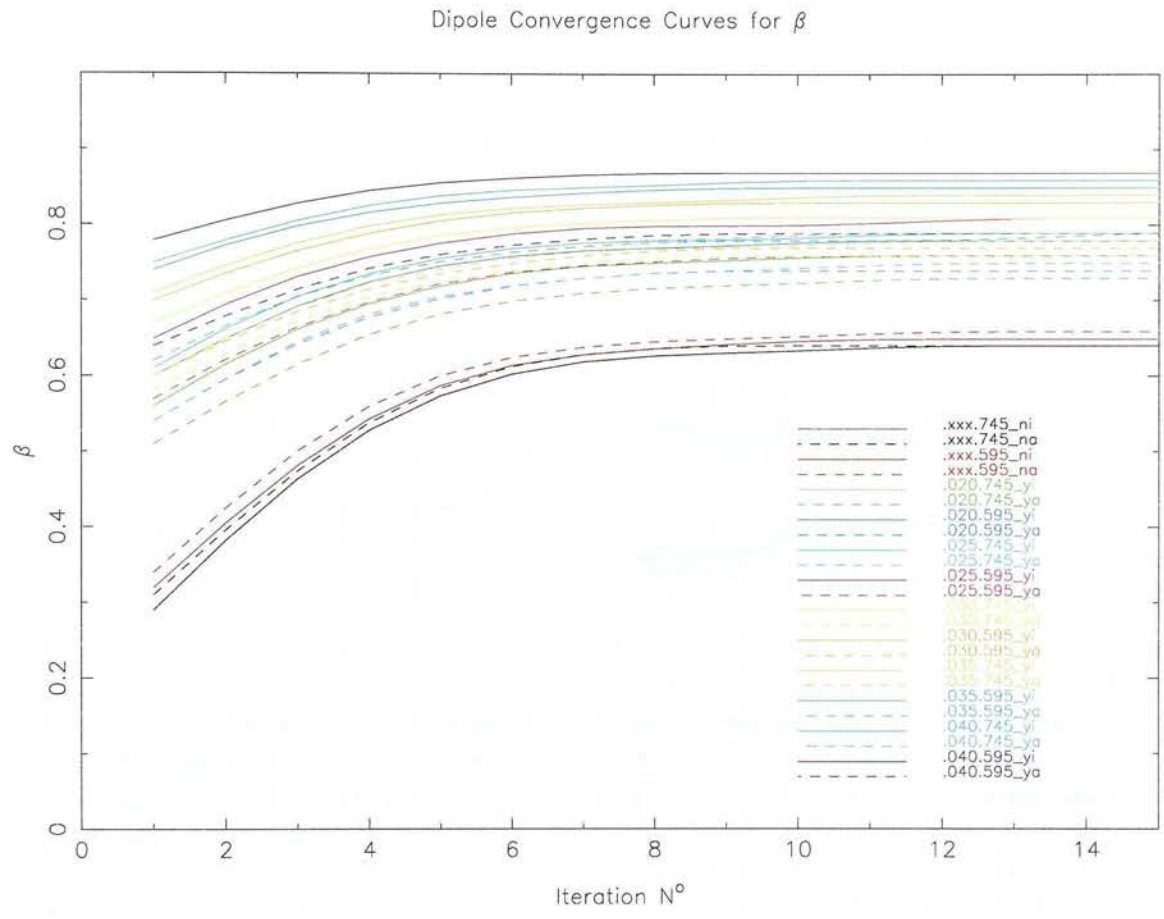

Figure 3.23: *β Convergence of the iterative dipole scheme. Convergence is fast and reliable. Notice that the red and black trials are for dipoles calculated without minimum variance weighting - all other trials employ the weighting. The key labels graphs according to the model parameters, as .k_c.f_{lim}_XX where f_{lim} is the flux limit and XX are the characters y/n (yes/no to minimum variance weighting) and i/a (immediate/adiabatic β introduction).*

indications that it is not an obvious defect in the catalogue.

Finally, the adiabatic introduction of β was explored, as a stability test. Figure 3.24 compares the effect of adiabatically introducing β throughout the course of each iteration, on the 0.595Jy PSCz + BTP dipoles with and without J_3 weighting (for which $k_c = 0.03$). It can be seen that the convergence values of β are robust to this perturbation, although the angular misalignment tends to suffer as previously detailed. Recall that this is predominantly because a large proportion of the dipole is generated at small distances, and this is precisely where the adiabatic technique hinders the proper reaction of the Local Group, and thus the adaptation of the calculation reference frame.

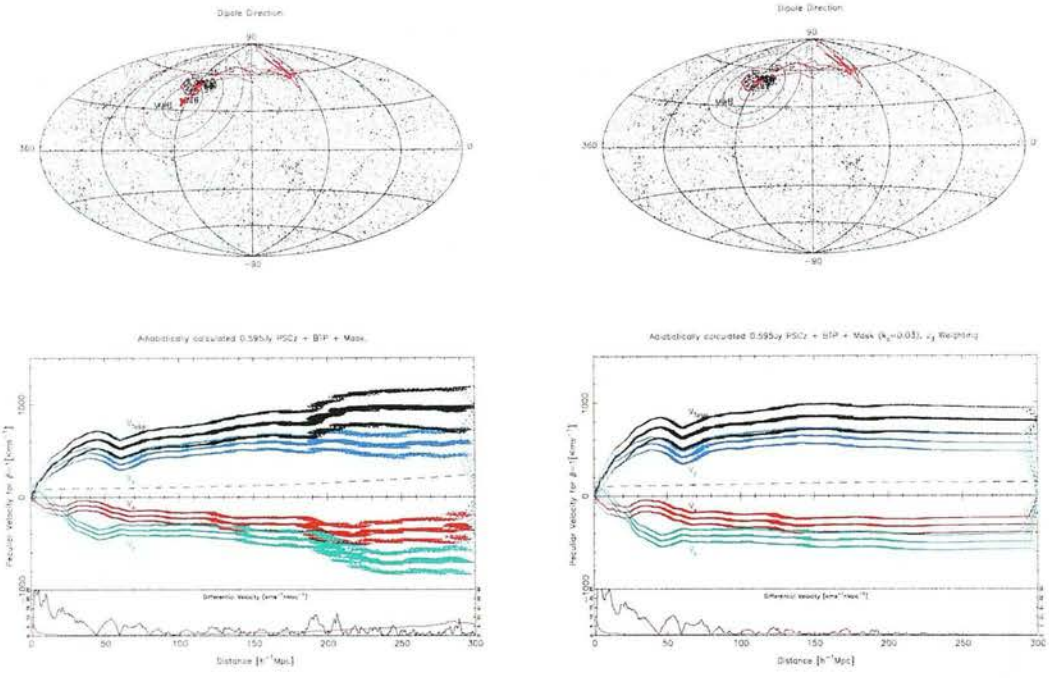

Figure 3.24: *Dipoles calculated on the* $0.595Jy$ *PSCz + BTP and mask, without (left) and with (right)* J_3 *weighting using* $k_c = 0.03$. β *has been introduced adiabatically, as a stability test. This method is curbs the reaction of the Local Group reference frame at small radii, where asymptotic divergence of the frame can occur. This iterative scheme does not suffer badly from this effect, so gradual introduction of* β *during the calculation was found to be unnecessary.* β *convergence is robust in the absence of* J_3 *weighting, but the directional misalignment tends to suffer. In the unweighted dipole, the differential velocity profile indicates peaks at the* 4σ *level around* $200h^{-1}Mpc$.

From table 3.3, it can be seen that all the dipole results converge to approximately $\beta = 0.65$, using an unweighted scheme, and with J_3 weighting, produce significantly higher values. The stability across variation of dataset and initial conditions is a promising feature of the method.

3.4.3 PIZA Dipoles

To address the problems of redshift-space distortions, many have attempted to reconstruct the true real-space positions of galaxies. This is a difficult task but much progress has been made in this area. The PIZA method (Path Interchange Zel'dovich Approximation) is one of the more recent methods to do this. Initially inspired by Croft & Gaztanaga (1997), the method has been extensively developed for application to the PSCz (Valentine, Saunders & Taylor (2000a),

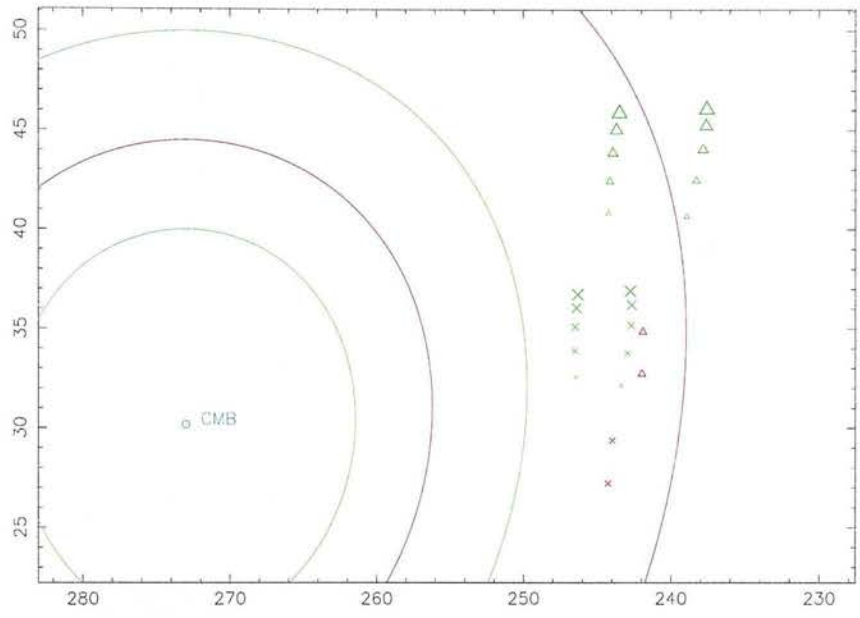

Figure 3.25: *A scatter plot of dipole directions, as quoted in table 3.3. Triangles are dipoles with adiabatically introduced β, and crosses are immediate. Red markers are without the minimum variance weighting scheme, whilst green include it, and have size corresponding to the k_c value used. Bold markers are for the higher flux cut of $0.745Jy$. The associated red and green contours are approximate 1- and 2-σ errors centred on the CMB dipole. Notice the distinct segregation of each category.*

Valentine (2000)). I have been able to calculate real-space dipoles using some PIZA reconstructions of the PSCz and PSCz/BTP kindly supplied by the authors of those works. Three reconstructions were used, one of the PSCz dataset only, and one on both the PSCz and BTP datasets. The specific details of the reconstructions can be found in Valentine (2000). The reconstruction process outputs an estimator of the Local Group dipole, so for comparison, dipoles were recalculated using the method described in section 3.3.1. The results are given here, and can be compared directly to those in the previous two sections. The dipoles calculated upon these data have been non-iterative, because the PIZA reconstruction has already dealt with the effects of redshift-space distortions, eliminating the need for a dipole calculated with a self-consistent set of assumed source distances.

A good feature of the PIZA method is that reconstruction of the velocity field is unaffected in most areas, by the absence of mass in the galactic plane. The reason for this is due to the nature of the PIZA method. PIZA works by minizing a weighted sum of distances between the set of galaxies and a set of randomly dis-

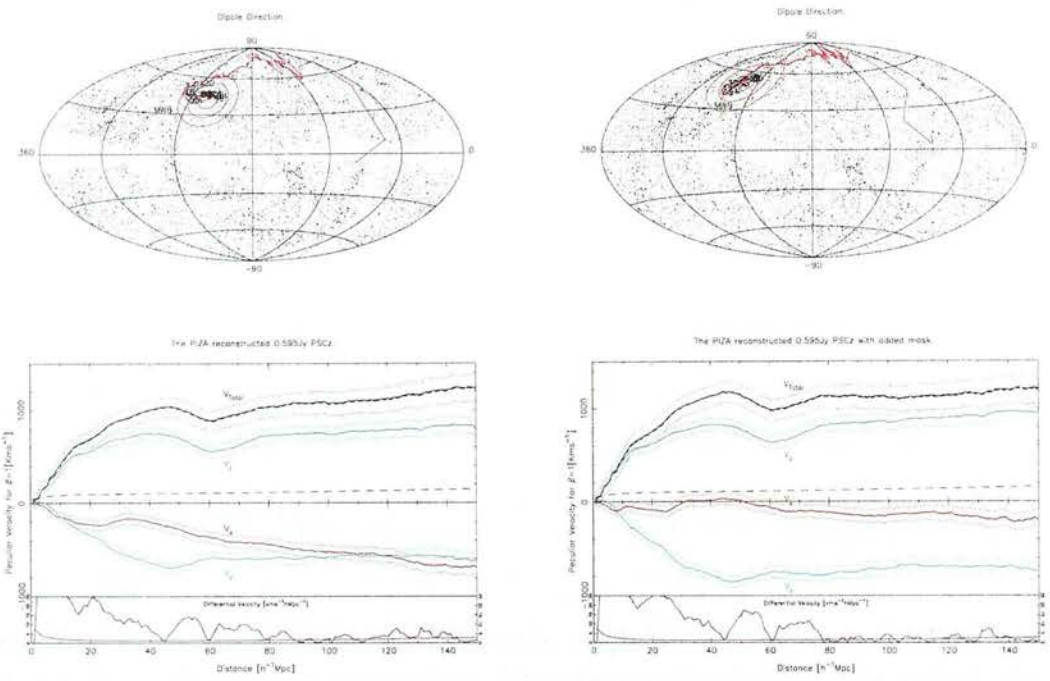

Figure 3.26: *Non-iterative, real-space dipoles calculated on the* $0.595Jy$ *PIZA reconstructed PSCz data. The mask data was added in (right) after the reconstruction process. PIZA reconstruction yields real-space dipoles in directional agreement with the pseudo real-space dipoles produced with the iterative scheme at* $150h^{-1}Mpc$*, although the greater amplitude pushes estimates of* β *down to* $\simeq 0.55 \pm 0.1$.

tributed points. Typically a few random points are assigned to each galaxy and then the assignments are interchanged in pairs until the sum is at a minimum. Crudely speaking, this results in the random points being associated to the most nearby galaxies. The initial points are unclustered, mimicking the initial matter density, and by the principle of least action, represent the equivalent initial Lagrangian position of the galaxy to which they are assigned. Therefore the average vector that can be drawn between the initial points and the host galaxy is representative of the galaxy's true velocity via the gravitational instability formalism in section 1.2.2. A detailed discussion of this process is given in Valentine's thesis work.

The practical implication of this is that a PIZA reconstruction works naturally on local scales. Therefore the bulk of the reconstructed volume is effectively blind to the absence of data in the galactic plane, and only the edges of the mask are adversely affected. Therefore reconstructions with and without the prior inclusion of data within the galactic plane should yield similar dipole results.

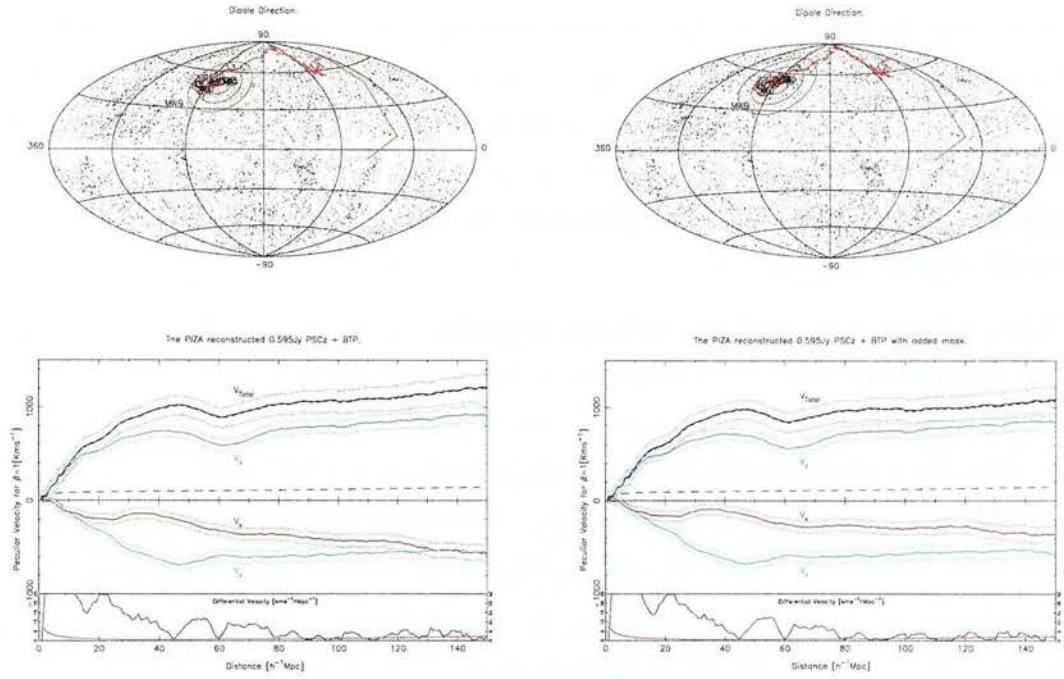

Figure 3.27: *Non-iterative dipoles calculated on the* $0.595Jy$ *PIZA reconstructed PSCz + BTP data + Mask. The mask was added in (right) after the reconstruction process. Again, the dipole direction is at high latitude, in agreement with iterative dipoles at* $150h^{-1}Mpc$*. Shot-noise errors on PIZA calculations are small due to the limited depth of the calculation. However, the misalignment is much greater.*

For exactly the same reasons, the velocity vector attributable to the Local Group particle is defined by its relation to the nearest few random points that are not assigned elsewhere. Therefore most of the dipole generated within PIZA is due to matter in the immediate vicinity, as is indeed the case in reality. Because of this mechanism, it is probable that PIZA generated dipoles do not include significant contributions from greater depths. Valentine (2000) quotes misalignment angles of the dipole of around 15°, but statistical errors on this are large. The main source of statistical error comes from being assigned a finite number of random points from which to determine the Local Group particle's velocity. Typically this number of points used was only of order a few tens, so the Poisson errors from this can therefore be far in excess of 20°.

However, PIZA generated dipoles are in good agreement with the full real-space dipoles calculated on the PIZA data at $cz \simeq 5{,}000\text{kms}^{-1}$ and $\simeq 15{,}000\text{kms}^{-1}$, although the from figures 3.26 and 3.27 they show no signs of settling at larger radii. This is a common feature of the dipoles calculated using PIZA reconstructed data,

and it has been proposed by Saunders/Taylor/Valentine that this could be due to a monopole in the resultant space distribution output by PIZA. The PIZA reconstructions including the mask yield altogether different results, most noticeably, the dipole direction is pushed up to higher latitudes, and the components appear slightly more stable in direction—a consequence of introducing galaxies in the masked region.

Table 3.4 shows the various calculation results. In general the dipole direction is far too high, but this is consistent with the iterative dipole results at $15,000\text{kms}^{-1}$, which only come down to $\simeq +30°$ at about $20,000\text{kms}^{-1}$. Given that the dipole at this depth has not settled completely, a linear theory estimate of β cannot be reliably made from these dipoles alone. While the dipole has not converged to the suspected CMB value, its magnitude cannot be properly normalised.

It is apparent that the agreement between the velocity dipoles as calculated by the above methods is good, but their agreement with the CMB dipole direction—whilst still acceptable—is not so good. The directions and amplitudes both fall into two camps, those that employ the minimum variance weighting, and those that do not. Dipoles calculated without this weighting scheme are all consistently better in alignment, and show a strong peak in the velocity differential. The unweighted dipoles are also in consistently better agreement with current estimates in the literature of β_{IRAS}. The implications of these results are detailed, and point firmly toward the possible existence of a large concentration near the limiting depth of the reliable portion of the PSCz. The resultant consistent misalignment seen in the unweighted dipoles as well as in the dipoles calculated by others in Table 3.2 raises another issue. The agreement between all these dipoles is good, but their agreement with the CMB is somewhat poorer. This points toward a more local problem of Local Group correction, which is independent of the gravitational acceleration analyses and included as an external correction to the calculated Local Group acceleration. As shown in section 3.2.6, incorrect assumptions about the heliocentric to Local Group barycentre velocity correction can lead to large systematic changes in the calculated dipole.

k_c	ϕ_{lim}	J_3	β_{ad}	Mag.	β	Velocity Components	Direction (l, b)	$\Delta\theta$ 1σ	θ_{cmb}
-	0.595	n	n	968.56	0.65	$(-374.1, -775.6, 443.3)$	$(244.25, 27.24)$	12.99	27.92
-	0.595	n	y	955.48	0.66	$(-377.8, -709.0, 517.1)$	$(241.95, 32.77)$	13.47	29.08
-	0.745	n	n	985.17	0.64	$(-376.8, -771.0, 483.7)$	$(243.95, 29.41)$	15.95	27.75
-	0.745	n	y	975.30	0.64	$(-377.0, -705.6, 557.6)$	$(241.88, 34.88)$	15.93	29.06
0.020	0.595	y	n	805.40	0.78	$(-305.7, -609.4, 428.6)$	$(243.36, 32.16)$	11.56	27.93
0.020	0.595	y	y	842.14	0.74	$(-329.6, -547.1, 548.8)$	$(238.93, 40.67)$	10.50	31.79
0.020	0.745	y	n	827.46	0.76	$(-278.6, -639.1, 445.5)$	$(246.44, 32.58)$	12.32	25.31
0.020	0.745	y	y	862.50	0.73	$(-283.8, -587.6, 563.9)$	$(244.22, 40.83)$	11.39	27.88
0.025	0.595	y	n	777.87	0.81	$(-294.2, -575.5, 432.6)$	$(242.92, 33.80)$	11.53	28.22
0.025	0.595	y	y	824.13	0.76	$(-319.7, -516.8, 556.6)$	$(238.26, 42.48)$	10.18	32.57
0.025	0.745	y	n	796.54	0.79	$(-263.4, -606.2, 444.4)$	$(246.51, 33.91)$	12.08	25.24
0.025	0.745	y	y	839.56	0.75	$(-270.5, -557.5, 566.4)$	$(244.12, 42.43)$	10.91	28.34
0.030	0.595	y	n	754.62	0.83	$(-283.0, -547.8, 435.0)$	$(242.68, 35.20)$	11.64	28.41
0.030	0.595	y	y	809.86	0.77	$(-310.1, -492.5, 563.1)$	$(237.81, 44.05)$	9.99	33.19
0.030	0.745	y	n	770.07	0.81	$(-251.4, -577.4, 443.0)$	$(246.47, 35.12)$	12.05	25.31
0.030	0.745	y	y	820.99	0.76	$(-260.2, -531.4, 569.0)$	$(243.91, 43.88)$	10.62	28.90
0.035	0.595	y	n	735.04	0.85	$(-272.5, -526.5, 434.4)$	$(242.64, 36.23)$	11.81	28.48
0.035	0.595	y	y	798.43	0.79	$(-301.3, -474.6, 566.9)$	$(237.60, 45.24)$	9.88	33.60
0.035	0.745	y	n	748.19	0.84	$(-242.3, -554.1, 440.4)$	$(246.38, 36.07)$	12.11	25.46
0.035	0.745	y	y	806.56	0.78	$(-252.8, -510.9, 570.6)$	$(243.67, 45.03)$	10.43	29.44
0.040	0.595	y	n	718.31	0.87	$(-263.1, -510.4, 431.4)$	$(242.73, 36.92)$	12.02	28.45
0.040	0.595	y	y	789.06	0.79	$(-293.5, -461.8, 568.4)$	$(237.56, 46.08)$	9.81	33.83
0.040	0.745	y	n	729.96	0.86	$(-235.1, -535.5, 436.7)$	$(246.29, 36.74)$	12.22	25.60
0.040	0.745	y	y	795.07	0.79	$(-247.3, -495.1, 570.7)$	$(243.46, 45.88)$	10.31	29.87

Table 3.3: *Results from the iterative dipole scheme: All employed successive corrections to the distortion of the surrounding density field due to the growth of relative velocity of the Local Group, and in all cases, this scheme converged within 15 iterations. Those that employed the minimum variance weighting scheme (indicated by $J_3 = y$) were calculated for a range of turnover scales, k_c, of the model power spectrum. $\beta_{ad} = y$ indicates the adiabatic introduction of β within each iteration of the method. A distinct difference can be seen between the results obtained with, and obtained without the minimum variance scheme (this can be seen clearly in figure 3.25). All other variations in the initial conditions do not affect the result in a significant systematic manner.*

Run Description	Mag.	β	Velocity Components	Direction	$\Delta\theta$ 1σ	θ_{cmb}
PSCz only	1236.99	0.51	(-693.44, -621.09, 814.57)	(221.85,41.19)	6.83	44.72
PSCz+mask	1212.35	0.52	(-196.94, -744.19, 936.58)	(255.18,50.58)	7.45	25.81
PSCz+BTP	1211.16	0.52	(-567.57, -570.33, 905.25)	(225.14,48.37)	6.88	42.53
PSCz+BTP+mask	1085.70	0.56	(-373.99, -579.91, 838.20)	(237.18,50.54)	7.87	35.41

Table 3.4: *PIZA reconstruction dipole results. The dipole latitude is consistently too high, but is in agreement with iterative dipole directions at 15,000kms^{-1}.*

Chapter 4

Conclusions

4.1 A Greater Attractor?

The major result of this work is the possible discovery of an unexpectedly large mass concentration beyond the Great Attractor, at approximately $l = 300$, $b = 0$, $cz = 20,000 \mathrm{kms}^{-1}$. There are three main pointers toward this suggestion, namely: 1. the inferred existence of a concentration in the spherical harmonic interpolated maps; 2. the dipolar misalignment caused by adopting a weighting scheme which is only optimal in the event that no unusual structures are present; 3. The weighting dependent convergence of the β parameter gives estimates of β that are inconsistent with those in current literature if this concentration is excluded.

4.1.1 Spherical Harmonic Interpolation

The spherical harmonic maps interpolating across the Galactic plane reveal what could be a larger structure beyond the Great Attractor. This could perhaps be treated on its own as somewhat circumstantial—the harmonic interpolation relies upon the density immediately above and below the plane, and any fluctuations in this could in principle, affect the result. However, upon the appearance of this feature in the maps, heavy suppression was applied to the formation of overestimated peaks due to a sudden rise in source density close to the mask edge, but in spite of this suppression, the peak remained. Whilst the peak is robust to measures taken to reduce it, it is nevertheless difficult to assess its significance at face value. What appears as a 3σ peak in the density field could equally be attributable to extrapolation from the unusually high source density encountered

at the edges of the survey data in this region. The source density in the locality of the concentration is visibly much higher than the mean, as seen in the data itself (figure 2.1), and is especially apparent in the BTP region, where higher extinction levels make the contrast even more significant. Qualitatively, it seems very reasonable that the extended structures seen above and below the plane at $l \simeq 300^\circ$ will be linked across the plane.

4.1.2 Reduction in Dipole Misalignment at 20,000kms^{-1}

Minimum variance weighted dipole components suffer a cut off in additional contribution beyond $\simeq 20,000\text{kms}^{-1}$, which is exactly where a large and significant change in the dipole occurs—a change that reduces the dipolar misalignment by half. This change can be seen clearly in the differential velocity profiles as a 3σ peak at 18,000kms^{-1}. By curbing the influence of the structure at this depth, the dipole is left up at high latitude. As seen before, the minimum variance technique relies on some assumptions about the density field, *i.e.* it is approximately Gaussian, with no unusual features in it. It is precisely this last part that allows it to cut the influence of noisy sparse data at large radii, without worrying too much about the real effect it will have on the dipole; structures at the cut-off distance are not expected to be very influential, as shown in the calculation of cosmic variance. The presence of an unusually large structure at this distance will therefore be regarded as spurious by the weighting scheme, and its influence significantly reduced. In this case, applying the minimum variance weighting scheme has associated with it the corresponding penalties of increased misalignment and inconsistent β convergence.

4.1.3 β Convergence

The minimum variance weighting causes the convergence of β onto a consistently higher value than without the weighting, yielding (with current estimates of the bias parameter) $\Omega_m = 0.4$. This result remains robust under significant variation of the initial conditions and assumptions for the self-consistent dipole calculation, and is in disagreement with majority of current estimates in the literature (Nusser *et al.* (2001) ($\beta = 0.5 \pm 0.1$), Valentine, Saunders & Taylor (2000b) ($\beta \simeq 0.6$), Hamilton, Tegmark & Padmanabhan (2000) ($\beta = 0.41^{+0.13}_{-0.12}$), Tadros *et al.* (1999) ($\beta = 0.47 \pm 0.16$), as detailed in 3.4.1). The mechanism by which this can happen

is simple. By curtailing the contributions of significant structures, the integral in equation 1.32 is systematically underestimated if the influential structure is in the direction of Local Group motion, and overestimated if not. The concentration in question is in the general direction of our motion, and so the integral is underestimated. By normalisation with the Local Group velocity, this forces the prefactor to be overestimated, thus pushing β up to a higher value.

4.1.4 Interpretation of Differential Velocity Profiles

In figures 3.18 through 3.22 the differential velocity profiles of the calculated dipoles collectively indicate an influential structure at around 20,000kms^{-1}. The appearance of this object is subject to the weighting scheme adopted as detailed in section 3.4.1, but in the absence of measures taken to curb it, the peak is significant at the 4σ level, as indicated in the figures. This is a remarkably strong feature and is arguably the last significant structure encountered up to the survey limit. The marked change in dipole direction and amplitude after 20,000kms^{-1} reflects this, and when included gives results in agreement with other analyses as detailed above and in chapter 3.

4.1.5 Probability of Existence

These three features point toward the application of a minimum variance weighting scheme being incorrect in this case, and the implications of this are massive: a structure at this distance that is influential to the degree that the minimum variance scheme severely degrades the dipole result, must be very large. So large in fact, that it could cast doubts on our assumptions of the mass distribution throughout the Universe. To see how probable the existence of such a concentration within our survey volume is, we can calculate the expected number density of objects as a function of their mean overdensity, and characteristic size. We can write

$$nm = P(>\delta)\bar{\rho}, \quad P(>\delta) \equiv G(>\delta|\sigma) \tag{4.1}$$

where m is the mass of the object, and n is the number density of these objects, and $P(>\delta)$ is the probability. If we assume Gaussianity of the density field, then we can express this probability as the integral over a Gaussian tail of width σ, which is in turn defined by the integral over the power spectrum, convolved with

a suitable window function. If we assume a spherical top-hat overdensity, then we get (in Fourier space)

$$\sigma_R = 4\pi \int_k k^2 P(k) \left(\frac{\sin(kR) - kR\cos(kR)}{(kR)^3} \right)^2 \mathrm{d}k \tag{4.2}$$

Once the number density n is known, it is possible to estimate the number of these objects expected to appear in the survey volume. This is simply a Poisson distribution,

$$P(N_{GA} \geq 1) = 1 - e^{-nV_{PSCz}}. \tag{4.3}$$

It is possible to constrain the influence of the concentration by differencing the dipole components before and after encountering the lump (at $180\mathrm{h}^{-1}$Mpc, and 240^{-1}Mpc respectively). The resultant impulse due to the intermediate region is $v_{180-240} = 300\mathrm{kms}^{-1}$, and this in turn, yields a set of δ, σ pairs that satisfy this criterion. Figure 4.1 shows the probability of a concentration capable of that influence at $20{,}000\mathrm{kms}^{-1}$, as a function of concentration size (*ie.* for a given σ); an intrinsically smaller concentration would require a higher mean density. A rough estimate for the size of this object can again, be read from the dipole component plots, and is approximately $60h^{-1}$Mpc across. This implies that the probability of finding this within the survey is $\simeq 10^{-4}$.

4.1.6 Possible Explanations

The calculated probability of this object occurring within the PSCz volume given the assumed power spectrum can be seen to be literally tiny ($\simeq 10^{-4}$), and so we are forced to consider one of three alternatives.

One possibility is that we rather unfortunately live in an region of the Universe unrepresentative of the whole, in which case assumptions of Gaussianity are unjustified and the minimum variance method breaks down. Alternatively, The power spectrum assumed could be wrong: as seen before, it is ill constrained at the large scale end, and there has been debate in the literature of the possibility of spikes or bumps at these large scales (although mostly speculative). Thirdly, there is the possibility of it being an artifact in the data; this is something that has not been fully explored yet, and is beyond the scope of this thesis. However, most initial pointers suggest this to be unlikely.

In an attempt to steer clear of Anthropic arguments, I will discard the first of the above explanations from this discussion. In this case, this concentration

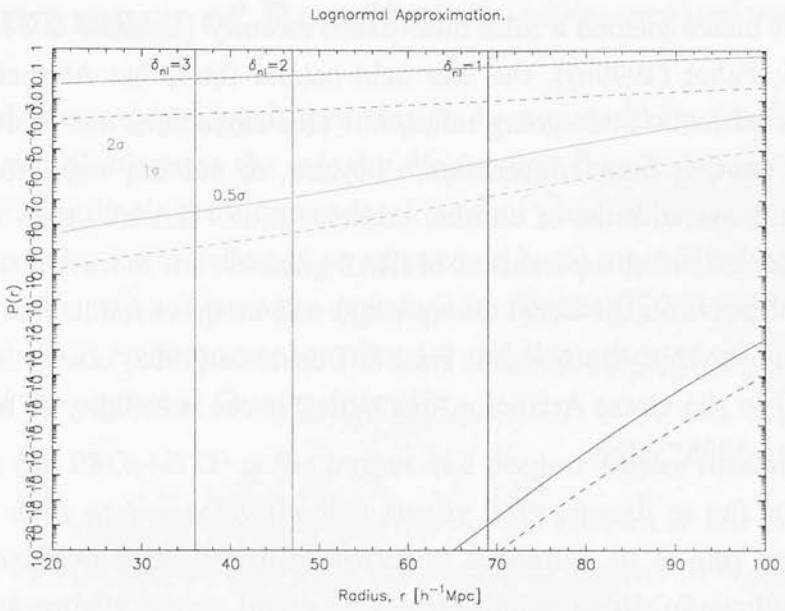

Figure 4.1: *The probability of finding a concentration capable of influencing the dipole by 300kms^{-1} from a distance of 20,000kms^{-1}, as a function of concentration size. Three classes are shown, for $\sigma_{calc} = \{0.5, 1, 2\}\,\sigma$ (red, green, blue). Solid lines are given by equation 4.3, while corresponding dotted lines by equation 4.1. Given an estimated characteristic concentration size of $40 < r < 70h^{-1}Mpc$, this calculation points toward its existence within our survey being not at all likely.*

(hereafter named the *Greater Attractor*) could be bad news for current CDM models, which do not posses enough power on large scales to account for this type of large structure occurring as frequently as would be acceptable for us to see one in our local Universe. As the large scale end of the power spectrum is weakly constrained, this does remain a significant possibility.

Some credence can be given to this argument because of the independence of the results of the spherical harmonic maps and of the dipole normalisation/β determination. In Appendix C, Aitoff projections of PSCz + BTP harmonic decomposition are shown at increasing radii. These feature an extended structure at $l \simeq 300, b = \{-40, 20\}$ beginning at $\simeq$15,000kms^{-1}, and lasting up to the survey limit.

It should be mentioned that the existence of another large concentration directly behind the Great Attractor is not a particularly new idea: in early POTENT days it was unclear if outflow behind the Great Attractor was observed, possibly indicating the presence of a greater concentration behind it. However, there were worries about the validity of this result, incase the inaccurate treatment of

Malmquist biases yielded a false flow. More recently (Dressler & Faber (1990a), Dressler & Faber (1990b)), the flow field behind the Great Attractor has been demonstrated to be undergoing infall, but this alone does not exclude the possibility of another mass concentration beyond, or put any tight constraints on the physical size or mass of another concentration. Indeed, Allen *et al.* (1990) mentions an extended supercluster of IRAS galaxies, but indicated that its gravitational influence on the Local Group could well be quite small. But there is still contention over this, Mathewson, Ford & Buchhorn (1992) claims no detectable back infall to the Great Attractor, but indicates the possibility of bulk flows on scales up to $130h^{-1}$Mpc.

4.2 Residual Misalignment of the Dipole

The application of a minimum variance weighting scheme was seen to significantly impair the directional alignment of the dipole. However, even in the absence of this weighting scheme, the dipole remains at lower galactic *longitude* than can be attributed to survey sampling noise, and cosmic variance. This is also the case with previous attempts to calculate the dipole (Table 3.2). The misalignment with the CMB is significant, but agreement between different results is good. This points toward incorrect assumptions about correction applied to compensate for the relative motion of the helocentric reference frame, and that of the Local Group barycentre. As shown in section 3.2.6, this has a large systematic effect on the dipole. It is possible that previous analyses of the Local Group correction have been based on an incomplete list of group members. The seminal analysis of Yahil, Tammann & Sandage (1977), and of more recent analyses using the same candidate list (*e.g.* Rauzy & Gurzadyan (1998)) are in good agreement with eachother, indicating a certain reliability in their determination. However, if the list of Local Group members is incomplete, then there may be unaccounted dynamical influences in these analyses. The BTP uncovered a number of objects at effectively zero redshift, as can be expected for a survey across 9% of the sky. They are not confirmed to be Local Group galaxies, although this is a matter to be resolved in future work. It is not impossible that these may be dynamically significant and therefore have bearing on the systematic misalignment of almost all Local Group acceleration analyses to date.

4.3 Summary of Results

This remarkable agreement indicates that we have most likely accounted for all the major contributions to the velocity dipole, and that it is possible that we have reached the dipole convergence depth beyond which things may not change. That said, we also see the effect of an what could be an unusually large structure which, if correct, will not be easily explained by current CDM models. We seem to have arrived at an inconsistency of sorts, and this raises questions regarding existence of the suspected Greater Attractor.

Given that the PSCz+BTP is the largest and deepest all-sky redshift survey of its kind to date, and possibly the first survey large enough to put strong limits upon a maximum scale length of structure formation, it is also possible that it could put equally strong limits on the maximum depth of significant dipole contributions. The assumption of having reached the dipole's final convergence depth is crucial, and any inference of β and/or Ω_m is reliant on this. A debate still continues in the literature as to whether the maximum scale of structure formation had been determined; Pietronero & Sylos Labini (2001) continue to suggest that the galaxy distribution is inhomogeneous on very large scales, while recent multifractal analysis of the PSCz by Pan & Coles (2000) yields a promising determination of a maximum scale.

The implications this holds for the Greater Attractor are serious. There is still the issue of this being an artifact in the data, but if so, estimates of Ω_m become inconsistent. Perhaps the Greater Attractor is just a very rare occurrence, and we're a little (un?)lucky. This thesis has raised more questions than it has provided answers to, and this issue is certainly worthy of future investigation. Future work in resolving this matter more fully would initially involve targeted statistical testing of the PSCz + BTP datasets in the Greater Attractor region, to quantify the reliability of the data, and if reliable, then possible follow up observations to probe the region more carefully could prove useful, perhaps in a manner similar to that applied to the Great Attractor.

Acknowledgments

The Digitized Sky Surveys were produced at the Space Telescope Science Institute under U.S. Government grant NAG W-2166. The images of these surveys are based on photographic data obtained using the Oschin Schmidt Telescope on Palomar Mountain and the UK Schmidt Telescope. The plates were processed into the present compressed digital form with the permission of these institutions.

The National Geographic Society - Palomar Observatory Sky Atlas (POSS-I) was made by the California Institute of Technology with grants from the National Geographic Society.

The Second Palomar Observatory Sky Survey (POSS-II) was made by the California Institute of Technology with funds from the National Science Foundation, the National Geographic Society, the Sloan Foundation, the Samuel Oschin Foundation, and the Eastman Kodak Corporation.

The Oschin Schmidt Telescope is operated by the California Institute of Technology and Palomar Observatory.

The UK Schmidt Telescope was operated by the Royal Observatory Edinburgh, with funding from the UK Science and Engineering Research Council (later the UK Particle Physics and Astronomy Research Council), until 1988 June, and thereafter by the Anglo-Australian Observatory. The blue plates of the southern Sky Atlas and its Equatorial Extension (together known as the SERC-J), as well as the Equatorial Red (ER), and the Second Epoch [red] Survey (SES) were all taken with the UK Schmidt.

Bibliography

Adler R. J., 1981. *The Geometry of Random Fields*, The Geometry of Random Fields, Chichester: Wiley, 1981.

Allen D. A., Staveley-Smith L., Meadows V. S., Roche P. F., Norris R. P., 1990. *Nature*, **343**, 45+.

Barnes J., 1993. *NOAO IRAF Documentation*, .

Barnes D. G., 1998. In: *ASP Conf. Ser. 145: Astronomical Data Analysis Software and Systems VII*, 32+.

Beacom J. F., Boyd R. N., Mezzacappa A., 2000. *Physical Review Letters*, **85**, 3568.

Beichmann C. A., 1985. *Infrared Astronomical Satellite (IRAS) catalogs and atlases. Explanatory supplement*, Pasadena: Jet Propulsion Laboratory, 1985, edited by Beichmann, C.A.

Coles P., Jones B., 1991. *Monthly Notices of the Royal Astronomical Society*, **248**, 1.

Coles P. C., Sahni V., 1996. *The Observatory*, **116**, 25.

Condon J. J., Anderson M. L., Helou G., 1991. *Astrophysical Journal*, **376**, 95.

Condon J. J., Cotton W. D., Greisen E. W., Yin Q. F., Perley R. A., Taylor G. B., Broderick J. J., 1998. *Astronomical Journal*, **115**, 1693.

Croes G. A., 1993. In: *ASP Conf. Ser. 52: Astronomical Data Analysis Software and Systems II*, 156+.

Croft R. A. C., Gaztanaga E., 1997. *Monthly Notices of the Royal Astronomical Society*, **285**, 793.

Davis M., Huchra J., 1982. *Astrophysical Journal*, **254**, 437.

Djorgovski S., Lasker B. M., Weir W. N., Postman M., Reid I. N., Laidler V. G., 1992. In: *American Astronomical Society Meeting*, 1307+.

Dressler A., Faber S. M., 1990. *Astrophysical Journal*, **354**, 13.

Dressler A., Faber S. M., 1990. *Astrophysical Journal, Letters*, **354**, L45.

Fukuda Y., and Collaborators, 1998. *Physical Review Letters*, **81**, 1562.

Glendenning B. E., 1996. In: *ASP Conf. Ser. 101: Astronomical Data Analysis Software and Systems V*, 271+.

Hamilton A. J. S., Tegmark M., Padmanabhan N., 2000. *Monthly Notices of the Royal Astronomical Society*, **317**, L23.

Hamilton A. J. S., 1998. In: *ASSL Vol. 231: The Evolving Universe*, 185+.

Harmon R. T., Lahav O., Meurs E. J. A., 1987. *Monthly Notices of the Royal Astronomical Society*, **228**, 5P.

Horne K., 1986. *Publications of the ASP*, **98**, 609.

Huchra J., Tollestrup E., Schneider S., Skrutski M., Jarrett T., Chester T., Cutri R., 1998. *Highlights in Astronomy*, **11**, 487+.

Huchra J. P., Geller M. J., Corwin H. G., 1995. *Astrophysical Journal, Supplement*, **99**, 391+.

Huchra J. P., Vogeley M. S., Geller M. J., 1999. *Astrophysical Journal, Supplement*, **121**, 287.

Huchra J. P., 2000. In: *ASP Conf. Ser. 201: Cosmic Flows Workshop*, 96+.

Joint IRAS Science Working Group, 1988. In: *IRAS Point Source Catalog (1988)*, 0+.

Kaiser N., Lahav O., 1989. *Monthly Notices of the Royal Astronomical Society*, **237**, 129.

Kaiser N., 1987. *Monthly Notices of the Royal Astronomical Society*, **227**, 1.

Kolb E. W., Turner M. S., 1990. *The early universe*, Frontiers in Physics, Reading, MA: Addison-Wesley, 1988, 1990.

Lahav O., Fisher K. B., Hoffman Y., Scharf C. A., Zaroubi S., 1994. *Astrophysical Journal, Letters*, **423**, L93.

Lahav O., Lynden-Bell D., Rowan-Robinson M., 1988. *Monthly Notices of the Royal Astronomical Society*, **234**, 677.

Lahav O., 1987. *Monthly Notices of the Royal Astronomical Society*, **225**, 213.

Lahav O., 1991. In: *AIP Conf. Proc. 222: After the first three minutes*, p. 421.

Lawrence A., Rowan-Robinson M., Ellis R. S., Frenk C. S., Efstathiou G., Kaiser N., Saunders W., Parry I. R., Xiaoyang X., Crawford J., 1999. *Monthly Notices of the Royal Astronomical Society*, **308**, 897.

Lynden-Bell D., Lahav O., Burstein D., 1989. *Monthly Notices of the Royal Astronomical Society*, **241**, 325.

Marsh T. R., 1989. *Publications of the ASP*, **101**, 1032.

Massey P., Valdes F., Barnes J., 1992. *NOAO IRAF Documentation*, .

Massey P., 1997. *NOAO IRAF Documentation*, .

Mathewson D. S., Ford V. L., Buchhorn M., 1992. *Astrophysical Journal, Letters*, **389**, L5.

Meiksin A., Davis M., 1986. *Astronomical Journal*, **91**, 191.

Nusser A., da Costa L. N., Branchini E., Bernardi M., Alonso M. V., Wegner G., Willmer C. N. A., Pellegrini P. S., 2001. *Monthly Notices of the Royal Astronomical Society*, **320**, L21.

Pan J., Coles P., 2000. *Monthly Notices of the Royal Astronomical Society*, **318**, L51.

Peebles P. J. E., 1993. *Principles of Physical Cosmology*, Princeton Univesity Press.

Pellegrini P. S., da Costa L. N., 1990. *Astrophysical Journal*, **357**, 408.

Penzias A. A., Wilson R. W., 1965. *Astrophysical Journal*, **142**, 419.

Pietronero L., Sylos Labini F., 2001. In: *Current Topics in Astrofundamental Physics: the Cosmic Microwave Background*, 391+.

Rauzy S., Gurzadyan V. G., 1998. *Monthly Notices of the Royal Astronomical Society*, **298**, 114.

Rowan-Robinson M., Lawrence A., Saunders W., Crawford J., Ellis R., Frenk C. S., Parry I., Xiaoyang X., Allington-Smith J., Efstathiou G., Kaiser N.,

1990. *Monthly Notices of the Royal Astronomical Society*, **247**, 1+.

Rowan-Robinson M., Sharpe J., Oliver S. J., Keeble O., Canavezes A., Saunders W., Taylor A. N., Valentine H., Frenk C. S., Efstathiou G. P., McMahon R. G., White S. D. M., Sutherland W., Tadros H., Maddox S., 2000. *Monthly Notices of the Royal Astronomical Society*, **314**, 375.

Sachs R. K., Wolfe A. M., 1967. *Astrophysical Journal*, **147**, 73+.

Sandage A., Tammann G. A., van den Bergh S., 1981. *Journal of the Royal Astronomical Society of Canada*, **75**, 267+.

Saunders W., Ballinger W. E., 2000. In: *ASP Conf. Ser. 218: Mapping the Hidden Universe: The Universe behind the Mily Way - The Universe in HI*, 181+.

Saunders W., Collaborators, 2000. In: *ASP Conf. Ser. 201: Cosmic Flows Workshop*, 228+.

Saunders W., D'Mellow K., Tully R. B., Mobasher B., Maddox S., Sutherland W., Carrasco E., Clements D., Staveley-Smith L., 2000a. In: *ASP Conf. Ser. 201: Cosmic Flows Workshop*, 237+.

Saunders W., D'Mellow K., Tully R. B., Mobasher B., Maddox S., Sutherland W., Carrasco E., Clements D., Staveley-Smith L., 2000b. In: *ASP Conf. Ser. 201: Cosmic Flows Workshop*, 237+.

Saunders W., Sutherland W. J., Maddox S. J., Keeble O., Oliver S. J., Rowan-Robinson M., McMahon R. G., Efstathiou G. P., Tadros H., White S. D. M., Frenk C. S., Carramiñana A., Hawkins M. R. S., 2000. *Monthly Notices of the Royal Astronomical Society*, **317**, 55.

Saunders W., Sutherland W. J., Maddox S. J., Keeble O., Oliver S. J., Rowan-Robinson M., McMahon R. G., Efstathiou G. P., Tadros H., White S. D. M., Frenk C. S., Carramiñana A., Hawkins M. R. S., 2000. *Monthly Notices of the Royal Astronomical Society*, **317**, 55.

Schmoldt I., Branchini E., Teodoro L., Efstathiou G., Frenk C. S., Keeble O., McMahon R., Maddox S., Oliver S., Rowan-Robinson M., Saunders W., Sutherland W., Tadros H., White S. D. M., 1999. *Monthly Notices of the Royal Astronomical Society*, **304**, 893.

Schweizer F., van Gorkom J. H., Seitzer P., 1989. *Astrophysical Journal*, **338**, 770.

Skrutskie M. F., Beichman C., Capps R., Carpenter J., Chester T., Cutri R., Elias J., Elston R., Huchra J., Liebert J., Lonsdale C., Monet D., Price S., Schneider S., Seitzer P., Stiening R., Strom S., Weinberg M., 1995. *American Astronomical Society Meeting*, **27**, 1392+.

Slipher V. M., 1917. *The Observatory*, **40**, 304.

Smoot G. F., Bennett C. L., Kogut A., Wright E. L., Aymon J., Boggess N. W., Cheng E. S., de Amici G., Gulkis S., Hauser M. G., Hinshaw G., Jackson P. D., Janssen M., Kaita E., Kelsall T., Keegstra P., Lineweaver C., Loewenstein K., Lubin P., Mather J., Meyer S. S., Moseley S. H., Murdock T., Rokke L., Silverberg R. F., Tenorio L., Weiss R., Wilkinson D. T., 1992. *Astrophysical Journal, Letters*, **396**, L1.

Staveley-Smith L., Wilson W. E., Bird T. S., Disney M. J., Ekers R. D., Freeman K. C., Haynes R. F., Sinclair M. W., Vaile R. A., Webster R. L., Wright A. E., 1996. *Publications of the Astronomical Society of Australia*, **13**, 243.

Staveley-Smith L., 1985. *PhD thesis*, Ph D thesis, University of Manchester, (1985).

Staveley-Smith L., 2000. In: *Imaging at Radio through Submillimeter Wavelengths. Edited by Jeff Mangum. Publisher: The Astronomical Society of the Pacific, Conference Series, 2000. The conference was held June 6-8, 1999, in Tucson, Arizona.*, p. E64.

Strauss M. A., Yahil A., Davis M., Huchra J. P., Fisher K., 1992. *Astrophysical Journal*, **397**, 395.

Tadros H., Ballinger W. E., Taylor A. N., Heavens A. F., Efstathiou G., Saunders W., Frenk C. S., Keeble O., McMahon R., Maddox S. J., Oliver S., Rowan-Robinson M., Sutherland W. J., White S. D. M., 1999. *Monthly Notices of the Royal Astronomical Society*, **305**, 527.

Taylor A., Valentine H., 1999. *Monthly Notices of the Royal Astronomical Society*, **306**, 491.

Tody D., 1986. *Proceedings of the SPIE*, **627**, 733+.

Tody D., 1993. In: *ASP Conf. Ser. 52: Astronomical Data Analysis Software and Systems II*, 173+.

Valentine H., Saunders W., Taylor A., 2000. *Monthly Notices of the Royal Astronomical Society*, **319**, L13.

Valentine H. E. M., Saunders W., Taylor A., 2000b. In: *ASP Conf. Ser. 201: Cosmic Flows Workshop*, 246+.

Valentine H., 2000. *PhD thesis*, Ph D thesis, University of Edinburgh, (2000).

van Albada T. S., Bahcall J. N., Begeman K., Sancisi R., 1985. *Astrophysical Journal*, **295**, 305.

van de Weygaert R., Hoffman Y., 1999. In: *Evolution of Large Scale Structure : From Recombination to Garching*, 178+.

Villumsen J. V., Strauss M. A., 1987. *Astrophysical Journal*, **322**, 37.

Weinberg S., 1972. *Gravitation and cosmology: Principles and applications of the general theory of relativity*, New York: Wiley, —c1972.

Wouterloot J. G. A., Brand J., 1989. *Astronomy and Astrophysics, Supplement*, **80**, 149.

Yahil A., Tammann G. A., Sandage A., 1977. *Astrophysical Journal*, **217**, 903.

Yahil A., Walker D., Rowan-Robinson M., 1986. *Astrophysical Journal, Letters*, **301**, L1.

Appendix A

Probability of Detecting a 'Super-Lump' in the PSCz.

Let's start with the standard definitions given in Chapter 1 for the density and overdensity fields:

$$\rho = \bar{\rho}\,(1+\delta)\,, \quad \delta_g = b\delta \tag{A.1}$$

We can inquire about the total mass of this object: we know its influence ($300\mathrm{kms}^{-1}$), and its distance from us ($200h^{-1}\mathrm{Mpc}$), so

$$v_{LG} = \frac{H_0\beta}{4\pi}\int_{Vol}\frac{\delta\,(\mathbf{r})}{r^2}\mathrm{d}V = 300 \tag{A.2}$$

The volume integral collapses to a sphere at constant distance (in the distant observer limit). Therefore we find

$$300 = \frac{4\pi}{3}.200^3\frac{\delta H_0\beta}{4\pi}, \tag{A.3}$$

so explicitly for δ,

$$\delta = 36,000\beta^{-1}r^{-3}. \tag{A.4}$$

Now, the fraction of mass in the Universe due to these objects is

$$nm = \bar{\rho}\mathrm{P}(>\delta|\sigma(r)) \tag{A.5}$$

where n is the number density of these objects, m is the object mass, and $\mathrm{P}(>\delta|\sigma)$ is the one point probability distribution, given the variance of the field on smoothing scale r. The actual calculation of $\sigma(r)$ is easiest in Fourier space, but convolving with a suitable real space smoothing profile (a spherical top hat is simple

but adequate). The second moment of a scalar field is

$$\begin{aligned}\sigma^2 &= \left\langle \delta(r) - \bar{\delta} \right\rangle^2 \\ &= \left\langle \delta^2 \right\rangle - \left\langle \delta \right\rangle^2 \\ &= \int_V \delta^2(r) - 0 \mathrm{d}V \quad \text{(by the Ergodic Hypothesis)} \end{aligned} \tag{A.6}$$

which when put into Fourier space, becomes

$$\sigma^2(r) = \int_k k^2 P(k) \frac{j_1^2(kR)}{2\pi k^3} \mathrm{d}^3 k. \tag{A.7}$$

This becomes a simple integral over the power spectrum, $P(k)$, which can be done simply using a parameterisation for the form of $P(k)$.

There are now two avenues to choose to follow. In the Linear Approximation (*i.e.* for large r, $\sigma(r) \ll 1$) one can approximate $P(\delta)$ to a Gaussian:

$$\mathrm{P}(> \delta | \sigma(r)) \equiv \int_r^\infty G_{\sigma(r)}(\delta') \mathrm{d}\delta' \tag{A.8}$$

In this case, numerical integration of the Gaussian tail is a simple matter. However, in pushing to smaller scales can be done with the aid of the lognormal non-linear approximation, which is simply a transformation applied to non-linear quantities such that the resultant transformed quantity is Gaussian distributed. The lognormal approximation also preserves the one-point probability distribution function. The transformation for the density field is

$$\begin{aligned}\delta_{NL} &= \exp^{\left(\delta_L - \frac{1}{2}\sigma_L^2(r)\right)} - 1 \\ \delta_L &= \log\left(\delta_{NL} + 1\right) + \frac{1}{2}\sigma_L^2(r), \end{aligned} \tag{A.9}$$

where the variance changes as

$$\begin{aligned}\sigma_{NL}^2(r) &= \exp^{\left(\sigma_L^2(r)\right)} - 1 \\ \sigma_L^2(r) &= \log\left(1 + \sigma_{NL}^2(r)\right). \end{aligned} \tag{A.10}$$

These transformations are given in Coles & Jones (1991), Coles & Sahni (1996), and (esp. for δ) are quite straightforward. Now, a similar numerical integral can be done on the Gaussian distributed linearised field, δ_L, to yield an estimator for the non-linear probability, $\mathrm{P}(> \delta_N L | \sigma(r))$.

Once a probability is calculated, we can get a number density for these objects. We have,

$$\mathrm{P}\left((> \delta | \sigma(r)\right) = n V_{SL} \tag{A.11}$$

where V_{SL} is the object size ($= 4\pi/3r^3$). The expected number N of objects appearing in the survey volume V_{PSCz}, can now be calculated:

$$n = \frac{N}{V_{PSCz}} \tag{A.12}$$

Finally the probability of finding one object within V_{PSCz} can be taken from the Poisson Distribution (as this is now a discrete event), with $\sigma = \mu = N$:

$$\mathrm{Po}_\lambda(x) = \frac{\lambda^x \exp^{-\lambda}}{x!}. \tag{A.13}$$

This can be calculated directly, with $\mathrm{Po}_N(1)$, or by subtraction from a null result, $\mathrm{Po}_N(0)$. The final expression is therefore

$$\mathrm{Po}_N(1) = N \exp^{-N} \equiv 1 - \exp^{-N}, \quad N = \frac{\mathrm{P}\,(> \delta|\sigma(r))\, V_{PSCz}}{V_{SL}} \tag{A.14}$$

One note to be made is that the size of this object has been left as a free parameter, but from the variation in dipole components at this distance, a crude estimate of 50 - 70 h^{-1}Mpc seems to be about right. Given the mass constraint, this gives an overdensity δ of about 3, and therefore the lognormal approximation certainly is needed in this case.

Appendix B

Near Infrared Flatfielding Scripts

The two IRAF scripts developed for flatfielding as described in section 2.4.2 are presented. The first of these two scripts performs the majority of the work in constructing the flatfield, leaving the second to renormalize the flatfield, such that the image median is unity. Both parameter files are also presented, which supply IRAF with the correct input/output format for the image data and option variables.

Flatfielding Script 1: *flatfield1.cl*

```
procedure flatfield1 ()

begin

noao.twodspec

noao.twodspec.longslit

noao.twodspec.apextract

noao.twodspec.longslit.onedspec

print ("..bias frame..")

imcombine (zeroes, bias, combine="median", scale="none", zero="none",

weight="none", lthresh=INDEF, hthresh=INDEF, nlow=1, nhigh=1,

nkeep=1, mclip=yes, lsigma=3., hsigma=3.)

print ("..bias subtract..")

imarith (objlist, "-", bias, objlist//"//z")

imarith (flats, "-", bias, flats//"//z")

print ("..twilight frame..")

imcombine (flats//"//z"//section, "twisky.fits", combine="median",

scale="median", zero="none", weight="none", lthresh=INDEF,

hthresh=INDEF, nlow=1, nhigh=1, nkeep=1, mclip=yes,

lsigma=3., hsigma=3.)

print ("..spatial median filter..")

median ("twisky.fits", "twimed.fits", xwindow = xwin1,

ywindow = ywin1, boundary = bound1)

print ("..boxcar dispersion..")

boxcar ("twimed.fits", "twimedmed.fits", xwindow = xwin2,

ywindow = ywin2, boundary = "wrap")

print ("..sflat..")

imarith ("twimedmed.fits", "/", "twimed.fits", "medmed_on_med.fits")

imarith ("twisky.fits","*","medmed_on_med.fits", sflat)

print ("..display..")

display (sflat, frame=1)

print ("..now normalise sflat with midpt..")

imstat (sflat, fields="midpt")

end
```

Flatfielding Script 2: *flatfield1.cl*

```
procedure flatfield2 ()

begin

noao.twodspec

noao.twodspec.longslit

noao.twodspec.apextract

noao.twodspec.longslit.onedspec

print ("..renormalizing..")

imarith (sflat, "/", sflatnorm, "n//"//sflat)

imstat (sflat)

imstat ("n//"//sflat)

print ("..flatfield..")

imarith (objlist//"//z"//section, "/", "n//"//sflat, objlist//"//zf")

end
```

Parameter file 1: *flatfield1.par*

```
objlist,s,a,"@objlist",,,"Object frame(s)"

flats,s,a,"@sflist",,,"Skyflat frame(s)"

sflat,f,a,"sflat.fits",,,"Resultant skyflat frame"

zeroes,s,a,"@zlist",,,"Zero frame(s)"

bias,f,a,"bias.fits",,,"Resultant bias frame"

section,s,h,"[*,*]",,,"Section to use for processing"

xwin1,i,a,1,,,"X window size of median filter"

ywin1,i,a,41,,,"Y window size of median filter"

bound1,s,a,"reflect",,,"Boundary (constant,nearest,reflect,wrap)"

xwin2,i,a,1190,,,"X dimension of boxcar (1 or length of dispersion axis)"

ywin2,i,a,1,,,"Y dimension of boxcar (1 or length of dispersion axis)"
```

Parameter file 2: *flatfield2.par*

```
objlist,s,a,"@objlist",,,"Object frame(s)"

sflat,f,a,"sflat.fits",,,"Resultant skyflat frame"

sflatnorm,r,a,,,,"sflat normalisation"

section,s,h,"[*,*]",,,"Section to use for processing"
```

Appendix C

Spherical Harmonic Maps of the PSCz

Presented are a set of density maps in concentric shells of increasing radii out to the survey limit (Saunders & Collaborators 2000). These "onion skin" shells were constructed from using spherical harmonics and spherical Bessel functions applied to the the PSCz + BTP surveys. The extension of the harmonic modes across the galactic plane provides an estimator of the density in the unmapped regions. The angular resolution is varied as a function of radius to optimally depict structures within the data.

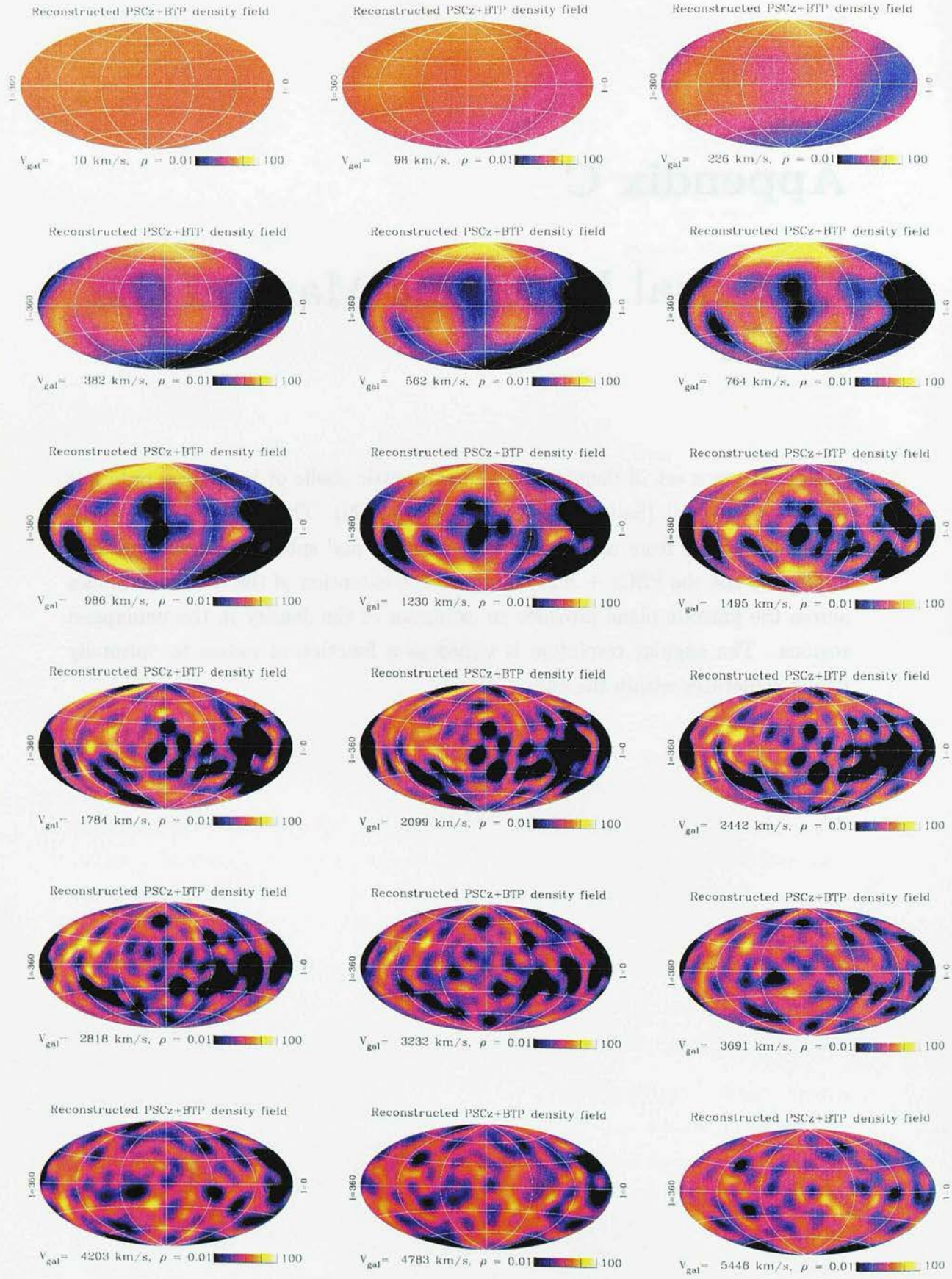
Reconstructed PSCz+BTP density field
l=360
l=0
V_{gal}= 10 km/s, ρ = 0.01
100
Reconstructed PSCz+BTP density field
l=360
l=0
V_{gal}= 98 km/s, ρ = 0.01
100
Reconstructed PSCz+BTP density field
l=360
l=0
V_{gal}= 226 km/s, ρ = 0.01
100
Reconstructed PSCz+BTP density field
l=360
l=0
V_{gal}= 382 km/s, ρ = 0.01
100
Reconstructed PSCz+BTP density field
l=360
l=0
V_{gal}= 562 km/s, ρ = 0.01
100
Reconstructed PSCz+BTP density field
l=360
l=0
V_{gal}= 764 km/s, ρ = 0.01
100
Reconstructed PSCz+BTP density field
l=360
l=0
V_{gal}= 986 km/s, ρ = 0.01
100
Reconstructed PSCz+BTP density field
l=360
l=0
V_{gal}= 1230 km/s, ρ = 0.01
100
Reconstructed PSCz+BTP density field
l=360
l=0
V_{gal}= 1495 km/s, ρ = 0.01
100
Reconstructed PSCz+BTP density field
l=360
l=0
V_{gal}= 1784 km/s, ρ = 0.01
100
Reconstructed PSCz+BTP density field
l=360
l=0
V_{gal}= 2099 km/s, ρ = 0.01
100
Reconstructed PSCz+BTP density field
l=360
l=0
V_{gal}= 2442 km/s, ρ = 0.01
100
Reconstructed PSCz+BTP density field
l=360
l=0
V_{gal}= 2818 km/s, ρ = 0.01
100
Reconstructed PSCz+BTP density field
l=360
l=0
V_{gal}= 3232 km/s, ρ = 0.01
100
Reconstructed PSCz+BTP density field
l=360
l=0
V_{gal}= 3691 km/s, ρ = 0.01
100
Reconstructed PSCz+BTP density field
l=360
l=0
V_{gal}= 4203 km/s, ρ = 0.01
100
Reconstructed PSCz+BTP density field
l=360
l=0
V_{gal}= 4783 km/s, ρ = 0.01
100
Reconstructed PSCz+BTP density field
l=360
l=0
V_{gal}= 5446 km/s, ρ = 0.01
100

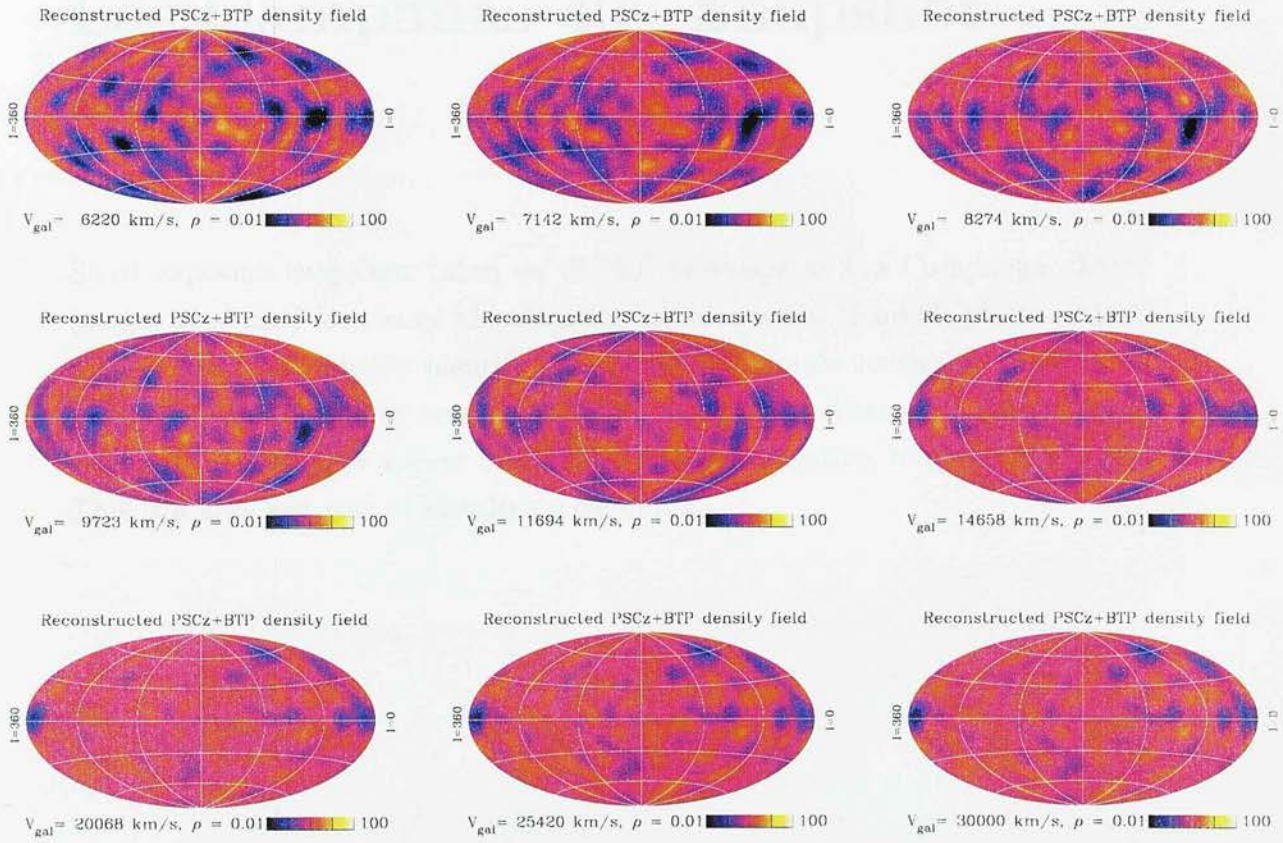

Figure C.1: *Spherical harmonic decomposition of the PSCz + BTP, interpolated across the plane. Each map represents an 'Onion skin' of increasing redshift slices.*

Appendix D

Las Campanas 40" Snapshot Data.

Short exposure snapshots taken on the 40" telescope at Las Campanas. These images were used for source identification in cases where Schmidt plates or DSS images could not reliably identify the candidate. Simple successive subtraction of image frames from one another serves as a quick reduction. As a consequence, features in the images appear in both positive and negative, but shifted slightly. This is a very fast way of identifying candidates.

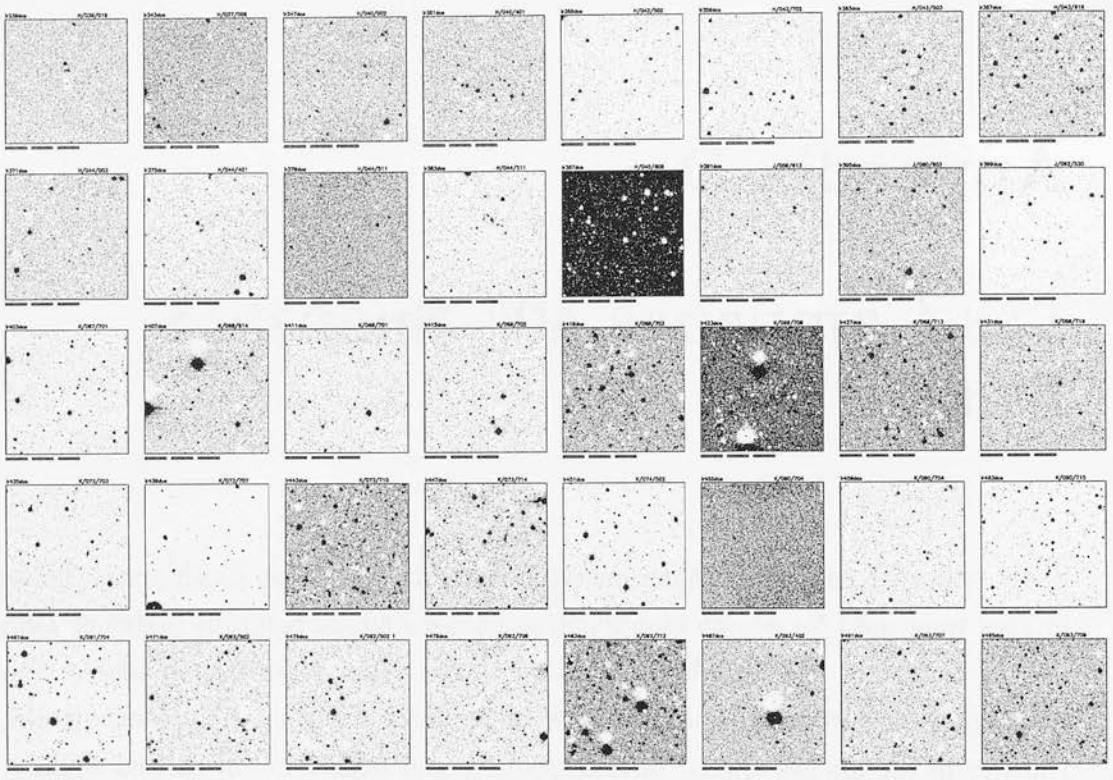

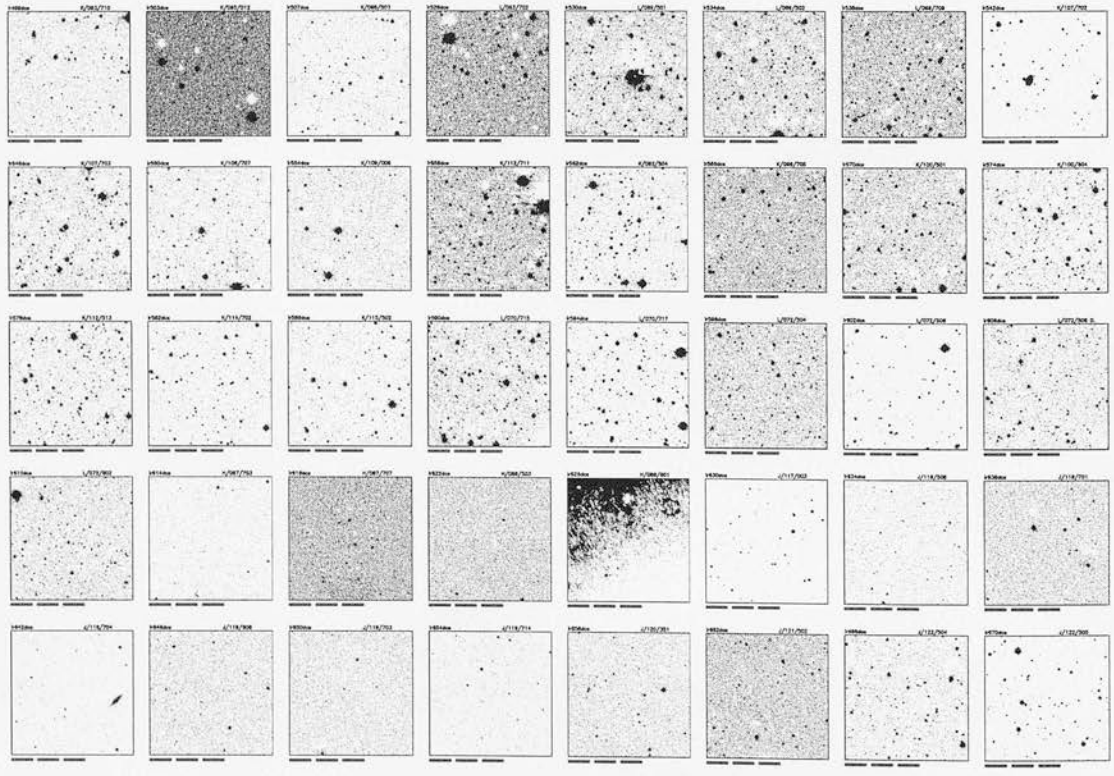

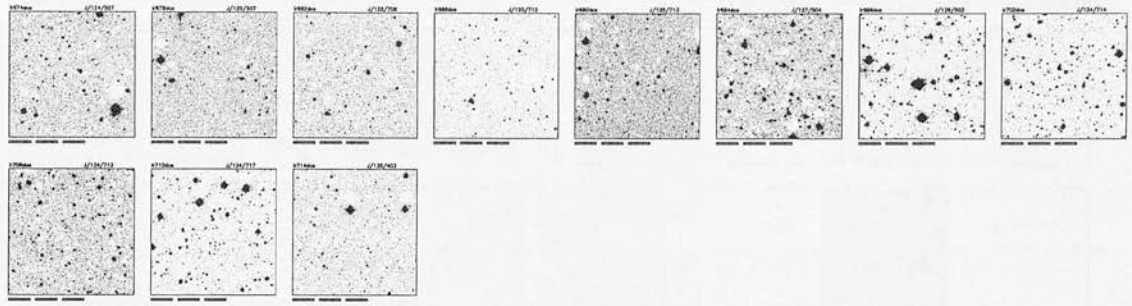

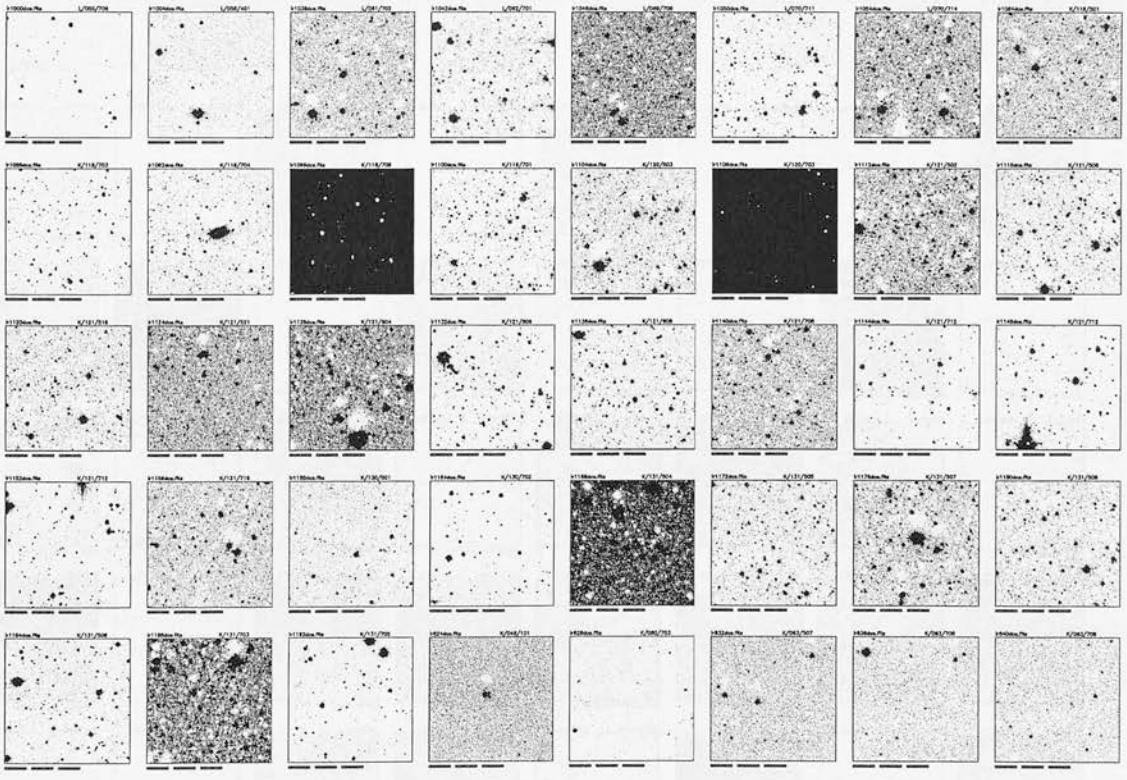

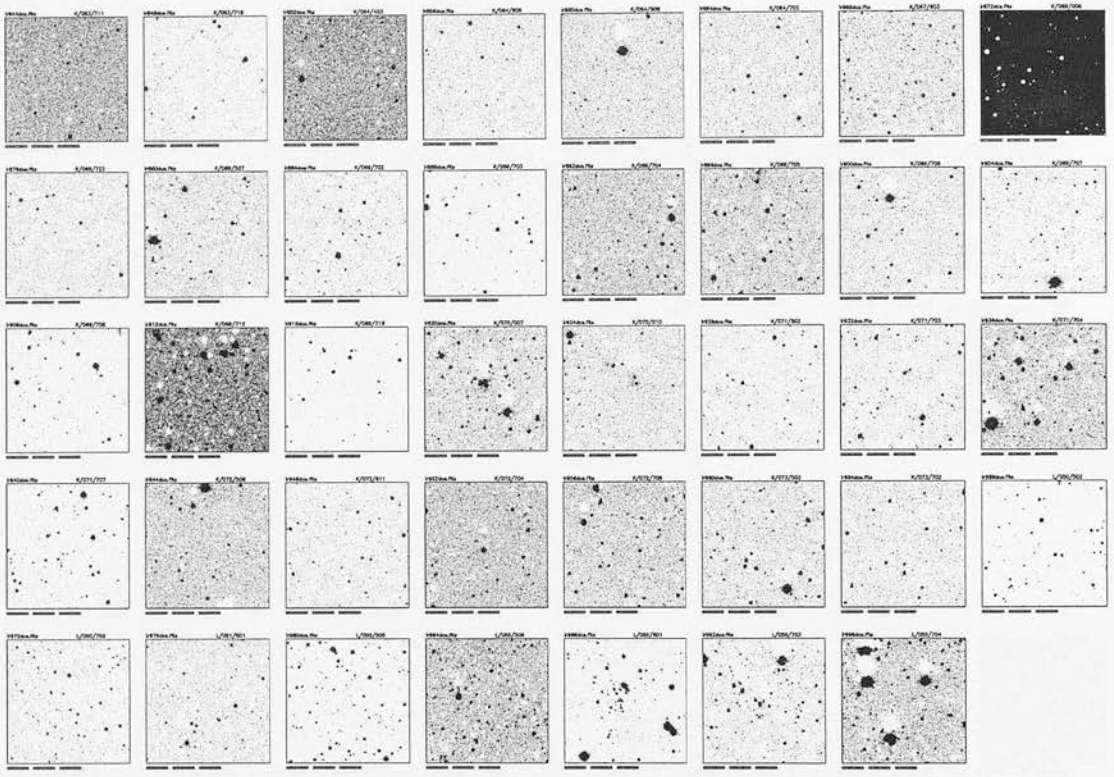

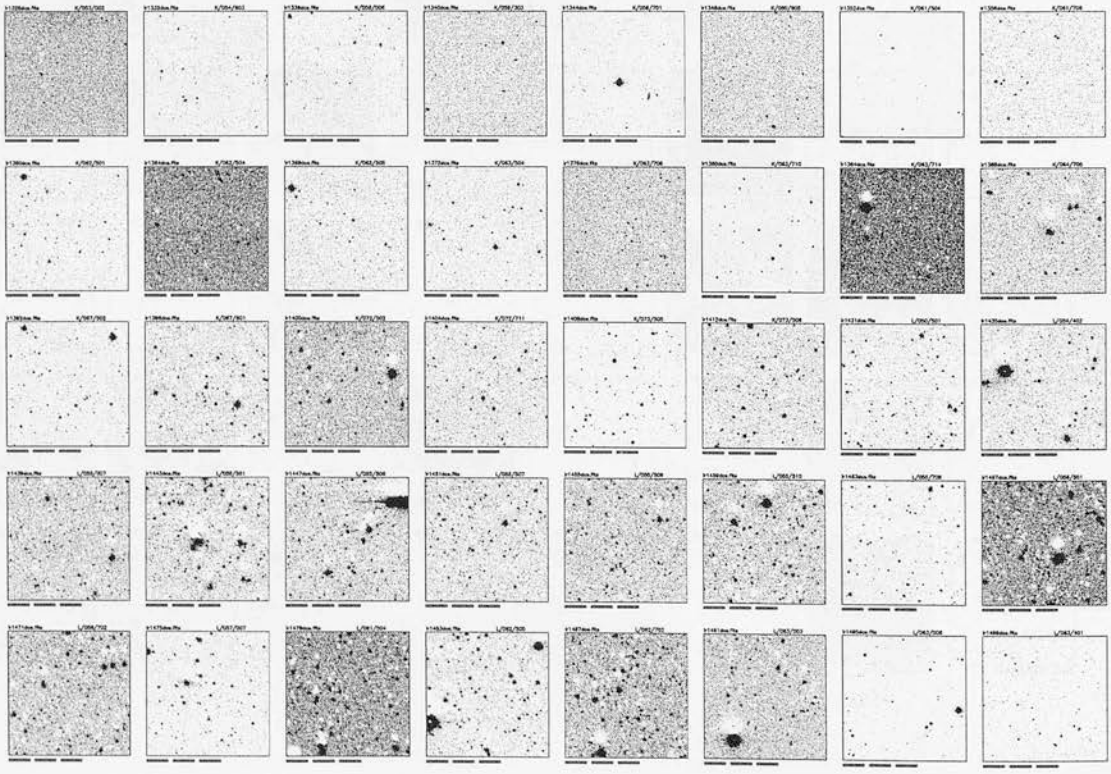

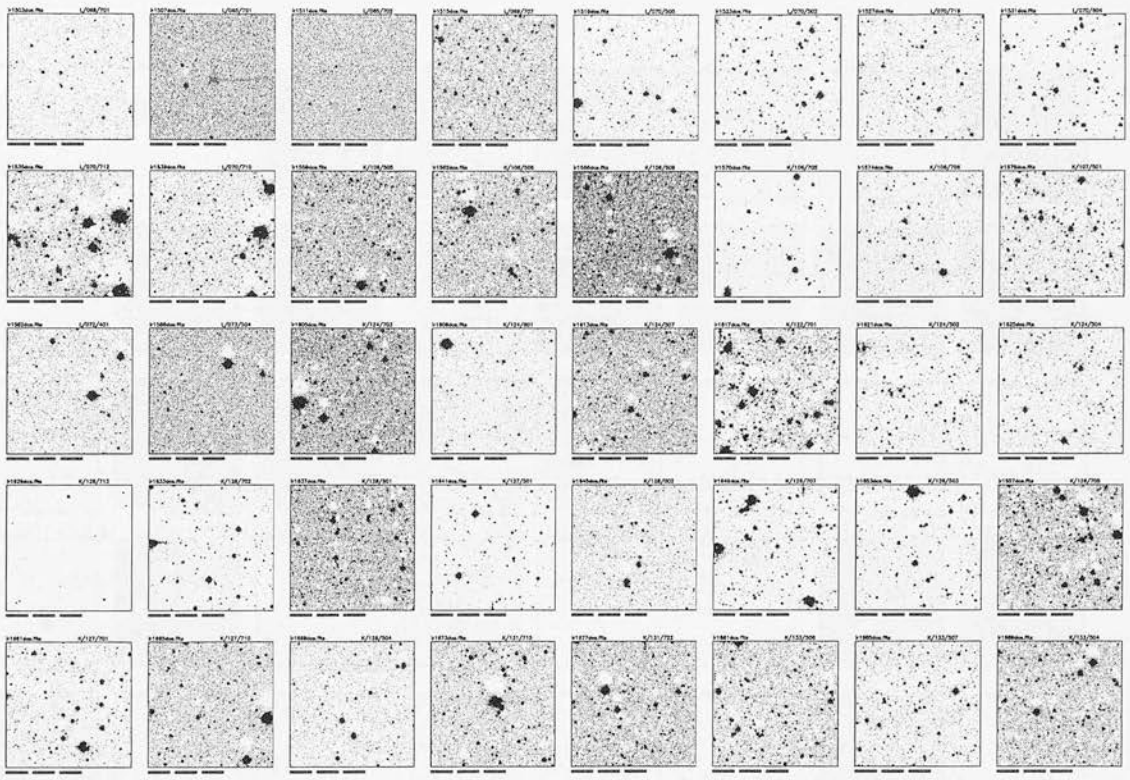

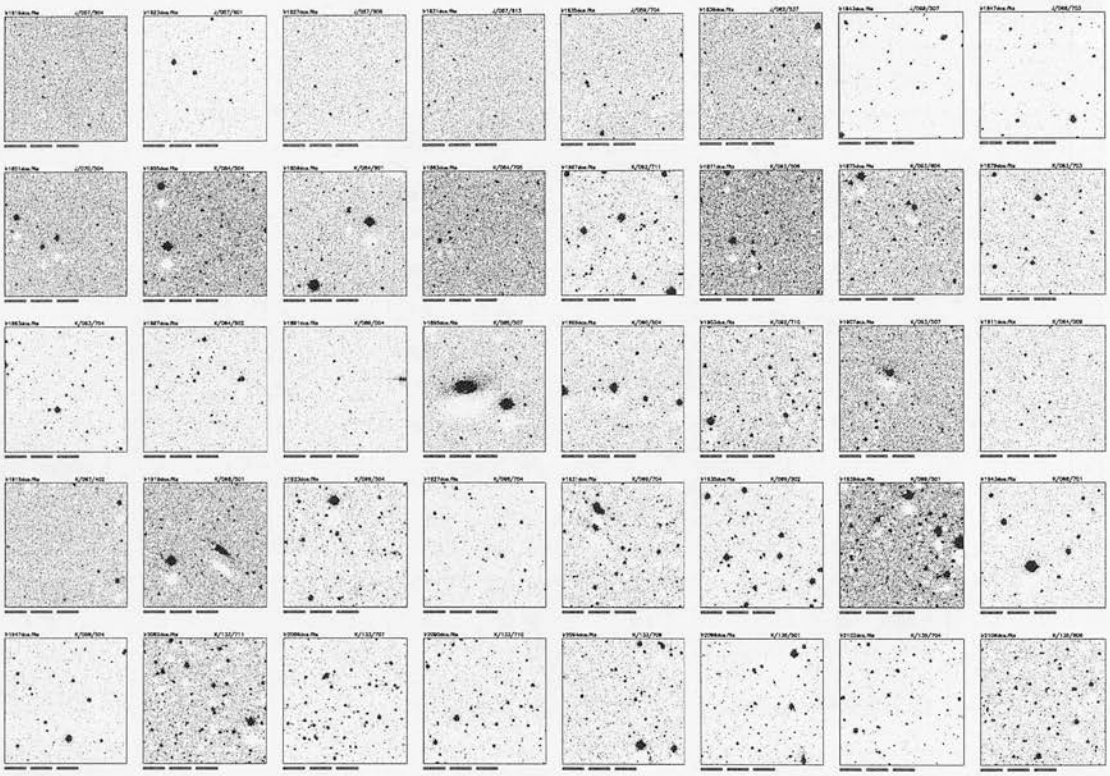

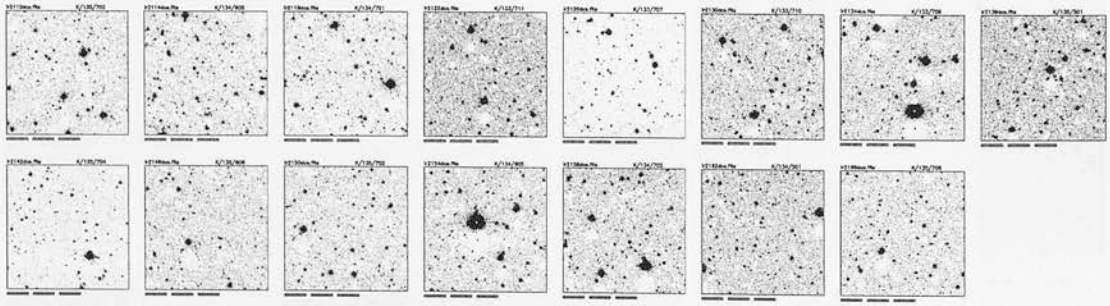

Appendix E

DSS Images of CTIO Candidates

Digitized Sky Survey images of candidates observed on the 60" and 4m telescopes at CTIO. These images aided the identification of candidates prior to the following spectral observations. The spectra obtained from these candidates are presented in Appendix G.

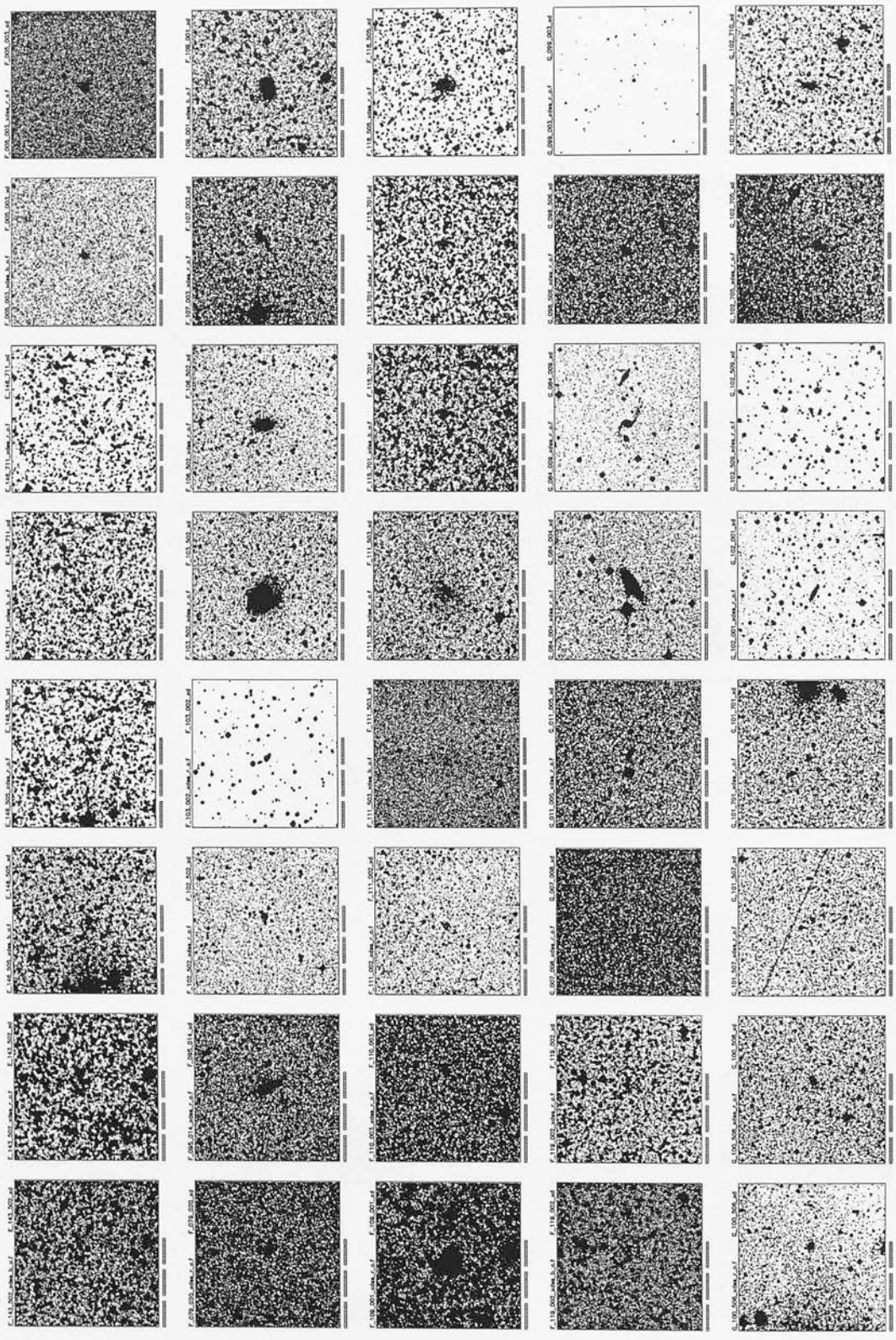

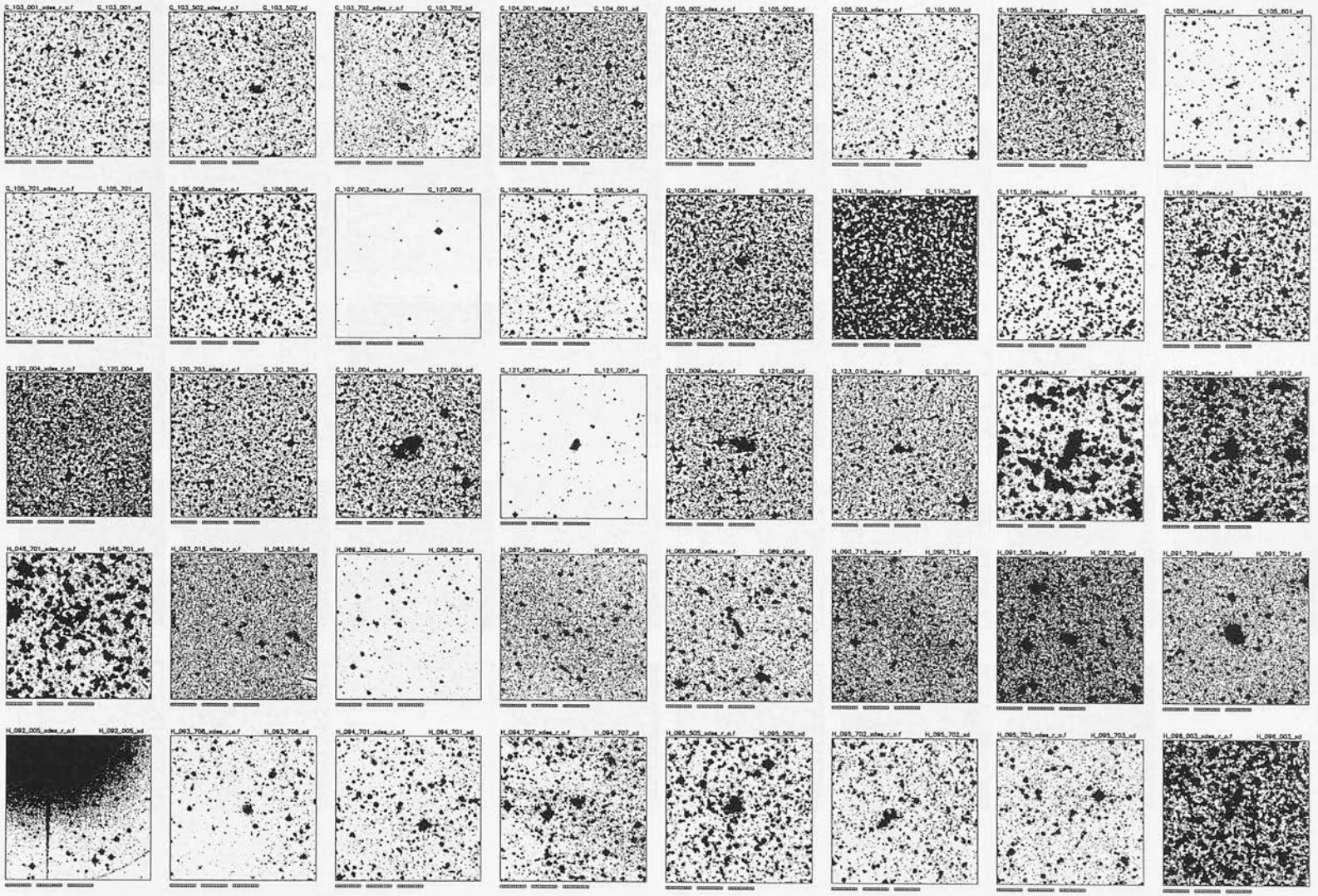

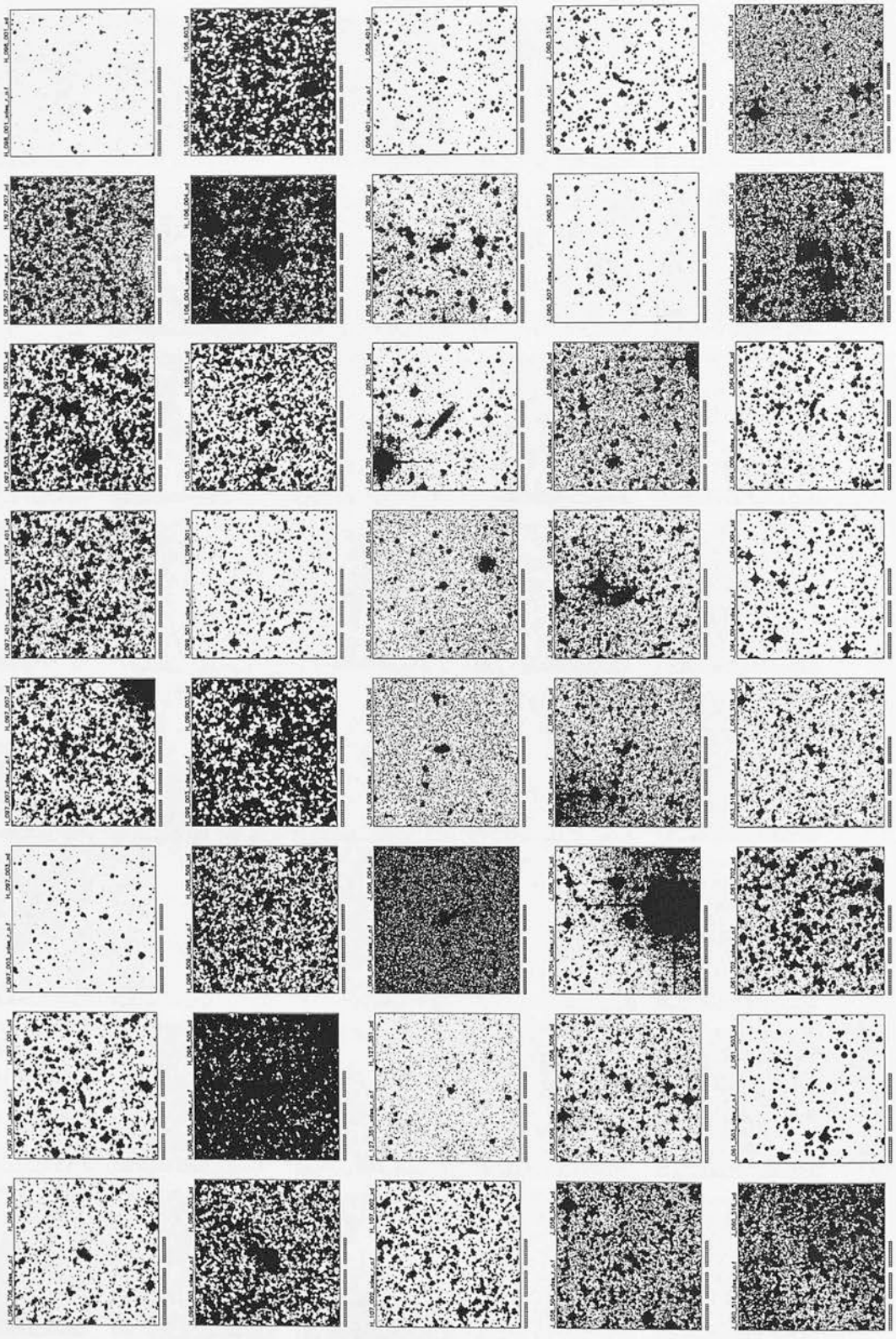

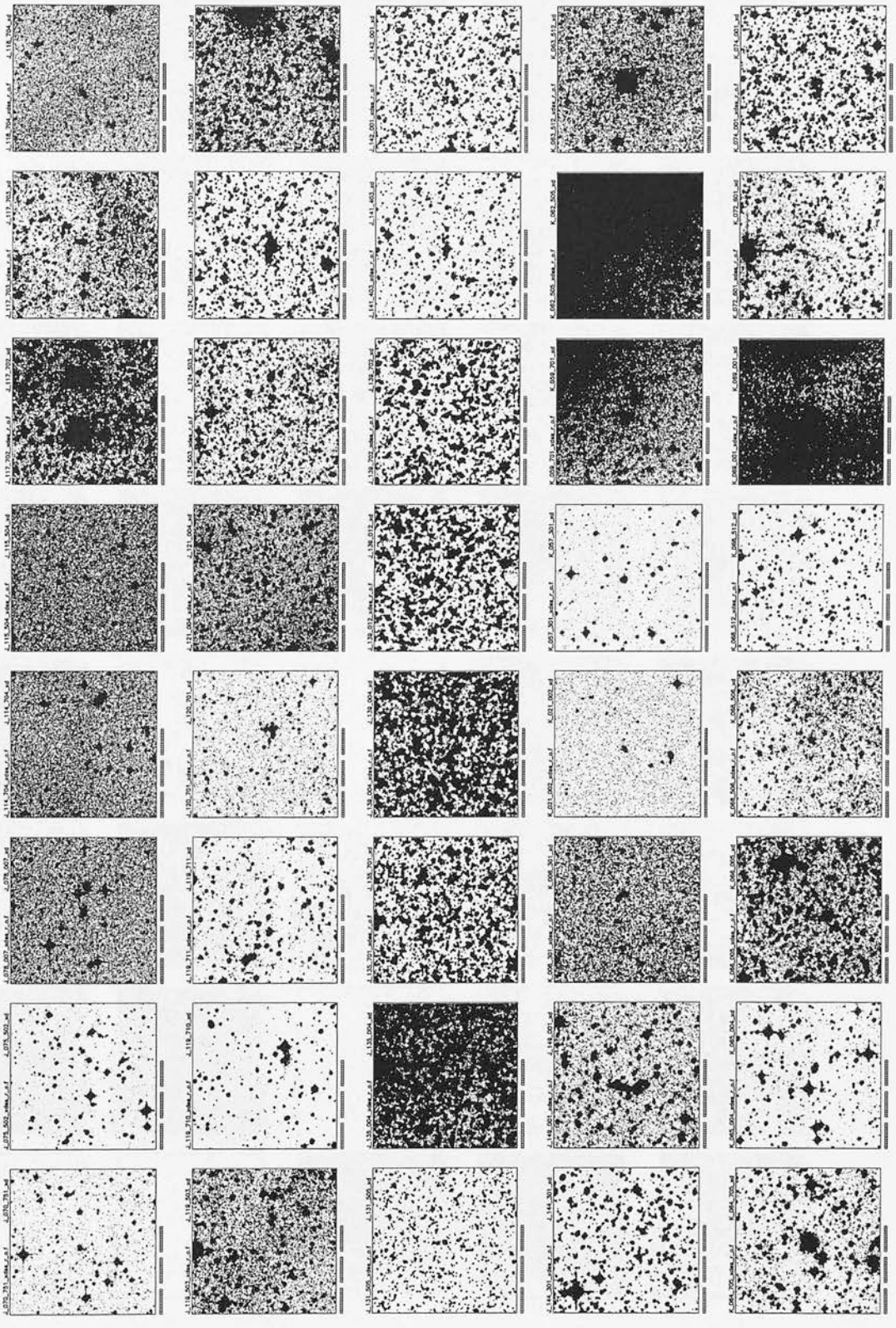

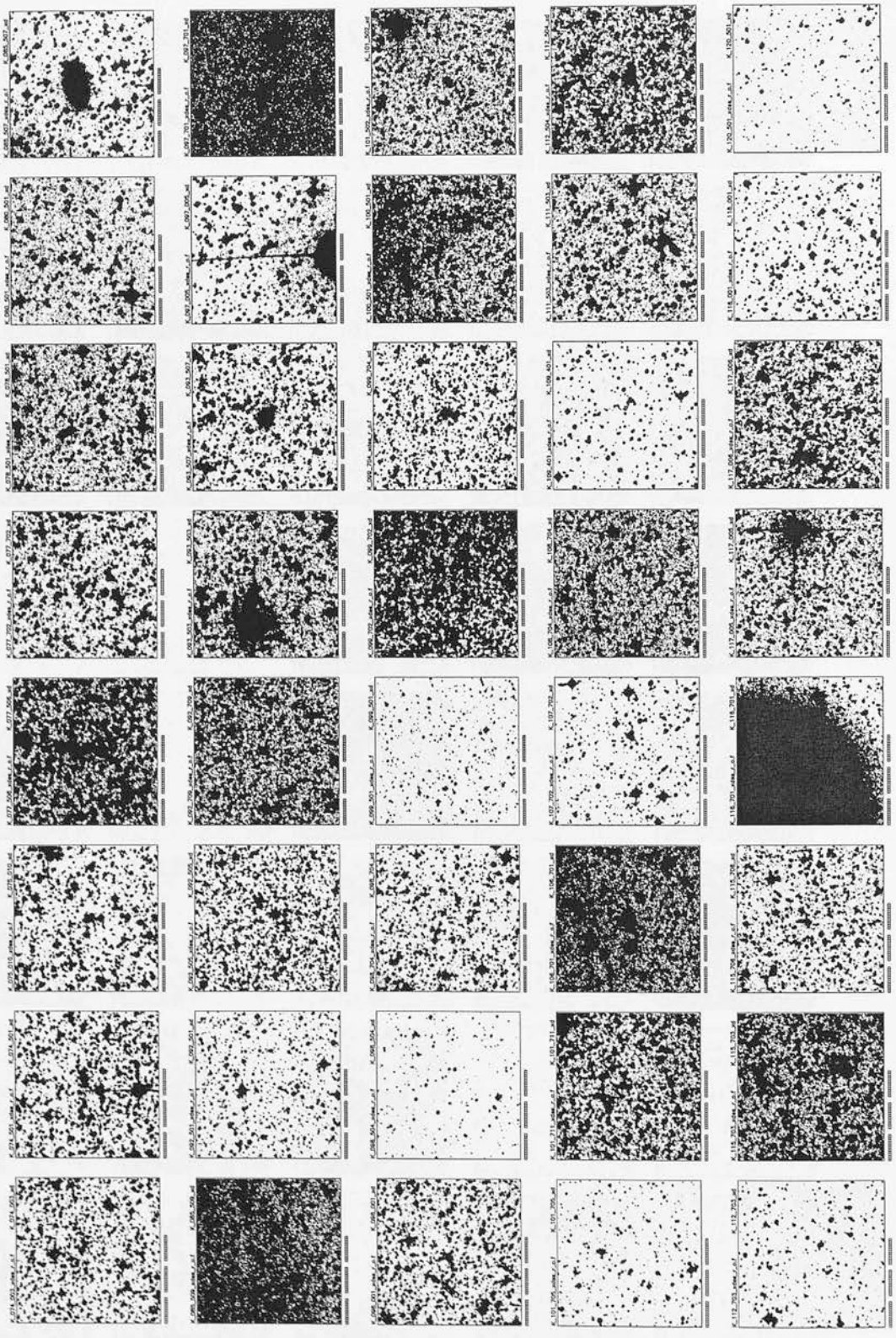

Appendix F

Spectra from 1996 Cananea Run

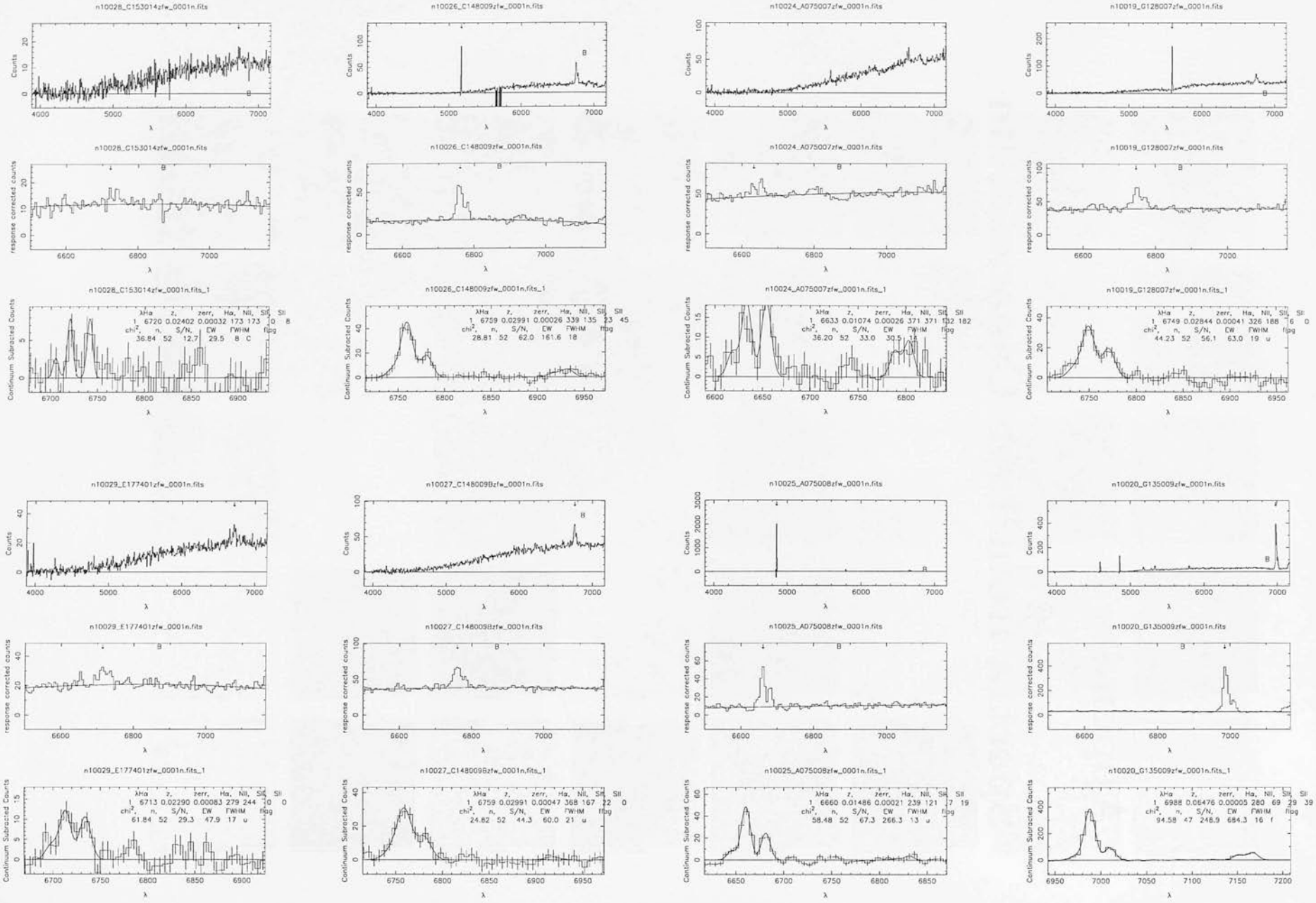
n10028_C153014zfw_0001n.fits
n10026_C148009zfw_0001n.fits
n10024_A075007zfw_0001n.fits
n10019_G128007zfw_0001n.fits
Counts
response corrected counts
Continuum Subtracted Counts
λ
λHa z zerr Ha NII SII SII
n10029_E177401zfw_0001n.fits
n10027_C148009Bzfw_0001n.fits
n10025_A075008zfw_0001n.fits
n10020_G135009zfw_0001n.fits

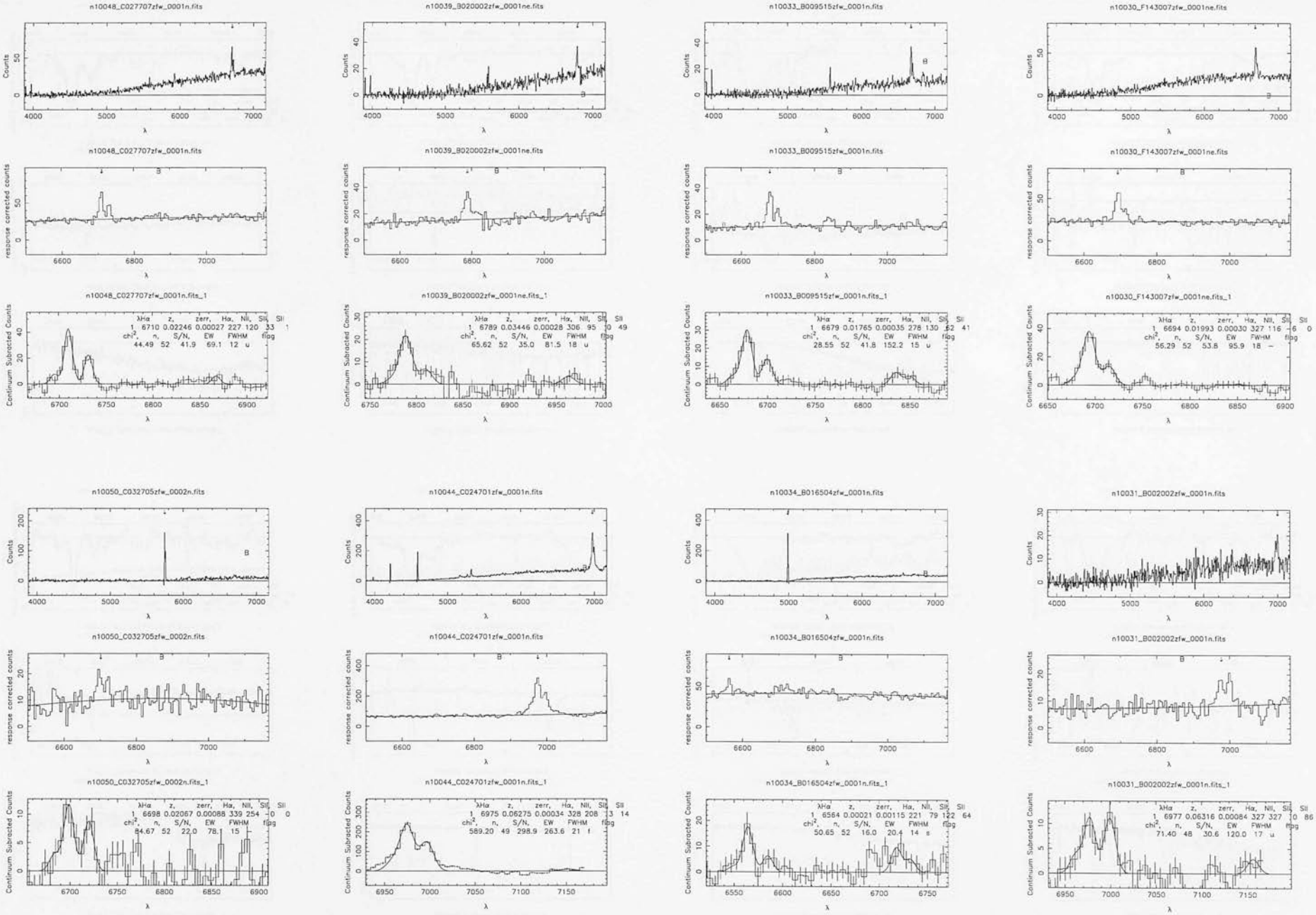
n10048_C027707zfw_0001n.fits
n10039_B020002zfw_0001ne.fits
n10033_B009515zfw_0001n.fits
n10030_F143007zfw_0001ne.fits
Counts
response corrected counts
Continuum Subracted Counts
λ
n10048_C027707zfw_0001n.fits_1
n10039_B020002zfw_0001ne.fits_1
n10033_B009515zfw_0001n.fits_1
n10030_F143007zfw_0001ne.fits_1
λHα z zerr Hα NII SII SII
1 6710 0.02246 0.00027 227 120 33 1
chi², n, S/N, EW FWHM flag
44.49 52 41.9 69.1 12 u
1 6789 0.03446 0.00028 306 95 10 49
65.62 52 35.0 81.5 18 u
1 6679 0.01765 0.00035 278 130 52 41
28.55 52 41.8 152.2 15 u
1 6694 0.01993 0.00030 327 116 6 0
56.29 52 53.8 95.9 18 –
n10050_C032705zfw_0002n.fits
n10044_C024701zfw_0001n.fits
n10034_B016504zfw_0001n.fits
n10031_B002002zfw_0001n.fits
n10050_C032705zfw_0002n.fits_1
n10044_C024701zfw_0001n.fits_1
n10034_B016504zfw_0001n.fits_1
n10031_B002002zfw_0001n.fits_1
1 6698 0.02067 0.00088 339 254 0 0
84.67 52 22.0 78.1 15
1 6975 0.06275 0.00034 328 208 13 14
589.20 49 298.9 263.6 21 f
1 6564 0.00021 0.00115 221 79 122 64
50.65 52 16.0 20.4 14 s
1 6977 0.06316 0.00084 327 327 10 86
71.40 48 30.6 120.0 17 u

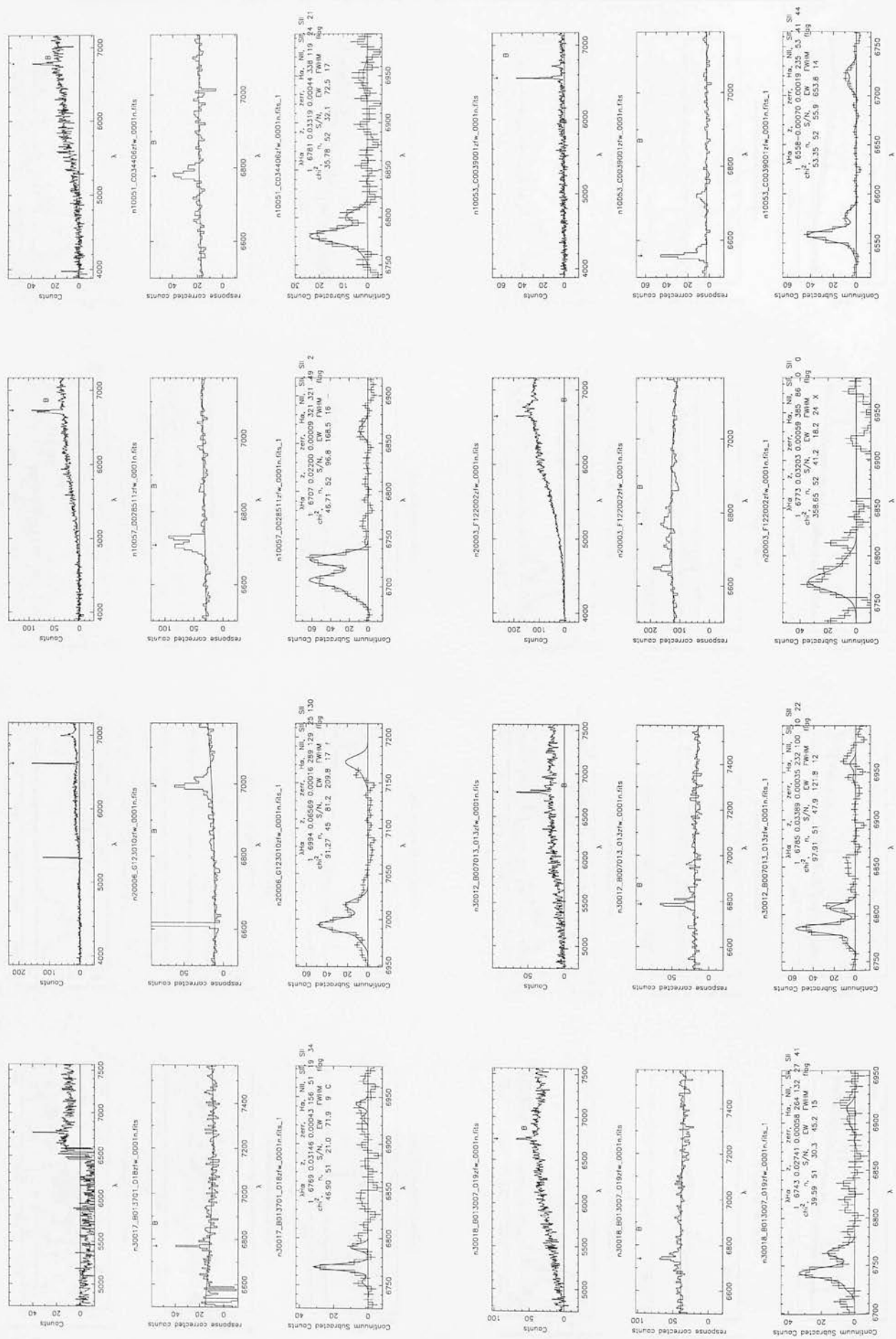

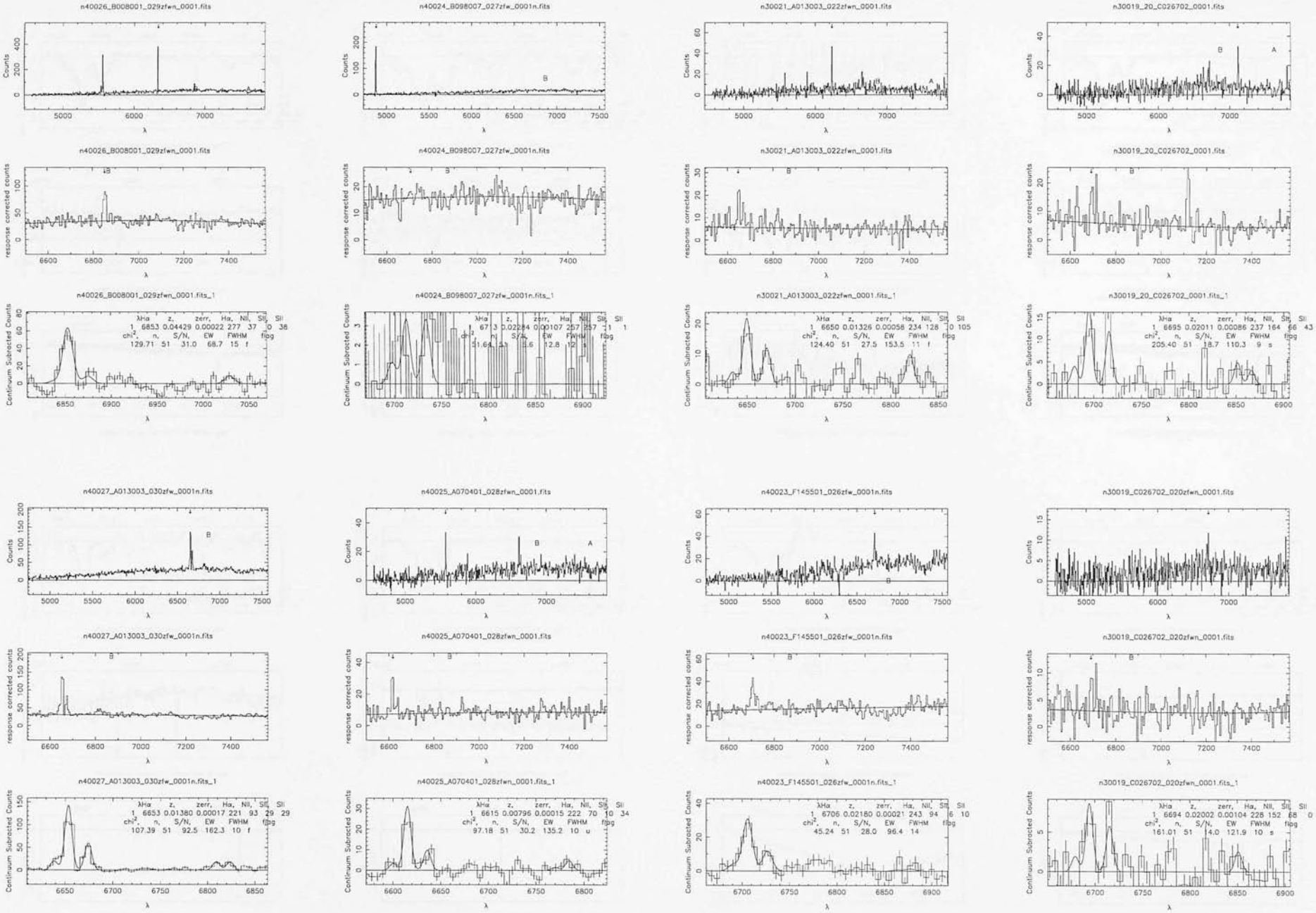
n40026_B008001_029zfwn_0001.fits
n40024_B098007_027zfw_0001n.fits
n30021_A013003_022zfwn_0001.fits
n30019_20_C026702_0001.fits
Counts
λ
response corrected counts
n40026_B008001_029zfwn_0001.fits_1
n40024_B098007_027zfw_0001n.fits_1
n30021_A013003_022zfwn_0001.fits_1
n30019_20_C026702_0001.fits_1
Continuum Subtracted Counts
λHα z zerr Ha NII SII SII
1 6853 0.04429 0.00022 277 37 0 38
chi² n S/N EW FWHM flag
129.71 51 31.0 68.7 15 f
1 6713 0.02284 0.00107 257 257 -1 1
chi² n S/N EW FWHM flag
51.64 51 6.6 12.8 12 s
1 6650 0.01326 0.00058 234 128 0 105
chi² n S/N EW FWHM flag
124.40 51 27.5 153.5 11 f
1 6695 0.02011 0.00086 237 164 66 43
chi² n S/N EW FWHM flag
205.40 51 18.7 110.3 9 s
n40027_A013003_030zfw_0001n.fits
n40025_A070401_028zfwn_0001.fits
n40023_F145501_026zfw_0001n.fits
n30019_C026702_020zfwn_0001.fits
n40027_A013003_030zfw_0001n.fits_1
n40025_A070401_028zfwn_0001.fits_1
n40023_F145501_026zfw_0001n.fits_1
n30019_C026702_020zfwn_0001.fits_1
1 6653 0.01380 0.00017 221 93 29 29
chi² n S/N EW FWHM flag
107.39 51 92.5 162.3 10 f
1 6615 0.00796 0.00015 222 70 10 34
chi² n S/N EW FWHM flag
97.18 51 30.2 135.2 10 u
1 6706 0.02180 0.00021 243 94 6 10
chi² n S/N EW FWHM flag
45.24 51 28.0 96.4 14
1 6694 0.02002 0.00104 228 152 68 0
chi² n S/N EW FWHM flag
161.01 51 14.0 121.9 10 s

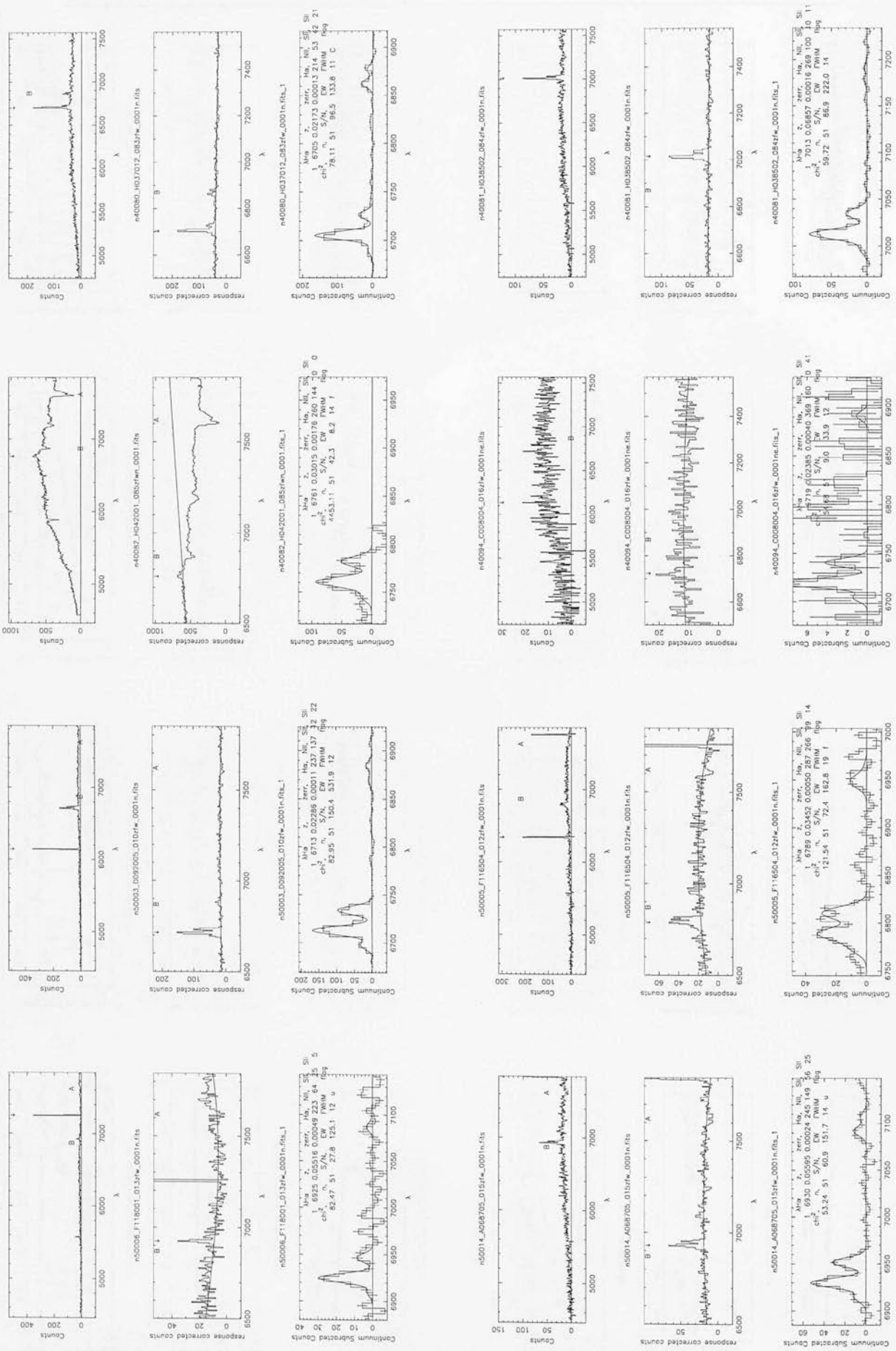

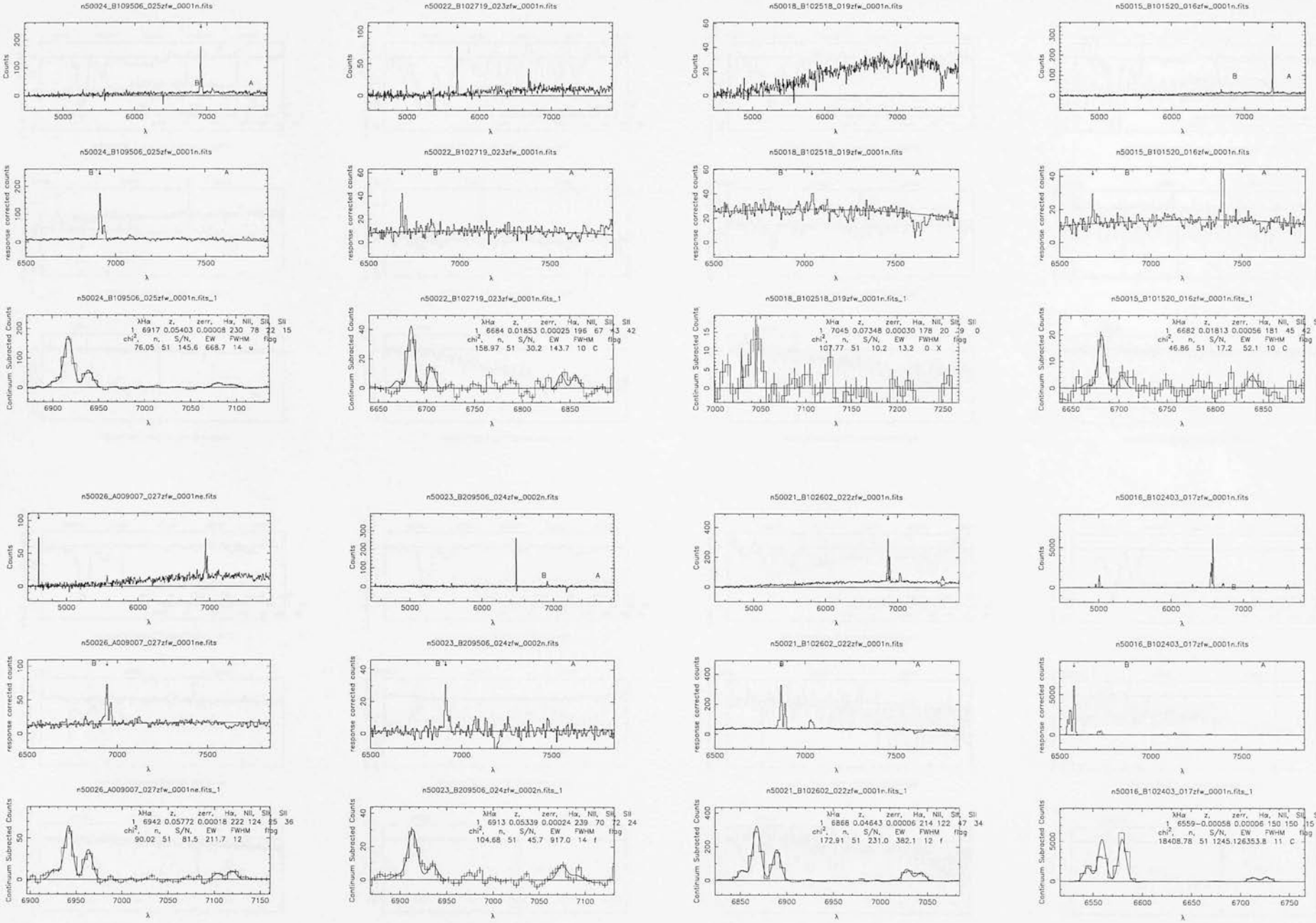
n50024_B109506_025zfw_0001n.fits
n50022_B102719_023zfw_0001n.fits
n50018_B102518_019zfw_0001n.fits
n50015_B101520_016zfw_0001n.fits
Counts
response corrected counts
Continuum Subracted Counts
λ
λHα z zerr Hα NII SII SII
1 6917 0.05403 0.00008 230 78 22 15
chi² n S/N EW FWHM flag
76.05 51 145.6 668.7 14 u
1 6684 0.01853 0.00025 196 67 43 42
158.97 51 30.2 143.7 10 C
1 7045 0.07348 0.00030 178 20 9 0
107.77 51 10.2 13.2 0 X
1 6682 0.01813 0.00056 181 45 42 0
46.86 51 17.2 52.1 10 C
n50026_A009007_027zfw_0001ne.fits
n50023_B209506_024zfw_0002n.fits
n50021_B102602_022zfw_0001n.fits
n50016_B102403_017zfw_0001n.fits
1 6942 0.05772 0.00018 222 124 25 36
90.02 51 81.5 211.7 12
1 6913 0.05339 0.00024 239 70 72 24
104.68 51 45.7 917.0 14 f
1 6868 0.04643 0.00006 214 122 47 34
172.91 51 231.0 382.1 12 f
1 6559 −0.00058 0.00006 150 150 15 17
18408.78 51 1245.126353.8 11 C

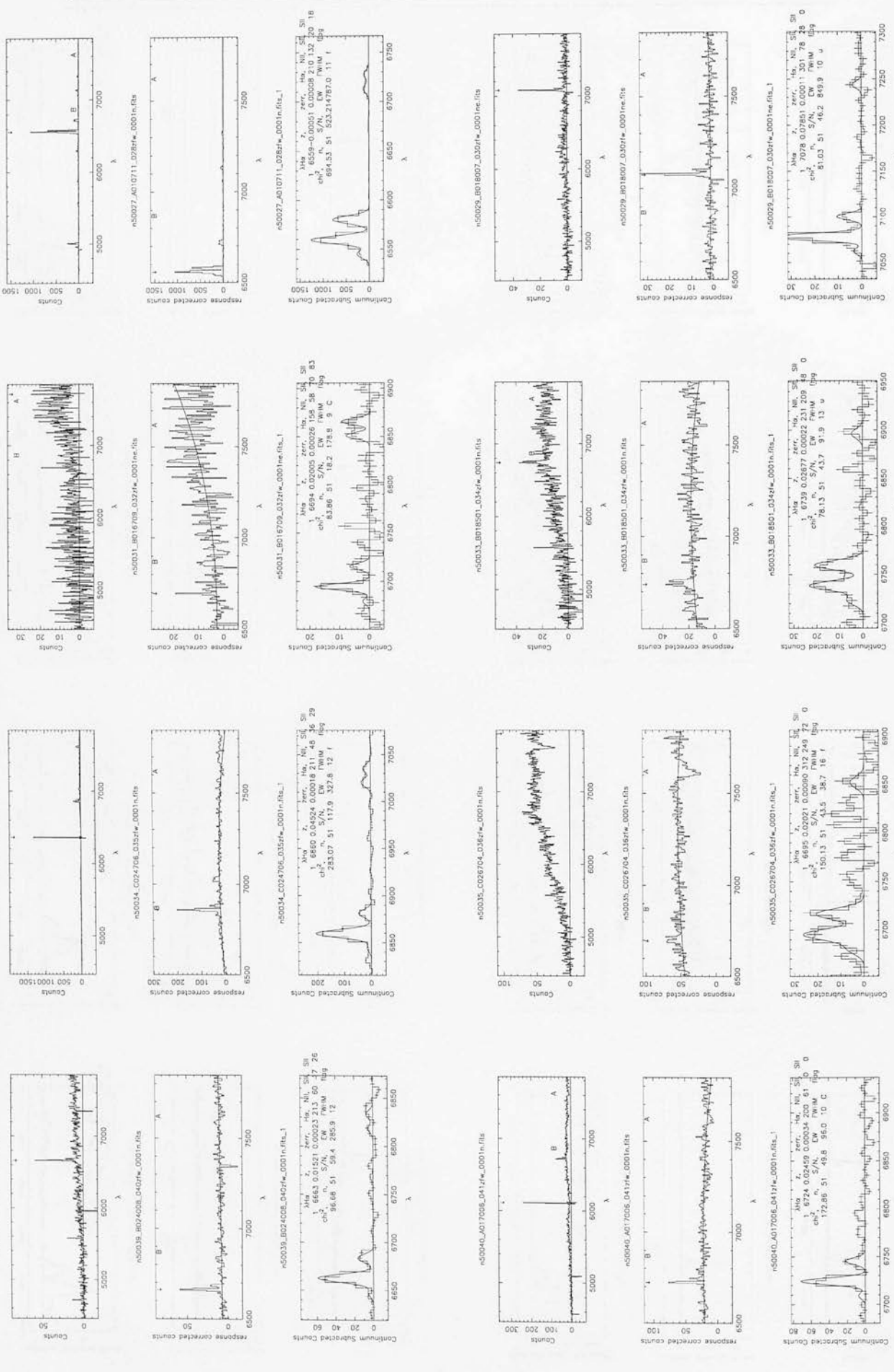

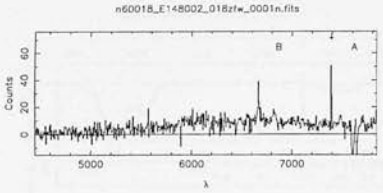
n60018_E148002_018zfw_0001n.fits
Counts
λ

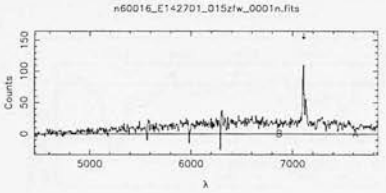
n60016_E142701_015zfw_0001n.fits
Counts
λ

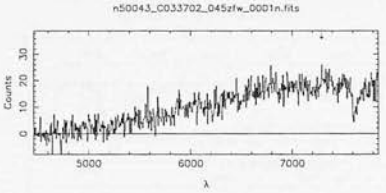
n50043_C033702_045zfw_0001n.fits
Counts
λ

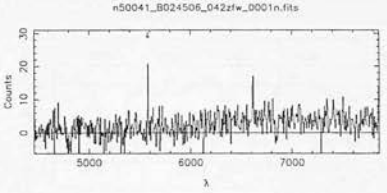
n50041_B024506_042zfw_0001n.fits
Counts
λ

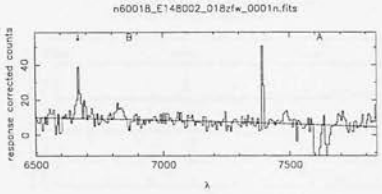
n60018_E148002_018zfw_0001n.fits
response corrected counts
λ

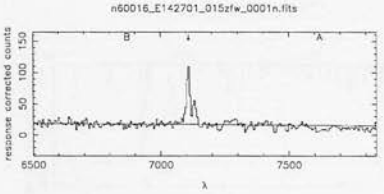
n60016_E142701_015zfw_0001n.fits
response corrected counts
λ

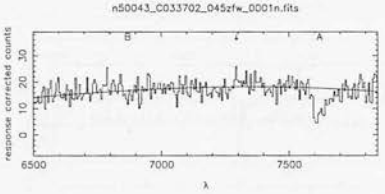
n50043_C033702_045zfw_0001n.fits
response corrected counts
λ

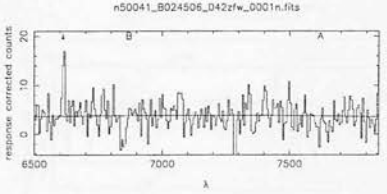
n50041_B024506_042zfw_0001n.fits
response corrected counts
λ

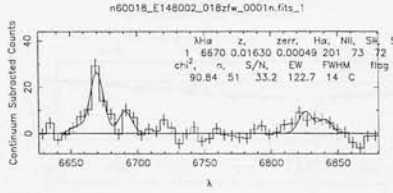
n60018_E148002_018zfw_0001n.fits_1
λHα z zerr Hα NII SII SII
1 6670 0.01630 0.00049 201 73 72 46
chi² n S/N EW FWHM flag
90.84 51 33.2 122.7 14 C
Continuum Subtracted Counts
λ

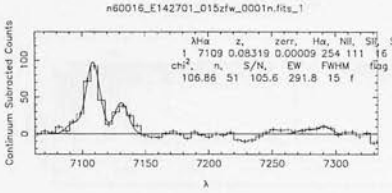
n60016_E142701_015zfw_0001n.fits_1
λHα z zerr Hα NII SII SII
1 7109 0.08319 0.00009 254 111 16 29
chi² n S/N EW FWHM flag
106.86 51 105.6 291.8 15 f
Continuum Subtracted Counts
λ

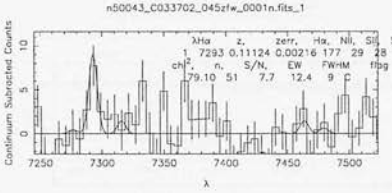
n50043_C033702_045zfw_0001n.fits_1
λHα z zerr Hα NII SII SII
1 7293 0.11124 0.00216 177 29 28 12
chi² n S/N EW FWHM flag
79.10 51 7.7 12.4 9 C
Continuum Subtracted Counts
λ

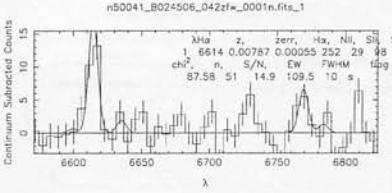
n50041_B024506_042zfw_0001n.fits_1
λHα z zerr Hα NII SII SII
1 6614 0.00787 0.00055 252 29 98 19
chi² n S/N EW FWHM flag
87.58 51 14.9 109.5 10 s
Continuum Subtracted Counts
λ

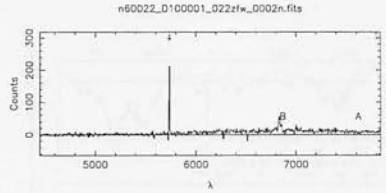
n60022_D100001_022zfw_0002n.fits
Counts
λ

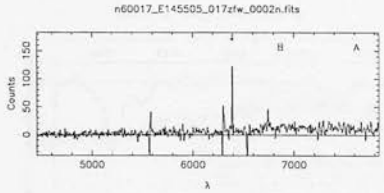
n60017_E145505_017zfw_0002n.fits
Counts
λ

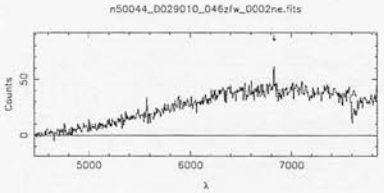
n50044_D029010_046zfw_0002ne.fits
Counts
λ

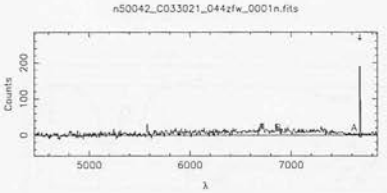
n50042_C033021_044zfw_0001n.fits
Counts
λ

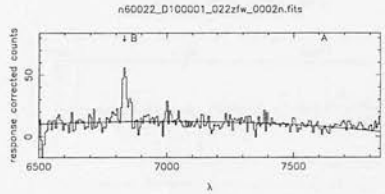
n60022_D100001_022zfw_0002n.fits
response corrected counts
λ

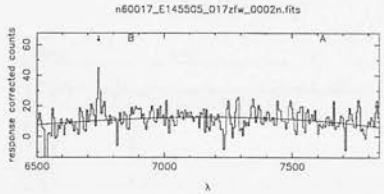
n60017_E145505_017zfw_0002n.fits
response corrected counts
λ

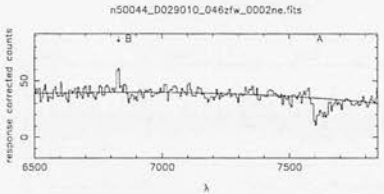
n50044_D029010_046zfw_0002ne.fits
response corrected counts
λ

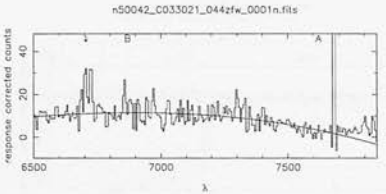
n50042_C033021_044zfw_0001n.fits
response corrected counts
λ

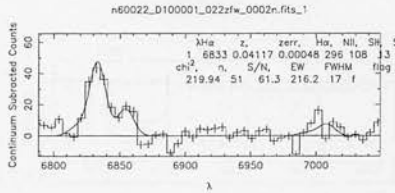
n60022_D100001_022zfw_0002n.fits_1
λHα z zerr Hα NII SII SII
1 6833 0.04117 0.00048 296 108 13 47
chi² n S/N EW FWHM flag
219.94 51 61.3 216.2 17 f
Continuum Subtracted Counts
λ

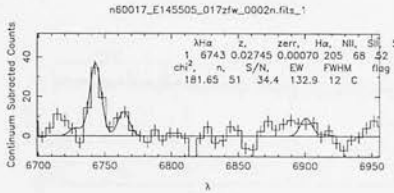
n60017_E145505_017zfw_0002n.fits_1
λHα z zerr Hα NII SII SII
1 6743 0.02745 0.00070 205 68 52 6
chi² n S/N EW FWHM flag
181.65 51 34.4 132.9 12 C
Continuum Subtracted Counts
λ

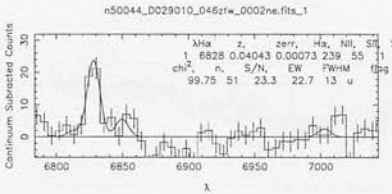
n50044_D029010_046zfw_0002ne.fits_1
λHα z zerr Hα NII SII SII
1 6828 0.04043 0.00073 239 55 11 25
chi² n S/N EW FWHM flag
99.75 51 23.3 22.7 13 u
Continuum Subtracted Counts
λ

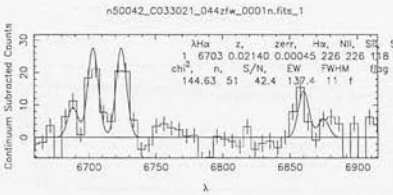
n50042_C033021_044zfw_0001n.fits_1
λHα z zerr Hα NII SII SII
1 6703 0.02140 0.00045 226 226 118 47
chi² n S/N EW FWHM flag
144.63 51 42.4 137.4 11 f
Continuum Subtracted Counts
λ

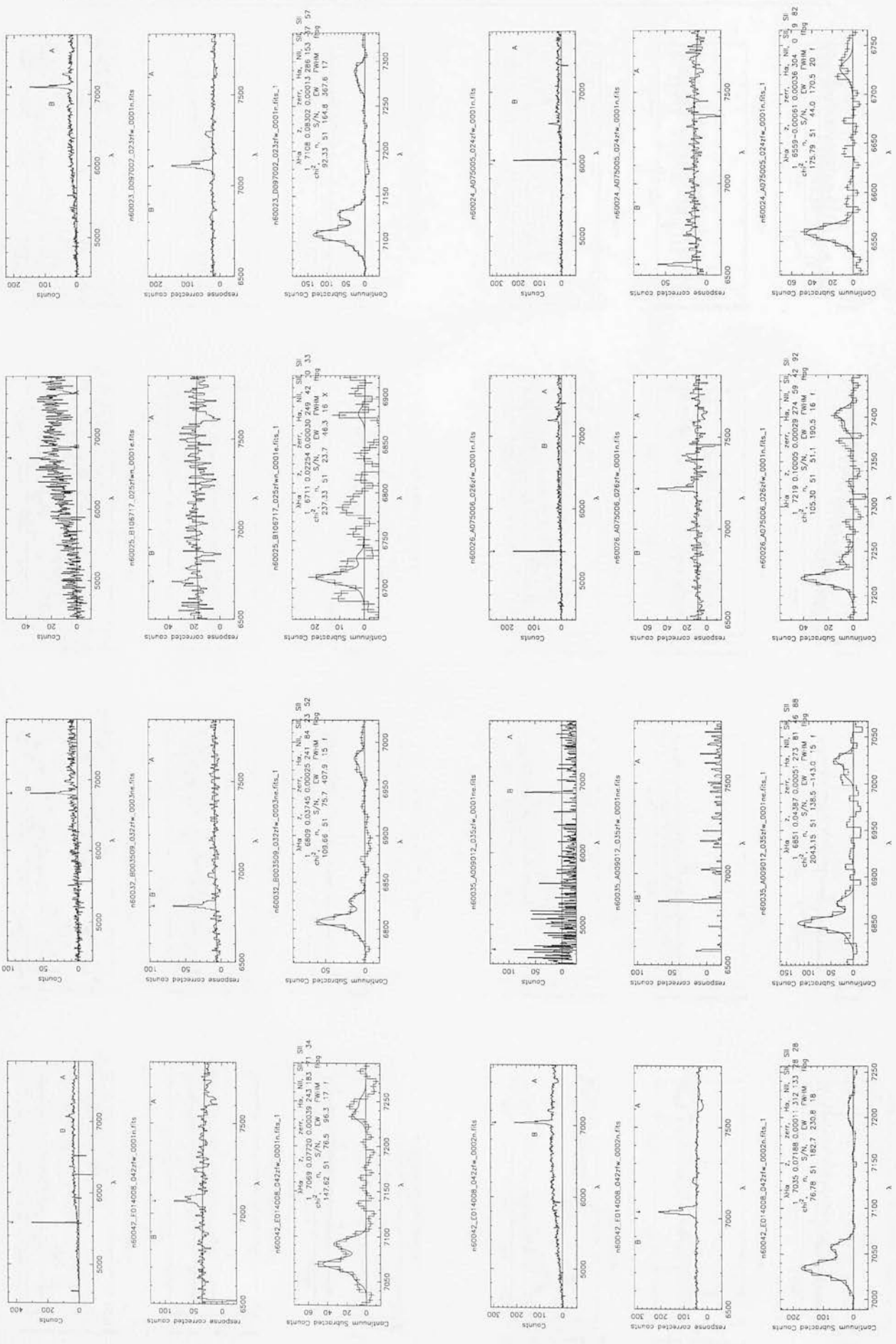

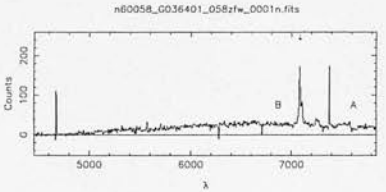
n60058_G036401_058zfw_0001n.fits
Counts
λ
B
A

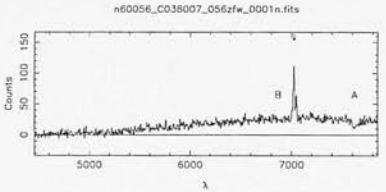
n60056_C038007_056zfw_0001n.fits
Counts
λ
B
A

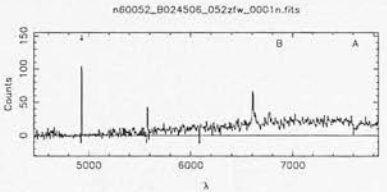
n60052_B024506_052zfw_0001n.fits
Counts
λ
B
A

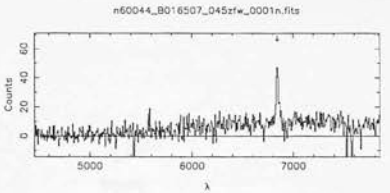
n60044_B016507_045zfw_0001n.fits
Counts
λ

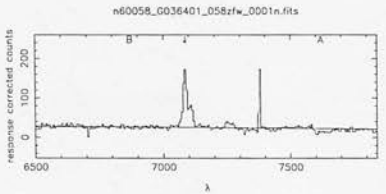
n60058_G036401_058zfw_0001n.fits
response corrected counts
λ
B
A

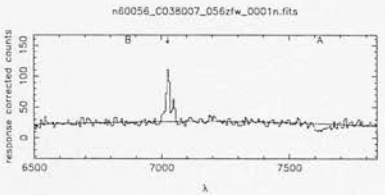
n60056_C038007_056zfw_0001n.fits
response corrected counts
λ
B
A

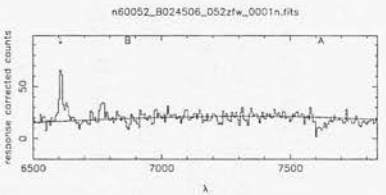
n60052_B024506_052zfw_0001n.fits
response corrected counts
λ
B
A

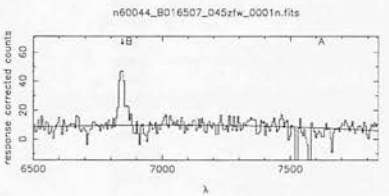
n60044_B016507_045zfw_0001n.fits
response corrected counts
λ
B
A

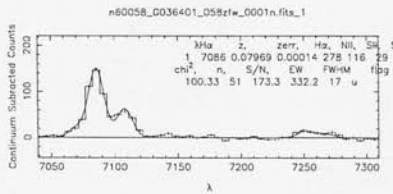
n60058_G036401_058zfw_0001n.fits_1
Continuum Subtracted Counts
λ
λHα z, zerr, Hα, NII, SII SII
1 7086 0.07969 0.00014 278 116 29 18
chi², n, S/N, EW FWHM flag
100.33 51 173.3 332.2 17 u

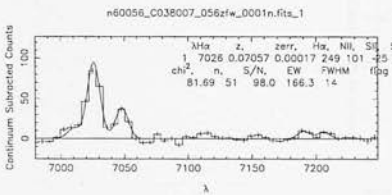
n60056_C038007_056zfw_0001n.fits_1
Continuum Subtracted Counts
λ
λHα z, zerr, Hα, NII, SII SII
1 7026 0.07057 0.00017 249 101 25 21
chi², n, S/N, EW FWHM flag
81.69 51 98.0 166.3 14

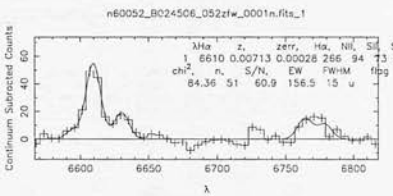
n60052_B024506_052zfw_0001n.fits_1
Continuum Subtracted Counts
λ
λHα z, zerr, Hα, NII, SII SII
1 6610 0.00713 0.00028 266 94 73 52
chi², n, S/N, EW FWHM flag
84.36 51 60.9 156.5 15 u

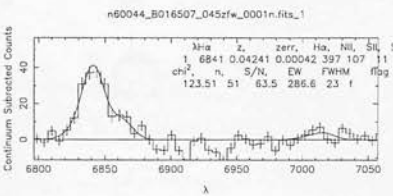
n60044_B016507_045zfw_0001n.fits_1
Continuum Subtracted Counts
λ
λHα z, zerr, Hα, NII, SII SII
1 6841 0.04241 0.00042 397 107 11 37
chi², n, S/N, EW FWHM flag
123.51 51 63.5 286.6 23 f

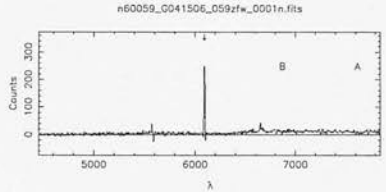
n60059_G041506_059zfw_0001n.fits
Counts
λ
B
A

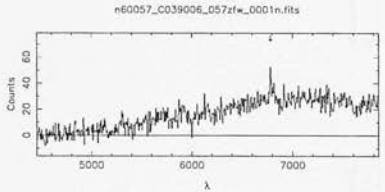
n60057_C039006_057zfw_0001n.fits
Counts
λ

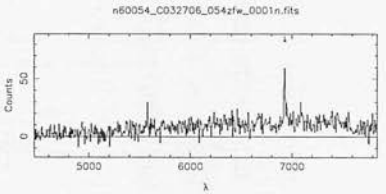
n60054_C032706_054zfw_0001n.fits
Counts
λ

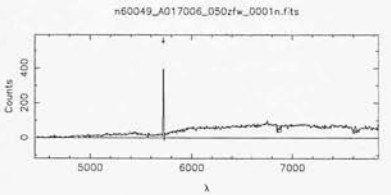
n60049_A017006_050zfw_0001n.fits
Counts
λ

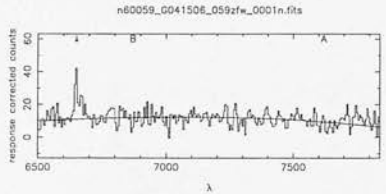
n60059_G041506_059zfw_0001n.fits
response corrected counts
λ
B
A

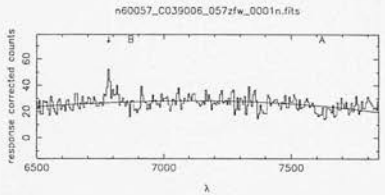
n60057_C039006_057zfw_0001n.fits
response corrected counts
λ
B
A

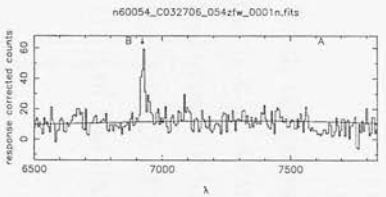
n60054_C032706_054zfw_0001n.fits
response corrected counts
λ
B
A

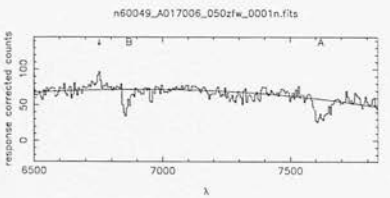
n60049_A017006_050zfw_0001n.fits
response corrected counts
λ
B
A

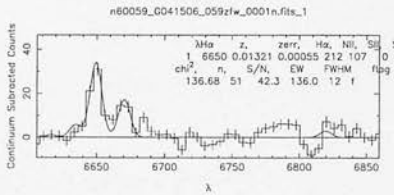
n60059_G041506_059zfw_0001n.fits_1
Continuum Subtracted Counts
λ
λHα z, zerr, Hα, NII, SII SII
1 6650 0.01321 0.00055 212 107 0 18
chi², n, S/N, EW FWHM flag
136.68 51 42.3 136.0 12 f

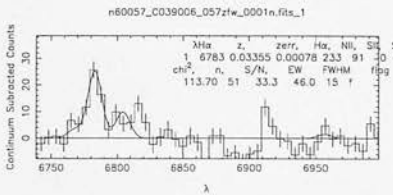
n60057_C039006_057zfw_0001n.fits_1
Continuum Subtracted Counts
λ
λHα z, zerr, Hα, NII, SII SII
1 6783 0.03355 0.00078 233 91 30 14
chi², n, S/N, EW FWHM flag
113.70 51 33.3 46.0 15 f

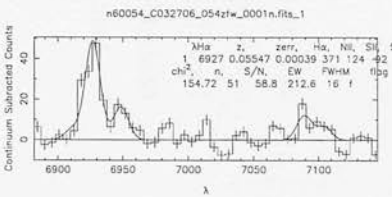
n60054_C032706_054zfw_0001n.fits_1
Continuum Subtracted Counts
λ
λHα z, zerr, Hα, NII, SII SII
1 6927 0.05547 0.00039 371 124 42 50
chi², n, S/N, EW FWHM flag
154.72 51 58.8 212.6 16 f

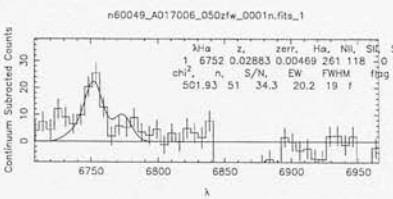
n60049_A017006_050zfw_0001n.fits_1
Continuum Subtracted Counts
λ
λHα z, zerr, Hα, NII, SII SII
1 6752 0.02883 0.00469 261 118 0 0
chi², n, S/N, EW FWHM flag
501.93 51 34.3 20.2 19 f

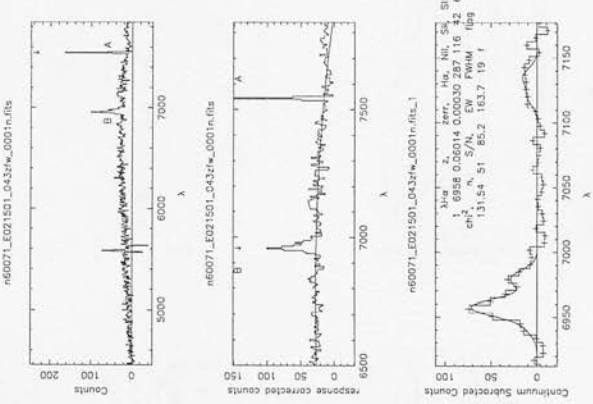
n60071_E021501_043rw_0001n.fits
Counts
λ
response corrected counts
Continuum Subtracted Counts
λHe
Zc
Zerr
Ha
NII
SII
FWHM
EW
S/N

Appendix G

Spectra from CTIO 60" (1999)

Spectra obtained at CTIO on the 60" (1.5m) telescope. Each spectrum occurs in three frames, showing the original reduced spectrum (top), a close up of the portion of the spectrum containing measurable emission features (middle), and the continuum subtracted and profile fitted spectum (bottom). Much of the data is presented here to provide an idea of the overall high quality of the dataset.

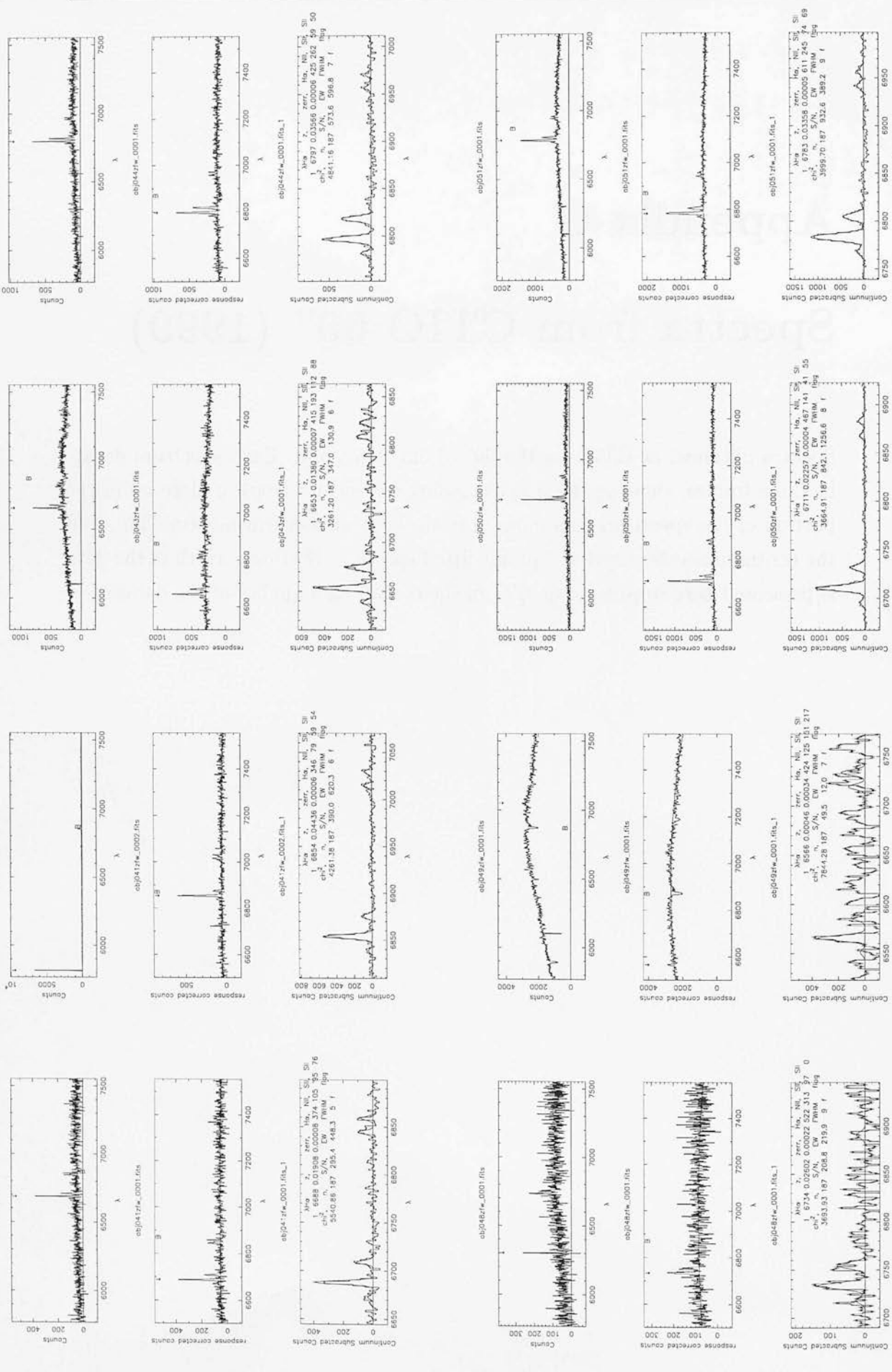

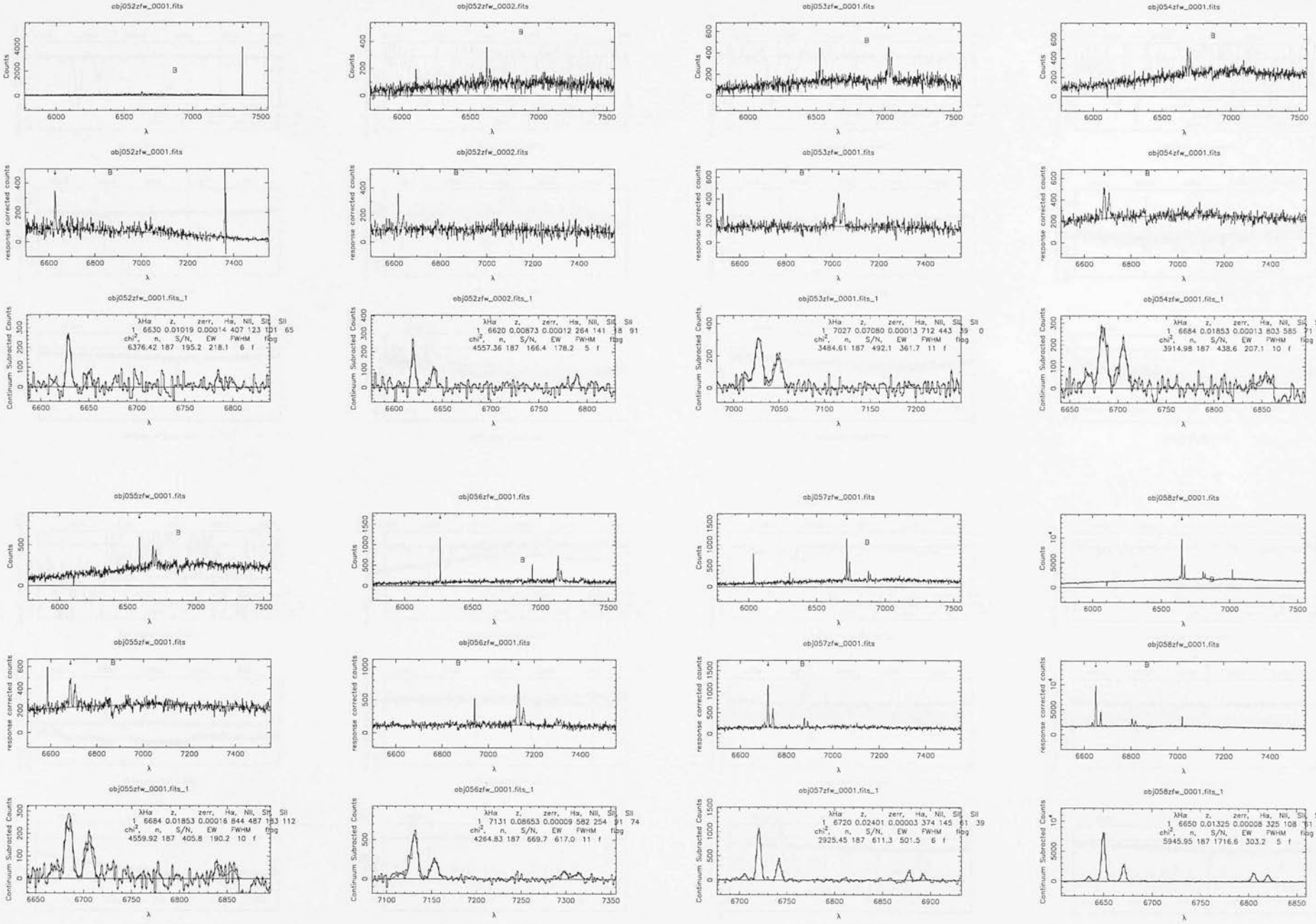
obj052zfw_0001.fits
obj052zfw_0002.fits
obj053zfw_0001.fits
obj054zfw_0001.fits
Counts
λ
response corrected counts
obj052zfw_0001.fits_1
obj052zfw_0002.fits_1
obj053zfw_0001.fits_1
obj054zfw_0001.fits_1
Continuum Subtracted Counts
λHα z zerr Hα NII SII SII
1 6630 0.01019 0.00014 407 123 101 65
chi² n S/N EW FWHM flag
6376.42 187 195.2 218.1 6 f
1 6620 0.00873 0.00012 264 141 18 91
chi² n S/N EW FWHM flag
4557.36 187 166.4 178.2 5 f
1 7027 0.07080 0.00013 712 443 39 0
chi² n S/N EW FWHM flag
3484.61 187 492.1 361.7 11 f
1 6684 0.01853 0.00013 803 585 71 172
chi² n S/N EW FWHM flag
3914.98 187 438.6 207.1 10 f
obj055zfw_0001.fits
obj056zfw_0001.fits
obj057zfw_0001.fits
obj058zfw_0001.fits
obj055zfw_0001.fits_1
obj056zfw_0001.fits_1
obj057zfw_0001.fits_1
obj058zfw_0001.fits_1
1 6684 0.01853 0.00016 844 487 183 112
chi² n S/N EW FWHM flag
4559.92 187 405.8 190.2 10 f
1 7131 0.08653 0.00009 582 254 91 74
chi² n S/N EW FWHM flag
4264.83 187 669.7 617.0 11 f
1 6720 0.02401 0.00003 374 145 61 39
chi² n S/N EW FWHM flag
2925.45 187 611.3 501.5 6 f
1 6650 0.01325 0.00008 325 108 51 49
chi² n S/N EW FWHM flag
5945.95 187 1716.6 303.2 5 f

obj059zfw_0001.fits
obj059zfw_0001.fits
obj059zfw_0001.fits_1
obj060zfw_0001.fits
obj060zfw_0001.fits
obj060zfw_0001.fits_1
obj061zfw_0001.fits
obj061zfw_0001.fits
obj061zfw_0001.fits_1
obj062zfw_0001.fits
obj062zfw_0001.fits
obj062zfw_0001.fits_1
obj063zfw_0001.fits
obj063zfw_0001.fits
obj063zfw_0001.fits_1
obj064zfw_0001.fits
obj064zfw_0001.fits
obj064zfw_0001.fits_1
obj065zfw_0001.fits
obj065zfw_0001.fits
obj065zfw_0001.fits_1
obj066zfw_0001e.fits
obj066zfw_0001e.fits
obj066zfw_0001e.fits_1
obj067zfw_0001.fits
obj067zfw_0001.fits
obj067zfw_0001.fits_1
Counts
response corrected counts
Continuum Subtracted Counts
λ

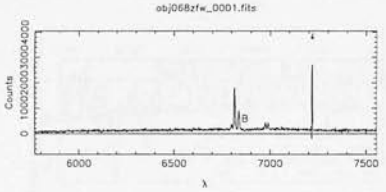
obj068zfw_0001.fits
Counts
λ

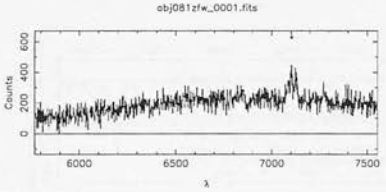
obj081zfw_0001.fits
Counts
λ

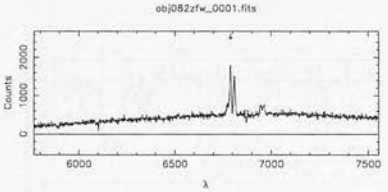
obj082zfw_0001.fits
Counts
λ

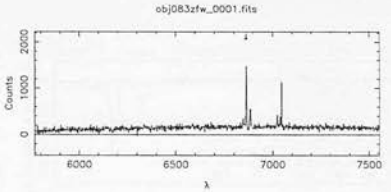
obj083zfw_0001.fits
Counts
λ

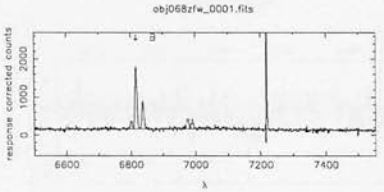
obj068zfw_0001.fits
response corrected counts
λ

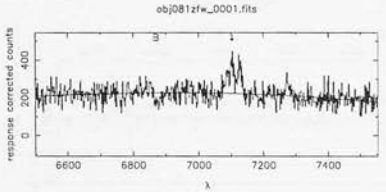
obj081zfw_0001.fits
response corrected counts
λ

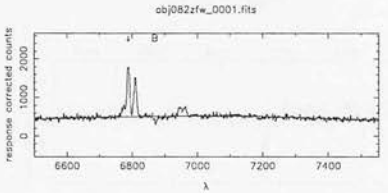
obj082zfw_0001.fits
response corrected counts
λ

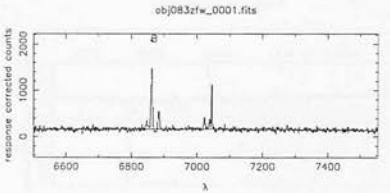
obj083zfw_0001.fits
response corrected counts
λ

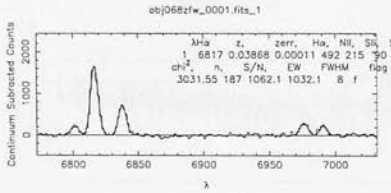
obj068zfw_0001.fits_1
λHα z zerr Ha NII SII SII
1 6817 0.03868 0.00011 492 215 90 69
chi², n, S/N, EW FWHM flag
3031.55 187 1062.1 1032.1 8 f
Continuum Subracted Counts
λ

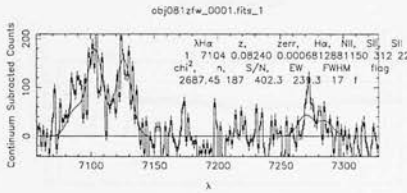
obj081zfw_0001.fits_1
λHα z zerr Ha NII SII SII
1 7104 0.08240 0.00068128811501 312 221
chi², n, S/N, EW FWHM flag
2687.45 187 402.3 231.3 17 f
Continuum Subracted Counts
λ

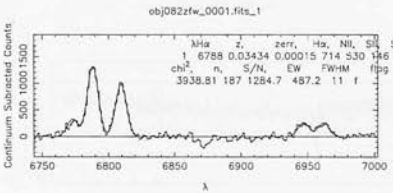
obj082zfw_0001.fits_1
λHα z zerr Ha NII SII SII
1 6788 0.03434 0.00015 714 530 146 142
chi², n, S/N, EW FWHM flag
3938.81 187 1284.7 487.2 11 f
Continuum Subracted Counts
λ

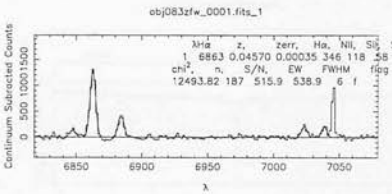
obj083zfw_0001.fits_1
λHα z zerr Ha NII SII SII
1 6863 0.04570 0.00035 346 118 58 54
chi², n, S/N, EW FWHM flag
12493.82 187 515.9 538.9 6 f
Continuum Subracted Counts
λ

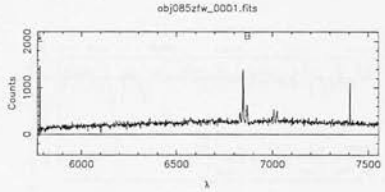
obj085zfw_0001.fits
Counts
λ

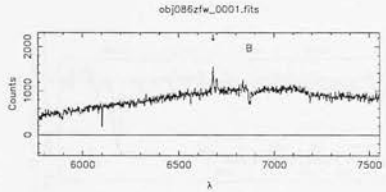
obj086zfw_0001.fits
Counts
λ

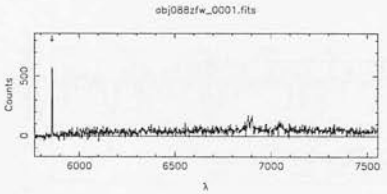
obj088zfw_0001.fits
Counts
λ

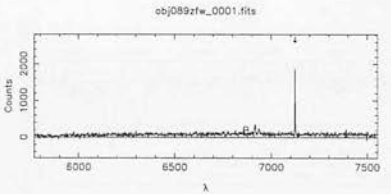
obj089zfw_0001.fits
Counts
λ

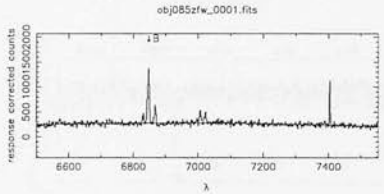
obj085zfw_0001.fits
response corrected counts
λ

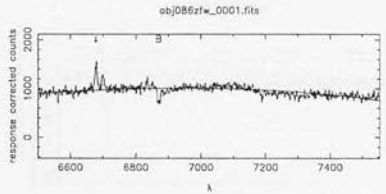
obj086zfw_0001.fits
response corrected counts
λ

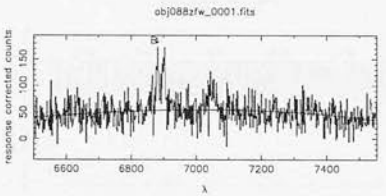
obj088zfw_0001.fits
response corrected counts
λ

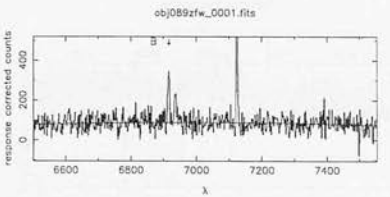
obj089zfw_0001.fits
response corrected counts
λ

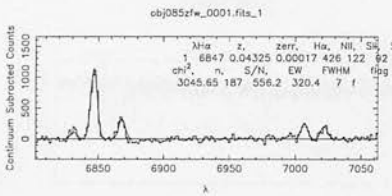
obj085zfw_0001.fits_1
λHα z zerr Ha NII SII SII
1 6847 0.04325 0.00017 426 122 92 78
chi², n, S/N, EW FWHM flag
3045.65 187 556.2 320.4 7 f
Continuum Subracted Counts
λ

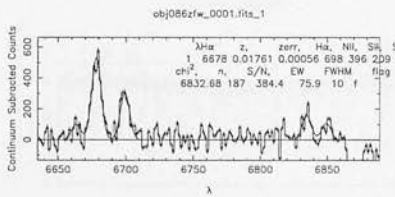
obj086zfw_0001.fits_1
λHα z zerr Ha NII SII SII
1 6878 0.01761 0.00056 698 396 209 141
chi², n, S/N, EW FWHM flag
6832.68 187 384.4 75.9 10 f
Continuum Subracted Counts
λ

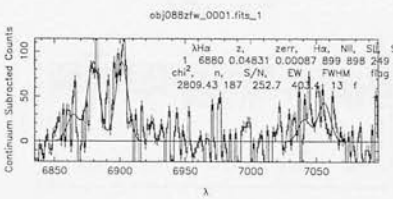
obj088zfw_0001.fits_1
λHα z zerr Ha NII SII SII
1 6880 0.04831 0.00087 899 898 249 440
chi², n, S/N, EW FWHM flag
2809.43 187 252.7 403.4 13 f
Continuum Subracted Counts
λ

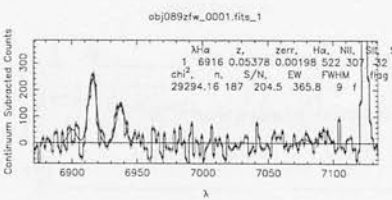
obj089zfw_0001.fits_1
λHα z zerr Ha NII SII SII
1 6916 0.05378 0.00198 522 307 32 99
chi², n, S/N, EW FWHM flag
29294.16 187 204.5 365.8 9 f
Continuum Subracted Counts
λ

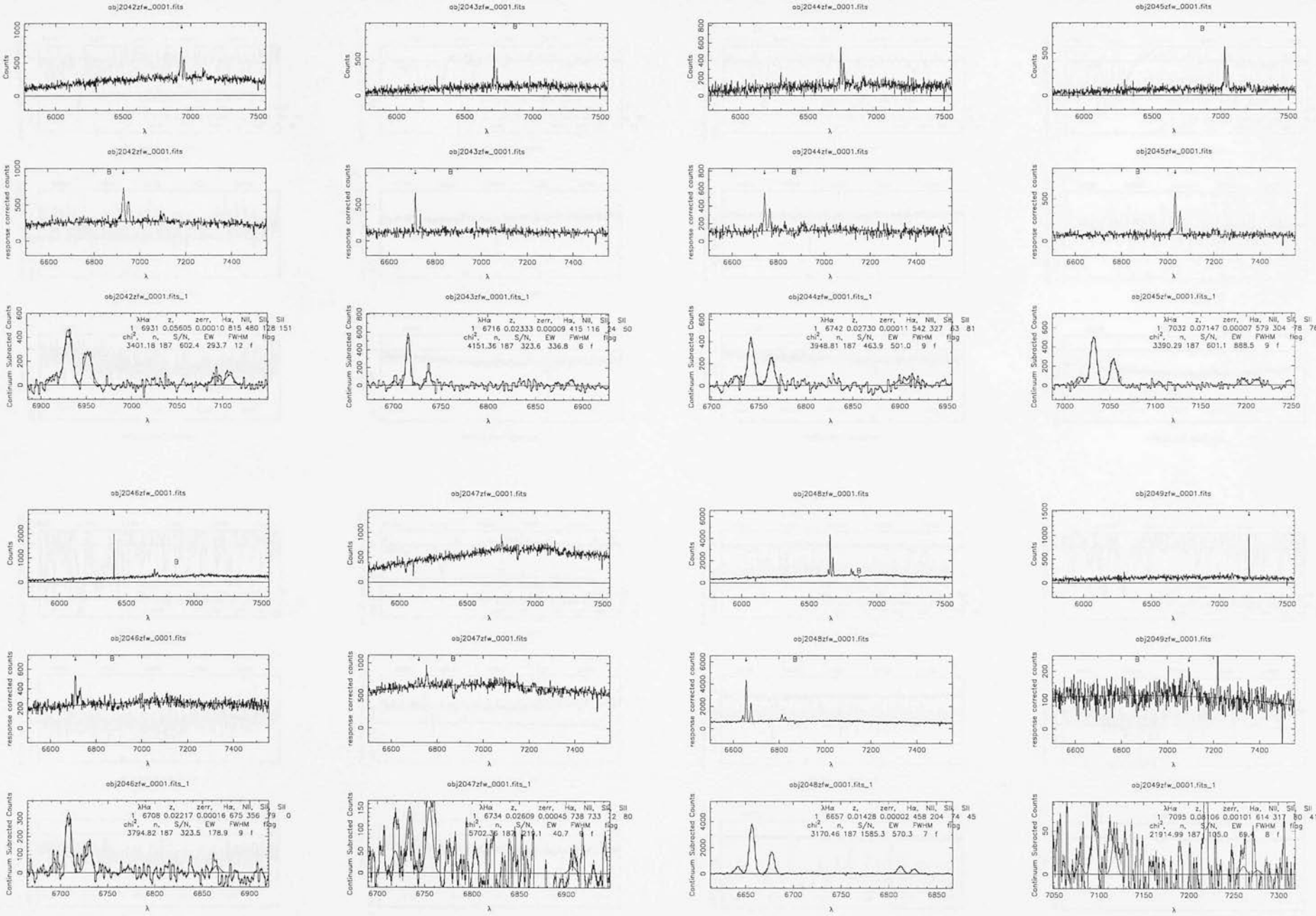
obj2042zfw_0001.fits
obj2043zfw_0001.fits
obj2044zfw_0001.fits
obj2045zfw_0001.fits
Counts
λ
obj2042zfw_0001.fits
obj2043zfw_0001.fits
obj2044zfw_0001.fits
obj2045zfw_0001.fits
response corrected counts
λ
obj2042zfw_0001.fits_1
obj2043zfw_0001.fits_1
obj2044zfw_0001.fits_1
obj2045zfw_0001.fits_1
Continuum Subtracted Counts
λHα z, zerr, Hα, NII, SII SII
1 6931 0.05605 0.00010 815 480 128 151
chi², n, S/N, EW FWHM flag
3401.18 187 602.4 293.7 12 f
λHα z, zerr, Hα, NII, SII SII
1 6716 0.02333 0.00009 415 116 24 50
chi², n, S/N, EW FWHM flag
4151.36 187 323.6 336.8 6 f
λHα z, zerr, Hα, NII, SII SII
1 6742 0.02730 0.00011 542 327 63 81
chi², n, S/N, EW FWHM flag
3948.81 187 463.9 501.0 9 f
λHα z, zerr, Hα, NII, SII SII
1 7032 0.07147 0.00007 579 304 78 76
chi², n, S/N, EW FWHM flag
3390.29 187 601.1 888.5 9 f
obj2046zfw_0001.fits
obj2047zfw_0001.fits
obj2048zfw_0001.fits
obj2049zfw_0001.fits
Counts
λ
obj2046zfw_0001.fits
obj2047zfw_0001.fits
obj2048zfw_0001.fits
obj2049zfw_0001.fits
response corrected counts
λ
obj2046zfw_0001.fits_1
obj2047zfw_0001.fits_1
obj2048zfw_0001.fits_1
obj2049zfw_0001.fits_1
Continuum Subtracted Counts
λHα z, zerr, Hα, NII, SII SII
1 6708 0.02217 0.00016 675 356 79 0
chi², n, S/N, EW FWHM flag
3794.82 187 323.5 178.9 9 f
λHα z, zerr, Hα, NII, SII SII
1 6734 0.02609 0.00045 738 733 12 80
chi², n, S/N, EW FWHM flag
5702.36 187 219.1 40.7 9 f
λHα z, zerr, Hα, NII, SII SII
1 6657 0.01428 0.00002 458 204 74 45
chi², n, S/N, EW FWHM flag
3170.46 187 1585.3 570.3 7 f
λHα z, zerr, Hα, NII, SII SII
1 7095 0.08106 0.00101 614 317 80 41
chi², n, S/N, EW FWHM flag
21914.99 187 105.0 69.4 8 f
λ

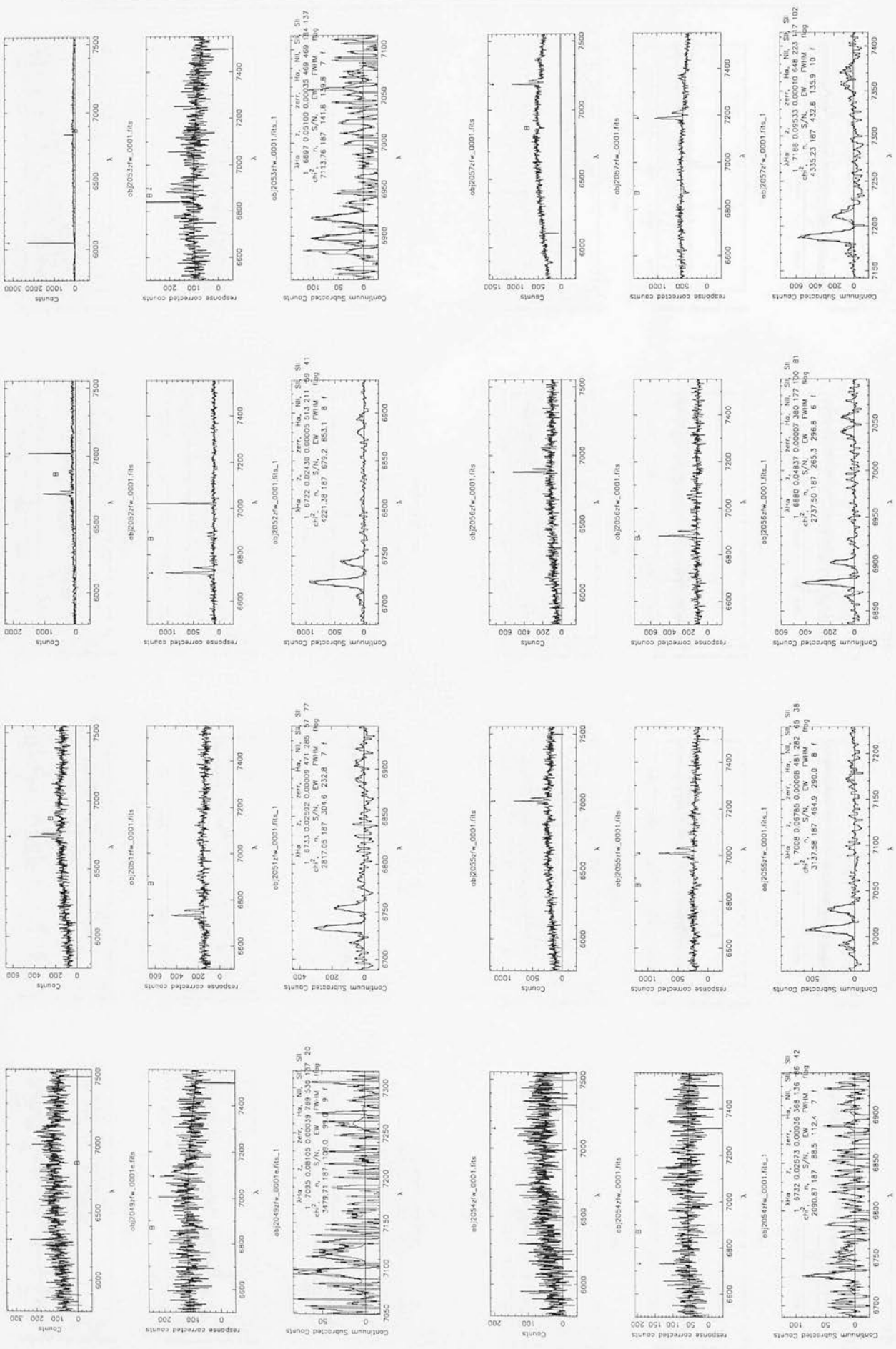

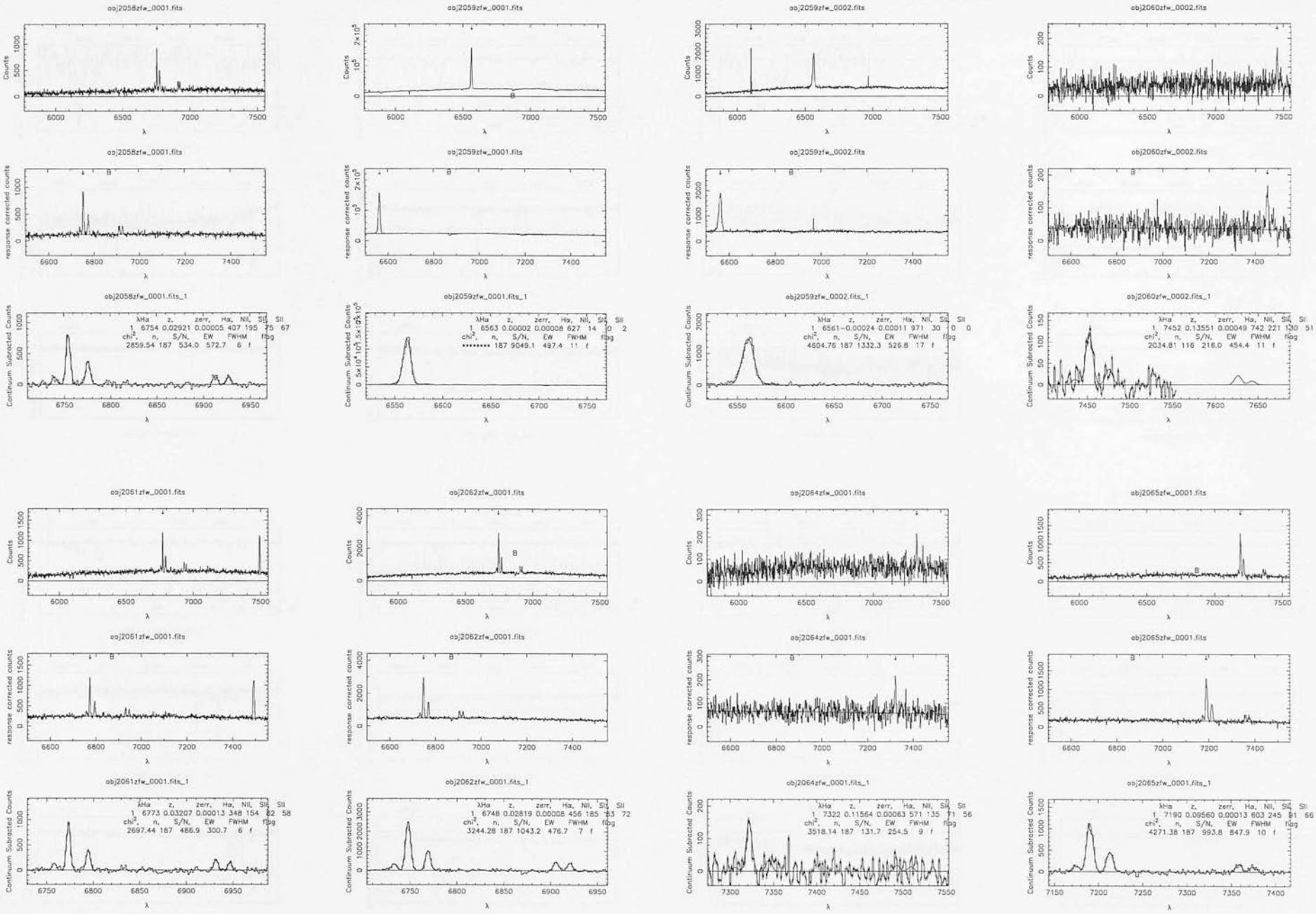
obj2058zfw_0001.fits
obj2059zfw_0001.fits
obj2059zfw_0002.fits
obj2060zfw_0002.fits
obj2058zfw_0001.fits_1
obj2059zfw_0001.fits_1
obj2059zfw_0002.fits_1
obj2060zfw_0002.fits_1
obj2061zfw_0001.fits
obj2062zfw_0001.fits
obj2064zfw_0001.fits
obj2065zfw_0001.fits
obj2061zfw_0001.fits_1
obj2062zfw_0001.fits_1
obj2064zfw_0001.fits_1
obj2065zfw_0001.fits_1
Counts
response corrected counts
Continuum Subtracted Counts
λ

obj2065zfw_0002.fits
obj2065zfw_0002.fits_1
obj2066zfw_0001.fits
obj2066zfw_0001.fits_1
obj2067zfw_0001.fits
obj2067zfw_0001.fits_1
obj2068zfw_0001.fits
obj2068zfw_0001.fits_1
obj2069zfw_0001.fits
obj2069zfw_0001.fits_1
obj2070zfw_0001.fits
obj2070zfw_0001.fits_1
obj2071zfw_0001.fits
obj2071zfw_0001.fits_1
obj2072zfw_0001.fits
obj2072zfw_0001.fits_1
obj2073zfw_0001.fits
obj2073zfw_0001.fits_1
obj2074zfw_0001.fits
obj2074zfw_0001.fits_1
obj2076zfw_0001.fits
obj2076zfw_0001.fits_1
Counts
response corrected counts
Continuum Subtracted Counts
λ

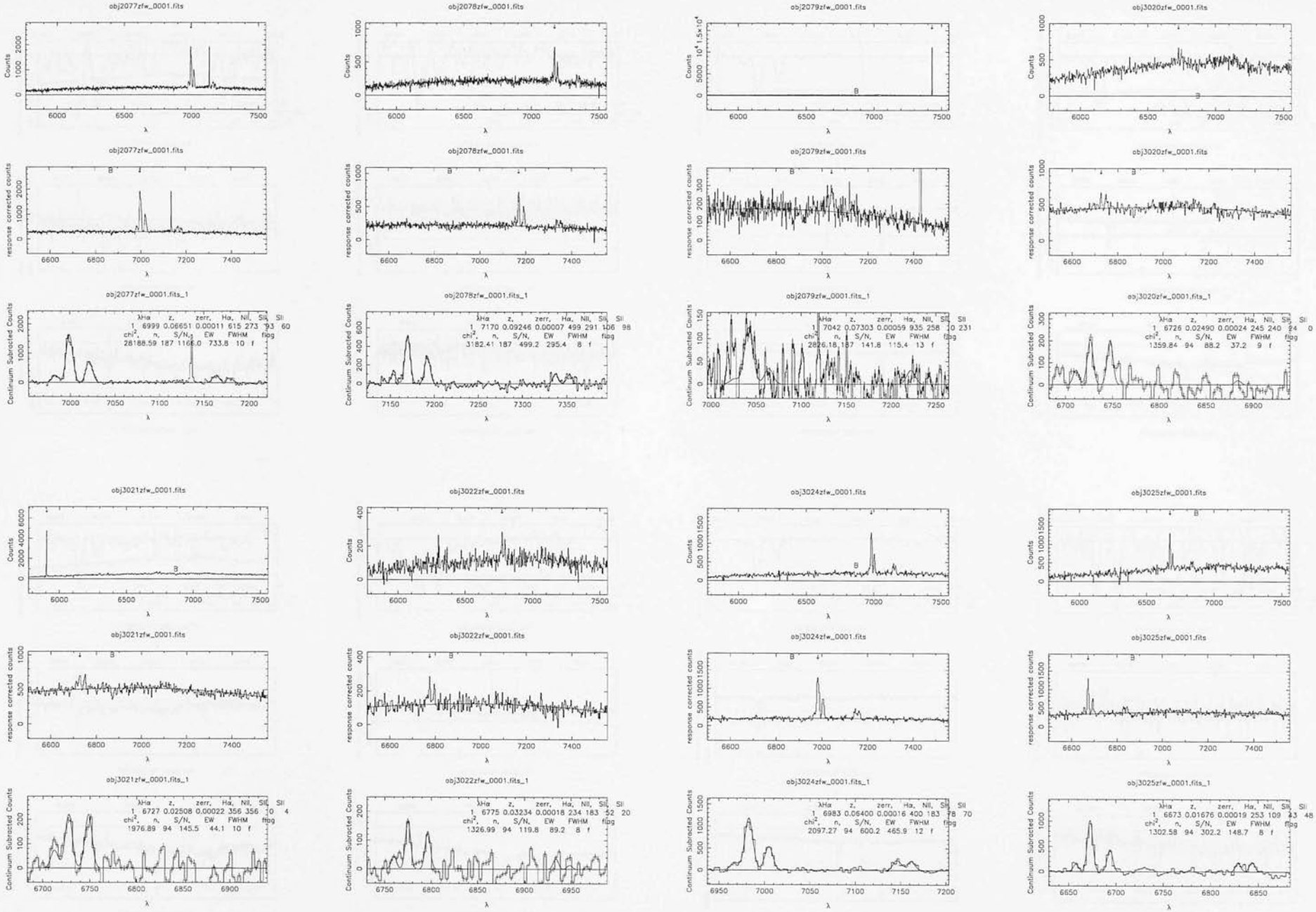
obj2077zfw_0001.fits
obj2078zfw_0001.fits
obj2079zfw_0001.fits
obj3020zfw_0001.fits
Counts
λ
response corrected counts
obj2077zfw_0001.fits_1
obj2078zfw_0001.fits_1
obj2079zfw_0001.fits_1
obj3020zfw_0001.fits_1
Continuum Subtracted Counts
λHα z zerr Hα NII SII SII
1 6999 0.06651 0.00011 615 273 93 60
chi² n S/N EW FWHM flag
28188.59 187 1166.0 733.8 10 f
1 7170 0.09246 0.00007 499 291 106 98
3182.41 187 499.2 295.4 8 f
1 7042 0.07303 0.00059 935 258 10 231
2826.18 187 141.8 115.4 13 f
1 6726 0.02490 0.00024 245 240 24 0
1359.84 94 88.2 37.2 9 f
obj3021zfw_0001.fits
obj3022zfw_0001.fits
obj3024zfw_0001.fits
obj3025zfw_0001.fits
obj3021zfw_0001.fits_1
obj3022zfw_0001.fits_1
obj3024zfw_0001.fits_1
obj3025zfw_0001.fits_1
1 6727 0.02508 0.00022 356 356 10 4
1976.89 94 145.5 44.1 10 f
1 6775 0.03234 0.00018 234 183 52 20
1326.99 94 119.8 89.2 8 f
1 6983 0.06400 0.00016 400 183 78 70
2097.27 94 600.2 465.9 12 f
1 6673 0.01676 0.00019 253 109 43 48
1302.58 94 302.2 148.7 8 f

obj3025zfw_0002.fits
obj3025zfw_0002.fits
obj3025zfw_0002.fits_1
obj3026zfw_0001.fits
obj3026zfw_0001.fits
obj3026zfw_0001.fits_1
obj3027zfw_0001.fits
obj3027zfw_0001.fits
obj3027zfw_0001.fits_1
obj3028zfw_0001.fits
obj3028zfw_0001.fits
obj3028zfw_0001.fits_1
obj3029zfw_0001.fits
obj3029zfw_0001.fits
obj3029zfw_0001.fits_1
obj3031zfw_0002.fits
obj3031zfw_0002.fits
obj3031zfw_0002.fits_1
obj3058zfw_0001.fits
obj3058zfw_0001.fits
obj3058zfw_0001.fits_1
obj3059zfw_0001.fits
obj3059zfw_0001.fits
obj3059zfw_0001.fits_1
Counts
response corrected counts
Continuum Subtracted Counts
λ

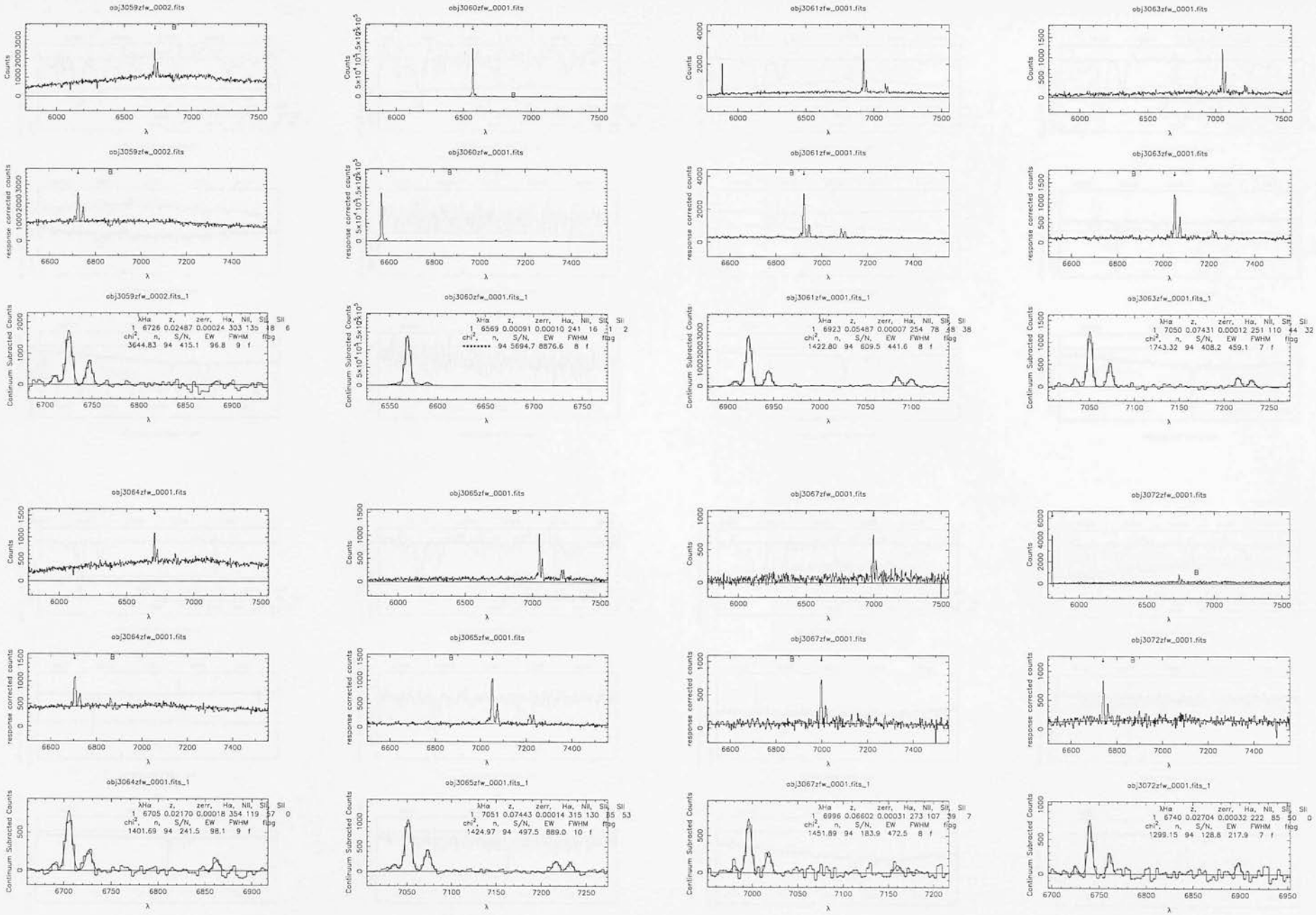
obj3059zfw_0002.fits
obj3060zfw_0001.fits
obj3061zfw_0001.fits
obj3063zfw_0001.fits
Counts
response corrected counts
Continuum Subtracted Counts
λ
obj3059zfw_0002.fits_1
λHα z zerr Hα NII SII SII
1 6726 0.02487 0.00024 303 135 48 6
chi², n, S/N, EW FWHM flag
3644.83 94 415.1 96.8 9 f
obj3060zfw_0001.fits_1
λHα z zerr Hα NII SII SII
1 6569 0.00091 0.00010 241 16 11 2
chi², n, S/N, EW FWHM flag
94 5694.7 8876.6 8 f
obj3061zfw_0001.fits_1
λHα z zerr Hα NII SII SII
1 6923 0.05487 0.00007 254 78 48 38
chi², n, S/N, EW FWHM flag
1422.80 94 609.5 441.6 8 f
obj3063zfw_0001.fits_1
λHα z zerr Hα NII SII SII
1 7050 0.07431 0.00012 251 110 44 32
chi², n, S/N, EW FWHM flag
1743.32 94 408.2 459.1 7 f
obj3064zfw_0001.fits
obj3065zfw_0001.fits
obj3067zfw_0001.fits
obj3072zfw_0001.fits
obj3064zfw_0001.fits_1
λHα z zerr Hα NII SII SII
1 6705 0.02170 0.00018 354 119 57 0
chi², n, S/N, EW FWHM flag
1401.69 94 241.5 98.1 9 f
obj3065zfw_0001.fits_1
λHα z zerr Hα NII SII SII
1 7051 0.07443 0.00014 315 130 65 53
chi², n, S/N, EW FWHM flag
1424.97 94 497.5 889.0 10 f
obj3067zfw_0001.fits_1
λHα z zerr Hα NII SII SII
1 6996 0.06602 0.00031 273 107 39 7
chi², n, S/N, EW FWHM flag
1451.89 94 183.9 472.5 8 f
obj3072zfw_0001.fits_1
λHα z zerr Hα NII SII SII
1 6740 0.02704 0.00032 222 85 50 0
chi², n, S/N, EW FWHM flag
1299.15 94 128.8 217.9 7 f

obj3076z1w_0001.fits
Counts
λ
obj3076z1w_0001.fits
response corrected counts
λ
obj3076z1w_0001.fits_1
Continuum Subtracted Counts
λ
obj3077z1w_0001.fits
Counts
λ
obj3077z1w_0001.fits
response corrected counts
λ
obj3077z1w_0001.fits_1
Continuum Subtracted Counts
λ
obj3078z1w_0001.fits
Counts
λ
obj3078z1w_0001.fits
response corrected counts
λ
obj3078z1w_0001.fits_1
Continuum Subtracted Counts
λ
obj3075z1w_0001.fits
Counts
λ
obj3075z1w_0001.fits
response corrected counts
λ
obj3075z1w_0001.fits_1
Continuum Subtracted Counts
λ
obj3079z1w_0001e.fits
Counts
λ
obj3079z1w_0001e.fits
response corrected counts
λ
obj3079z1w_0001e.fits_1
Continuum Subtracted Counts
λ
obj3080z1w_0001.fits
Counts
λ
obj3080z1w_0001.fits
response corrected counts
λ
obj3080z1w_0001.fits_1
Continuum Subtracted Counts
λ
obj3083z1w_0001.fits
Counts
λ
obj3083z1w_0001.fits
response corrected counts
λ
obj3083z1w_0001.fits_1
Continuum Subtracted Counts
λ
obj3087z1w_0001.fits
Counts
λ
obj3087z1w_0001.fits
response corrected counts
λ
obj3087z1w_0001.fits_1
Continuum Subtracted Counts
λ

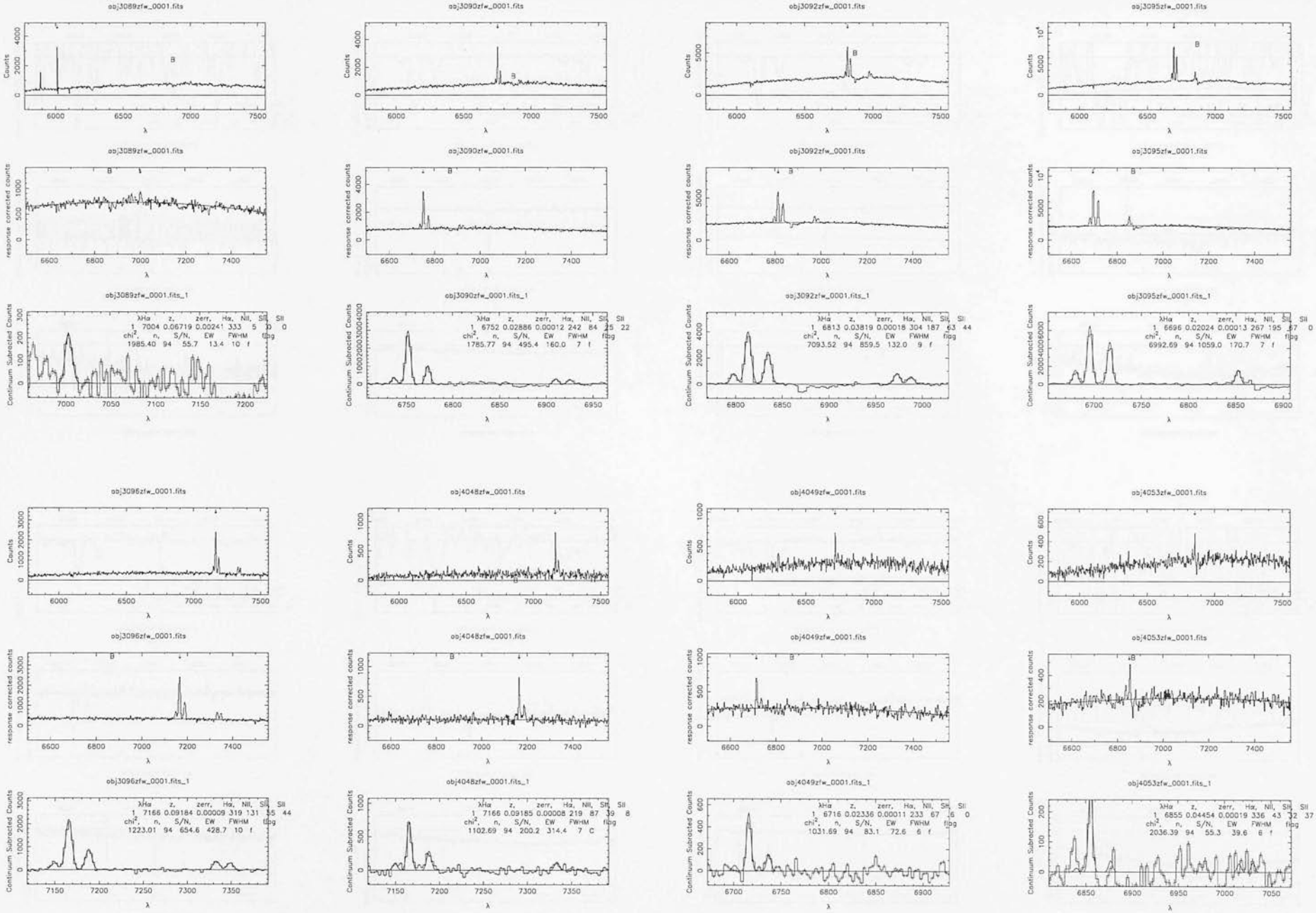
obj3089zfw_0001.fits
obj3090zfw_0001.fits
obj3092zfw_0001.fits
obj3095zfw_0001.fits
Counts
response corrected counts
Continuum Subtracted Counts
λ
obj3089zfw_0001.fits_1
obj3090zfw_0001.fits_1
obj3092zfw_0001.fits_1
obj3095zfw_0001.fits_1
obj3096zfw_0001.fits
obj4048zfw_0001.fits
obj4049zfw_0001.fits
obj4053zfw_0001.fits
obj3096zfw_0001.fits_1
obj4048zfw_0001.fits_1
obj4049zfw_0001.fits_1
obj4053zfw_0001.fits_1

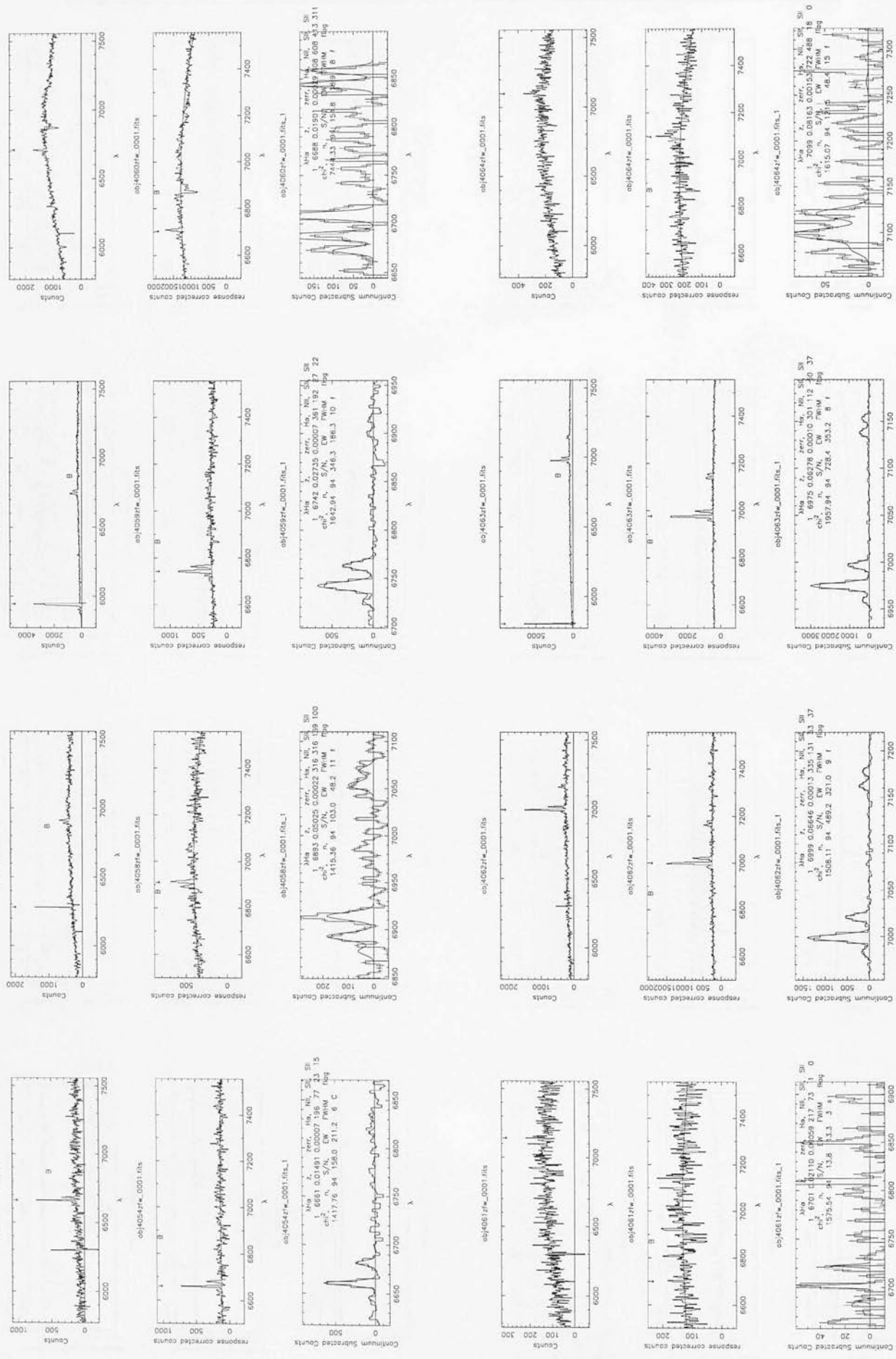

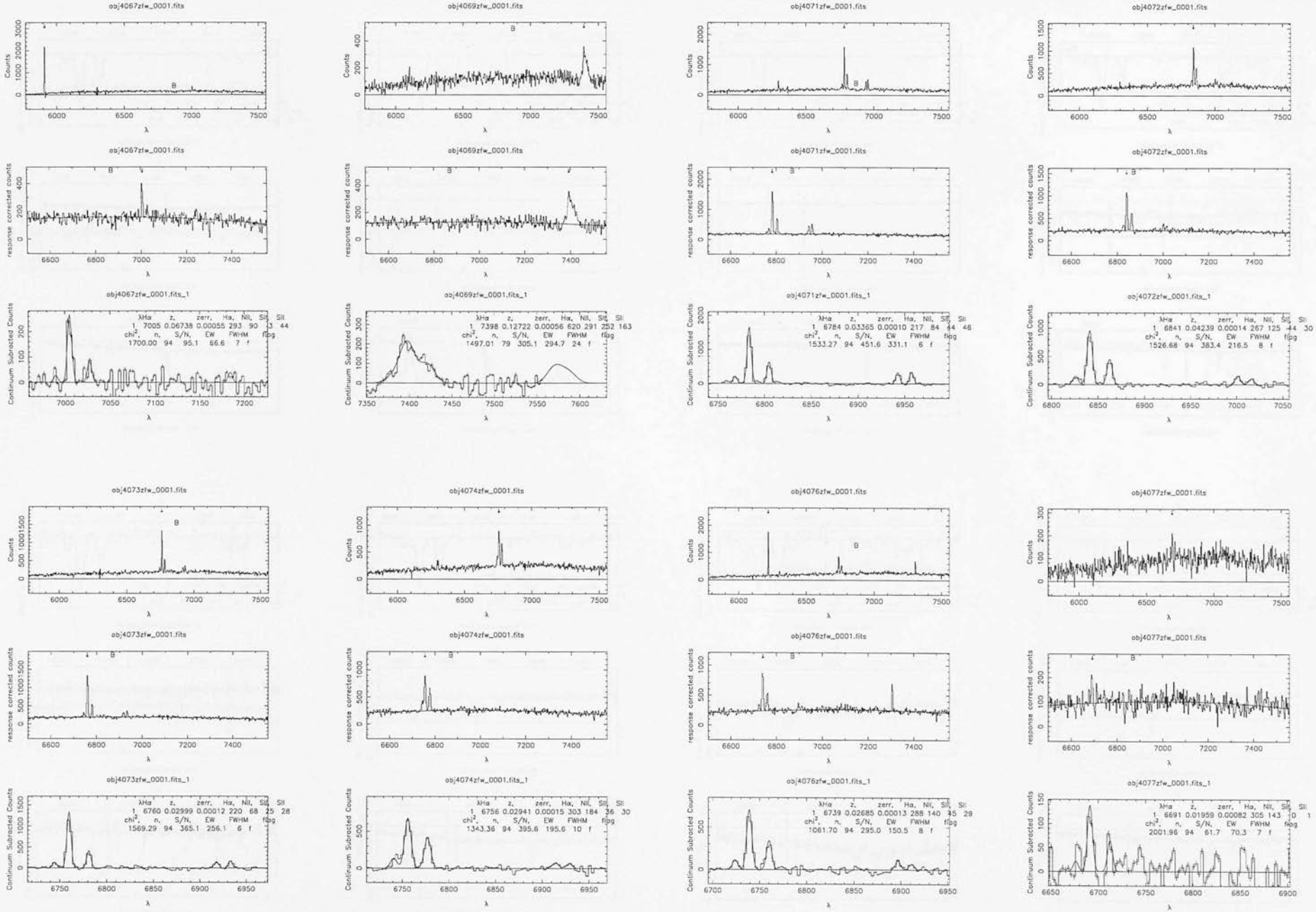
obj4067zfw_0001.fits
obj4069zfw_0001.fits
obj4071zfw_0001.fits
obj4072zfw_0001.fits
obj4067zfw_0001.fits_1
obj4069zfw_0001.fits_1
obj4071zfw_0001.fits_1
obj4072zfw_0001.fits_1
obj4073zfw_0001.fits
obj4074zfw_0001.fits
obj4076zfw_0001.fits
obj4077zfw_0001.fits
obj4073zfw_0001.fits_1
obj4074zfw_0001.fits_1
obj4076zfw_0001.fits_1
obj4077zfw_0001.fits_1
Counts
response corrected counts
Continuum Subracted Counts
λ

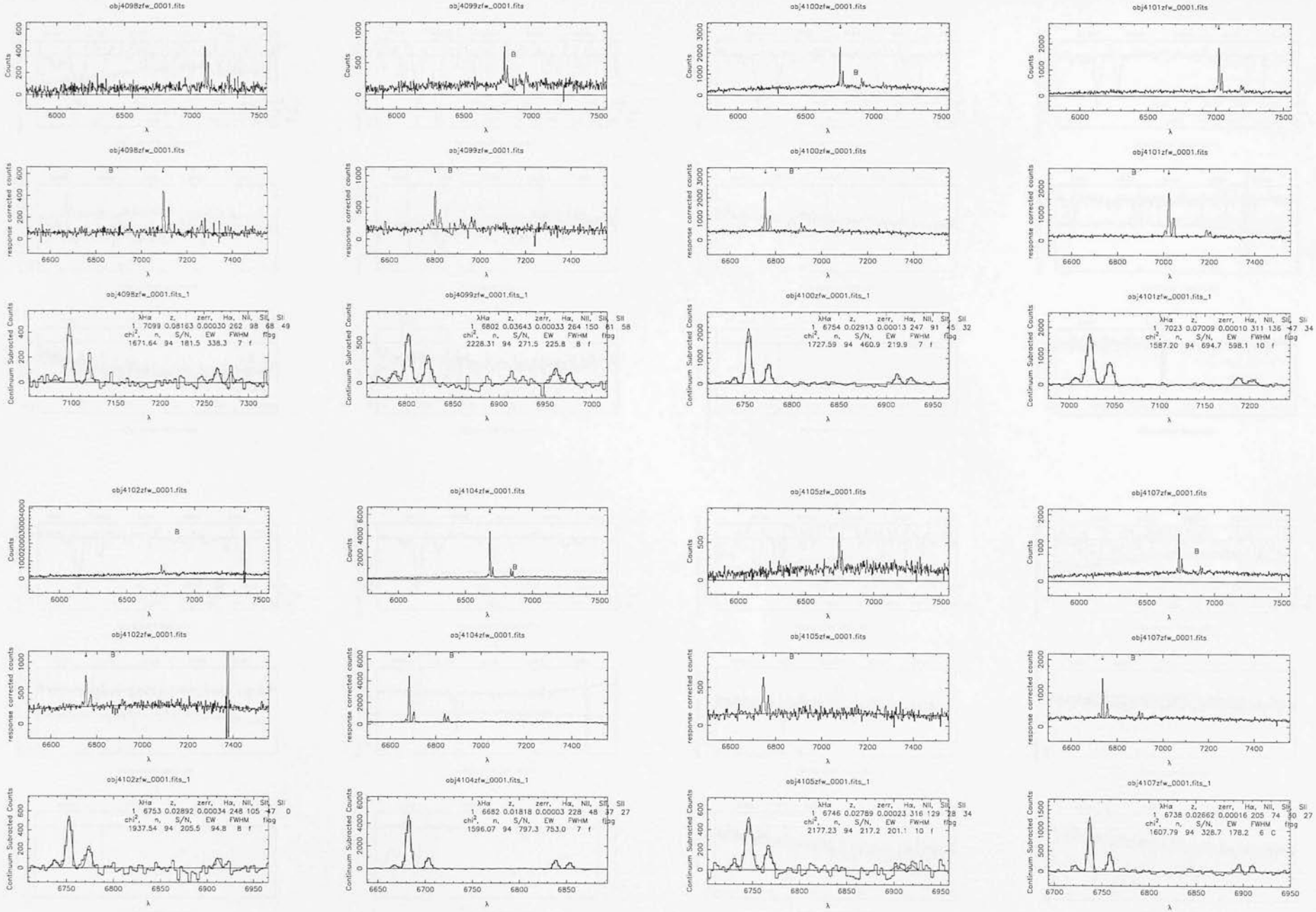
obj4098zfw_0001.fits
obj4099zfw_0001.fits
obj4100zfw_0001.fits
obj4101zfw_0001.fits
Counts
λ
obj4098zfw_0001.fits
obj4099zfw_0001.fits
obj4100zfw_0001.fits
obj4101zfw_0001.fits
response corrected counts
λ
obj4098zfw_0001.fits_1
obj4099zfw_0001.fits_1
obj4100zfw_0001.fits_1
obj4101zfw_0001.fits_1
Continuum Subtracted Counts
λ
obj4102zfw_0001.fits
obj4104zfw_0001.fits
obj4105zfw_0001.fits
obj4107zfw_0001.fits
Counts
λ
obj4102zfw_0001.fits
obj4104zfw_0001.fits
obj4105zfw_0001.fits
obj4107zfw_0001.fits
response corrected counts
λ
obj4102zfw_0001.fits_1
obj4104zfw_0001.fits_1
obj4105zfw_0001.fits_1
obj4107zfw_0001.fits_1
Continuum Subtracted Counts
λ

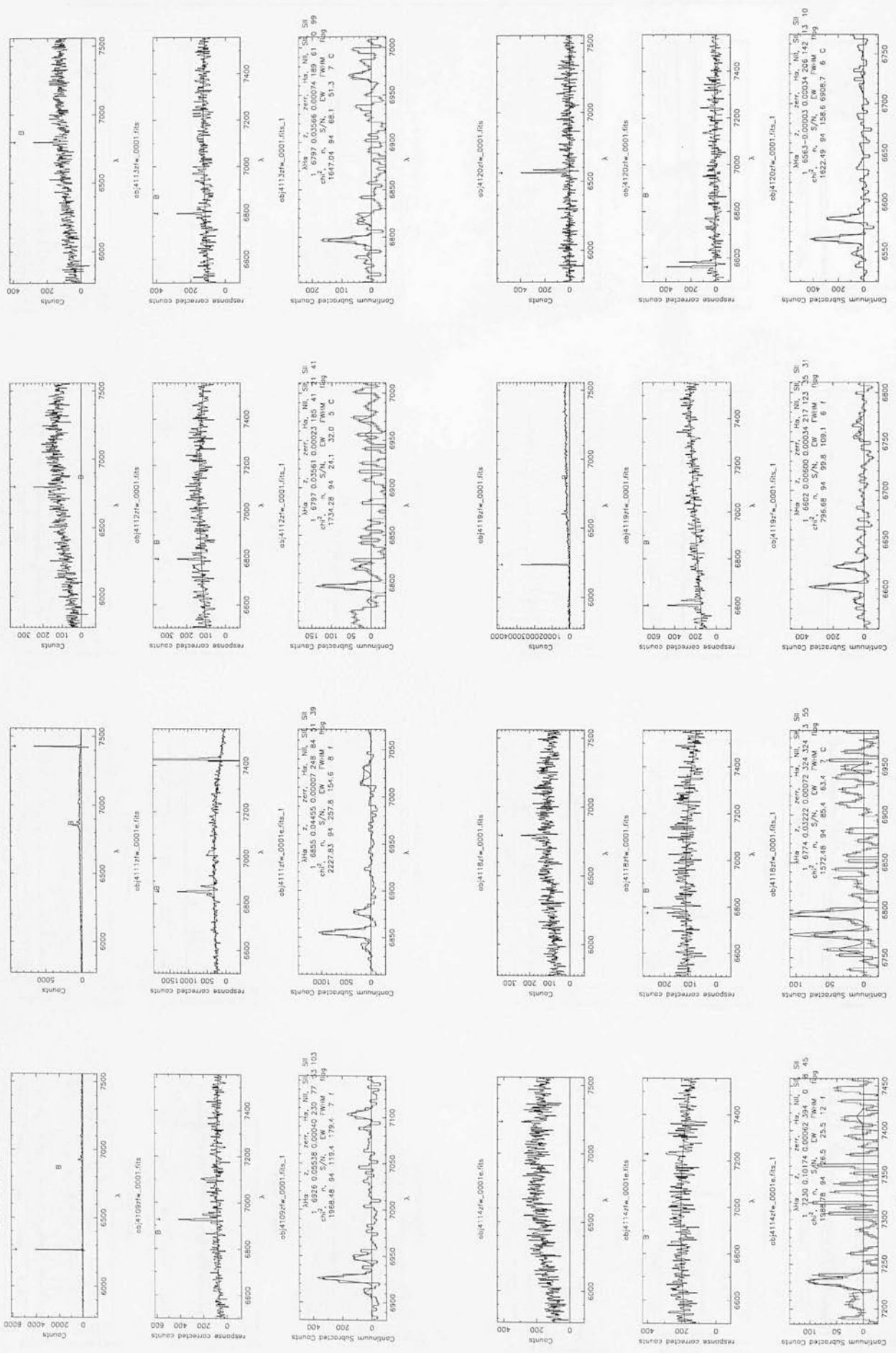

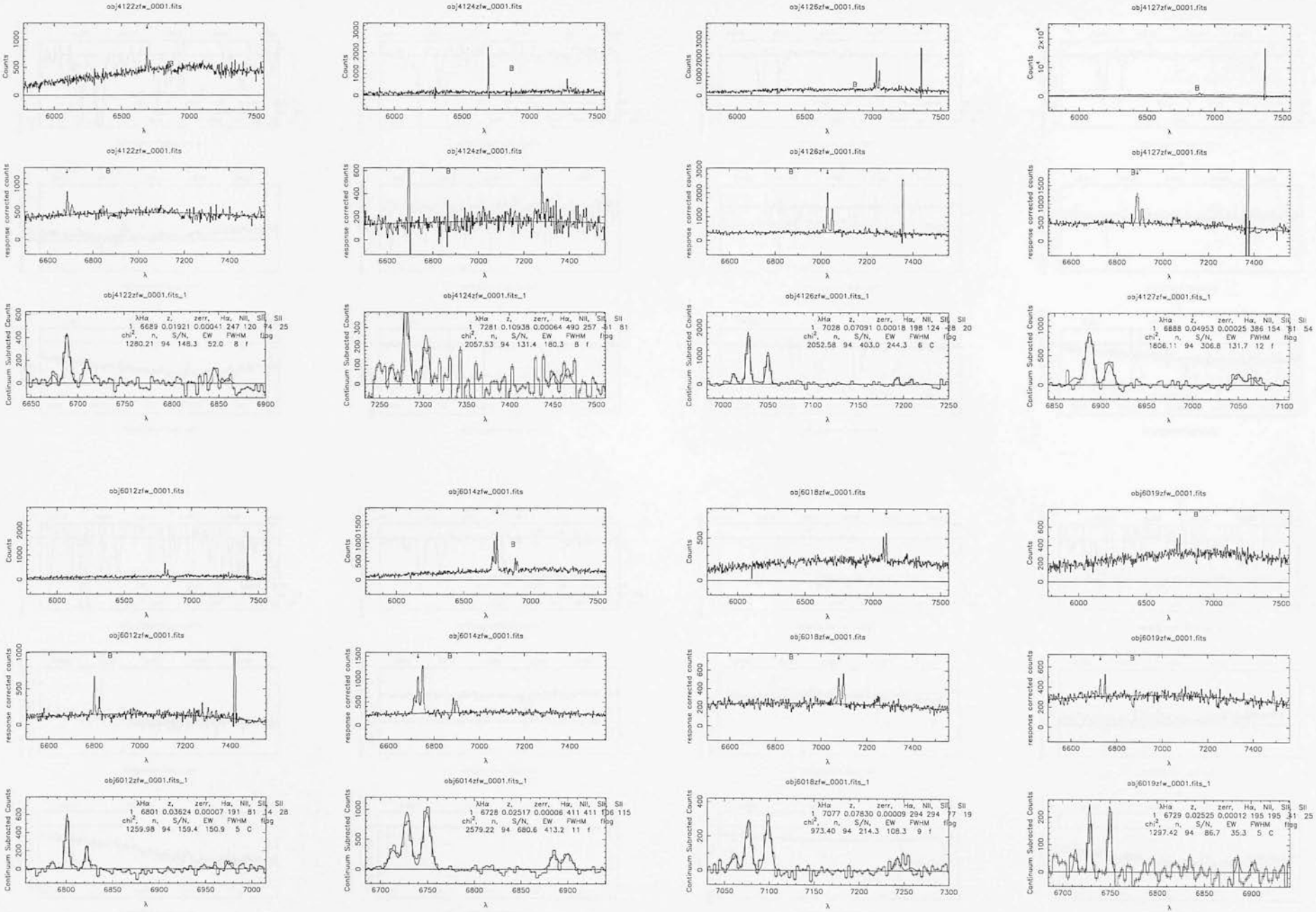
obj4122zfw_0001.fits
obj4124zfw_0001.fits
obj4126zfw_0001.fits
obj4127zfw_0001.fits
Counts
response corrected counts
Continuum Subtracted Counts
λ
obj4122zfw_0001.fits_1
obj4124zfw_0001.fits_1
obj4126zfw_0001.fits_1
obj4127zfw_0001.fits_1
λHα z zerr Hα NII SII SII
1 6689 0.01921 0.00041 247 120 74 25
chi² n S/N EW FWHM flag
1280.21 94 148.3 52.0 8 f
1 7281 0.10938 0.00064 490 257 81 81
2057.53 94 131.4 180.3 8 f
1 7028 0.07091 0.00018 198 124 28 20
2052.58 94 403.0 244.3 6 C
1 6888 0.04953 0.00025 386 154 81 54
1806.11 94 306.8 131.7 12 f
obj6012zfw_0001.fits
obj6014zfw_0001.fits
obj6018zfw_0001.fits
obj6019zfw_0001.fits
obj6012zfw_0001.fits_1
obj6014zfw_0001.fits_1
obj6018zfw_0001.fits_1
obj6019zfw_0001.fits_1
1 6801 0.03624 0.00007 191 81 14 28
1259.98 94 159.4 150.9 5 C
1 6728 0.02517 0.00006 411 411 106 115
2579.22 94 680.6 413.2 11 f
1 7077 0.07830 0.00009 294 294 77 19
973.40 94 214.3 108.3 9 f
1 6729 0.02525 0.00012 195 195 31 25
1297.42 94 86.7 35.3 5 C

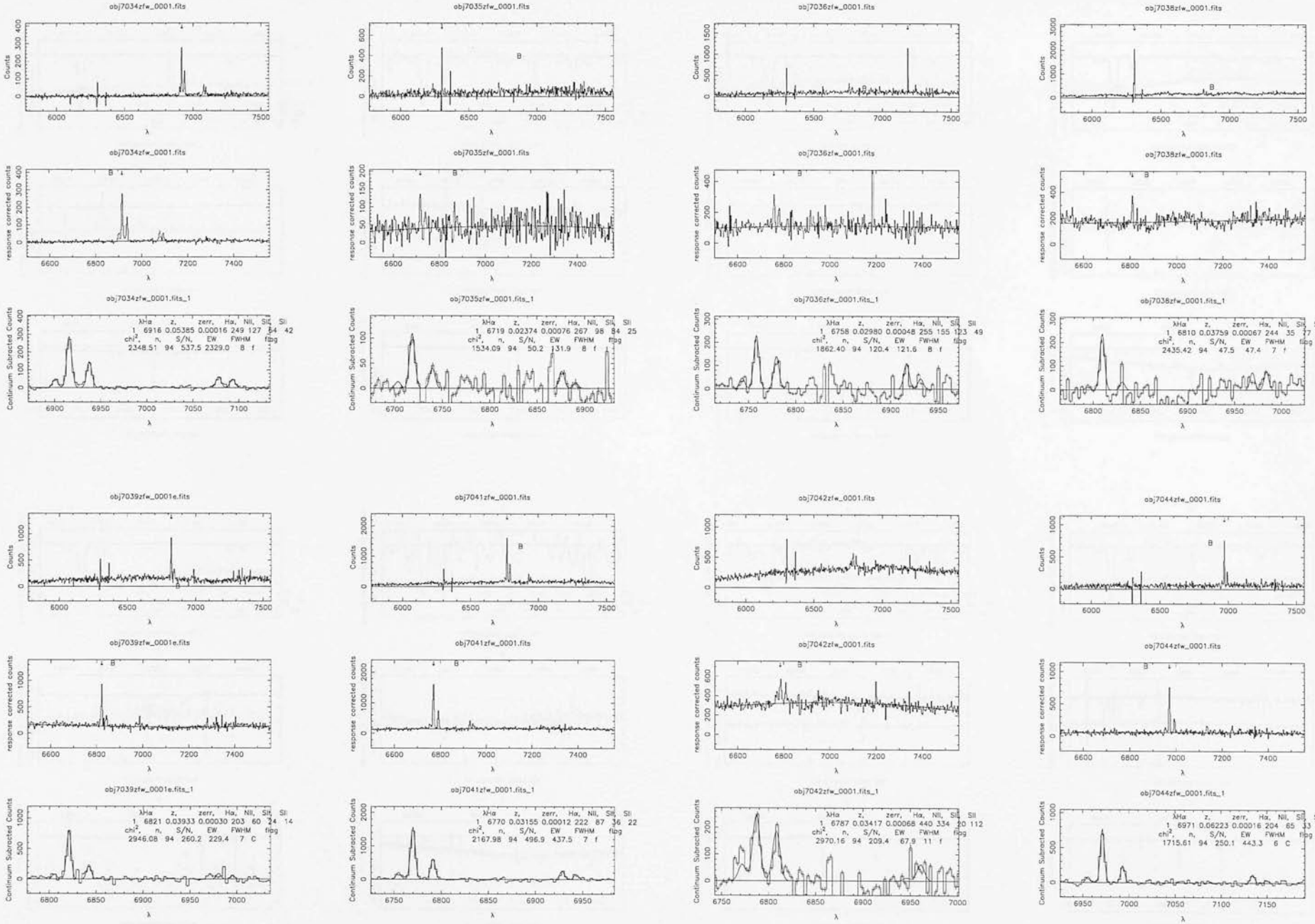
obj7034zfw_0001.fits
obj7035zfw_0001.fits
obj7036zfw_0001.fits
obj7038zfw_0001.fits
Counts
response corrected counts
Continuum Subtracted Counts
λ
obj7034zfw_0001.fits_1
λHα z zerr Hα NII SII SII
1 6916 0.05385 0.00016 249 127 64 42
chi² n S/N EW FWHM flag
2348.51 94 537.5 2329.0 8 f
obj7035zfw_0001.fits_1
λHα z zerr Hα NII SII SII
1 6719 0.02374 0.00076 267 98 84 25
chi² n S/N EW FWHM flag
1534.09 94 50.2 131.9 8 f
obj7036zfw_0001.fits_1
λHα z zerr Hα NII SII SII
1 6758 0.02980 0.00048 255 155 123 49
chi² n S/N EW FWHM flag
1862.40 94 120.4 121.6 8 f
obj7038zfw_0001.fits_1
λHα z zerr Hα NII SII SII
1 6810 0.03759 0.00067 244 35 77 81
chi² n S/N EW FWHM flag
2435.42 94 47.5 47.4 7 f
obj7039zfw_0001e.fits
obj7041zfw_0001.fits
obj7042zfw_0001.fits
obj7044zfw_0001.fits
obj7039zfw_0001e.fits_1
λHα z zerr Hα NII SII SII
1 6821 0.03933 0.00030 203 60 24 14
chi² n S/N EW FWHM flag
2946.08 94 260.2 229.4 7 C
obj7041zfw_0001.fits_1
λHα z zerr Hα NII SII SII
1 6770 0.03155 0.00012 222 87 36 22
chi² n S/N EW FWHM flag
2167.98 94 496.9 437.5 7 f
obj7042zfw_0001.fits_1
λHα z zerr Hα NII SII SII
1 6787 0.03417 0.00068 440 334 20 112
chi² n S/N EW FWHM flag
2970.16 94 209.4 67.9 11 f
obj7044zfw_0001.fits_1
λHα z zerr Hα NII SII SII
1 6971 0.06223 0.00016 204 65 33 10
chi² n S/N EW FWHM flag
1715.61 94 250.1 443.3 6 C

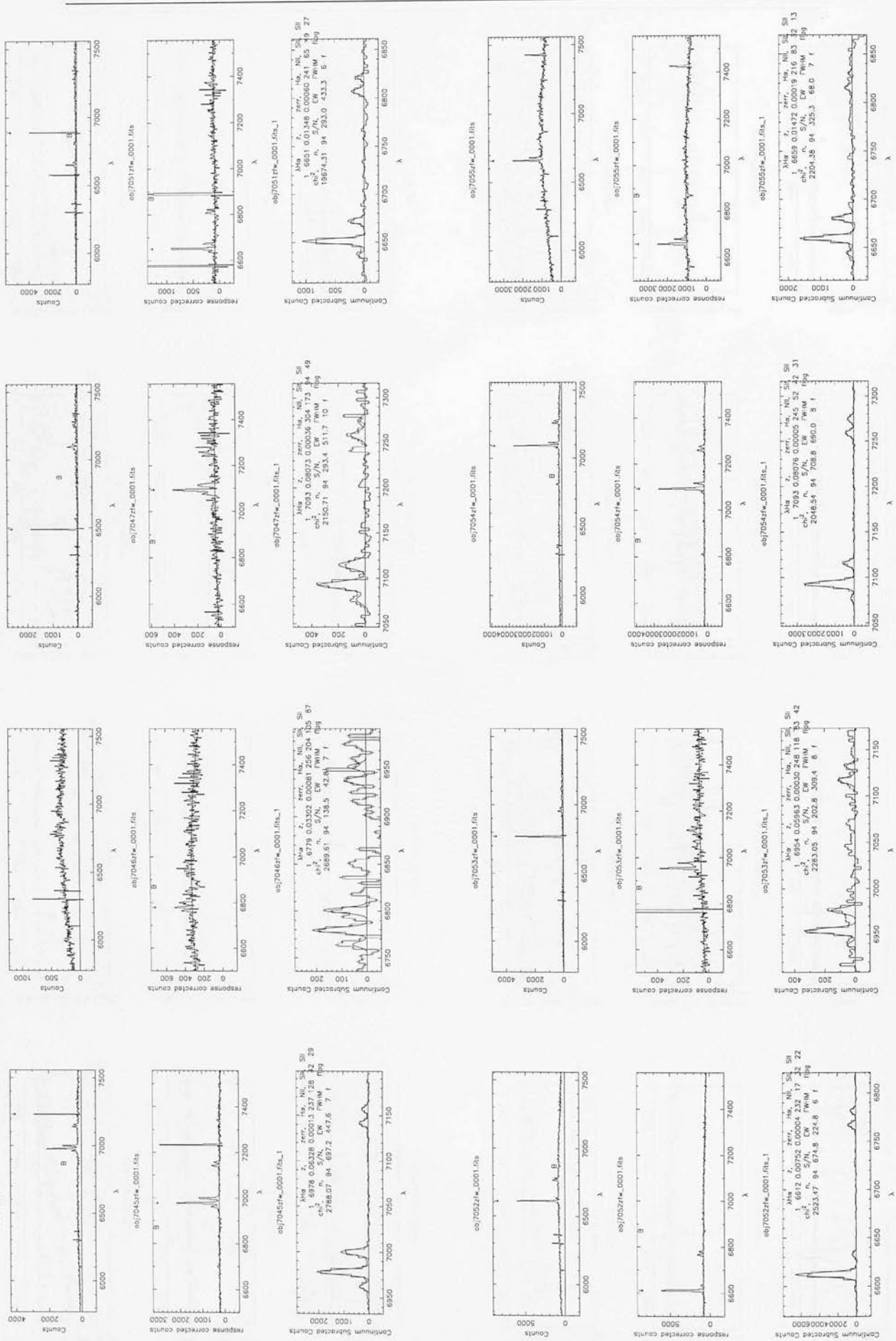

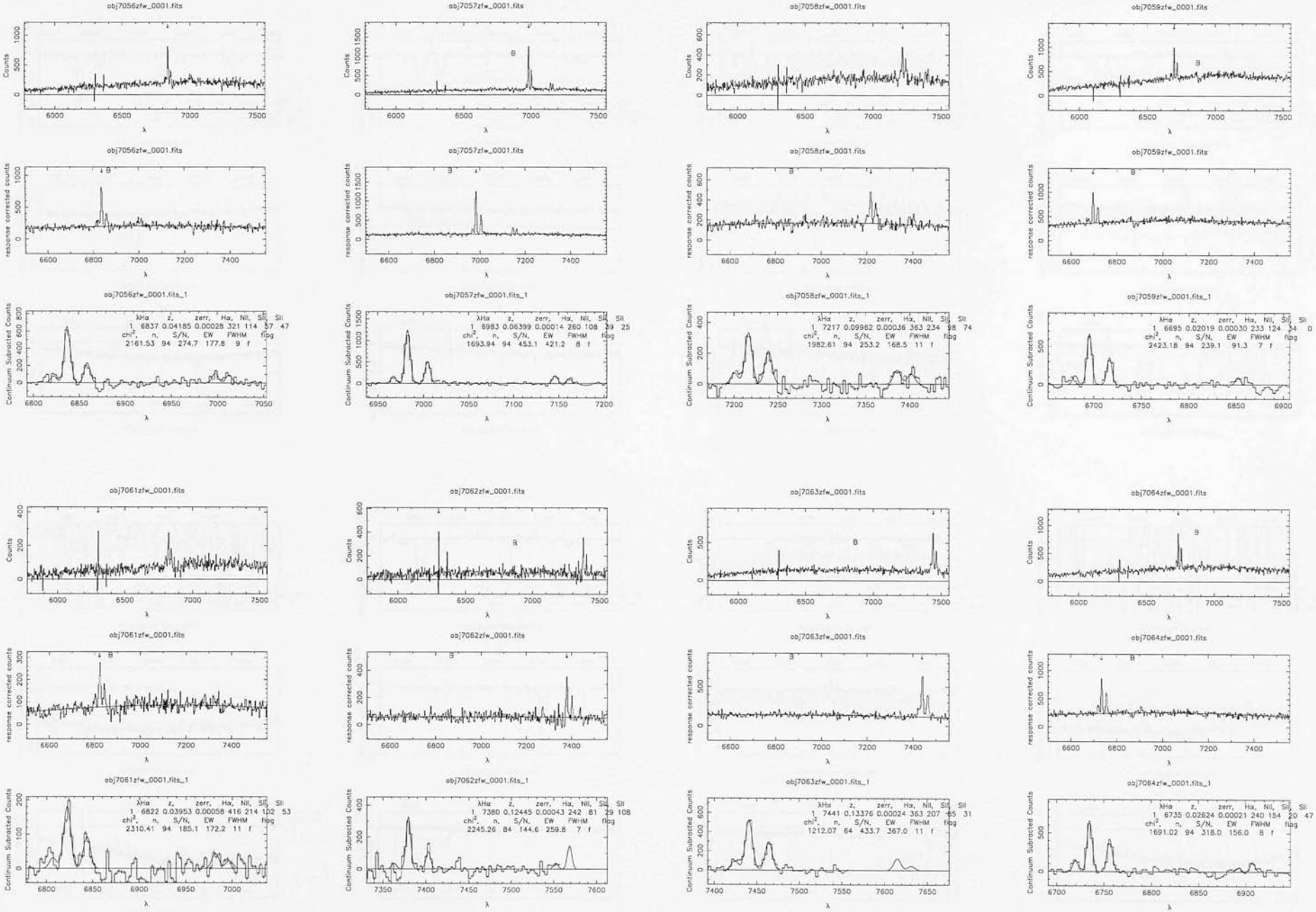
obj7056zfw_0001.fits
obj7057zfw_0001.fits
obj7058zfw_0001.fits
obj7059zfw_0001.fits
Counts
response corrected counts
Continuum Subracted Counts
λ
λHα z, zerr, Hα, NII, SII, SII
1 6837 0.04185 0.00028 321 114 57 47
chi², n, S/N, EW FWHM flag
2161.53 94 274.7 177.8 9 f
1 6983 0.06399 0.00014 260 108 39 25
1693.94 94 453.1 421.2 8 f
1 7217 0.09962 0.00036 363 234 98 74
1982.61 94 253.2 168.5 11 f
1 6695 0.02019 0.00030 233 124 34 0
2423.18 94 239.1 91.3 7 f
obj7061zfw_0001.fits
obj7062zfw_0001.fits
obj7063zfw_0001.fits
obj7064zfw_0001.fits
1 6822 0.03953 0.00058 416 214 102 53
2310.41 94 185.1 172.2 11 f
1 7380 0.12445 0.00043 242 81 29 108
2245.26 84 144.6 259.8 7 f
1 7441 0.13376 0.00024 363 207 65 31
1212.07 64 433.7 367.0 11 f
1 6735 0.02624 0.00021 240 154 20 47
1691.02 94 318.0 156.0 8 f

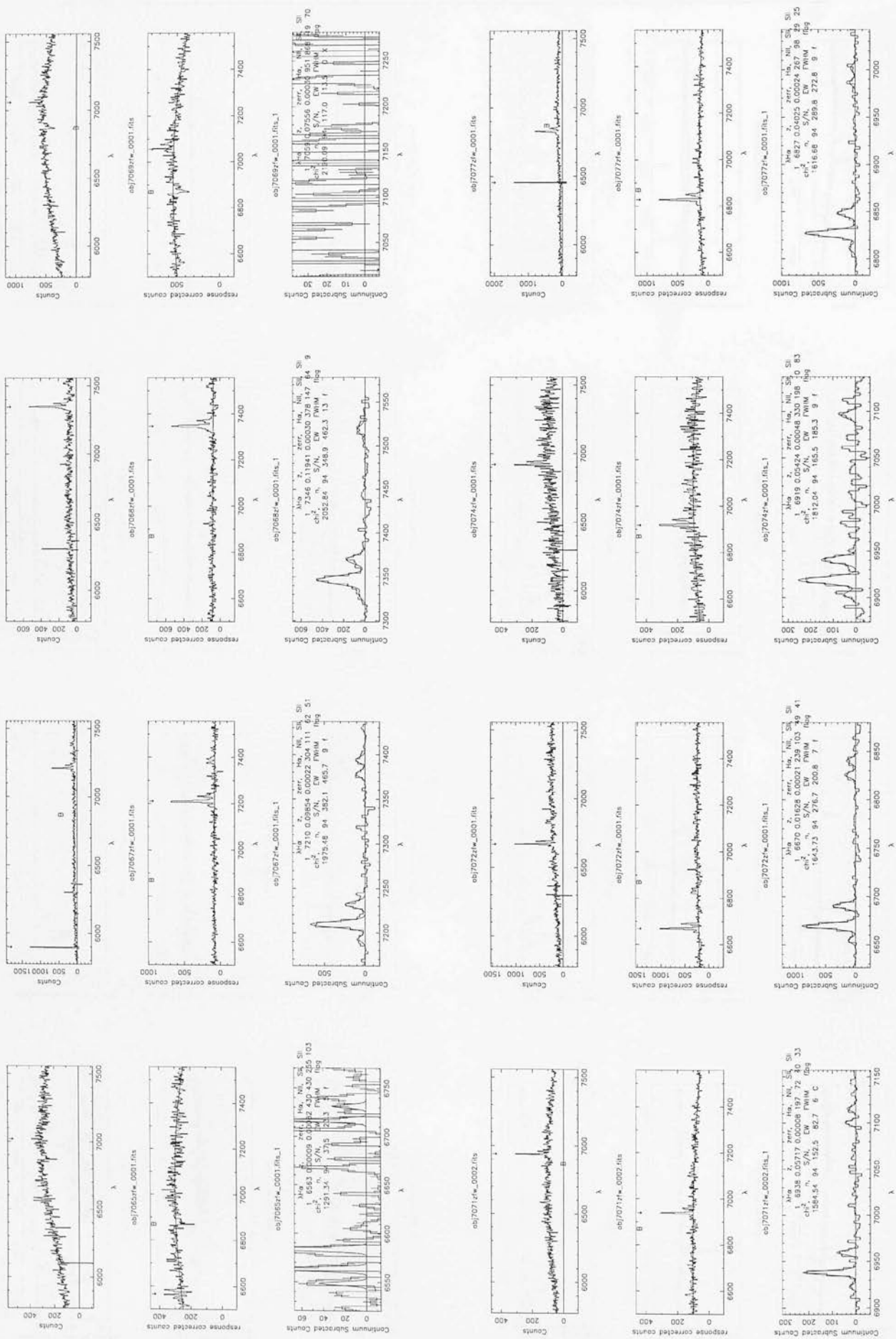

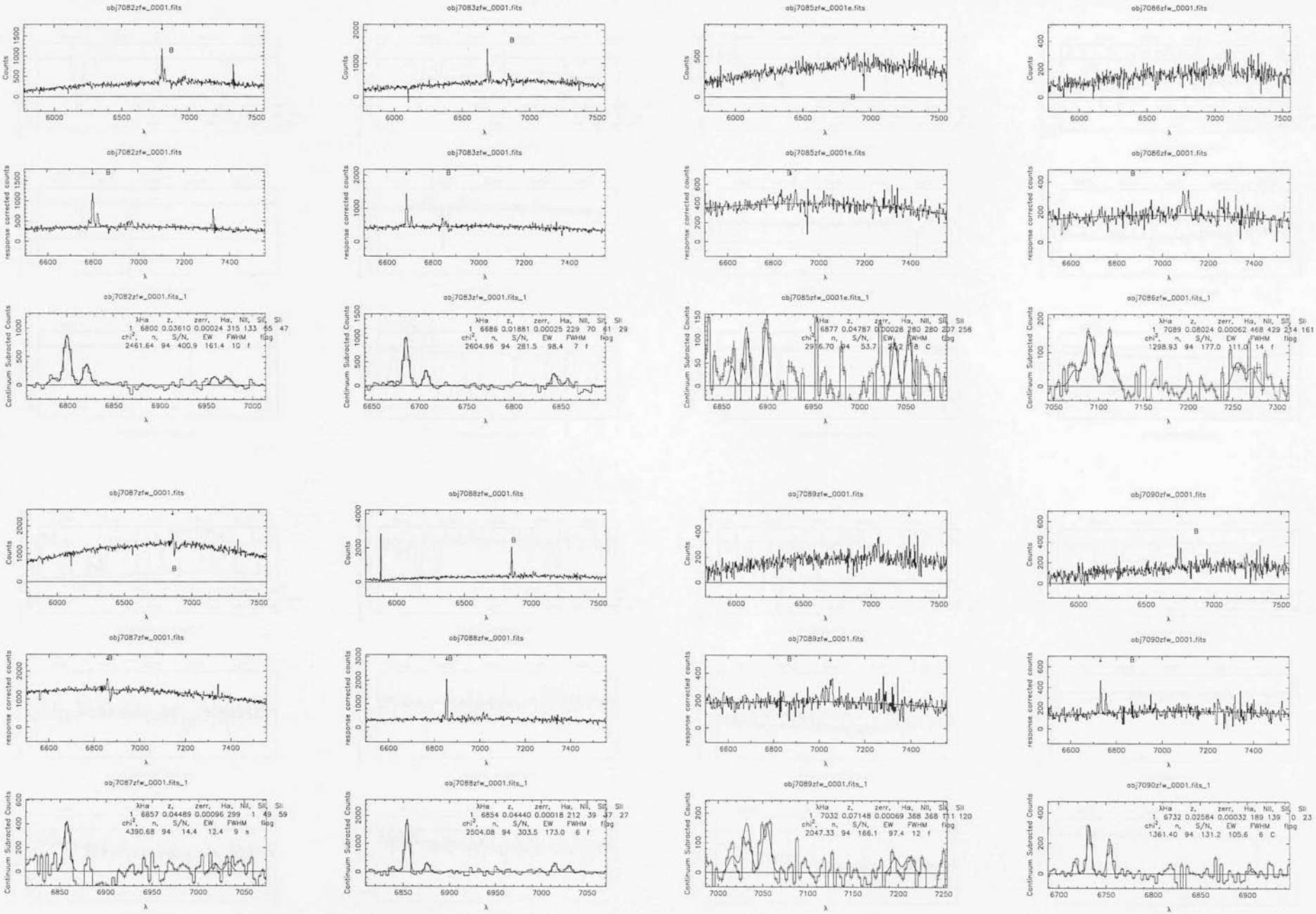
obj7082zfw_0001.fits
obj7083zfw_0001.fits
obj7085zfw_0001e.fits
obj7086zfw_0001.fits
Counts
response corrected counts
Continuum Subtracted Counts
λ
obj7082zfw_0001.fits_1
obj7083zfw_0001.fits_1
obj7085zfw_0001e.fits_1
obj7086zfw_0001.fits_1
λHα z zerr Hα NII SII SII
1 6800 0.03610 0.00024 315 133 55 47
chi² n S/N EW FWHM flag
2461.64 94 400.9 161.4 10 f
1 6686 0.01881 0.00025 229 70 61 29
chi² n S/N EW FWHM flag
2604.96 94 281.5 98.4 7 f
1 6877 0.04787 0.00028 280 280 207 258
chi² n S/N EW FWHM flag
2956.70 94 53.7 24.2 18 C
1 7089 0.08024 0.00062 468 429 214 161
chi² n S/N EW FWHM flag
1298.93 94 177.0 111.0 14 f
obj7087zfw_0001.fits
obj7088zfw_0001.fits
obj7089zfw_0001.fits
obj7090zfw_0001.fits
obj7087zfw_0001.fits_1
obj7088zfw_0001.fits_1
obj7089zfw_0001.fits_1
obj7090zfw_0001.fits_1
1 6857 0.04489 0.00096 299 1 49 59
chi² n S/N EW FWHM flag
4390.68 94 14.4 12.4 9 s
1 6854 0.04440 0.00018 212 39 37 27
chi² n S/N EW FWHM flag
2504.08 94 303.5 173.0 6 f
1 7032 0.07148 0.00069 368 368 111 120
chi² n S/N EW FWHM flag
2047.33 94 166.1 97.4 12 f
1 6732 0.02584 0.00032 189 139 70 23
chi² n S/N EW FWHM flag
1361.40 94 131.2 105.6 6 C

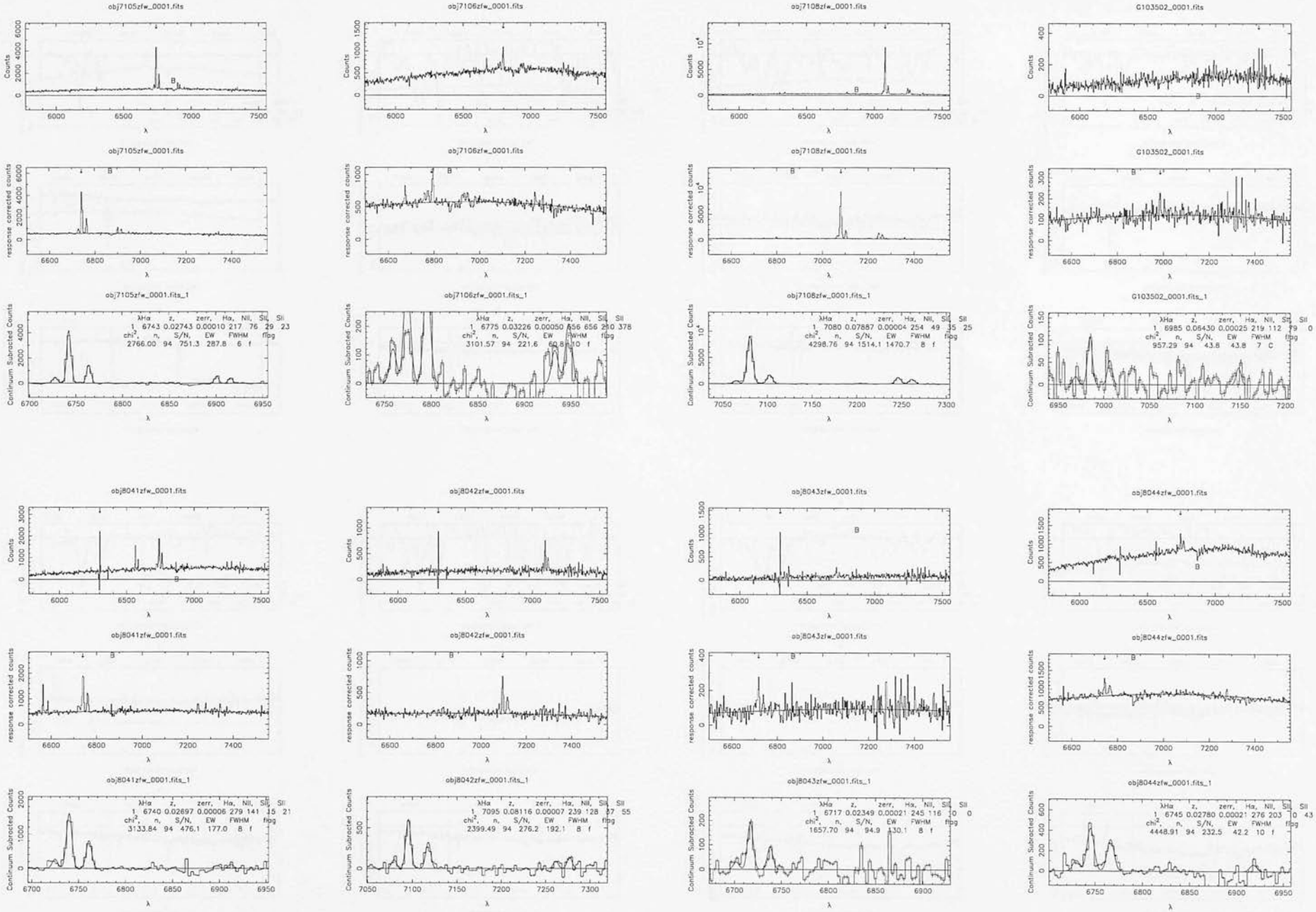
obj7105zfw_0001.fits
obj7106zfw_0001.fits
obj7108zfw_0001.fits
G103502_0001.fits
Counts
λ
B
obj7105zfw_0001.fits
obj7106zfw_0001.fits
obj7108zfw_0001.fits
G103502_0001.fits
response corrected counts
λ
B
obj7105zfw_0001.fits_1
obj7106zfw_0001.fits_1
obj7108zfw_0001.fits_1
G103502_0001.fits_1
Continuum Subtracted Counts
λ
λHα z, zerr, Hα, NII, SII, SII
1 6743 0.02743 0.00010 217 76 29 23
chi², n, S/N, EW FWHM flag
2766.00 94 751.3 287.8 6 f
1 6775 0.03226 0.00050 656 656 210 378
3101.57 94 221.6 68.8 10 f
1 7080 0.07887 0.00004 254 49 35 25
4298.76 94 1514.1 1470.7 8 f
1 6985 0.06430 0.00025 219 112 79 0
957.29 94 43.8 43.8 7 C
obj8041zfw_0001.fits
obj8042zfw_0001.fits
obj8043zfw_0001.fits
obj8044zfw_0001.fits
Counts
λ
B
obj8041zfw_0001.fits
obj8042zfw_0001.fits
obj8043zfw_0001.fits
obj8044zfw_0001.fits
response corrected counts
λ
B
obj8041zfw_0001.fits_1
obj8042zfw_0001.fits_1
obj8043zfw_0001.fits_1
obj8044zfw_0001.fits_1
Continuum Subtracted Counts
λ
λHα z, zerr, Hα, NII, SII, SII
1 6740 0.02697 0.00006 279 141 15 21
chi², n, S/N, EW FWHM flag
3133.84 94 476.1 177.0 8 f
1 7095 0.08116 0.00007 239 128 87 55
2399.49 94 276.2 192.1 8 f
1 6717 0.02349 0.00021 245 116 10 0
1657.70 94 94.9 130.1 8 f
1 6745 0.02780 0.00021 276 203 0 43
4448.91 94 232.5 42.2 10 f

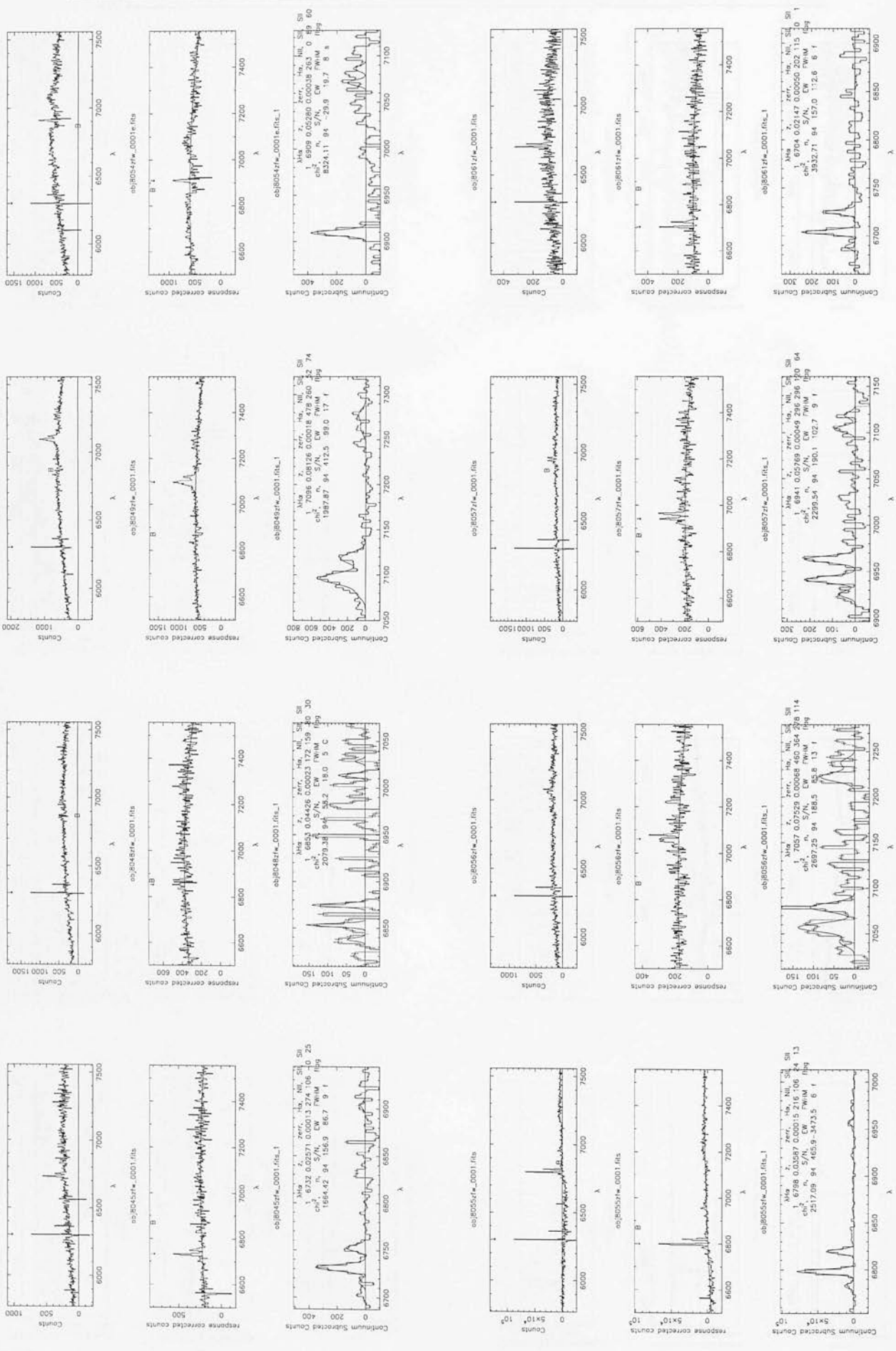

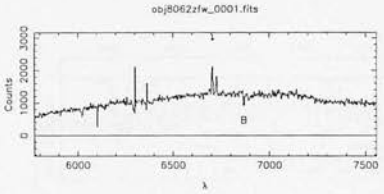
obj8062zfw_0001.fits
Counts
λ

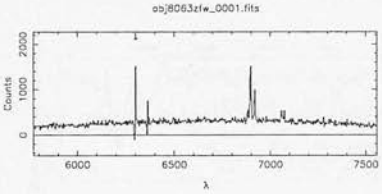
obj8063zfw_0001.fits
Counts
λ

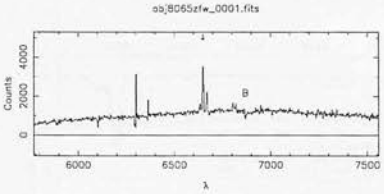
obj8065zfw_0001.fits
Counts
λ

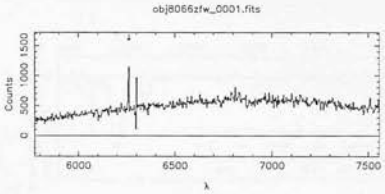
obj8066zfw_0001.fits
Counts
λ

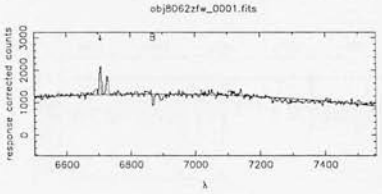
obj8062zfw_0001.fits
response corrected counts
λ

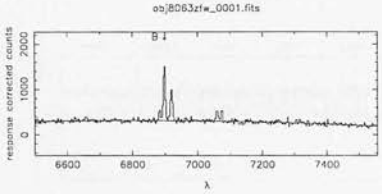
obj8063zfw_0001.fits
response corrected counts
λ

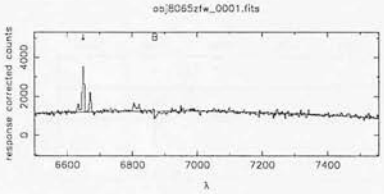
obj8065zfw_0001.fits
response corrected counts
λ

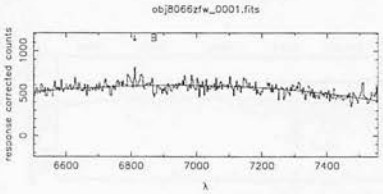
obj8066zfw_0001.fits
response corrected counts
λ

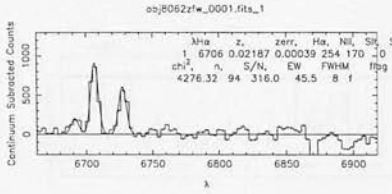
obj8062zfw_0001.fits_1
λHα z zerr Hα NII SII SII
1 6706 0.02187 0.00039 254 170 0 0
chi² n S/N EW FWHM flag
4276.32 94 316.0 45.5 8 f
Continuum Subracted Counts
λ

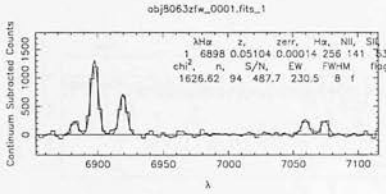
obj8063zfw_0001.fits_1
λHα z zerr Hα NII SII SII
1 6898 0.05104 0.00014 256 141 53 47
chi² n S/N EW FWHM flag
1626.62 94 487.7 230.5 8 f
Continuum Subracted Counts
λ

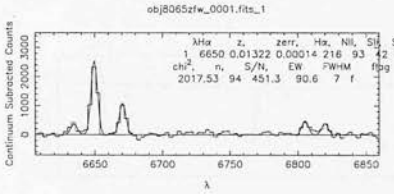
obj8065zfw_0001.fits_1
λHα z zerr Hα NII SII SII
1 6650 0.01322 0.00014 216 93 42 34
chi² n S/N EW FWHM flag
2017.53 94 451.3 90.6 7 f
Continuum Subracted Counts
λ

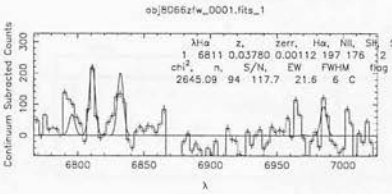
obj8066zfw_0001.fits_1
λHα z zerr Hα NII SII SII
1 6811 0.03780 0.00112 197 176 2 82
chi² n S/N EW FWHM flag
2645.09 94 117.7 21.6 6 C
Continuum Subracted Counts
λ

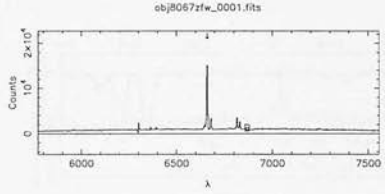
obj8067zfw_0001.fits
Counts
λ

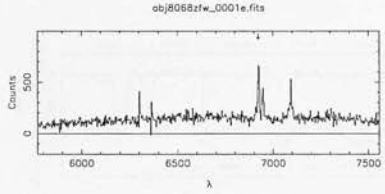
obj8068zfw_0001e.fits
Counts
λ

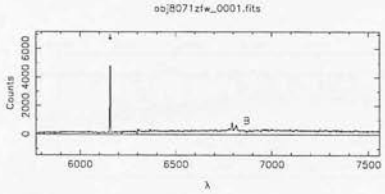
obj8071zfw_0001.fits
Counts
λ

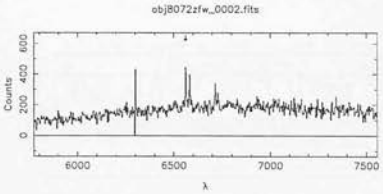
obj8072zfw_0002.fits
Counts
λ

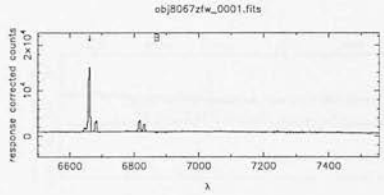
obj8067zfw_0001.fits
response corrected counts
λ

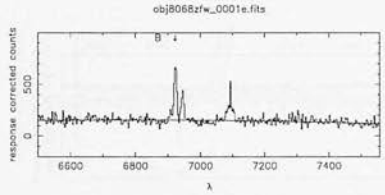
obj8068zfw_0001e.fits
response corrected counts
λ

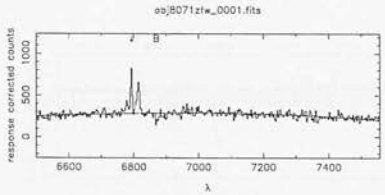
obj8071zfw_0001.fits
response corrected counts
λ

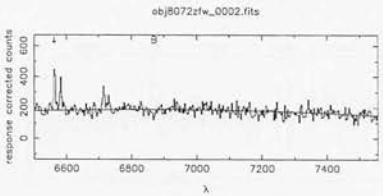
obj8072zfw_0002.fits
response corrected counts
λ

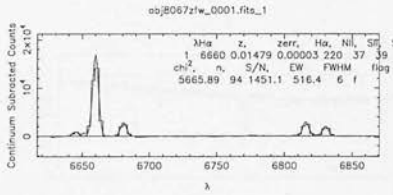
obj8067zfw_0001.fits_1
λHα z zerr Hα NII SII SII
1 6660 0.01479 0.00003 220 37 39 27
chi² n S/N EW FWHM flag
5665.89 94 1451.1 516.4 6 f
Continuum Subracted Counts
λ

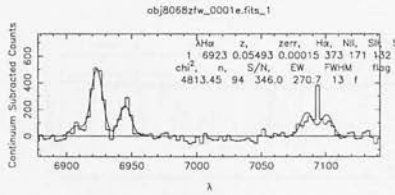
obj8068zfw_0001e.fits_1
λHα z zerr Hα NII SII SII
1 6923 0.05493 0.00015 373 171 152 120
chi² n S/N EW FWHM flag
4813.45 94 346.0 270.7 13 f
Continuum Subracted Counts
λ

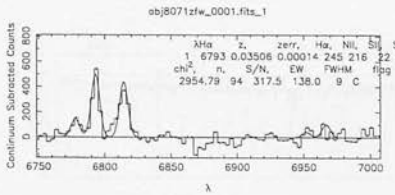
obj8071zfw_0001.fits_1
λHα z zerr Hα NII SII SII
1 6793 0.03506 0.00014 245 216 22 50
chi² n S/N EW FWHM flag
2954.79 94 317.5 138.0 9 C
Continuum Subracted Counts
λ

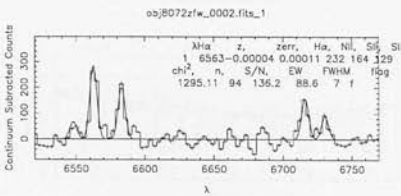
obj8072zfw_0002.fits_1
λHα z zerr Hα NII SII SII
1 6563-0.00004 0.00011 232 164 129 73
chi² n S/N EW FWHM flag
1295.11 94 136.2 88.6 7 f
Continuum Subracted Counts
λ

obj8064r#_0001.fits
Counts
response corrected counts
Continuum Subtracted Counts
λ
obj8064r#_0001.fits_1
λHa z zerr Ha NII SII
1 7103 0.08232 0.00054 457 340 84 98
chi² n S/N EW FWHM flag
2078.94 94 283.3 93.5 16 f
obj8080r#_0001.fits
obj8080r#_0001.fits_1
λHa z zerr Ha NII SII
1 6993 0.06560 0.00027 268 93 41 28
chi² n S/N EW FWHM flag
2116.41 94 257.8 199.2 8 f
obj8077r#_0001.fits
obj8077r#_0001.fits_1
λHa z zerr Ha NII SII
1 6860 0.04532 0.00016 279 96 46 48
chi² n S/N EW FWHM flag
1738.04 94 359.3 236.5 8 f
obj8076r#_0001.fits
obj8076r#_0001.fits_1
λHa z zerr Ha NII SII
1 6741 0.02722 0.00020 259 224 17 36
chi² n S/N EW FWHM flag
1447.48 94 384.1 154.8 9 f
obj8092r#_0001.fits
obj8092r#_0001.fits_1
λHa z zerr Ha NII SII
1 7239 0.10308 0.00007 331 100 38 32
chi² n S/N EW FWHM flag
1997.42 94 608.8 884.3 10 f
obj8091r#_0001.fits
obj8091r#_0001.fits_1
λHa z zerr Ha NII SII
1 6800 0.03618 0.00010 279 157 46 48
chi² n S/N EW FWHM flag
2671.97 94 695.6 314.3 9 f
obj8090r#_0001.fits
obj8090r#_0001.fits_1
λHa z zerr Ha NII SII
1 7331 0.11705 0.00030 354 192 55 36
chi² n S/N EW FWHM flag
1749.59 94 251.7 311.7 12 f
obj8089r#_0001.fits
obj8089r#_0001.fits_1
λHa z zerr Ha NII SII
1 7007 0.06769 0.00007 271 69 25 19
chi² n S/N EW FWHM flag
3796.50 94 1234.1 1568.1 9 f

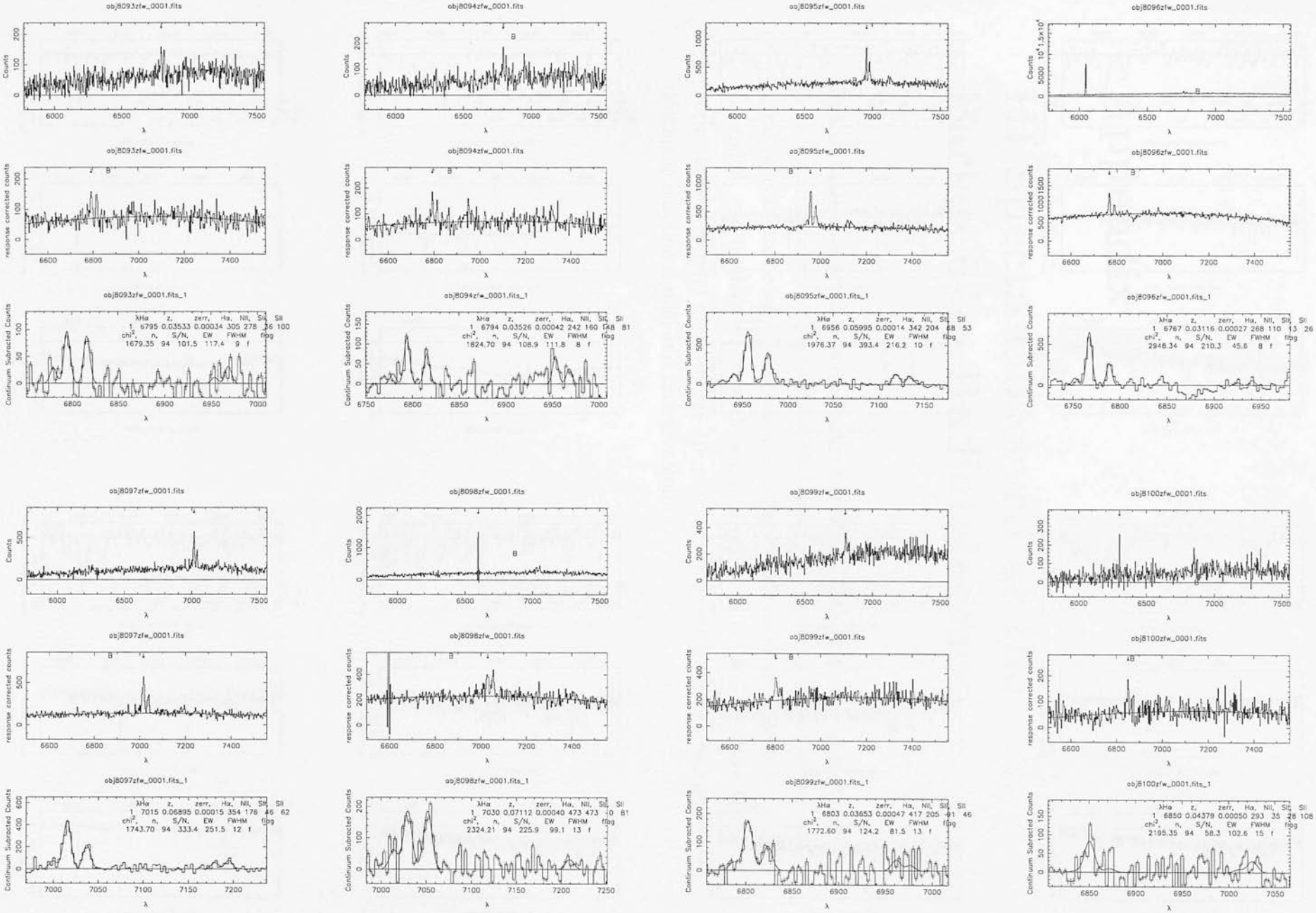
obj8093zfw_0001.fits
obj8094zfw_0001.fits
obj8095zfw_0001.fits
obj8096zfw_0001.fits
obj8093zfw_0001.fits_1
obj8094zfw_0001.fits_1
obj8095zfw_0001.fits_1
obj8096zfw_0001.fits_1
obj8097zfw_0001.fits
obj8098zfw_0001.fits
obj8099zfw_0001.fits
obj8100zfw_0001.fits
obj8097zfw_0001.fits_1
obj8098zfw_0001.fits_1
obj8099zfw_0001.fits_1
obj8100zfw_0001.fits_1
Counts
response corrected counts
Continuum Subracted Counts
λ

obj8101zfw_0001.fits
Counts
obj8101zfw_0001.fits
response corrected counts
obj8101zfw_0001.fits_1
Continuum Subtracted Counts
obj8102zfw_0001.fits
Counts
obj8102zfw_0001.fits
response corrected counts
obj8102zfw_0001.fits_1
Continuum Subtracted Counts
obj8104zfw_0001.fits
Counts
obj8104zfw_0001.fits
response corrected counts
obj8104zfw_0001.fits_1
Continuum Subtracted Counts
obj8105zfw_0001.fits
Counts
obj8105zfw_0001.fits
response corrected counts
obj8105zfw_0001.fits_1
Continuum Subtracted Counts
obj8106zfw_0001.fits
Counts
obj8106zfw_0001.fits
response corrected counts
obj8106zfw_0001.fits_1
Continuum Subtracted Counts
obj8108zfw_0001.fits
Counts
obj8108zfw_0001.fits
response corrected counts
obj8109zfw_0001.fits_1
Continuum Subtracted Counts
obj8111zfw_0001.fits
Counts
obj8111zfw_0001.fits
response corrected counts
obj8111zfw_0001.fits_1
Continuum Subtracted Counts
obj8114zfw_0001.fits
Counts
obj8114zfw_0001.fits
response corrected counts
obj8114zfw_0001.fits_1
Continuum Subtracted Counts

Appendix H

HI Specta Observed at the Parkes 64m Radiotelescope

Extracted 21cm spectra from the Parkes Multibeam instrument are presented. In the majority of cases, the classic double-horned profile characteristic of edge-on spiral galaxies can be very clearly seen, allowing measurement of redshift, velocity dispersion, and luminosity. As such, much of this data is ideal for Tully-Fisher work. Less successful observations are also apparent, with classic examples of dominant baseline ripple, and excessive noise.

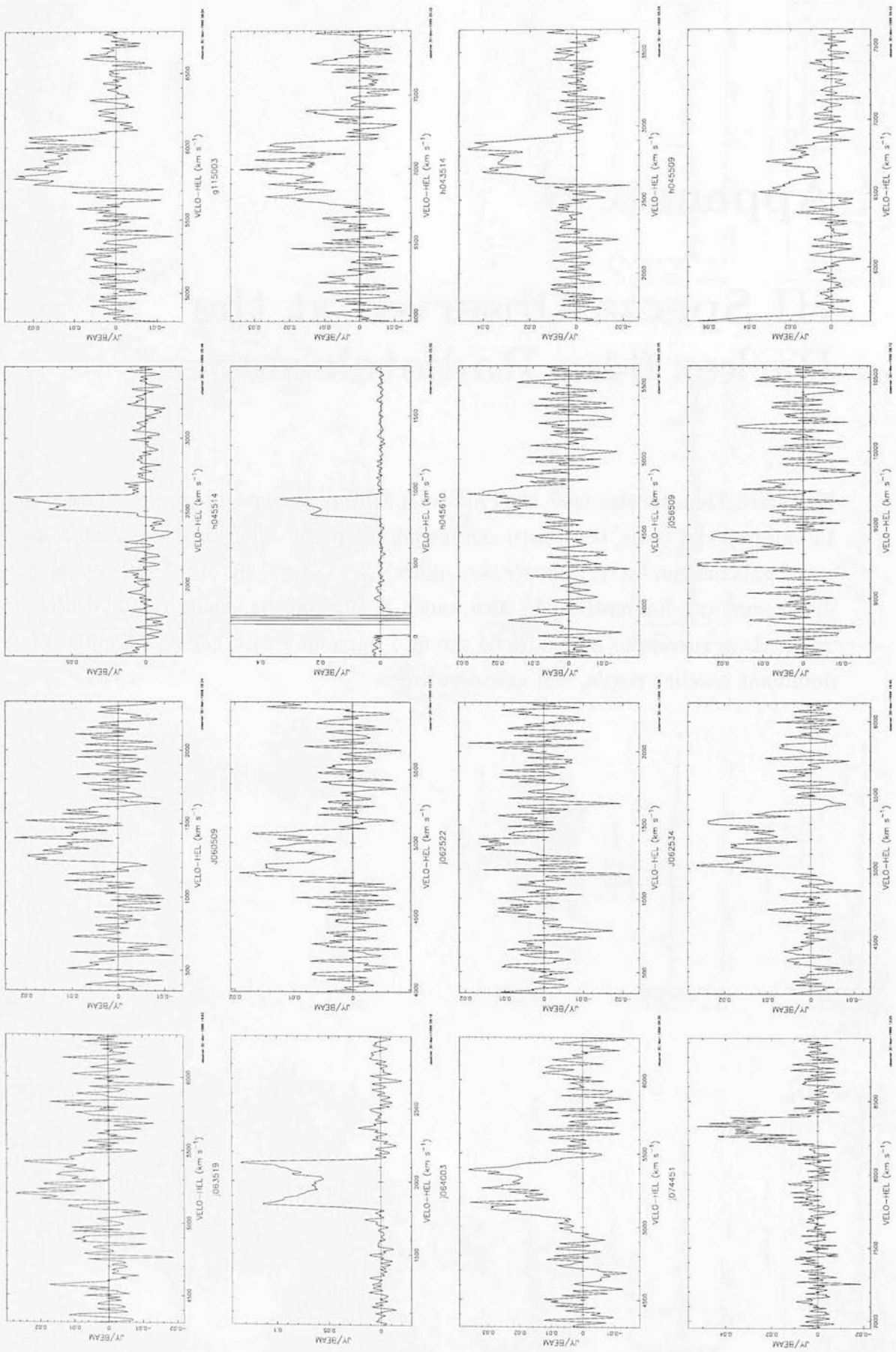
g043503
g115003
h043514
h045509
h045514
h045514
h045610
j065509
j065702
j065509
j062522
j062534
j062535
j063519
j064003
j074451
VELO-HEL (km s⁻¹)
Jy/BEAM

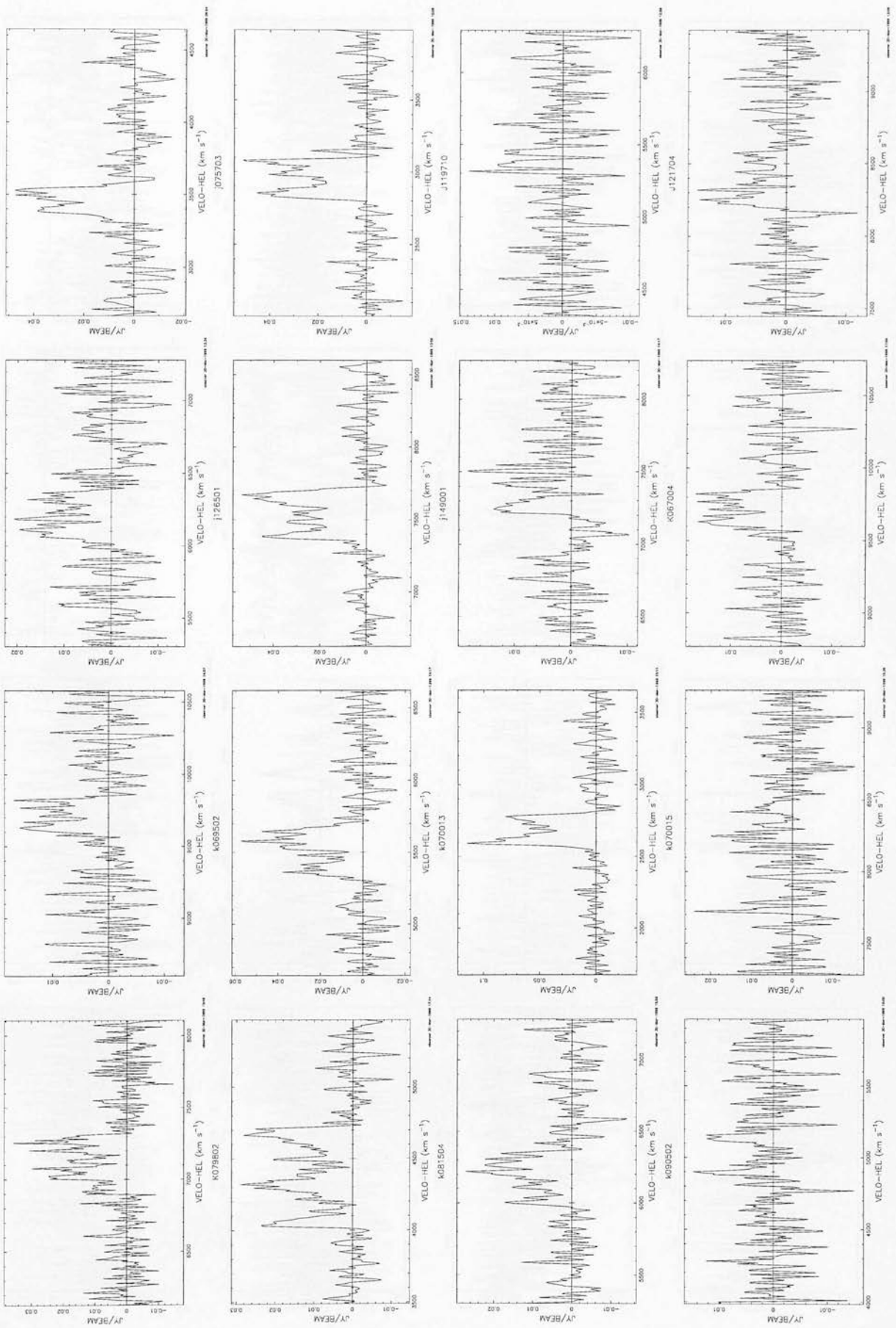
j075702
j075703
j119710
j121704
j124502
j126501
j149001
k067004
k067004
k069502
k070013
k070015
k073701
k079802
k081504
k090502
VELO-HEL (km s^{-1})
uv/BEAM

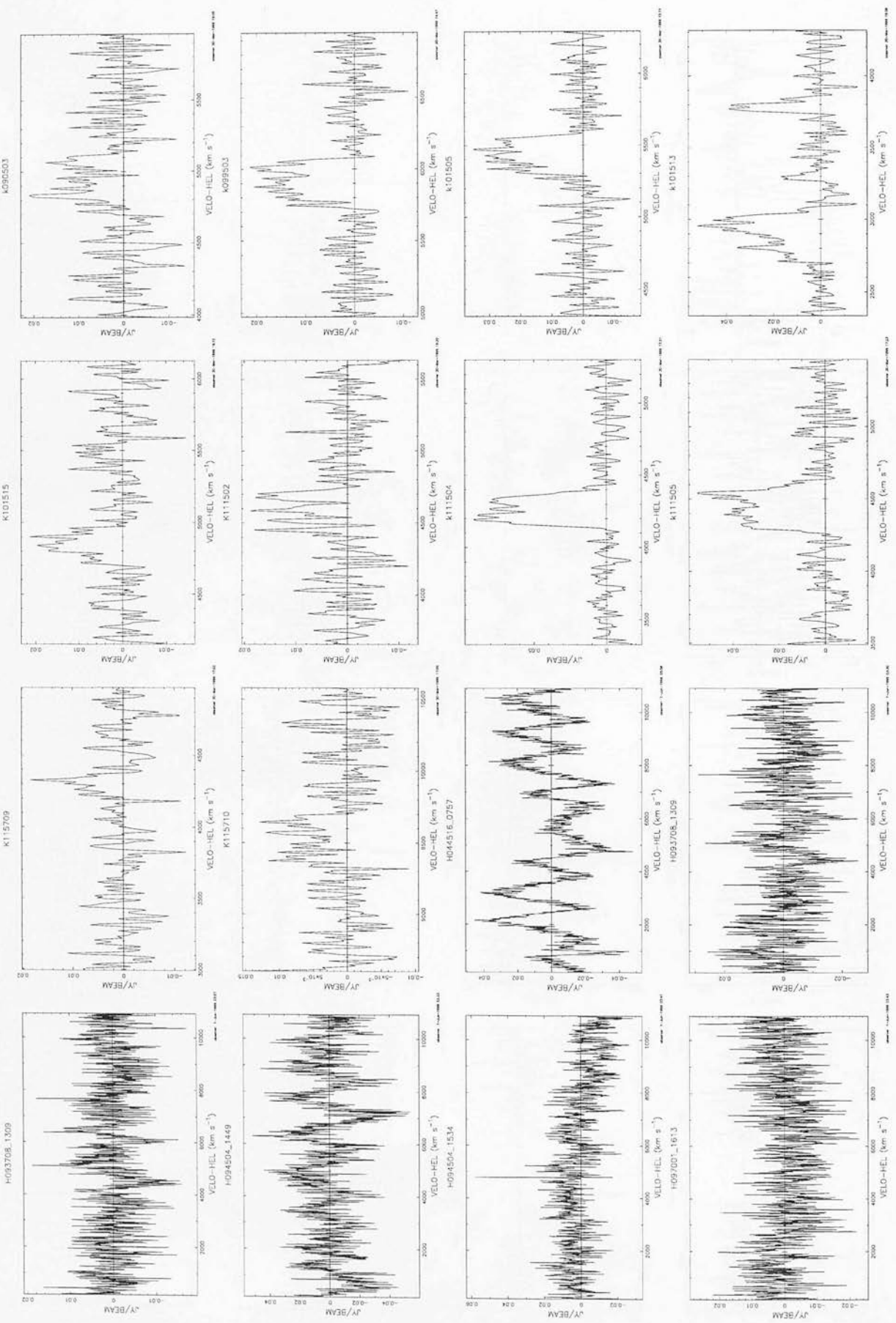
k090503
k099503
k101505
k101513
K101515
K111502
k111504
k111505
K115709
K115710
H044516_0757
H093708_1309
H093708_1309
H094504_1449
H094504_1534
H097001_1613
VELO-HEL (km s^{-1})
Jy/BEAM

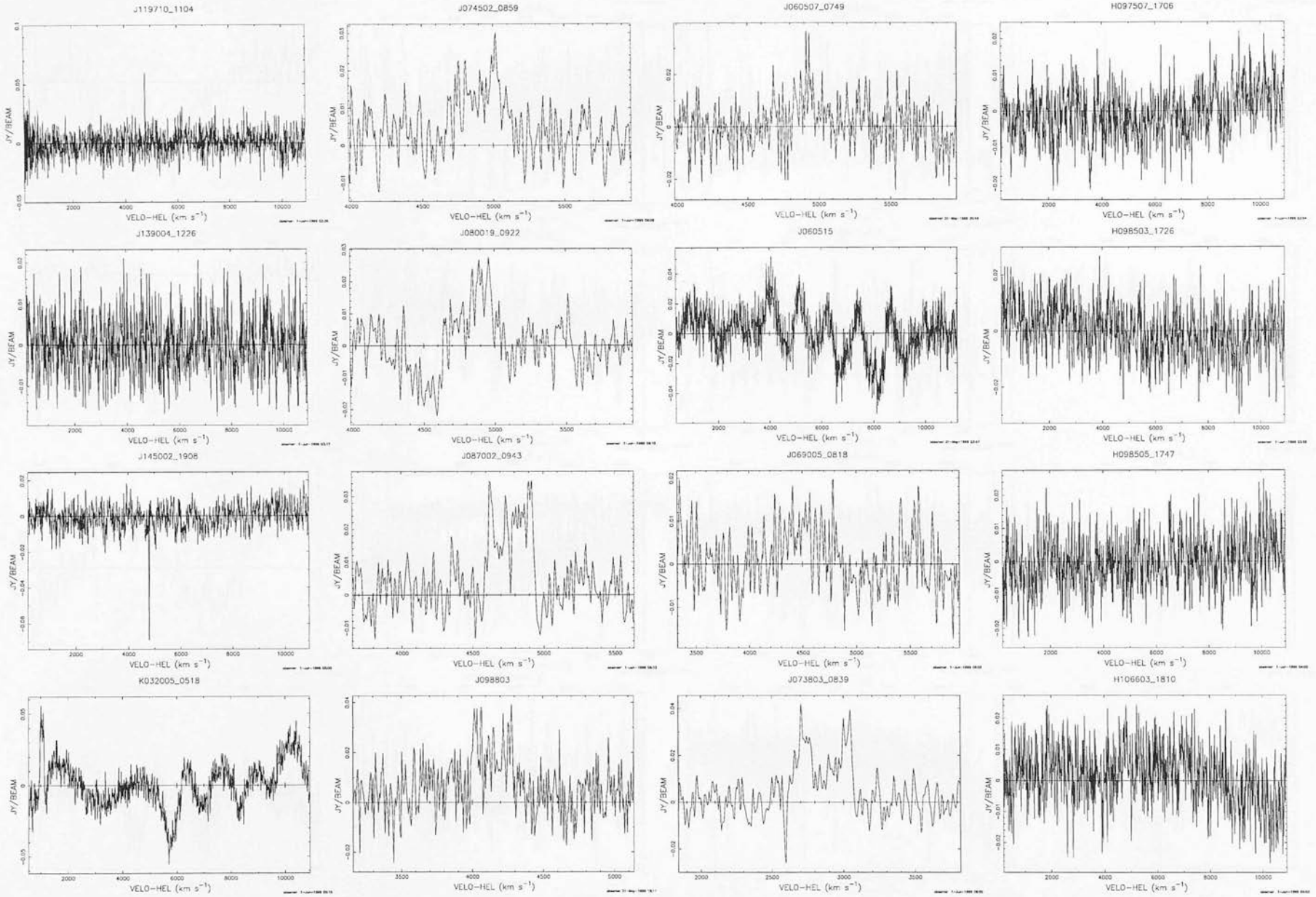
J119710_1104
J074502_0859
J060507_0749
H097507_1706
J139004_1226
J080019_0922
J060515
H098503_1726
J145002_1908
J087002_0943
J069005_0818
H098505_1747
K032005_0518
J098803
J073803_0839
H106603_1810
JY/BEAM
VELO-HEL (km s^{-1})

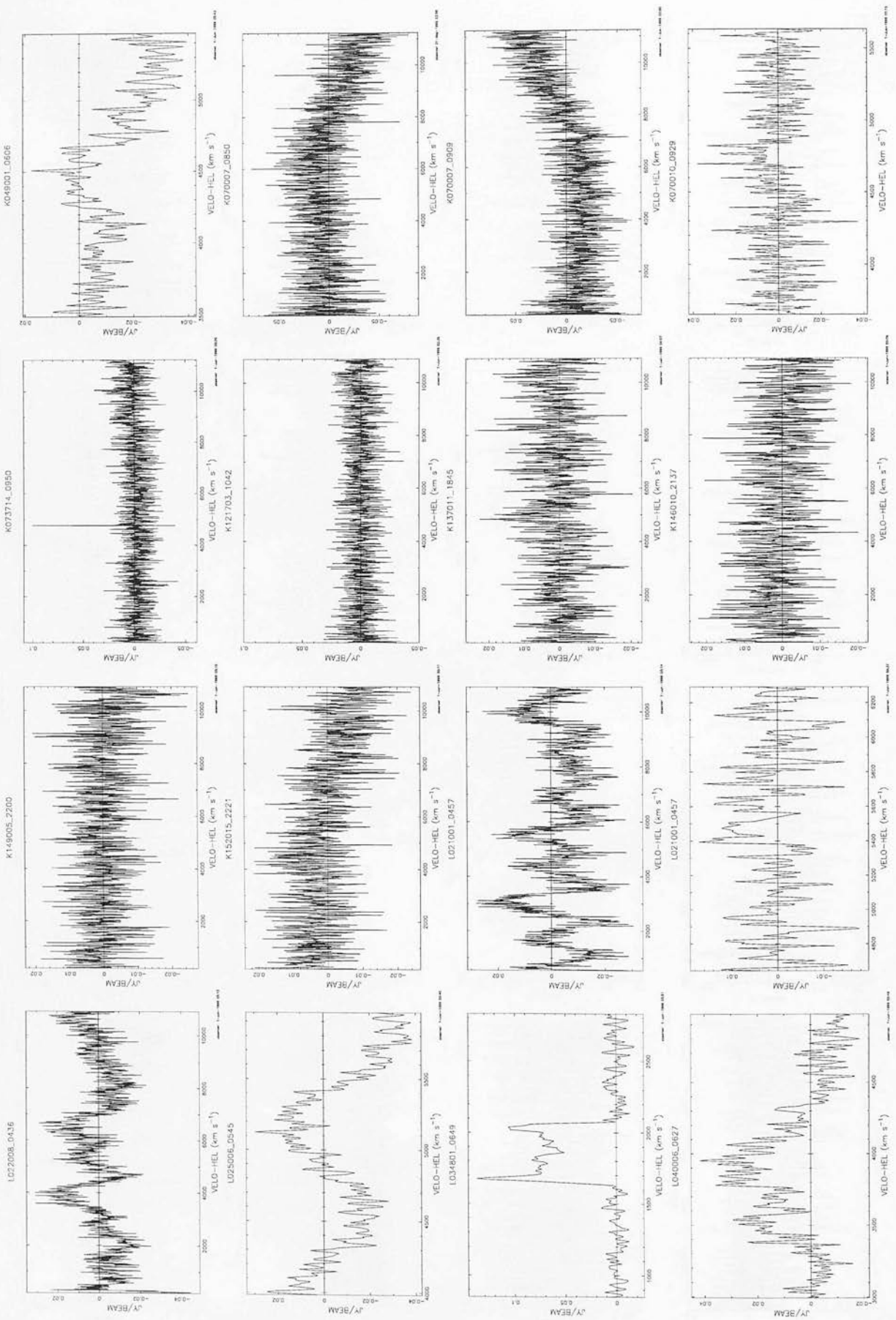
K049001_0606
K070007_0850
K070007_0909
K070010_0929
K073714_0950
K121703_1042
K137011_1845
K146010_2137
K149005_2200
K152015_2221
L021001_0457
L021001_0457
L022008_0436
L025006_0545
L034801_0649
L040006_0627
VELO-HEL (km s^{-1})
Jy/BEAM

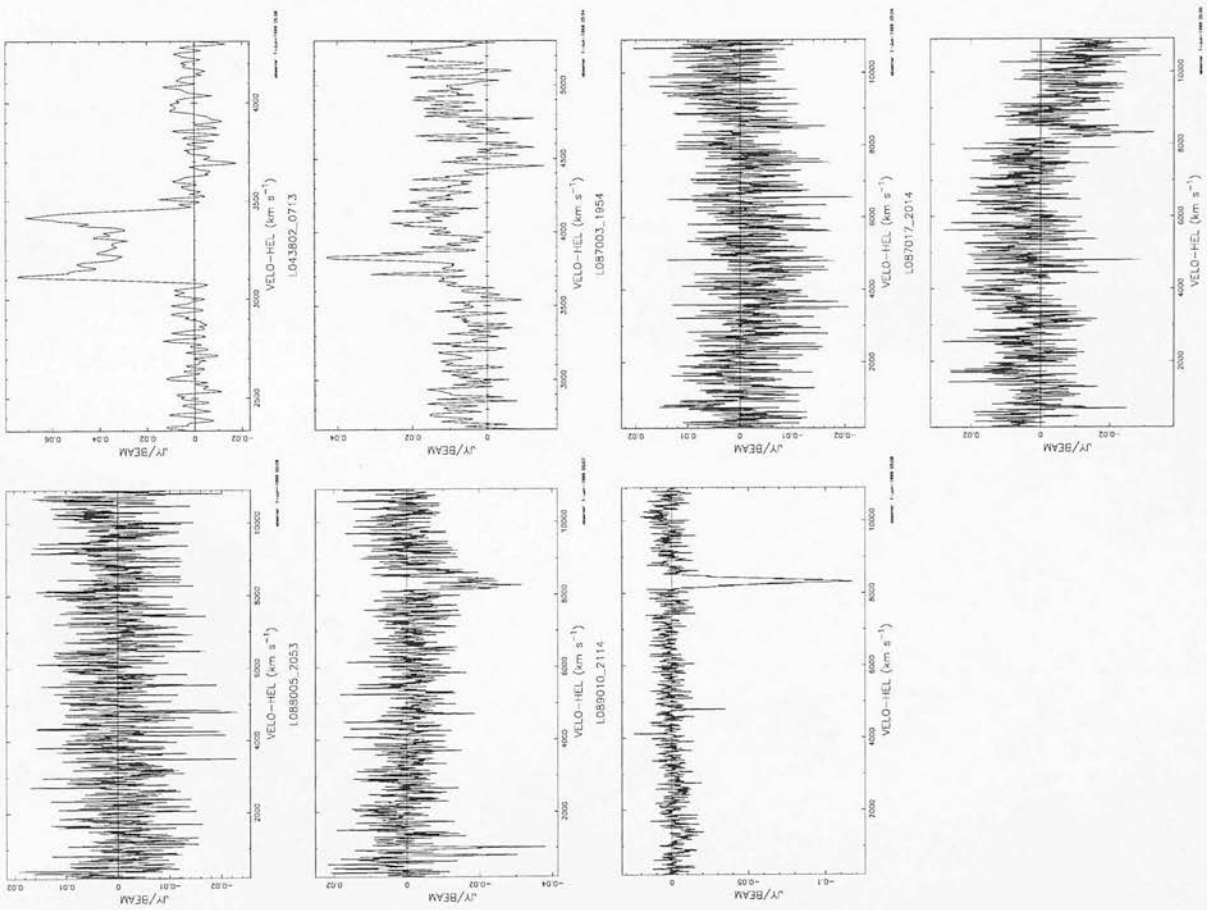
L042005_0733
L043802_0713
L087003_1954
L087017_2014
L087501_2034
L088005_2053
L089010_2114
VELO-HEL (km s^{-1})
μV/BEAM